ELECTRONIC PROPERTIES
OF SOME ZINC-TRANSITION METAL COMPOUNDS

Thesis submitted for the Degree of Doctor of Philosophy

in the University of London

by

J. B. DUNLOP

Physics Department

Imperial College of Science and Technology

London, S.W.7.

April, 1972

ABSTRACT

The ζ-phase intermetallic compounds $MnZn_{13}$, $FeZn_{13}$ and $CoZn_{13}$ are crystallographically well-ordered, with no nearest neighbour transition metal atoms. Magnetic susceptibility, specific heat and electrical resistivity measurements have been made on these compounds while bearing in mind their relationships to two limiting cases in the theory of magnetism :- the dilute transitional impurity dissolved in a free-electron-like solvent and the pure transition metal. The high temperature susceptibility of $MnZn_{13}$ fits a Curie-Weiss law with $p_{eff} = 1.8\,\mu_B$ and $\theta = 36$ K, and orders magnetically at about 20 K. The susceptibilities of $CoZn_{13}$ and $FeZn_{13}$ are almost temperature independent but $FeZn_{13}$ is distinctly more paramagnetic than $CoZn_{13}$.

The electronic specific heat coefficient of $FeZn_{13}$ is increased with respect to that of $CoZn_{13}$.

The compounds have resistance ratios between 10 and 30 and the low temperature resistivities are strongly temperature dependent, that of $MnZn_{13}$ being proportional to $T^{\frac{3}{2}}$ and due to scattering by spin excitations, while $FeZn_{13}$ shows T^2 behaviour, indicative of electron-electron scattering.

The close correlation between the magnetic properties of the compounds and the corresponding dilute solutions in zinc, where Mn, Fe and Co are respectively magnetic, on the borderline, and non-magnetic suggests that the magnetic state of a transition atom in the compounds is determined by the local environment and may be thought of as forming a virtual bound state. This implies that s - d hybridization, and not d - d overlap, is the dominant factor in determining the electronic properties and band structure.

ACKNOWLEDGEMENTS

I would like to express my sincere thanks to Professor B. R. Coles and Dr. A. D. Caplin for their supervision of this work and for their continuous interest and encouragement.

I am indebted to Dr. J. R. Cooper for the use of his specific heat apparatus at the University of Genoa and for his cooperation in making all the measurements. I would also like to thank the members of the Genoa Solid State Group for their hospitality.

I am grateful to Mr. R. H. Taylor for making the E.S.R. measurements which are reported in this work and to Dr. J. B. Forsyth at Harwell for neutron diffraction measurements on one of our samples.

My thanks are due to Dr. A. M. Stewart for his assistance in the x-ray structural analysis of the compounds, to Dr. H. E. N. Stone for his help with the metallurgy and to all members of the Solid State Group for their help and valuable discussions.

I would also like to thank my wife Wendy for her encouragement and for typing the thesis.

I am grateful to the S. R. C. for providing a Research Studentship during the course of this work and to the U.K.A.E.A. for a research bursary during its later stages.

CONTENTS

		Page number
ABSTRACT		2
ACKNOWLEDGEMENTS		3
CONTENTS		4
INTRODUCTION		9
CHAPTER 1	THEORY AND PAST WORK	10
1.1	THEORY OF THE ISOLATED SOLUTE ATOM	10
	Introduction	10
	Friedel Sum Rule and Virtual Bound States	10
	The Anderson Model	13
	Generalisation of the Anderson Model to the Case of Degenerate Orbitals and the Inclusion of J, the Coulomb Exchange energy	18
	Wolff-Clogston Model	20
	Validity of the Hartree-Fock Approximation and Electron-Correlation Effects	21
	The Schrieffer-Wolff Transformation	23
	The Kondo Effect and the s - d Exchange Hamiltonian	24
	Developments since Kondo's Original Paper	27
	Localised Spin Fluctuations	28
1.2	INTERACTION MECHANISMS BETWEEN SOLUTE ATOMS	31
	Zener	31
	The R.K.K.Y. Interaction	31
	Blandin and Friedel	35
	Caroli	35
	Alexander and Anderson	39
	Moriya	40
	Kim	40
	Treatment of interactions in disordered systems	42

		Page number
1.3	THEORY OF DILUTE INTERMETALLIC COMPOUNDS	43
	Discussion of theoretical approaches	43
	Daniel's hybrid band picture	47
	Hargitai	49
	Treatment of magnetic interactions in ordered compounds	52
1.4	PHYSICAL PROPERTIES OF MATERIALS	54
	SPECIFIC HEAT	54
	The lattice specific heat	55
	Electronic specific heat	58
	Contribution to the specific heat from resonant states	60
	Spin-wave specific heat	61
	MAGNETIC SUSCEPTIBILITY	61
	Permanent magnetic moments	62
	Pauli spin paramagnetism	64
	Contribution to Pauli paramagnetism from virtual bound states	65
	Core diamagnetism	66
	Conduction electron diamagnetism	67
	ELECTRICAL RESISTIVITY	68
	Phonon resistivity	70
	Inter-band scattering	71
	Electron-electron scattering	72
	Spin disorder resistivity	73
	Impurity resistivity	74
1.5	REVIEW OF THE PROPERTIES OF DILUTE SOLUTIONS OF TRANSITION METAL ATOMS DISSOLVED IN ZINC	75
	The Zn-Mn System	75

		Page number
	The Zn-Fe System	76
	The Zn-Co System	77
	Residual Resistivities of 3d Impurities in zinc	77
1.6	PREVIOUS WORK ON DILUTE TRANSITION METAL COMPOUNDS	79
	Zinc-rich Transition Metal compounds	79
	Beryllium-rich Transition Metal compounds	81
	Aluminium-rich Transition Metal compounds	82
	Charge Transfer in Aluminium-Transition compounds	83
CHAPTER 2	THE ζ-PHASE COMPOUNDS	85
	Phase Diagrams and crystal structure	85
	Specimen Preparation	90
	Metallurgical Examination	92
	(a) Microscopic	93
	(b) Electron Microprobe Analysis	93
	(c) X-ray Powder Spectra	94
	Machining of Resistivity Specimens	98
	Machining of Susceptibility Specimens	99
	Specific Heat Specimens	100
	Single Crystals of $MnZn_{13}$	100
	ζ-Phase $CrZn_{13}$ (?)	104
	Additional Specimens	106
	$Mn_{0.05}Fe_{0.95}Zn_{13}$	106
	The δ_1-phase in the MnZn System	106
CHAPTER 3	EXPERIMENTAL METHODS AND APPARATUS	108
	Magnetic Susceptibility	108
3.1	The Magnetic Susceptibility Balance	108

		Page number
	Thermometry	113
	Thermometer Calibrations	114
	Magnetic Field Constants	117
	Balance Calibration and Sensitivity	119
	Experimental Proceedure	119
	Specimen Replacement and Positioning	119
	Force Measurement	120
	Temperature Control	122
3.2	The Vibration Magnetometer	123
	Thermometers and their Calibration	126
	Temperature Control	127
	Magnetic Field Calibration	128
	Nulling-coil Calibration	128
	Nulling-coil Heating Effects	128
	Experimental Proceedure	129
3.3	The Specific Heat Aparatus	131
	Thermometers	133
	Experimental Proceedure	133
3.4	Electrical Resistivity Apparatus	140
	Thermometers and Temperature Control	141
CHAPTER 4	EXPERIMENTAL RESULTS	144
	Introduction	144
	Specific Heat Measurements	144
	Magnetic Susceptibility	151
	Electrical Resistivity	174
	Magneto-resistance	176

		Page number
	E.S.R.	193
	Neutron Diffraction	193
CHAPTER 5	DISCUSSION	198
	Introduction	198
	Specific Heat	203
	Magnetic Susceptibility	205
	Electrical Resistivity	214
	Conclusion	218
REFERENCES		220

INTRODUCTION

The ζ-phase intermetallic compounds are crystallographically well ordered and have the stoichiometric composition XZn_{13}, where X can be Mn, Fe or Co. The transition atoms are well separated ($\sim 5A^{o}$) and compounds of this type represent an interesting intermediate situation between the dilute transitional impurity dissolved in a free-electron-like solvent and the pure transition metal itself. They combine the localised nature of the former problem with the periodicity of the latter.

Chapter 1 begins by reviewing some of the theories of dilute solutions of transition atoms in simple metal hosts, and the possible interaction mechanisms between the solute atoms. Although no specific theory for the class of dilute compounds exists, proposals are suggested for various directions from which a theory might develop. There is also a brief review of the various factors which contribute towards the magnetic susceptibility, specific heat and electrical resistivity of such materials. The properties of dilute solid solutions of transition atoms in zinc are reviewed, as are previous measurements on the ζ-phase compounds and others of their type.

Chapter 2 is concerned with the metallurgy of the ζ-phase compounds, including phase diagrams, crystal structures, preparation techniques and examination proceedures.

Experimental apparatus and proceedures are described in chapter 3. The results of our measurements are presented in chapter 4 and discussed in chapter 5.

CHAPTER 1

THEORY AND PAST WORK

THEORY OF THE ISOLATED SOLUTE ATOM

Introduction

The 3d transition series atoms show a remarkable variation in their magnetic and electronic properties when dissolved in metallic matrices. For example Waszink (1) has investigated the localised magnetic moments of 3d transition series atoms dissolved in alloys of copper and zinc and found large variations as the electron per atom ratio of the matrix was changed. Two theoretical models were proposed to account for this behaviour by taking into consideration the large interaction between the d electrons of the solute atoms and the conduction electrons. Both models are based on the concept of virtual bound states first introduced into the theory of dilute alloys by Friedel (2).

Friedel Sum Rule and Virtual Bound States

Friedel (2) analyses the scattering of conduction electrons by an impurity, represented by a spherically symmetrical potential V(r), in terms of spherical harmonics and their associated phase shifts η_l in the free electron approximation. The resultant expression for the screening charge per unit k inside a large sphere of radius R is:

$$\int_0^R \frac{d}{dk}(\rho-\rho_0)4\pi r^2 dr = \frac{2}{\pi}\sum_l (2l+1)\left[\frac{d\eta_l}{dk} - \frac{1}{k}\sin\phi_l \cos(2kR+\eta_l - l\pi)\right] \qquad 1.1$$

Integrating this expression up to k_F gives the total screening charge within the sphere.

$$= \frac{2}{\pi}\sum_{\ell}(2\ell+1)\eta_\ell(E_F)$$

From charge neutrality considerations this total screening charge must equal the excess impurity charge Z, giving the Friedel Sum Rule:

$$Z = \frac{2}{\pi}\sum_{\ell}(2\ell+1)\eta_\ell(E_F) \qquad 1.2$$

The presence of the impurity also induces long range charge oscillations in the conduction band of the host material having the asymptotic form at large distances (r):

$$\Delta\rho^{\sigma}(r) \cong \frac{-1}{4\pi^2} k_F^3 \sum_{\ell}(-)^{\ell}(2\ell+1)\sin\eta_\ell^{\sigma} \frac{\cos(2k_F r+\eta_\ell^{\sigma})}{(k_F r)^3} \qquad 1.3$$

where k_F is the Fermi wave vector and σ the spin index. Similar charge oscillation effects are observed in alternative approaches to the impurity screening problem by Kohn and Vosko (3) and by March and Murray (4).

Friedel adapted the concept of virtual bound states to the transition metal impurity problem. He considered an atom with a spherically symmetrical potential just strong enough to accept on ℓ^{th} bound state. If the potential becomes weaker the energy of this ℓ^{th} state will rise until it merges into the continuum where it is broadened in energy due to its resonance

with the ℓ^{th} spherical component of the continuum states and may be considered as a virtual bound level. This is shown schematically in figure 1.1

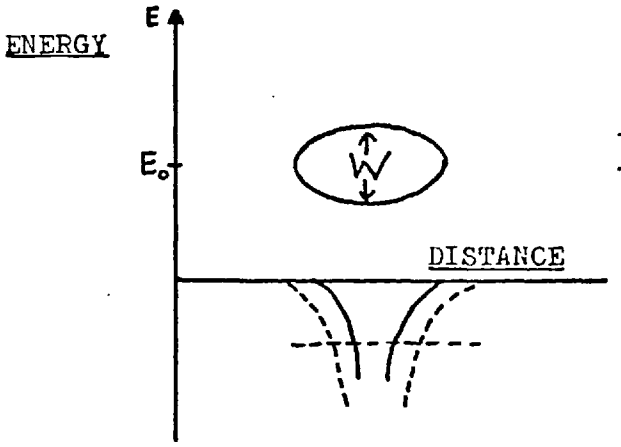


FIGURE 1.1

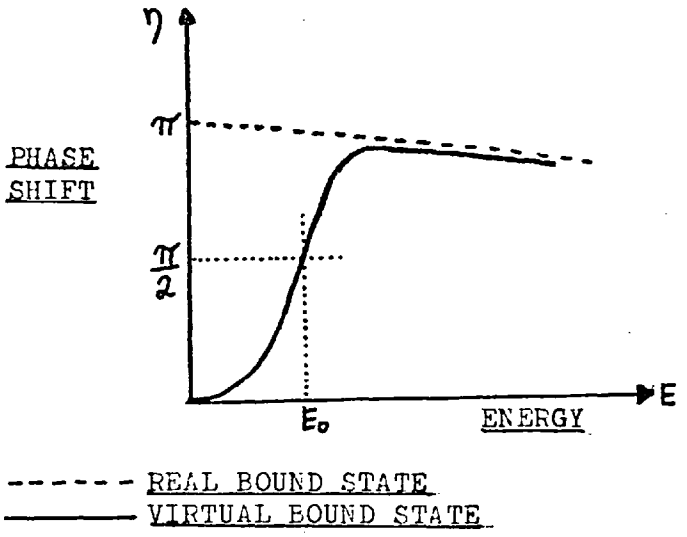


FIGURE 1.2

AFTER REFERENCE (5)

It is interesting to compare the behaviour of the phase shift η_ℓ as a function of energy for the cases of real and virtual bound states, this is shown in figure 1.2. It can be seen that η_ℓ increases rapidly from nearly zero to nearly π in a region of width W around E_o. The form of the density of states associated with the virtual bound state may be determined by differentiating equation 1.2 with respect to energy.

$$n(E) = \frac{2}{\pi}\sum_{\ell}(2\ell + 1)\frac{d\eta_\ell}{dE} \qquad 1.4$$

The maximum value occurs at the point of inflexion of η_ℓ versus E in figure 1.2 i.e. at E_o. As the incident electron energy is raised the resonant scattering passes through a maximum at $E = E_o$

Friedel was able to account for the observed resistivities of 3d transitional atoms dissolved in aluminium. The broad maximum centred around the middle of the transition series is interpreted as due to strong resonant scattering when the virtual bound state (capable of holding ten electrons) crosses the Fermi level.

Both Friedel and later Blandin and Friedel (5) investigated the possibility that the virtual bound state will split into two states of different spin directions due to exchange correlations. The condition for this to occur is that

$$p\Delta E > w$$

where p is the number of d electrons or holes and ΔE the exchange energy per electron.

A spin-split virtual bound state will lead to two separate peaks in the resistivities of 3d transition metal solutes as each half crosses the Fermi level. This behaviour is observed for transition metal impurities dissolved in copper or gold.

The Anderson Model

The next important development came with the publication of Anderson's classic paper (6) in which he considered a localised transition metal d state in a free electron gas. His model Hamiltonian is of the form:

$$H = H_s + H_d + H_{sd} \qquad 1.5$$

H_s is the unperturbed free electron energy, which may be

expressed in 2nd quantised notation as:

$$H_s = \sum_{k\sigma} \epsilon_{k\sigma} n_{k\sigma} \qquad \text{and} \qquad n_{k\sigma} = c^{\dagger}_{k\sigma} c_{k\sigma}$$

where $\epsilon_{k\sigma}$ is the energy of the state of wave vector k and spin σ, $n_{k\sigma}$ is the number operator for wave vector k and spin σ and $c_{k\sigma}$ and $c^{\dagger}_{ko}$ are the usual destruction and creation operators.

$$H_d = E_d(n_{d\uparrow} + n_{d\downarrow}) + U\, n_{d\uparrow}\, n_{d\downarrow}$$

and represents the essential atomic physics of an isolated impurity orbital. E_d is the unperturbed impurity atom d state energy and U the direct coulomb interaction energy between two electrons:

$$U = \int \left|\phi_d(\underline{r}_1)\right|^2 \left|\phi_d(\underline{r}_2)\right|^2 \frac{e^2}{\underline{r}_1 - \underline{r}_2}\, d\tau_1\, d\tau_2$$

and it is this interaction which tends to keep the impurity orbital singly occupied and hence cause magnetism. Its magnitude may be estimated as of the order of $\frac{e^2}{\text{Bohr radius}}$ i.e. approximately 20 eV.

The final term in Anderson's model Hamiltonian is the "admixture term"

$$H_{sd} = \sum_{k\sigma} V_{kd}(c^{\dagger}_{k\sigma} c_{d\sigma} + c^{\dagger}_{d\sigma} c_{k\sigma})$$

which represents the interaction between the localised d state and its environment, the free electron gas. It may be viewed physically as a process in which a d electron hops off the impurity or a band electron hops on to the impurity, the effect of which is to broaden the otherwise narrow free-atom like d state into a virtual bound level.

Anderson treated the Hamiltonian within the Hartree-Fock approximation and obtained an exact self consistent solution using a Green's function technique. The density of states and energy level scheme for the case when $V_{kd} = 0$, i.e. no interaction between the d state and the conduction electron, is shown in figure 1.3. It can be seen that the spin↑ state lies below the Fermi level and is occupied, whereas the spin↓ state has energy $E_d + U$, lies above the Fermi level and is empty. This situation corresponds to the magnetic state.

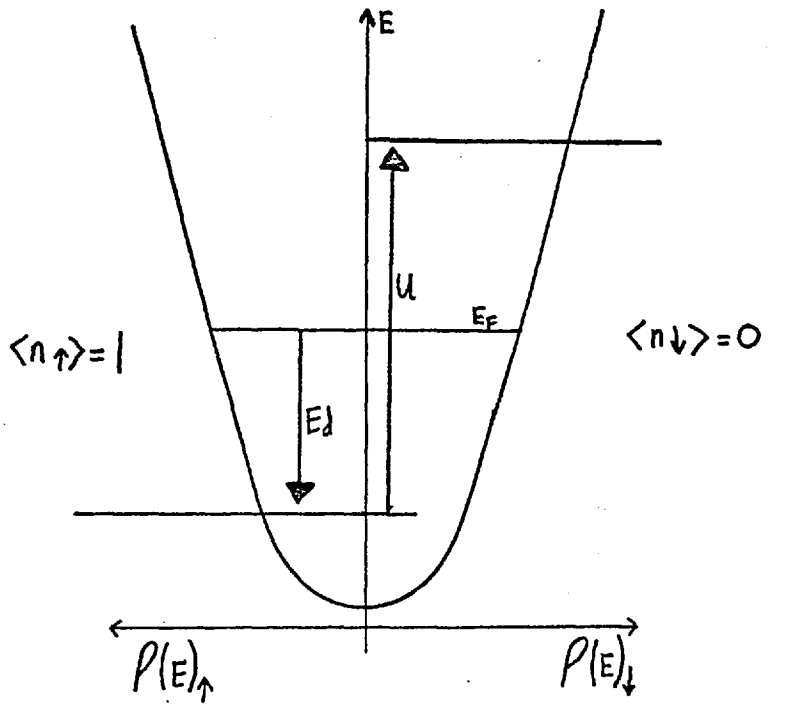


FIGURE 1.3 UNPERTURBED ENERGY LEVELS WITH $V_{kd} = 0$ AFTER REF. (6)

The effect of "turning on" the admixture term V_{kd} can be seen in figure 1.4; both spin↑ and spin↓ states are shifted toward the Fermi-level, and the energy of the state of spin σ is now given by:

$$E_\sigma = E_d + U\langle n_{d-\sigma}\rangle \qquad 1.6$$

The levels are also broadened in energy into virtual states, whose width Δ is given by:

$$\Delta = \pi\langle V_{kd}^2\rangle_{Av}\rho(E_F) \qquad 1.7$$

where $\rho(E_F)$ is the host metal conduction electron density of states at the Fermi energy. The additional density of states due to the presence of the d state impurity is given by:

$$\rho_{d\sigma}(E) = \frac{1}{\pi}\frac{\Delta}{(E-E_{d\sigma})^2 + \Delta^2} \qquad 1.8$$

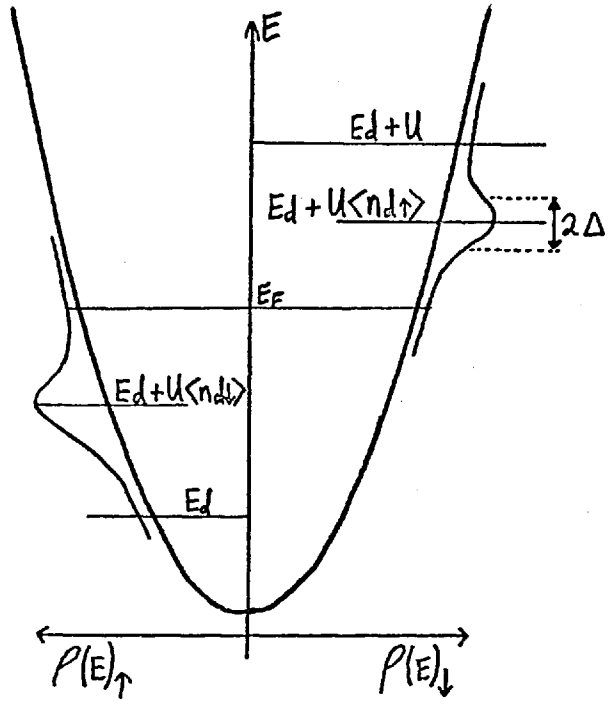


FIG.1.4 ENERGY LEVELS AND DENSITY OF STATES FOR FINITE V_{kd} AFTER REF. (6)

$\langle n_{d\sigma} \rangle$, the number of d electrons of spin σ, is found by integrating equation 1.8 up to the Fermi energy:

$$\langle n_{d\sigma} \rangle = \frac{1}{\pi} \int_{o}^{E_F} \frac{\Delta \, dE}{(E-E_\sigma)^2 + \Delta^2} = \frac{1}{\pi} \cot^{-1}\left(\frac{E_\sigma - E_F}{\Delta} \right) \qquad 1.9$$

Using equation 1.6

$$\langle n_{d\uparrow} \rangle = \frac{1}{\pi} \cot^{-1}\left(\frac{E_d - E_F + U\langle n_{d\downarrow} \rangle}{\Delta} \right) \qquad 1.10$$

and $$\langle n_{d\downarrow} \rangle = \frac{1}{\pi} \cot^{-1}\left(\frac{E_d - E_F + U\langle n_{d\uparrow} \rangle}{\Delta} \right)$$

For self-consistency these coupled equations must be solved simultaneously. Anderson introduces two dimensionless parameters $y = \frac{U}{\Delta}$ the ratio between the coulomb energy and the virtual bound state width and $x = \frac{(E_F - E_d)}{U}$ which indicates the position of the virtual bound state with respect to the Fermi-level, obviously for a magnetic solution to exist x must lie between the limits 0 and 1. The most favourable situation for magnetism occurs when $x = \frac{1}{2}$, that is the level energies E_d and $E_d + U$ are symmetrically disposed about the Fermi-level, then the condition for magnetism is that $y > \pi$.

$$\text{Or } \frac{U}{\pi\Delta} > 1 \qquad 1.11$$

The behaviour for varying x and y is summarised in figure 1.5.

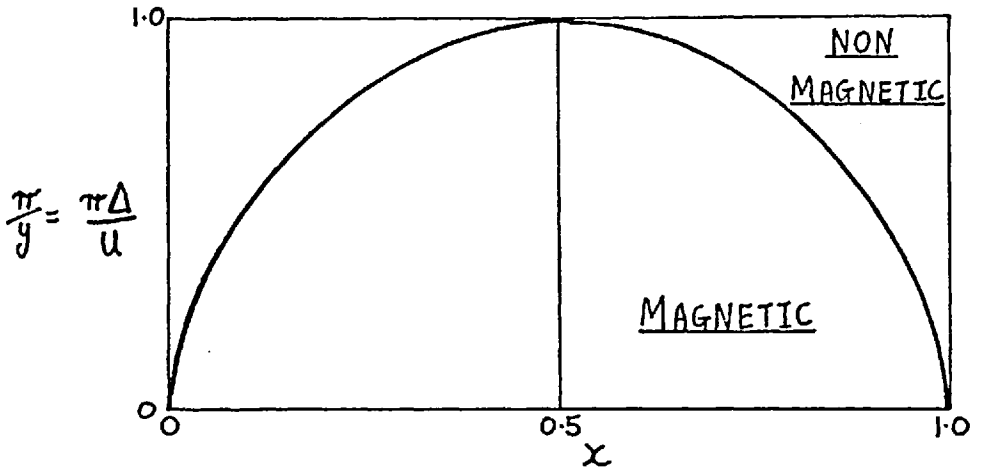


FIGURE 1.5 MAGNETIC AND NON-MAGNETIC REGIONS. AFTER REF. (6)

Generalisation of the Anderson Model to the Case of Degenerate Orbitals and the Inclusion of J the Coulomb Exchange Energy

Anderson, in an appendix to his paper (6), considered the case of degenerate impurity orbitals and also the effect of including the exchange part of the coulomb interaction J and this has since been studied in detail by Yosida et.al. (7) and Klein and Heeger (8). The Hamiltonian still takes the form:

$$H = H_s + H_d + H_{sd}$$

but H_d is rewritten to take into account orbital degeneracy and the exchange interaction J:

$$H_d = \sum_{i,\sigma} E_d n_{i\sigma} + U \sum_{i,j} n_{i\sigma} n_{j-\sigma} + \frac{1}{2}(U - J) \sum_{i \neq j,\sigma} n_{i\sigma} n_{j\sigma} \qquad 1.12$$

where E_d is the one-electron energy level and $n_{i\sigma} = c^{\dagger}_{i\sigma} c_{i\sigma}$ is the number operator for electrons in the i^{th} d-orbital. Again it is possible to obtain exact solutions providing one works within a Hartree-Fock approximation. The d state energies may be written as:

$$E_{i\sigma} = E_d + (U-J)\sum_{i\neq j}\langle n_{j\sigma}\rangle + U\sum_{j}\langle n_{j-\sigma}\rangle \qquad 1.13$$

and the problem is simplified into determining the averages $\langle n_{i\sigma}\rangle$ self consistently. It is also assumed that crystal field splitting is less than the virtual level width and that $E_{i\sigma} = E_{d\sigma}$ for all i. The additional density of states due to the d state virtual level may be written as:

$$\rho_{d\sigma}(E) = \frac{2\ell+1}{\pi}\,\frac{\Delta}{(E-E_{d\sigma})^2+\Delta^2} \qquad 1.14$$

and the number of d electrons of spin σ as:

$$\langle n_{d\sigma}\rangle = \int_0^{E_F}\rho_{d\sigma}(E)\,dE = \frac{2\ell+1}{\pi}\cot^{-1}\left(\frac{E_{d\sigma}-E_F}{\Delta}\right) \qquad 1.15$$

The condition for magnetism in the most favourable situation of a virtual bound state at the Fermi level is now

$$\frac{(U+4J)}{\pi\Delta} \geq 1 \qquad 1.16$$

and the condition for quenching of orbital angular momentum is:

$$\frac{U - J}{\pi} < 1$$

Wolff-Clogston Model

The isolated impurity local moment problem has been approached from a different direction by Wolff (9) and similarly by Clogston (10). They consider the scattering of Bloch waves by the potential V of an isolated substitutional impurity. It is assumed that the wave functions may be expanded in terms of Wannier functions from a single band

$$\psi = \sum_{R_i} U_n(R_i)\, a_n(r-R_i)$$

and that the only in-band matrix elements of V connect two Wannier functions centred on the impurity

$$\langle a_n(r-R_i)|V|a_{n'}(r-R_j)\rangle = V_{nn'}\delta_{nn'}\delta(R_i-R_o)\,\delta(R_j-R_o)$$

Solutions for ψ are obtained from the Schroedinger equation

$$\psi = \phi_{km} + \left[\frac{1}{E_m(k) - H_o + i\varepsilon}\right] V\psi \qquad 1.17$$

In the subsequent analysis the solution for $U_m(R_o)$ is obtained, and this tends towards a large value for a particular energy E_o. If E_o is outside the band then

$U_m(R_o) \to \infty$ as $E \to E_o$ implying that there is a bound state at energy E_o. However if E_o is within the band then $U_m(R_o)$ just shows a resonance maximum. The resonance is a Friedel virtual bound state. Wolff continues by considering the band structure of Koster and Slater (11):

$$E(k) = 2\mathcal{E}(1)\left[\cos(k_x a) + \cos(k_y a) + \cos(k_z a)\right]$$

and adding spin dependent or exchange potentials $\delta V_\uparrow$ and $\delta V_\downarrow$ to V. The effect of introducing spin dependent wave function amplitudes $U_\uparrow(R_o)$ and $U_\downarrow(R_o)$ on the impurity field is calculated in the Hartree-Fock approximation and simultaneous equations for the potentials $\delta V_\uparrow$ and $\delta V_\downarrow$ obtained and their solutions examined. Their conclusions are qualitatively the same as those of Anderson, in particular that the most favourable conditions for the formation of a local moment occur when the virtual bound state is narrow and centred about the Fermi level. Wolff also shows that the most important matrix element in the exchange potential corresponds to Anderson's $U\, n_{d\uparrow} n_{d\downarrow}$. The Wolff-Clogston model is applicable to dilute alloys of transition atoms in other metals of the transition series.

Validity of the Hartree-Fock Approximation and Electron-Correlation Effects

In a Hartree-Fock approximation it is assumed that a scattered conduction electron (i.e. one hopping onto and then off an impurity) interacts only with an "average" number of

localised electrons. For this condition to be valid the time which the electron spends on the impurity ($=\frac{\hbar}{\Delta}$) must be shorter than a characteristic time required to obtain detailed information about the instantaneous configuration or ionization state of the impurity ($=\frac{\hbar}{U}$); otherwise the single electron picture breaks down.

That is $\frac{\hbar}{\Delta} < \frac{\hbar}{U}$ or $\frac{U}{\Delta} < 1$

which implies that a Hartree-Fock approximation is only strictly valid for the non-magnetic region in the Anderson model.

The only two-body interaction considered in Anderson's model is the direct Coulomb interaction U of two opposite spin electrons occupying the d orbital. Schrieffer and Mattis (12) and Kjollerstrom et al. (13) have examined the influence of electron correlation effects beyond the Hartree-Fock approximation, in particular they investigated the so called "low density limit" where the number of electrons (or holes) occupying the virtual level is small i.e. < 0.3. They find that the Coulomb interaction U is reduced by correlations and may be expressed in the form:

$$\bar{U} = \frac{U}{1 + \left(\frac{U}{\pi E_d}\right)\tan^{-1}\left(\frac{E_d}{\Delta}\right)} \qquad 1.18$$

and that even for infinite U, localised moments will not occur in Anderson's single orbital model in this "low density limit", i.e. when $|E_d| \gtrsim \Delta$

However they suggest that for the more realistic case of d-orbital degeneracy and with the inclusion of the Coulomb exchange interaction J (which favours parallel spin alignment) then a magnetic solution may occur even here.

The Schrieffer-Wolff Transformation

Schrieffer and Wolff have shown (14) that in the magnetic limit the Anderson Hamiltonian may be transformed into an s-d exchange form similar to that used by Kondo (15) and others (16,17). The conditions for the validity of the transformation are $\left|\frac{E_d - E_F}{\Delta}\right| \gg 1$ and $\left|\frac{E_d + U - E_F}{\Delta}\right| \gg 1$

The Anderson Hamiltonian is separated into two parts $H = H_o + H_1$, where all the terms involving V_{kd} are contained in H_1:

$$H_1 = \sum_{k\sigma}\left\{V_{kd} c^{\dagger}_{k\sigma} c_{d\sigma} + H.C.\right\}$$

and $$H_o = \sum_{k\sigma}\epsilon_k n_{k\sigma} + \sum_{\sigma} E_d n_{d\sigma} + U\, n_{d\uparrow} n_{d\downarrow}$$

One may perform a canonical transformation upon H, $\tilde{H} = e^{S} H\, e^{-S}$, while choosing S so as to eliminate V_{kd} to first order i.e.

$$H_1 + [H_o, S] = 0$$

Then $\tilde{H} = H_o + \frac{1}{2}[S, H_1] + \frac{1}{3}[S,[S,H_1]] + \cdots\cdots$

For $\left|\frac{E_d - E_F}{\Delta}\right| \gg 1$ and $\left|\frac{E_d + U - E_F}{\Delta}\right| \gg 1$, this may be

approximated to $\tilde{H} = H_o + H_2$, where $H_2 = \frac{1}{2}\left[S,H_1\right]$. H_2 contains four separate terms, the most important of which is an effective s-d exchange interaction $J_{kk'}$, which for k and k' $\cong k_F$ is given by:

$$J_{k_F k_F} = 2\left|V_{kd}\right|^2 \frac{U}{E_d(E_d + U)} \qquad 1.19$$

As E_d is negative (with respect to the Fermi energy) the sign of the effective exchange interaction $J_{k_F k_F}$ will be negative also. Anderson (6) had previously suggested that the mixing interaction V_{kd} should give rise to an effective negative interaction between the localised electrons and the conduction electrons.

The Kondo Effect and the s-d Exchange Hamiltonian

The term "Kondo Effect" is generally used to describe the resistance minimum phenomenon in alloys. Even before the publication of Kondo's famous paper (15) it was becoming apparent that there was a close connection between the existence of localised magnetic moments on solute atoms and the occurence of a resistance minimum. This was made especially clear with the work of Sarachik (18) on Fe dissolved in Nb-Mo and Mo-Re alloys where the existence of local moments on the Fe atoms is sensitive to host composition.

Kasuya (16) and Yosida (17) had investigated the effect on the conduction electron scattering cross section of an s-d exchange Hamiltonian of the form:

$$H = -J(\underline{k},\underline{k}')\underline{S}.\underline{s} \qquad 1.20$$

where $\underline{S}$ is the impurity spin, $\underline{s}$ the conduction electron spin and $J(\underline{k},\underline{k}')$ is the exchange energy. In the mathematical treatment of an interaction of this form various approximations are made as to the dependence of $J(\underline{k},\underline{k}')$ on the momenta $\underline{k}$ and $\underline{k}'$. It is sometimes assumed that J depends only on $|\underline{k}-\underline{k}'|$ but the simplest approximation,and the one in fact most often used, is that J is a constant.

In the first order Born approximation and for zero applied magnetic field they found a <u>temperature independent</u> contribution to the resistivity:

$$R = \frac{3\pi m\Omega c}{2e^2\hbar E_F} J^2 S(S+1) \qquad 1.21$$

and the matrix element for scattering a conduction electron from $\underline{k}\uparrow$ to $\underline{k}'\uparrow$ is:

$$-\left(\frac{J}{N}\right)S_z \qquad 1.22$$

Kondo proceeded to the second order Born approximation, which introduces scattering processes consisting of two successive events, leading to the inclusion of the following two types of scattering mechanisms.

(1) An electron of $\underline{k}\uparrow$ is scattered to $\underline{k}''\uparrow$ (or $\underline{k}''\downarrow$) and then

$\underline{k}\uparrow$ (or $\underline{k}''\downarrow$) is scattered to $\underline{k}'\uparrow$. In the intermediate state the impurity spin is unchanged for $\underline{k}''\uparrow$ or increased by one unit for $\underline{k}''\downarrow$. The matrix element for this scattering channel is:

$$-\left(\frac{J}{N}\right)^2 (S_z^2 + S_- S_+) \sum_{k''} \frac{(1-f_{k''})}{\epsilon_k - \epsilon_{k''}} \qquad 1.23$$

where S_+ and S_- are the usual raising and lowering operators, S_z the z component of the impurity spin and $f_{k''}$ the Fermi-Dirac distribution function, introduced to take into account the Pauli exclusion principle in the intermediate state.

(2) An electron in state $\underline{k}''\uparrow$ (or $\underline{k}''\downarrow$) is scattered to $\underline{k}'\uparrow$ and then $\underline{k}\uparrow$ is scattered to $\underline{k}''\uparrow$ (or $\underline{k}''\downarrow$), with the corresponding changes in impurity spin. The matrix element for this scattering channel is:

$$\left(\frac{J}{N}\right)^2 (S_z^2 + S_+ S_-) \sum_{k''} \frac{f_{k''}}{\epsilon_{k''} - \epsilon_k} \qquad 1.24$$

Subject to total energy conservation i.e. $\epsilon_k = \epsilon_{k'}$, these terms combine to give a total matrix element:

$$\left(\frac{J}{N}\right)^2 \left[S_z^2 + \frac{1}{2}\left(S_+ S_- + S_- S_+\right)\right] \sum_{k''} \frac{1}{\epsilon_k - \epsilon_{k''}}$$
$$+ \left(\frac{J}{N}\right)^2 \left(S_- S_+ - S_+ S_-\right) \sum_{k''} \frac{f_{k''} - \frac{1}{2}}{\epsilon_{k''} - \epsilon_k} \qquad 1.25$$

The first term is smaller by a factor $\left(\frac{J}{E_F}\right)$ than 1.22 and is neglected.

The second term = $\left(\frac{J}{N}\right)^2 \left[S_+, S_-\right] \sum_{k''} \frac{f_{k''} - \frac{1}{2}}{\epsilon_{k''} - \epsilon_k}$, where the commuttator $\left[S_+, S_-\right]$ is non zero and the sum $\sum_{k''} \frac{f_{k''} - \frac{1}{2}}{\epsilon_{k''} - \epsilon_k}$ is a strongly varying function of energy. At T = 0, when $f_{k''}$ is a step function, the summation may be replaced by an integral up to the Fermi energy and becomes:

$$= \text{constant.} \quad \log_e\left(\frac{E - E_F}{E_F}\right)$$

which diverges logarithmically at the Fermi energy.

For finite temperatures a proper calculation produces a term proportional to $\log_e$ (T) in the impurity resistivity:

$$\rho = c\rho_M\left[1 + \left(\frac{3zJ}{E_F}\right) \log_e T\right] \qquad 1.26$$

and $$\rho_M = \frac{3\pi m \Omega}{2e^2 E_F \hbar} J^2 S(S + 1) \qquad 1.27$$

It is clear that for negative J this will give rise to a logarithmically increasing impurity resistivity as $T \rightarrow 0$ and which, when combined with the normal phonon resistivity, will lead to a resistance minimum.

Developments since Kondo's Original Paper

Although Kondo's paper had in principle resolved the long standing resistance minimum phenomenum it had also introduced a whole range of new theoretical problems. The major difficulty lay in the breakdown of perturbation theory and the prediction of an infinite impurity resistivity at T = 0.

One would expect a finite limiting low temperature resistivity corresponding to the maximum possible partial scattering cross-section, which is $\sigma_{\ell} = \left(\frac{4\pi}{k_F}\right)^2 (2\ell + 1)$, so obviously any development should take into account this limiting value.

Abrikosov (19) used a method of "infinite sums" in an attempt to overcome the perturbation theory difficulties and found that for positive J the resistivity $\rightarrow 0$ as $T \rightarrow 0$ but for negative J it diverged at $T = \frac{E_F}{K_B} \exp\left(\frac{-1}{|J|\rho}\right)$ before decreasing as $(\log_e T)^2$ as $T \rightarrow 0$.

Since the initial attempt of Abrikosov, non-perturbative treatments have been developed by Suhl (20), Nagaoka (21), Hamann (22), Bloomfield and Hamann (23), Zittartz and Muller-Hartmann (24) who have derived theoretical expressions for impurity properties such as electrical resistivity, specific heat, magnetic susceptibility and thermo-power.

One of the more interesting concepts, that of a low temperature compensated state (or ground state singlet) in which the conduction electrons surrounding the impurity spin are polarised so as to effectively compensate the impurity magnetic moment as T approaches 0, was suggested in Nagaoka's paper (21).

Localised Spin Fluctuations

Localised Spin fluctuation theories, first introduced by Lederer and Mills (25) to explain properties of Pd - Ni alloys, represent an alternative approach to the local moment problem starting from the non-magnetic region. The concept was used by Caplin and Rizzuto (26) to explain resistivity and susceptibility properties of Al-Mn and Al-Cr alloys and

has undergone further theoretical development by Rivier and Zuckermann (27) and by Suhl and coworkers (28).

For U = 0 and at a finite temperature T the solute atom virtual bound state may fluctuate $\sim$ kT in energy about the Fermi level leading to corresponding changes in the spin $\uparrow$ and spin $\downarrow$ populations $n_{d\uparrow}$ and $n_{d\downarrow}$ and in their difference $n_{d\uparrow} - n_{d\downarrow}$. These fluctuations may be characterised by a lifetime τ_{sf} given by:

$$\tau_{sf} = \pi \rho_d(E_F) \qquad 1.28$$

The effect of increasing U is to introduce correlations into $n_{d\uparrow}$ and $n_{d\downarrow}$ leading to fluctuation amplitudes of the order of ηkT and an increased fluctuation lifetime:

$$\tau_{sf} = \frac{\pi \rho_d(E_F)}{1 - U\rho_d(E_F)} = \eta \pi \rho_d(E_F) \qquad 1.29$$

and the enhancement factor $\eta = \left[1 - U\rho_d(E_F)\right]^{-1}$

The localised spin fluctuation model provides an excellent description of the experimental results in the Al-Mn and Al-Cr systems (Caplin and Rizzuto (26) and Alloul et al. (29)). Both these systems show temperature independent enhanced Pauli para-magnetism and weak low temperature resistance minima, where the impurity resistivity is of the form:

$$\rho(T) = \rho_o\left[1 - \left(\frac{T}{\theta}\right)^2\right] \qquad 1.30$$

This form of resistivity behaviour may be obtained in the Friedel theory for the case of a virtual bound state centred on the Fermi level. The impurity scattering cross section for a conduction electron is related to the phase shifts η_ℓ and hence to the occupation number of the virtual bound state which leads to a resistivity:

$$\rho(T) = \rho_o\left[1 - \frac{\pi^2}{3}\left(\frac{kT}{\Delta}\right)^2\right] \qquad 1.31$$

Caplin and Rizzuto suggest that for the case of finite U the relevant energy range for thermal averaging is η kT and not kT, so that

$$\rho(T) = \rho_o\left[1 - \frac{\pi^2}{3}\left(\frac{\eta kT}{\Delta}\right)^2\right] \qquad 1.32$$

Rivier (30) has shown the equivalence between the Nagaoka condensation with high Kondo temperature T_K and the localised spin fluctuation theory for small enhancement factor $\eta \approx 1$. When the parameter $\frac{U}{\Delta}$ is altered so as to approach the Friedel-Anderson critical condition for the appearance of a magnetic moment the localised spin fluctuation lifetime τ_{sf} becomes long compared with other relevant times, for example the temporary magnetic moment may have time to equilibriate in an applied magnetic field and give a Curie-Weiss like susceptibility or to spin flip a conduction electron. Thus it is possible to visualise a smooth transition between magnetic and non magnetic behaviour.

1.2 INTERACTION MECHANISMS BETWEEN SOLUTE ATOMS

Zener

Zener (31) suggested that a ferromagnetic coupling may exist between local atomic moments via a uniform polorization of the conduction electrons induced by a positive exchange interaction between conduction electrons and local moments. A similar type of interaction mechanism had earlier been suggested by Frohlich and Nabarro (32) who investigated the interaction between nuclear spins via a uniform polarization of the conduction electrons.

The R.K.K.Y. interaction

The indirect coupling between moments via an "s-d" exchange has been examined in detail by Yosida (17) using an "s-d" exchange interaction of the form used by Kasuya (16) and by Mitchell (33).

This s-d interaction has the following diagonal matrix elements:

$$- N^{-1}J(0)\ (n_+ - n_-)\ S^z \qquad 1.33$$

where N is the total number of lattice points, S^z the impurity spin operator, $J(\underline{k} - \underline{k}')$ the exchange integral between a conduction electron, with wave vectors $\underline{k}$ and $\underline{k}'$, and the impurity spin, and $n(\pm)$ the total numbers of electrons with $\pm$ spins. Assuming a spherical Fermi surface Yosida shows:

$$n(\pm) = n \pm \left(\frac{3n}{2E_F}\right) N^{-1}J(0)\ S^z \qquad 1.34$$

where the total number of electrons is 2n. This is the same result as found by Frohlich and Nabarro, and Zener. However Yosida pointed out that the difference between the first order perturbed wave functions for spin up and spin down electrons contributes a comparable polarization to that of equation 1.34. The first-order perturbed wave function is:

$$\phi_k = \phi_k^o + \sum_{k'} \frac{H_{kk'}}{E_k - E_{k'}} \phi_{k'}^o \qquad 1.35$$

where ϕ_k^o is the plane wave $\left(\frac{1}{V}\right)^{\frac{1}{2}} \exp(i\underline{k}.\underline{r})$ and $H_{kk'}$ is the s-d interaction Hamiltonian.

This leads to a density of spin up (or down) electrons at a distance r given by :

$$\rho_{\pm}(r) = \rho_o\left\{1 \pm \frac{3}{8E_F N} \sum_q J(q) f(q) \left[\exp(i\underline{q}.\underline{r}) + \exp(-i\underline{q}.\underline{r})\right] S^z \right. \qquad 1.36$$

where ρ_o is the mean conduction electron density, $\underline{q} = \underline{k} - \underline{k}'$ and f(q) is given by:

$$f(q) = 1 + \frac{4k_F^2 - q^2}{4k_F q} \log \left| \frac{2k_F + q}{2k_F - q} \right| \qquad 1.37$$

$\rho_{\pm}(r)$ depends critically on the form of $J(\underline{q})$, if $J(q) = J(0)$ for all q, then:

$$\rho_{\pm}(r) = \rho_o\left\{1 \mp \frac{18\pi}{E_F}\left(\frac{n}{N}\right) J(0) F(2k_F r) S^z\right\} \qquad 1.38$$

where the function F(x) is defined by

$$F(x) = \frac{x \cos x - \sin x}{x^4} \qquad 1.39$$

Equation 1.38 is now known as the R.K.K.Y. spin polarization. Unfortunately $\rho_{\pm}(r)$ diverges as $r \rightarrow 0$ and this is due to the chosen dependence of J(q) upon q. Yosida then makes the approximation

$$J(q)f(q) = 2J(0) \quad \text{for } q < 2k_F$$
$$= 0 \quad \text{for } q > 2k_F$$

and obtains:

$$\rho_{\pm}(r) = \rho_o \left\{ 1 \mp \frac{36}{E_F} \left(\frac{n}{N}\right) J(0)\ 2k_F r\ F(2k_F r)\ S^2 \right\} \qquad 1.40$$

which no longer diverges as $r \rightarrow 0$.

Freeman and Watson (34) have calculated the exchange coupling constant $J(\underline{q})$ between the localised $4f^7$ shell of Gd^{3+} and conduction electrons, treated as orthogonalized plane waves, as a function of $\underline{q}$. They find that the form of the spin polarization is modified from that of the R.K.K.Y., in particular the maximum in the spin density is no longer at the centre of the solute atom site, however at larger distances the same oscillatory behaviour is observed.

The energy of interaction between two solute atoms local moments coupled via the R.K.K.Y. interaction is given by:

$$E(R) = 9\pi\left(\frac{2n}{N}\right)^2 \frac{J^2}{E_F} F(2k_F R)\ \underline{S}_1 \cdot \underline{S}_2 \qquad 1.41$$

where $\underline{S}_1$ and $\underline{S}_2$ are the solute atom spins and R their separation. This coupling has the same form as that obtained by Ruderman and Kittel (35) (for the coupling between nuclear spins).

In the derivation of the R.K.K.Y. spin polarization and coupling, the conduction electron mean free path has been assumed to be infinite. De Gennes (36) has considered the effect of a finite electronic mean free path λ and introduces a multiplying factor $\exp\left(-\frac{R}{\lambda}\right)$ into equation 1.38.

In the preceeding discussion we have assumed that $J(\underline{k},\underline{k}')$ is just the simple exchange integral between plane wave conduction electron states and a well localised magnetic moment on the solute atom.. Typically this will be of the form:

$$J(\underline{k},\underline{k}') = \left\langle \psi_d(\underline{r}_1)\, \phi^o_{\underline{k}}(\underline{r}_2) \left| V(\underline{r}_1,\underline{r}_2) \right| \psi_d(\underline{r}_2)\, \phi^o_{\underline{k}'}(\underline{r}_1) \right\rangle \qquad 1.42$$

where $V(\underline{r}_1,\underline{r}_2)$ is a coulomb or screened coulomb potential. This would appear to be a valid approximation in the case, for example, of rare earth solute atoms where the magnetic state is of real bound state character. However for the case of magnetic virtual bound states, of the type found in 3d transition metal solutes, Schrieffer and Wolff (14) have shown that the mixing term V_{kd} gives rise to a large negative effective interaction constant $J(\underline{k},\underline{k}')$ of the form:

$$J(\underline{k},\underline{k}') = 2\left|V_{kd}\right|^2 \frac{U}{E_d(E_d + U)}$$

Interaction Mechanisms Between Magnetic Virtual Bound States

Blandin and Friedel

A hybrid type of interaction mechanism has been suggested by Blandin and Friedel (5). They consider a magnetic virtual bound state which, because of the different phase shifts for spin up and spin down scattered conducting electrons, gives rise to a spin polarization oscillating in sign at large distances. The spin polarization is of the form:

$$\underline{s}(\underline{r}) = \frac{1}{2}\left[\Delta\rho_{+}(\underline{r}) - \Delta\rho_{-}(\underline{r})\right]\underline{u}_1 \qquad 1.43$$

where $\underline{u}_1$ is the unit vector in the direction of the magnetic moment on the solute atom. $\Delta\rho_{\pm}(\underline{r})$ is the electronic density variation in the conduction band and is given by equation 1.3. The spin $\underline{S}$ on a second solute atom will couple to this conduction electron spin polarization via an exchange interaction J. The asymptotic form of the interaction energy at large distances is given by:

$$E(R) = \frac{15}{4} JZ \sum_{\sigma} \sigma \sin\phi^{\sigma} \frac{\cos(2k_F R + \phi^{\sigma})}{(k_F R)^3} S\, \underline{u}_1 \cdot \underline{u}_2 \qquad 1.44$$

where Z is the number of conduction electrons per atom, R the distance between the two solute atoms and ϕ^{σ} the phase shift for a scattered conduction electron of spin σ.

Caroli

A second interaction mechanism between magnetic virtual bound states has been suggested by Caroli (37) in which two solute

atoms are coupled through the consecutive resonant scattering of conduction electrons. The wave function of an electron of spin σ and wave vector $\underline{k}$ scattered from the first solute atom is given, for large r, by:

$$\psi_k^\sigma(r) \cong e^{i\underline{k}\cdot\underline{r}} + \frac{e^{ikr}}{kr} e^{i\phi_1^\sigma} \sin\phi_1^\sigma \qquad 1.45$$

where ϕ_1^σ is the phase shift at the first impurity. The electron is then scattered from a second solute atom and the mixing between the conduction electron and the localised d electrons i.e. V_{kd_2} is treated exactly as in the Anderson model, except that the matrix element V_{kd_2}, which equals $\langle k|V_2|d_2\rangle$ in the Anderson treatment, is replaced by $\langle \psi_k^\sigma|V_2|d_2\rangle$ and becomes:

$$\langle \psi_k^\sigma|V_2|d_2\rangle = V_{kd_2}\left\{ e^{i\underline{k}\cdot\underline{R}} + \frac{e^{ikR}}{kR} e^{i\phi_1^\sigma} \sin\phi_1^\sigma \right\} \qquad 1.46$$

where R is the separation between the two solute atoms. The calculation leads to an interaction energy between the two non-degenerate virtual states for large R given by:

$$E(R) = \frac{E_F}{\pi} \sum_\sigma \sin\phi_1^\sigma \sin\phi_2^\sigma \frac{\cos(2k_FR + \phi_1^\sigma + \phi_2^\sigma)}{(k_FR)^3} \qquad 1.47$$

The final expression for the interaction energy after level degeneracy has been taken into account is

$$E(R) = \frac{25\, E_F}{2\pi} \sum_{\sigma\sigma'} \sigma\sigma' \sin\phi_1^\sigma \sin\phi_2^{\sigma'} \frac{\cos(2k_FR + \phi_1^\sigma + \phi_2^{\sigma'})}{(k_FR)^3} \underline{u}_1\cdot\underline{u}_2 \qquad 1.48$$

There are two conditions for the validity of the asymptotic form of the interaction. The first condition is that $k_F R > 1$ and the second that $k_F R > \frac{E_F}{\Delta}$. When $k_F R$ lies within the range $1 < k_F R < \frac{E_F}{\Delta}$ an alternative, and much more complex, expression has to be used.

Caroli compares the strengths of the possible interaction mechanisms for dilute Cu-Mn alloys using the virtual bound state splitting scheme of figure 1.6.

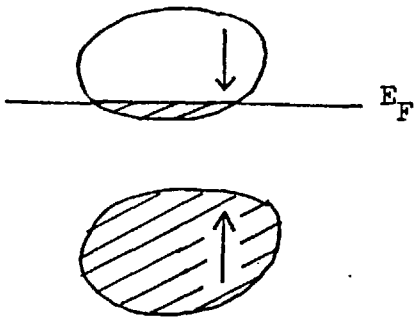


FIGURE 1.6

Assuming that the Mn atoms contribute one electron to the conduction band then $n_d^+ + n_d^- = 6$. The magnetic moment of Mn dissolved in Cu is of the order of $5\mu_B$ therefore, from $\rho_{eff} = 2\sqrt{S(S+1)}$ $n_d^+ - n_d^- = 4$. The phase shifts ϕ^σ are related to the d occupation numbers, n_d^σ, via the Friedel sum rule:

$$\phi^\sigma = \frac{\pi}{5} n_d^\sigma$$

Therefore with the splitting scheme of figure

$$\phi^+ = \pi \text{ and } \phi^- = \frac{\pi}{5} .$$

The strengths of the interactions given by the three mechanisms are:

R.K.K.Y. $$E(R) \cong \frac{9\pi}{8} \frac{Z^2 J^2}{E_F} \frac{\cos(2k_F R)}{(k_F R)^3} S(S+1)\, \underline{u}_1 \cdot \underline{u}_2$$

Blandin and Friedel $$E(R) \cong \frac{15}{4} JZ \sin\phi \frac{\cos(2k_F R + \phi)}{(k_F R)^3} S\, \underline{u}_1 \cdot \underline{u}_2$$

Caroli $$E(R) \cong \frac{25}{2\pi} E_F \sin^2\phi \frac{\cos(2k_F R + 2\phi)}{(k_F R)^3} \underline{u}_1 \cdot \underline{u}_2$$

For Cu-Mn alloys one may take $\phi = \frac{\pi}{5}$, $E_F = 7$ eV., $J \cong 0.2$ eV., $Z = 1$ and $S \cong 2$ giving

R.K.K.Y. $$E(R) \cong 7.7 \times 10^{-2} \frac{\cos(2k_F R)}{(k_F R)^3} \underline{u}_1 \cdot \underline{u}_2 \text{ eV.}$$

Blandin and Friedel $$E(R) \cong 8.8 \times 10^{-1} \frac{\cos(2k_F R + \frac{\pi}{5})}{(k_F R)^3} \underline{u}_1 \cdot \underline{u}_2 \text{ eV.}$$

Caroli $$E(R) \cong 9.6 \frac{\cos(2k_F R + \frac{2\pi}{5})}{(k_F R)^3} \underline{u}_1 \cdot \underline{u}_2 \text{ eV.}$$

The strength of each interaction exceeds the previous one by an order of magnitude. The coupling by the Caroli or "resonance-resonance" type is greater than the R.K.K.Y. by a factor $\approx \left(\frac{E_F \sin\phi}{J}\right)^2$. In the case of Rare Earth solute atoms the mixing between the well localised f electrons and the conduction electrons is very small and $\sin\phi$ is effectively zero, therefore the R.K.K.Y. mechanism dominates.

COUPLING BETWEEN NON-MAGNETIC VIRTUAL BOUND STATES

Alexander and Anderson (38) have investigated the situation of two neighbouring transition metal solute atoms assuming a model Hamiltonian of the form

$$H = H_s + H_d + H_{sd} \qquad 1.49$$

where $H_s = \sum_{k\sigma} E_k n_k^\sigma$ is the conduction electron Hamiltonian and E_k and n_k^σ are the energy and number operator for an electron with momentum $\underline{k}$ and spin σ.

$$H_d = E_o \sum_\sigma (n_1^\sigma + n_2^\sigma) + U(n_1^\uparrow n_1^\downarrow + n_2^\uparrow n_2^\downarrow) + \sum_\sigma (V_{12} c_1^{*\sigma} c_2^\sigma + V_{21} c_2^{*\sigma} c_1^\sigma) \qquad 1.50$$

where E_o is the self-energy of the localised states (1) and (2) in the absence of interactions, U is the Coulomb repulsion between two electrons in a localised state, and $V_{12} = V_{21}^* = \int \phi_1^*(\underline{r})\, \phi_2(\underline{r})\, H_d d\underline{r}$ is the transfer integral between the two d states. Finally

$$H_{sd} = \sum_{ik\sigma} (V_{ki} c^{\sigma *} c_i^\sigma + V_{ik} c_i^{\sigma *} c_k^\sigma) \qquad 1.51$$

describes the mixing between d states and conduction states.

Two important interaction mechanisms are observed, direct coupling via the transfer integral V_{12} and an indirect interaction via H_{sd}. The direct coupling is studied in the greater detail. The sign of the effective interaction depends upon the positions of the virtual bound states with respect to the Fermi energy. For the symmetric situation with both virtual levels far from the Fermi energy an anti-parallel (i.e. anti-ferromagnetic) coupling is favoured and the effect on the critical boundary between magnetic and non-magnetic behaviour is such as to make magnetic behaviour less probable:

For an asymmetric situation, one virtual level will lie close to the Fermi energy and this favours a parallel (ferromagnetic) coupling. The effect on the critical boundary is to relax the conditions for magnetism.

Moriya (39) has extended the model of Anderson and Alexander to the case of solute atoms with five-fold degenerate d-orbitals. The results of his analysis are in qualitative agreement in that the direct transfer type of interaction leads to an anti-ferromagnetic coupling between neighbouring solute atoms for approximately half full d shells and a ferromagnetic coupling otherwise.

Kim (40) has extended Anderson's single solute atom model to the case of finite concentrations. The Hamiltonian considered is

$$H = H_s + H_d + H_{dd} + H_{sd} + H_t \qquad 1.52$$

where H_s, H_d and H_{dd} are the same terms as appear in Anderson's original paper (c.f. equation 1.5). H_{sd} is the interaction term between the conduction and localised d electron (s-d mixing):

$$H_{sd} = \sum_{iko} (V_{ik}\, d^{\dagger}_{i\sigma}\, c_{k\sigma} + V^{*}_{ik}\, c^{\dagger}_{k\sigma}\, d_{i\sigma}) \qquad 1.53$$

and $V_{ik} = V_i(k)\, \exp(ikR_i)$, where R_i is the co-ordinate of the i^{th} solute atom site.

The final term in the Hamiltonian is the direct-transfer integral between the impurities

$$H_r = \sum_{ij\sigma} T_{ij}\, d^{\dagger}_{i\sigma}\, d_{j\sigma} \qquad 1.54$$

T_{ij} depends upon the distance between the i^{th} and j^{th} impurities and $T_{ii} = 0$.

Kim carries out a Greens function calculation within the Hartree-Fock approximation and presents the results in a simple way. He considers how the width Δ_i of the localised state of the i^{th} solute atom, which appears in the criterion for the formation of a local moment, is modified by the presence of the other surrounding impurities.

$$\Delta_i = \Delta_i^{\circ} + \delta\Delta_i$$

where Δ_i° is the width in the single solute atom limit and $\delta\Delta_i$ the change in Δ_i due to interactions. The change in the width consists of three separate contributions:

$$\delta\Delta_i = \delta\Delta_i^{(1)} + \delta\Delta_i^{(2)} + \delta\Delta_i^{(3)}$$

$\delta\Delta_i^{(1)}$ comes from the indirect inter-solute interaction through the host conduction band and may be written as $\delta\Delta_i^{(1)} \cong \pi V_j^2 \times$ [the change in $\rho(E_F)$ at the i^{th} solute atom site due to the other solute atoms j]. Therefore

$$\delta\Delta_i^{(1)} \cong V_i^2 \left(\frac{\Omega}{4\pi}\right)^2 \left(\frac{2m}{\hbar^2}\right)^2 \sum_{j(\neq i)} \frac{V_j^2 \sin(2k_F R_{ij} + \phi_j)}{\Delta_j^{\circ} R_{ij}^2} \qquad 1.55$$

where ϕ_j is the phase shift at the j^{th} site, Ω the atomic volume and k_F the Fermi wave number.

Also $\Delta_j^{\circ} = \pi V_j^2 \rho_c^{\circ}(E_F)$ where $\rho_c^{\circ}(E_F) = \left(\frac{mk_F}{2\pi^2\hbar^2}\right)\Omega$

is the unpeturbed host metal density of states. Therefore equation 1.55 is further reduced to:

$$\frac{\delta\Delta_i^{(1)}}{\Delta_i^{\circ}} = \frac{1}{k_F^2} \sum_{j(=i)} \frac{\sin(2k_F R_{ij} + \phi_j)}{R_{ij}^2} \qquad 1.56$$

For just two solute atoms separated by a distance d equation becomes:

$$\frac{\delta\Delta_i^{(1)}}{\Delta^\circ} = 4\,\frac{\sin(2k_F d + \phi)}{(2k_F d)^2}$$

which may be either positive or negative in sign.

The second contribution to $\delta\Delta_i$ is a term $\delta\Delta_i^{(2)}$ due to the direct transfer interaction between impurities and is always positive. Kim considers the simplifying condition that each virtual level is half full, then $\delta\Delta_i^{(2)}$ becomes:

$$\delta\Delta_i^{(2)} = \sum_{j(\neq i)} T_{ij}^2 \frac{1}{\Delta_j^\circ} \qquad 1.57$$

from which

$$\frac{\delta\Delta_i^{(2)}}{\Delta^\circ} = \sum_{j(\neq i)} \left(\frac{T}{\Delta^\circ}\right)^2 \qquad 1.58$$

and he considers the further simplification that $T_{ij} = T$ for nearest neighbours and = 0 otherwise.

$\delta\Delta_i^{(3)}$, the third contributing to $\delta\Delta_i$, is a cross term whose magnitude lies between that of $\delta\Delta_i^{(1)}$ and $\delta\Delta_i^{(2)}$.

Treatment of Interaction Effects in Disordered Systems

All the magnetic interaction mechanisms discussed above fluctuate both in magnitude and sign as a function of the distance between the solute atoms. Klein and Brout (41) and Klein (42) have developed a statistical theory for the distribution of internal fields P(H) seen by a solute atom due to its interactions with the random distribution of all the other solute atoms via an

R.K.K.Y. type of spin polarization. The computed P(H) distributions were successfully used to account for the observed low temperature specific heat behaviour of variable concentration alloys in the Cu-Mn, Cu-Fe and Cu-Co systems, where $\frac{\Delta C}{T}$ tends towards a constant value independent of impurity concentration as $T \rightarrow 0$. Further developments of the statistical theory for internal field distributions have been made by Liu (43).

1.3 THEORY OF DILUTE INTERMETALLIC COMPOUNDS

Firstly it is necessary to define the term "dilute" with reference to intermetallic compounds of transition metals with other metals. Here it will be taken to mean that at the interatomic distance between transition metal atoms found in the compound, there is negligible overlap between the wave functions describing the free atom d-states. This does not mean that there are no interactions between the transition atom d electrons, only that they are mediated via the conduction electrons.

Two alternative approaches to the dilute compound problem may be considered, these are the following:-

(1) The hybridization or mixing between localised d-orbital wave functions and the conduction electron wave functions is put in from the start. This immediately provides a resonance or virtual bound state picture of each transition atom. Then the compound is built up out of regular array of resonances together with a "filling" of simple metal atoms to provide the free-electron-like conduction band. The problem is then one of investigating the interaction effects between the transition atom resonances and the modification to parameters which characterise the individual resonances i.e. Δ, E_d, U etc.

(2) Consider a dilute compound where the transition atoms lie on a regular lattice. In the absence of s - d hybridization the d-band will be vanishingly narrow. What is the effect of "turning on" the hybridization or mixing interaction between the localised d electrons and the conduction electrons?

A single transition metal atom dissolved in a simple metal is well described by the Friedel-Anderson picture of a virtual bound state, or resonance. This is characterised by the parameters U, E_d and particularly the width Δ, which arises from the mixing, or hybridization, of the localised and conduction electron states. The question of local magnetic moment formation is then understood in terms of the ratio between the intra-atomic coulomb energy U (or U + 4J) and this width Δ.

We have also seen how these parameters might be modified by interactions. In particular Kim has shown (see section 1.2) how the presence of charge oscillations due to one virtual bound state modifies the local conduction electron density at a second virtual bound state and changes its width via the expression $\Delta = \pi \langle V_{kd}^2 \rangle \rho(E_F)$ and that the change may be of either sign depending upon the separation between the atoms.

In the limit of a very dilute intermetallic compound, i.e. at a sufficiently large separation of transition atoms, interactions between the resonant states will be negligible and we must recover the simple isolated impurity, Friedel-Anderson picture, with the appropriate numerical values for the parameters U, Δ, E_d etc. Then it is possible to visualise a band picture in which the d-band is simply a super-position of the resonances, or virtual bound states, on the individual transition metal atoms.

The "band" width will be the same value Δ as for the isolated atom and due solely to the hybridization (or mixing) at each atomic site.

The question is what happens as the separation between transition atoms decreases, i.e. the compound is made more concentrated, yet remaining within the original definition of dilute? Also it must be remembered that the transition metal atoms lie on a regular lattice.

The simplest model to take is that of a linear chain of transition atoms, with separation R, in a free electron gas. A further simplification is that an isolated transition atom in the same gas is well into the non-magnetic regime (in the Friedel-Anderson sense). Each transition atom sets up long range charge oscillations within the electron gas proportioned to $\frac{\sin\phi \cos(2k_F r + \phi)}{(k_F r)^3}$ (c.f. equation no. 1.3), where the phase shift ϕ is related to the number of d electrons n_d via the Friedel Sum rule. Choosing one transition atom as origin, the total charge modification due to all the other atoms in the chain may be found by summing this expression. Obviously the magnitude and sign of the local modification to the background charge depends upon the chain separation R, beginning at zero for $R = \infty$, and passing through successively larger maxima and minima as $k_f R + \phi$ decreases through even or odd multiples of π. The local modification to the electronic charge will alter Δ via the mixing term $\Delta = \pi \langle V_{kd}^2 \rangle \rho(E_F)$ and once again the change in Δ may be of either sign. What else happens to the individual resonances depends upon the constraints imposed on the system.

The simplest constraint is that the number of d electrons on the transition atoms is fixed. If the width Δ changes then the position of the centre of the resonance with respect to the Fermi-level has to adjust itself to maintain a constant value of n_d (apart from the special case of a half-full resonance when no shift is necessary).

A more interesting situation arises if the externally imposed constraint that n_d remains constant is removed. The resulting equilibrium values of Δ and $E_d - E_F$, which together determine n_d, will depend upon details of the changes in energies involved. Any change in n_d would alter the phase shift $\emptyset$ at each transition atom site and hence modify the electronic charge density and the problem has to be solved self-consistently. However it does raise the interesting prospect of charge transfer onto or off the resonance.

For a three dimensional lattice the total effect on the lattice sum of the charge oscillations would be "washed out" to a certain extent as, unlike the case of a linear chain, the transition atoms do not all lie at integer multiples of the smallest separation. However it would still seem reasonable to regard the d-band in the compounds as a super-position of individual resonances using the parameters Δ, U, E_d etc., although with different numerical values to those of the isolated solute atom limit.

One group of intermetallic compounds which have been the subject of experimental studies are the Heusler alloys, having compositions Cu_2MnAl, Cu_2MnIn, Cu_2MnSn etc.(44,45).The inter-atomic distance between the manganese atoms is large ($\sim$4.3 A^o)

and the magnetic properties, in particular their ferro-magnetic Curie temperatures, can be understood in terms of a picture proposed by Blandin and Caroli (46) in which spin split virtual bound states interact through a free-electron-like conduction band. Daniel (47) has suggested that even though there is no overlapping of the atomic manganese d-orbitals, their phases become interrelated because of their hybridization with the conduction electrons. In the ferro-magnetic region, where the electron scattering (i.e. both resonant and exchange scattering) is coherent, then the d-states of manganese atoms on their regular lattice sites must be described through Bloch type wave functions.

In his simple model Daniel starts with a single d-orbital of given spin on each Mn atom and constructs Bloch wave functions ϕ_{dk} of wave vector k and energy E_d. E_d is assumed to be independent of k because of the large separation between Mn atoms and hence the width of the corresponding d-band is vanishingly small. If ϕ_{ck} are the conduction electron Bloch wave functions and H_o an approximate Hamiltonian which neglects the hybridization between the conduction and d-wave functions then:

$$H_o\phi_{ck} = E_c(k)\ \phi_{ck} \quad \text{and} \quad H_o\phi_{dk} = E_d\phi_{dk} \qquad 1.59$$

The true Hamiltonian for the system is $H = H_o + H_1$ where H_1 is responsible for the hybridization and its only non-vanishing matrix elements mix conduction and local d-wave functions with the same k vector

$$\text{i.e.} \quad \langle \phi_{ck} | H_1 | \phi_{dk} \rangle = V(k)$$

The hybridized wave function ψ_k may be written as

$$\psi_k = \alpha_c(k)\,\phi_{ck} + \alpha_d(k)\,\phi_{dk} \quad \text{with} \quad |\alpha_c|^2 + |\alpha_d|^2 = 1$$

and satisifying the equation $(H_o + H_1)\psi_k = E(k)\psi_k$ 1.60

Using equations 1.59, 1.60 and the orthogonality condition gives the secular equation

$$E^2 - E(E_c + E_d) + E_cE_d - V^2 = 0 \qquad 1.61$$

which has two solutions for each wave vector k

$$E^{\pm} = \frac{1}{2}(E_c + E_d) \pm \left[\left(\frac{E_c - E_d}{2}\right)^2 + V^2\right]^{\frac{1}{2}}$$

In the case of five degenerate d-orbitals just one linear combination of the ϕ_d is mixed with the conduction electron states, the other four remain degenerate at E_d. Also the V^2 of equation 1.61 becomes $V^2 = \sum_{i=1}^{5} |V_i|^2$, where the V_i refer to the initial five ϕ_{di} Bloch waves.

Daniel continues the analysis for the states of opposite spin whose energies differ by some effective exchange energy (for the ferromagnetic regime) and constructs the schematic band structure of figure 1.7 with the Fermi level E_F lying between $E_d^{\uparrow}$ and $E_d^{\downarrow}$. Daniel states that "due to coherent hybridization .... the d-orbitals are spread into the conduction band over a range of energy of order $2V \approx 2eV$ ...." and ".... the width of the virtual bound states in the paramagnetic phase should be $\Delta \simeq \pi V^2 \rho(E_F)$, which is expected to be smaller than 2V as $V\rho(E_F) \ll 1$ for a broad conduction band."

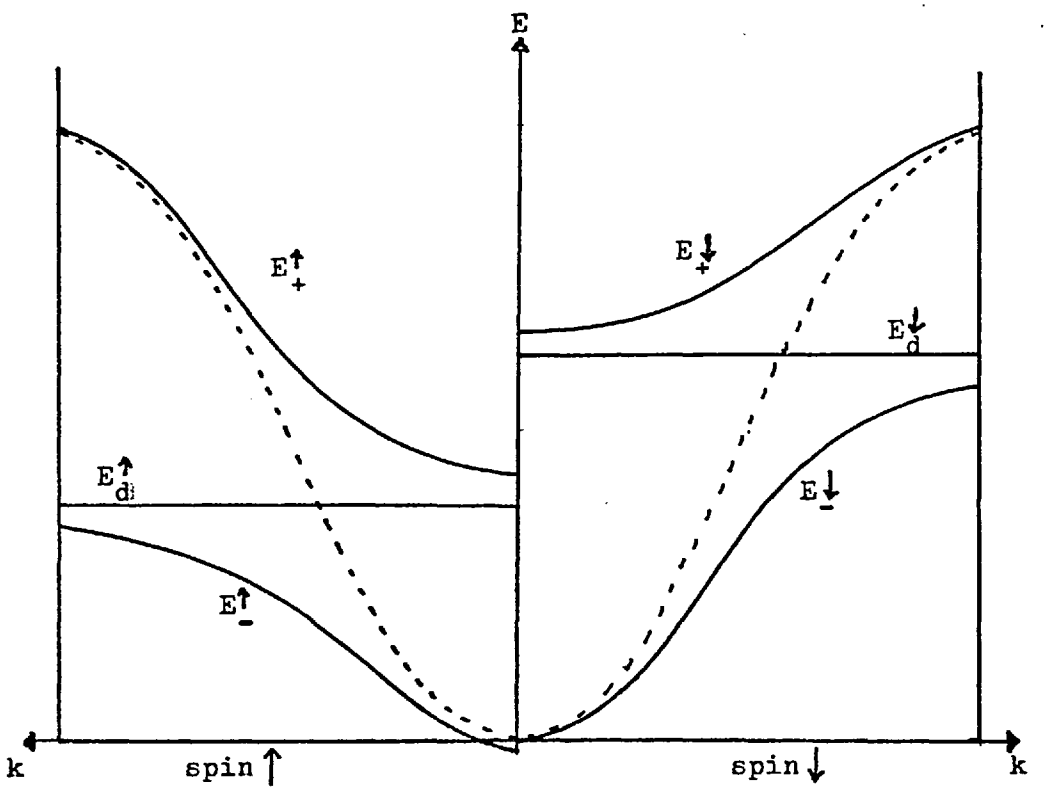


FIG 1.7 HYBRIDIZATION OF s AND d STATES IN FERROMAGNETIC HEUSLER ALLOYS . AFTER REF(47).

Several observations may be made. Firstly it is not obvious that the d-"band" width in the paramagnetic regime reverts to the isolated solute atom value given by $\Delta = \pi V^2 \rho(E_F)$ as, although the coherent exchange (spin dependent) scattering at each Mn site has been lost, the strong resonant scattering remains. Secondly, Daniel's model should be applicable to a dilute compound containing non-magnetic transition atoms as, in the sense that the electron scattering is again coherent at each atomic site, this is an analagous situation to the ferro-magnetic Heusler alloys and the conclusions about a broadening of the d-"band" in the compound relative to the isolated solute atom virtual bound state should still apply.

Hargitai (*) has suggested a model Hamiltonian for a dilute transition metal intermetallic compound in which the

* Private Communication . C. Hargitai.

localised d electrons on each transition metal atom hybridize with all the conduction electron bands. The Hamiltonian is of the form:-

$$H = \sum_{kn\sigma} \epsilon_{kn}\, a^{\dagger}_{kn\sigma} a_{kn\sigma} + E \sum_{i\sigma} d^{\dagger}_{i\sigma} d_{i\sigma} + U d^{\dagger}_{i\uparrow} d_{i\uparrow} d^{\dagger}_{i\downarrow} d_{i\downarrow}$$
$$+ V \sum_{kin\sigma} \left(e^{ikR_i}\, a^{\dagger}_{kn\sigma} d_{i\sigma} + c.c. \right) \qquad 1.62$$

where the subscript n labels the conduction electron bands, and i the d electrons. It is assumed that the hybridization matrix element V is a constant and that there is one transition metal atom per unit cell. All other symbols have their usual meaning.

Within the Hartree-Fock approximation the secular equation is of the form:

$$\det \begin{vmatrix} \epsilon_{k1} - E_k & & & & & Ve^{ikR_1} & Ve^{ikR_2} & \cdots \\ & \epsilon_{k2} - E_k & & & & \vdots & \vdots & \\ & & \ddots & & & & & \\ & & & \epsilon_{kn} - E_k & & Ve^{ikR_1} & Ve^{ikR_2} & \cdots \\ \overline{V^* e^{-ikR_1}} & \overline{V^* e^{-ikR_2}} & \cdots & \cdots & & & & \\ \vdots & \vdots & & & & & & \\ & & & & & E_d^{\sigma} - E_k & & \\ & & & & & & \ddots & \end{vmatrix} = 0 \qquad 1.63$$

$$\text{Hence} \quad (E_d^{\sigma} - E_k) - V^2 \sum_n \frac{1}{\epsilon_{kn} - E_k} = 0 \qquad 1.64$$

Following a similar treatment to that of Anderson (6), Hargitai finds a Green's function $G^{\sigma}_{dd}(\omega)$ given by:

$$G^{\sigma}_{dd}(\omega) = \left[\omega - E_d - V^2 \sum_n \frac{1}{\omega - \epsilon_{kn}}\right]^{-1} \qquad 1.65$$

which may be compared with that found in Anderson's paper:

$$G^{\sigma}_{dd}(\omega) = \left[\omega - E_d - \sum_k \frac{|V_{kd}|^2}{\omega - \epsilon_k}\right]^{-1} \qquad 1.66$$

The additional density of states due to the d-state resonance is given in terms of the Greens function G^{σ}_{dd} by

$$\rho_{d\sigma}(\epsilon) = -\frac{1}{\pi} \mathrm{Im}\left[G^{\sigma}_{dd}(\epsilon)\right] \qquad 1.67$$

The exact form of the resonance like d-band for a given intermetallic compound crystal structure will depend on the summation over the conduction electron bands n in equation 1.65.

One important case to be considered is that of extreme dilution of the intermetallic compound. By this we mean that if the compound has the composition MX_n where M is the transition metal and X a simple metal, then allow $n \to \infty$. The Brillouin zone of such a material will decrease in size and the number of conduction bands n show a corresponding increase. In the limit as $n \to \infty$ we have pure metal X with one transition metal impurity atom and the sum over n in equation 1.65 is replaced by a sum over k and the Greens function G^{σ}_{dd} is identical to that considered by Anderson (6) giving a virtual bound state width $\Delta = \pi V^2 \rho(E_F)$. It is a prerequisite of any theoretical model of intermetallic compounds that the Anderson isolated solute atom picture is retrieved in the limit of extreme dilution.

Treatment of Magnetic Interactions in Ordered Compounds

The treatment of interaction between localised moments in compounds compared with that in dilute solutions is simplified because the positions of all the atoms in the structure are, in principle, known. For the case of intermetallic compounds having as one constituent 3d transition metal atoms possessing localised magnetic moments we have seen that the predominant interaction mechanism is that described by Caroli. Caroli and Blandin (46) have used this form of interaction to calculate the ferromagnetic Curie temperatures of Heusler alloys. The energy of interaction between a magnetic virtual bound state at the origin and one at position $\underline{R}$ may be written (see equation 1.48) as:

$$E(R) = 25\,\frac{E_F}{2\pi}\sum_{\sigma,\sigma'}\sigma\sigma'\sin\phi^{\sigma}\sin\phi^{\sigma'}\cos(2k_FR + \phi^{\sigma} + \phi^{\sigma'})\,\frac{\underline{U}_o.\underline{U}_R}{(k_FR)^3} \qquad 1.68$$

where $\underline{U}_R$ and $\underline{U}_o$ are unit vectors in the direction of magnetic moment on the atoms at position R and at the origin. Treating the spins classically one may write

$$\underline{U}_o.\underline{U}_R = \frac{\underline{S}_o.\underline{S}_R}{S^2}$$

The total interaction energy is

$$\mathcal{H} = -\sum_{RR'} J(\underline{R} - \underline{R}')\underline{S}_R.\underline{S}_{R'} \qquad 1.69$$

with $$J(\underline{R}) = \frac{25\ E_F}{4S^2\pi} \sum_{\sigma,\sigma'} \sigma\sigma' \sin\phi^{\sigma} \sin\phi^{\sigma'} \frac{\cos(2k_F R + \phi^{\sigma} + \phi^{\sigma'})}{(k_F R)^3} \qquad 1.70$$

In the molecular field approximation the effect of all the other spins on the one at the origin is taken into account by introducing a magnetic field $\underline{H}_R$

where $$\underline{H}_R = \sum_{R \neq R'} 2J(\underline{R} - \underline{R}') \langle \underline{S}_{R'} \rangle$$

and $\langle \underline{S}_R \rangle$ is determined by

$$\langle \underline{S}_R \rangle = SL\left(\frac{SH_R}{k_B T}\right)$$ where L is the Langevin function. At high temperatures it gives:

$$\langle \underline{S}_R \rangle = \frac{S^2 \underline{H}_R}{3k_B T} = \frac{2S^2}{3k_B T} \sum_{R \neq R'} J(\underline{R} - \underline{R}') \langle \underline{S}_R \rangle \qquad 1.71$$

In the molecular field theory the paramagnetic Curie-Weiss temperature Θ and the ferromagnetic Curie temperature T_c are equal, and given by:-

$$k_B T_c \approx \frac{25E_F}{6\pi} \sum_{R \neq 0} \sum_{\sigma,\sigma'} \sigma\sigma' \sin\phi^{\sigma} \sin\phi^{\sigma'} \frac{\cos(2k_F R + \phi^{\sigma'} + \phi^{\sigma})}{(k_F R)^3} \qquad 1.72$$

The final expression for the Curie temperature does not depend explicitly upon the spins S, although of course the phase shifts ϕ^{σ} are determined in terms of the spin↑ and spin↓ virtual bound state occupation numbers (and hence the magnetic moment) by

the Friedel Sum Rule. Blandin and Caroli were able to account for the observed Curie temperatures of Cu_2MnAl and Cu_2MnIn to within 15%. From the form of equation 1.71 it can be seen that spiral or other complex types of magnetic ordering may arise.

1.4 PHYSICAL PROPERTIES OF MATERIALS

SPECIFIC HEAT

The specific heat of a material is defined by the relationship

$$C_{x,y..} = \underset{\delta T \to 0}{\text{limit}} \left(\frac{\delta Q}{\delta T}\right)_{x,y..} \qquad 1.73$$

where δT is the temperature rise and δQ the heat input (which is just equal to the change in internal energy it no external work is done). Theoretical calculations generally assume that the volume is constant, hence giving C_v. However experimentally, and particularly with metals, it is easier to measure C_p, the specific heat at constant pressure. C_p and C_v are related by the thermodynamic identity:

$$C_p - C_v = \frac{TV\beta^2}{k_T} \qquad 1.74$$

where β is the volume compressibility $= V^{-1}\left(\frac{\partial V}{\partial T}\right)_p$ and k_T the isothermal compressibility $= -V^{-1}\left(\frac{\partial V}{\partial P}\right)_T$. As an example of the size of this difference for a typical metal, $\frac{C_p - C_v}{C_p}$ has the following values for copper:- 11% at 1000 K, 2.6% at 300 K, 0.6% at 100 K and it falls even faster at lower temperatures.

There are several contributions to the specific heat of a pure metal or intermetallic compound which are of relevance here.

(1) The lattice specific heat

(2) The specific heat of the electrons

(3) A magnetic contribution to the specific heat from spin waves

The Lattice Specific Heat

Classically it is possible to regard each atom in a crystal as an independent harmonic oscillator. Each atom may oscillate in three dimensions and has, by the equipartition theorem, an energy of $3kT$, therefore the total internal energy of one mole of material is $E = 3NkT$, where N is Avogadro's number. Therefore the lattice specific heat C_v is,

$$C_v = \frac{\partial E}{\partial T} = 3Nk = 3R = 24.9 \text{ joules/mole.K}$$

Experimentally the constant value of $3R$ is only observed at high temperatures, and C_v tends towards zero as T approaches zero. This behaviour on lowering the temperature could only be explained after the development of quantum theory.

Einstein suggested a very simple model of the lattice vibrations in which all the atoms are considered to vibrate independantly of each other and at a fixed frequency ν_E. The vibrational energy levels of such an atom are:

$$\epsilon_n = \frac{1}{2} h\nu + nh\nu$$

where $\frac{1}{2}h\nu$ is the zero point energy.

Maxwell-Boltzman statistics have to be applied to determine the average energy $\bar{\epsilon}$ of each atom, which is then given by:

$$\bar{\epsilon} = \frac{\sum_n \epsilon_n \exp\left(-\frac{\epsilon_n}{kT}\right)}{\sum_n \exp\left(-\frac{\epsilon_n}{kT}\right)} = \frac{1}{2}h\nu + \frac{h\nu}{\exp\left(\frac{h\nu}{kT}\right) - 1}$$

and the specific heat per mole is

$$C = \frac{\partial(N\bar{\epsilon})}{\partial T} = 3R\left(\frac{h\nu}{kT}\right)^2 \frac{e^{\frac{h\nu}{kT}}}{\left[\exp\left(\frac{h\nu}{kT}\right) - 1\right]^2} \qquad 1.75$$

In the high temperature limit, this expression gives the classical value 3R. In the low temperature limit it gives:

$$C = 3R\left(\frac{h\nu}{kT}\right)^2 \exp\left(\frac{-h\nu}{kT}\right)$$

which, although tending to zero as T approaches zero, does not follow the experimentally observed dependence of $C \propto T^3$ as $T \to 0$.

The next development was due to Debye, who made the assumption that a crystal could be considered as an elastic homogeneous solid. The thermal energy will then be distributed among the normal modes of such a material. For one fixed value of the frequency ν there are three independant waves, one longitudinal with velocity C_L and two mutually perpendicular transverse waves with velocity C_T. It may be shown that the number of modes with frequencies between ν and $\nu + d\nu$ is

$$g(\nu)\, d\nu = 4\pi V(C_L^{-3} + 2C_T^{-3})\nu^2 d\nu \qquad 1.76$$

where V is the volume.

It was Debye's suggestion that the frequency spectrum given by the equation 1.76 should be applied to the atomic lattice, while taking into account its discrete nature by setting on upper limit to the allowed frequency ν_D. The limit ν_D is fixed by the normalizing condition that the total number of independent modes is 3N. Thus, for a molar volume V:

$$3N = \int_0^{\nu_D} g(\nu)\, d\nu = \frac{4\pi V}{3} (C_L^{-3} + 2C_T^{-3})\nu_D^3$$

$$\therefore \quad \nu_D = \left(\frac{9N}{4\pi V}\right) \frac{1}{3} (C_L^{-3} + 2C_T^{-3})^{-\frac{1}{3}}$$

and $$g(\nu) = 9N\frac{\nu^2}{\nu_D^3} \quad \text{for } \nu < \nu_D$$

$$= 0 \quad \text{for} \quad \nu > \nu_D$$

A characteristic temperature may be defined for the lattice vibrational spectrum, this is the Debye temperature, Θ_D, given by:-

$$\Theta_D = \frac{h\nu_D}{k} = \frac{h}{k} (C_L^{-3} + 2C_T^{-3})^{-\frac{1}{3}} \left(\frac{9n}{4V}\right)^{\frac{1}{3}}$$

The total lattice vibrational energy of the crystal is

$$E = 9N \int_0^{\nu_D} \left[\frac{1}{2}h\nu + \frac{h\nu}{e^{\frac{h\nu}{kT}} - 1}\right] \frac{\nu^2}{\nu_D^3}\, d\nu$$

and the lattice specific heat per mole is then:

$$C_V = 9R\left(\frac{T}{\Theta_D}\right)^3 \int_0^{\frac{\Theta_D}{T}} \frac{x^4 e^x}{(e^x-1)^2}\, dx \qquad 1.77$$

where $x = \frac{h\nu}{kT}$.

At high temperatures, this again gives the classical value of 3R. As T approaches zero, the upper limit of the integral may be taken as infinity and the integral takes the constant value $\frac{4\pi^4}{15}$ and the specific heat takes the limiting form:

$$C_V = 1944\left(\frac{T}{\Theta_D}\right)^3 \text{ Joules/mole.degree} \qquad 1.78$$

At intermediate temperatures the integral must be evaluated numerically and tables of values exist.

One may take experimental data for the lattice specific heat and calculate the value of Θ_D required to fit the experiment at each temperature. If the Debye model is correct, then all the Θ_D values should be identical. In practise this is not found to happen (48). The Θ_D value remains constant for temperatures up to $\simeq \frac{\Theta_D}{50}$, then falls and passes through a minimum before rising again to a constant value at temperatures above $\frac{\Theta_D}{2}$. This behaviour is due to the departure of the true density of states curve for lattice vibrational modes from the simple quadratic form of the over-simplified Debye model.

Electronic Specific Heat

Because electrons are indistinguishable and obey the Pauli Exclusion principle, Fermi-Dirac statistics have to be used when calculating the electron distribution among the allowed energy states. The Fermi-Dirac distribution function has the form:

$$f(E) = \frac{1}{1 + \exp\left[\frac{(E - E_F)}{kT}\right]}$$

The number of allowed electron states within a range dE of energy E is given by the density of States function n(E)dE, and at T = 0 all the states up to the Fermi energy E_F are occupied. The degeneracy temperature T_F associated with the conduction electrons $= \frac{E_F}{k_B}$ and is of the order of 10^4 to 10^5 K for typical metals, so that at room temperature and below only a small fraction $\approx \frac{T}{T_F}$ of the total number of electrons may be excited into vacant states. The electronic specific heat C_e is obtained by differentiating the internal energy U of the electronic system with respect to temperature, where

$$U = \int_0^\infty \frac{En(E)dE}{\exp\left[\frac{E - E_F}{kT}\right] + 1} = \frac{\pi^2 k^2}{6} n(E_F) T^2$$

giving $$C_e = \frac{\pi^2 k^2}{3} n(E_F) T = \gamma T \qquad 1.79$$

If γ is measured in units of milli-joules/mole.K^2 and the density of states $n(E_F)$ is defined in terms of states/eV. atom (including both spin directions) then the numerical relationship between them is $n(E_F) = 0.425\gamma$. The total specific heat of a pure simple metal is just the sum of the lattice and electronic contributions

$$C_{total} = C_{lattice} + C_e = \beta T^3 + \gamma T \qquad 1.80$$

and a plot of $\frac{C}{T}$ versus T^2 should therefore give a straight line with intercept γ on the $\frac{C}{T}$ axis and a gradient β.

Contribution to the Electronic Specific Heat from Resonant States

The presence of a virtual bound state on either an impurity in a pure metal, or on one of the constituent atom species of an intermetallic compound, will increase the density of states at the Fermi energy. Heeger (8) has calculated the additional specific heat per resonant state as

$$C = \frac{\pi^2 k^2}{3} \rho_i(E_F)\, T \qquad 1.81$$

where $$\rho_i(E_F) = \rho_d(E_F)\left[1 - \frac{(E_F - E_d)}{\rho(E_F)} \cdot \frac{d\rho(E_F)}{dE}\right]$$

$\rho(E_F)$ is the conduction electron density of states, $\rho_d(E_F)$ the additional density of states from the resonance and E_d the energy of the centre of the resonance. For a slowly varying $\rho(E)$ as a function of energy then

$\left|\frac{(E_F - E_d)}{\rho(E_F)} \cdot \frac{d\,(E)}{dE}\right| \ll 1$ and the additional specific heat per resonant state becomes

$$C = \frac{\pi^2 k^2}{3} \rho_d(E_F) T \qquad 1.82$$

There is a simple addition of the resonant density of states $\rho_d(E_F)$ to the conduction electron density of states.

Spin Wave Specific Heat

At finite temperatures in a magnetically ordered material, departures from perfect order are best described in terms of spin waves (or magnons), the collective excitations of the spin system. These are charactised by a frequency spectrum ω_q = some function of q, the wave vector.It may be shown (49) that for a ferromagnet or ferrimagnet the dispersion relation is $\omega_q \propto q^2$, while for anti-ferromagnets $\omega_q \propto q$. This results in a specific heat contribution proportional to $T^{\frac{3}{2}}$ for ferro and ferri-magnets and T^3 for anti ferromagnets. In either case it is difficult to separate the spin wave term from the electronic and lattice terms of the measured total specific heat.

Mackintosh (50) has suggested that when a gap Δ occurs in the spin-wave spectrum due to anisotropy, then this may be taken into account by multiplying the spin wave specific heat term by $\exp\left(-\frac{\Delta}{kT}\right)$. A gap must be present for an anti-ferromagnet

MAGNETIC SUSCEPTIBILITY

The response of a material to an applied magnetic field is determined by its magnetic susceptibility χ, which may be a function of both the field and the temperature, and is defined by the relation:

$$\underline{M} = \chi \underline{H}$$

where $\underline{M}$ is the magnetisation and $\underline{H}$ the applied field.

The measured total susceptibility may be the sum of several contributions, these are the following:-

(1) Tendency towards alignment of permanent atomic magnetic moments by the applied field.

(2) The "Van-Vleck" susceptibility, due to the perturbing effects of the magnetic field.

(3) Core or filled-shell diamagnetism.

(4) Pauli spin paramagnetism of the conduction electrons

(5) Diamagnetism of the conduction electrons.

Alignment of Permanent Atomic Moments and Van-Vleck Paramagnetism

Van-Vleck (51) has shown that the average magnetic moment, $\bar{m}_{Hnjm}$, associated with a given eigenstate characterised by quantum numbers njm and in magnetic field H is given by:

$$\bar{m}_{Hnjm} = -\frac{\partial E_{njm}}{\partial H} = \langle njm | m_H | njm \rangle$$

$$= \langle njm | m_H^o | njm \rangle + 2H \sum_{n'j'm' \neq njm} \frac{|\langle njm | m_H^o | n'j'm' \rangle|^2}{E_{n'j'm'} - E_{njm}} + \cdots \qquad 1.83$$

The total magnetisation of a material is the statistical mean of m_H weighted by the Boltzman factor $e^{-E_{njm}/kT}$ over all possible eigenstates. Thus the magnetisation per mole is:

$$M = N \frac{\sum_{njm} \langle njm | m_H | njm \rangle e^{-E_{njm}/kT}}{\sum_{njm} e^{-E_{njm}/kT}} \qquad 1.84$$

Using equations 1.83 and 1.84 Van Vleck arrives at the following expression for the field independent susceptibility

$$\chi = \frac{B}{kT} \sum_{jm} |\langle jm | m_H | jm \rangle|^2 e^{-E^o_{njm}/kT} \quad +$$

$$+ \; 2B \sum_{jm \neq j'm'} \frac{\left|\langle jm|\mu_H|j'm'\rangle\right|^2 e^{-E^o_{njm}/kT}}{E^o_{nj'm'} - E^o_{njm}}$$

$$+ \sum_{jmn'j'n'} \frac{\left|\langle njm|m^o_H|n'j'n'\rangle\right|^2 e^{-E^o_{njm}/kT}}{E^o_{n'j'm'} - E^o_{njm}} \qquad 1.85$$

where $\langle jm|\mu_H|j'm'\rangle = \langle njm|m^o_H|nj'm'\rangle$ and $B = \dfrac{N}{\sum_{jm} e^{-E^o_{njm}/kT}}$

The third term of equation 1.85 is the "Van Vleck" susceptibility and its magnitude depends upon the detailed nature of the eigenstates of the system and on their separation in energy. In situations where the energy change associated with changing the quantum number n is much larger that kT, then equation 1.85 becomes:

$$\chi = \frac{B}{kT} \sum_{jmj'm'} \left|\langle jm|\mu|j'm'\rangle\right|^2 e^{-E^o_{njm}/kT} + 2B \sum_{\substack{jmn'j'm' \\ (n \neq n)}} \frac{\left|\langle njm|m^o_H|n'j'm'\rangle\right|^2 e^{-E^o_{njm}/kT}}{E^o_{n'j'm'} - E^o_{njm}} \qquad 1.86$$

Two simple cases exist, the first when the multiplets are <u>narrow</u> compared to kT. The expression for the susceptibility becomes:

$$\chi = \frac{N\mu_B^2}{3kT}\left[4S(S+1) + L(L+1)\right] \quad (+ \text{ Van Vleck term}) \qquad 1.87$$

The second case is for multiplets <u>broad</u> compared to kT, when

$$\chi = \frac{N\mu_B^2 g^2 J(J+1)}{3kT} \qquad 1.88$$

where g is the Lande g-factor

$$g = 1 + \frac{S(S+1) + J(J+1) - L(L+1)}{2J(J+1)}$$

When measuring the susceptibility χ, it is often convenient to use an effective moment p_{eff}, such that

$$\chi = \frac{N\mu_B^2 p_{eff}^2}{3kT} = \frac{C}{T} \qquad 1.89$$

hence $$p_{eff} = \left(\frac{3kT\chi}{N\mu_B^2}\right)^{\frac{1}{2}} = \left(\frac{3kC}{N\mu_B^2}\right)^{\frac{1}{2}}$$

If the measured susceptibility is expressed in e.m.u. per mole the relationship between p_{eff} and C is

$$p_{eff} = 2.839\sqrt{C} \text{ Bohr magnetons} \qquad 1.90$$

It is found that experimentally determined values of p_{eff} for salts and dilute solid solutions (if a "good" moment exists at all) of 3d transition atoms agree well with the p_{eff} values calculated as if the orbital moment does not exist at all i.e. $p_{eff} = 2[S(S+1)]^{\frac{1}{2}}$. In these situations the orbital moment is said to be "quenched".

Pauli Spin Paramagnetism

The effect of an applied magnetic field H on the degenerate gas of conduction electrons of a material is to lower the energy of those electrons with spins parallel to the field by $\mu_B H$, where μ_B is the Bohr magneton, and to raise the energy of

those with spins anti-parallel to the field by the same amount. This leads to a redistribution of electrons and results in an excess of electrons with spins parallel to the field. Hence

$$N_+ - N_- = \frac{1}{2} \int_0^\infty \left[n(E + \mu_B H) - n(E - \mu_B H) \right] f(E) dE$$

where n(E) is the density of states (including both spin directions) and f(E) the Fermi-Dirac distribution function.

For small H and at T = 0 this yields a magnetisation of

$$M = \mu(N_+ - N_-) = H\mu_B^2 \int_0^\infty f(E) \frac{dN(E)}{dE} dE = H\mu_B^2 n(E_F)$$

and a magnetic susceptibility of

$$\chi = \frac{M}{H} = \mu_B^2 n(E_F) \qquad 1.91$$

For finite temperatures, but still small with respect to the degeneracy temperature T_F, (52) shows that the susceptibility becomes

$$\chi = \mu_B^2 n(E_F) \left[1 + \frac{\pi^2 (kT)^2}{6} \left(\frac{d^2 \log n(E)}{dE^2} \right)_{E_F} \right] \qquad 1.92$$

Contribution to the Pauli Paramagnetism from Virtual Bound States

The additional susceptibility per virtual bound state may be calculated from the change in d electron occupation numbers $n_{d\uparrow}$ and $n_{d\downarrow}$ due to an applied magnetic field. Anderson (6) and Klein and Heeger (8) have calculated this, and find that:

$$\chi_d = \frac{\mu_B^2 \rho_d(E_F)}{1 - (U + 4J)\frac{\rho_d(E_F)}{10}} \qquad 1.93$$

where $\rho_d(E_F)$ is the additional density of states at the Fermi level due to the presence of the virtual bound state.

$$\therefore \chi_d = \eta \mu_B^2 \rho_d(E_F) \qquad 1.94$$

This is the expression one would expect for the susceptibility due to the increased density of states at the Fermi energy apart from the enhancement factor $\eta = \left[1 - (U + 4J).\frac{\rho_d(E_F)}{10}\right]^{-1}$. As the critical condition for the appearance of a local moment is approached then $\eta \to \infty$.

Core Diamagnetism

The effect of an applied magnetic field on the motion of core electrons is to superimpose a precession about the field direction at the Larmor frequency ω_L, where

$$\omega_L = \frac{eB}{2mc}.$$

If there are Z core electrons per atom, this precession is equivalent to an electric current

$I = -\frac{Ze^2B}{4\pi mc}$ and hence to a magnetic moment of

$\mu = \frac{-Ze^2B\langle\rho^2\rangle}{4mc^2}$ where $\langle\rho^2\rangle$ is the mean square radius of the electrons from the magnetic axis. In the case of spherical symmetry $\langle\rho^2\rangle = \frac{2}{3}\langle r^2\rangle$, where $\langle r^2\rangle$ is the mean square radius of

the electron distribution.

Therefore the total diamagnetic susceptibility χ per atom is

$$\chi = \frac{\mu}{B} = \frac{-Ze^2\langle r^2\rangle}{6mc^2} \qquad 1.95$$

Contribution to Core Diamagnetism from Resonant Impurities

Flynn et.al. (53) have measured the magnetic susceptibility contribution of a number of impurities, of both simple and transition metals, dissolved in liquid aluminium. They estimate that the diamagnetism of the filled 3d shell is $\approx -20 \times 10^{-6}$ c.g.s./mole and that this contribution becomes less negative for the partially filled shells (or resonant states) of the lighter 3d elements, dropping to -15×10^{-6} c.g.s./mole for cobalt and $\approx -10 \times 10^{-6}$ c.g.s./mole for iron and manganese.

Conduction Electron Diamagnetism

According to arguments based upon classical mechanics the diamagnetic susceptibility of a free-electron gas should be zero. This arises from the fact that the free energy of the system depends only upon the velocity of the electrons, which does not change on applying a magnetic field. Even when the electrons are moving in a spatially varying field, a theorem due to Van Leeuwen (54) shows that the diamagnetic susceptibility is zero when treated by classical mechanics.

This result is no longer valid according to quantum mechanics, as the electrons moving in orbits about the field direction have to satisfy quantum restrictions. The diamagnetic susceptibility of a degenerate electron gas using Fermi-Dirac statistics was first obtained by Landau:

$$\chi_{\text{Landau}} = \frac{-4\pi m}{3h^2}\left(\frac{3N}{\pi}\right)^{\frac{1}{3}}\mu_B^2 \qquad 1.96$$

For free electrons, this is numerically equal to one-third of the Pauli-spin paramagnetic contribution.

Peierls (55) has investigated the effect of the periodic lattice potential on the conduction electron diamagnetism, using tight binding wave functions. A special case (56) is that in which the surfaces of constant energy form ellipsoids in k-space and the energy may be written

$$E = \frac{\hbar^2}{2m}\left(\alpha_1 k_x^2 + \alpha_2 k_y^2 + \alpha_3 k_z^2\right)$$

In this case if the magnetic field lies along the z-axis the Landau formula (equation 1.96) is multiplied by a factor:

$$\left(\frac{(\alpha_1\alpha_2)^2}{\alpha_3}\right)^{\frac{1}{3}}$$

and may take anomalously large or small values depending upon the detailed topography of the Fermi surface and Brillouin zone overlap.

ELECTRICAL RESISTIVITY

There are a number of electron scattering mechanisms which may contribute to the electrical resistivity of a metal or an intermetallic compound, and it is possible to think of the majority of these mechanisms as leading to the breakdown of translational symmetry within the material. The major contributions are the following:-

(1) Scattering by lattice vibrations (phonons), which is strongly temperature dependant.

(2) Scattering by lattice imperfections such as vacancies and dislocations.

(3) Electron-electron scattering, important for transition metals and transition metal intermetallic compounds.

(4) Spin disorder scattering in magnetic materials.

(5) Impurity scattering. This is separable into several contributions.

(a) Atomic size difference between impurity and host leading to lattice distortion.

(b) Potential scattering due to a valency difference between impurity and host atoms.

(c) Resonance scattering by an impurity virtual bound state.

(d) Exchange scattering by an impurity localised magnetic moment. This is temperature dependent when treated beyond first order in perturbation theory and is discussed in the section on the Kondo Effect.

Restricting ourselves to simple metals and ignoring contributions of the 5(d) type, it is possible to collect together all the temperature independent terms* into ρ_0, leaving the temperature dependence in the phonon term $\rho_L(T)$, where $\rho_L(T)$ is the phonon resistivity of the pure material. The total resistivity may then be written as

$$\rho = \rho_L(T) + \rho_0 \qquad 1.97$$

and this is known as Matthiessen's Rule. It implies that the phonon resistivity of the pure metal is unmodified by the addition

* i.e. assuming, although this is not strictly true, that terms (2) - (5) are temperature independent.

of impurities (including lattice imperfections). Experimentally the rule is reasonably well obeyed, although deviations have been observed. Theoretical explanations of these deviations from Matthiessen's rule are still the subject of considerable argument.

The Phonon Resistivity

The phonon resistivity of pure samples of many simple metals, e.g. sodium and potassium, is observed to vary as T^5 in the low temperature limit and as T at high temperatures. A simple theoretical approach by Bloch, assuming a spherical Fermi surface and ignoring Umklapp processes, predicted an equation for the phonon resistivity of the form:

$$\rho_L = \frac{C}{M\Theta_R}\left(\frac{T}{\Theta_R}\right)^5 \int_0^{\frac{\Theta_R}{T}} \frac{z^5 dz}{(e^z - 1)(1 - e^{-z})} \qquad 1.98$$

where C is a constant, M the atomic weight and Θ_R a characteristic temperature for the lattice vibrational spectrum which is relevant to the electrical resistivity and hence not necessarily equal to the Debye temperature. The integral reduces to a constant in the low temperature limit and to $\frac{1}{4}\left(\frac{\Theta_R}{T}\right)^4$ in the high temperature limit.

Hence $\rho_L = \frac{C}{4M\Theta_R^2} \cdot T$ at high T

and $\rho_L = \frac{124.4C}{M\Theta_R} \cdot \frac{T^5}{\Theta_R^5}$ at low T

Gruneisen (57) suggested that equation 1.98 should give the correct form of the phonon resistivity at intermediate temperatures also and it is now known as the Gruneisen-Bloch equation. Ziman (58) has examined the magnitude of the phonon resistivity in the high temperature limit for the more realistic situation of Fermi surface zone contact and including both Normal and Umklapp scattering processes. His final expression is of the form

$$\rho_L = \frac{CQT}{M\Theta_D} \cdot n_c^{\frac{2}{3}} \left(\frac{S_{f.e.}}{S}\right)^2 \qquad 1.99$$

where C is a constant independent of the material under consideration, Q the radius of the Debye sphere (and inversely proportional to the cube root of the unit cell volume), n_c the number of conduction electrons per atom, S the actual Fermi surface area and $S_{f.e.}$ the calculated Fermi-surface area using the free electron model with n_c conduction electrons per atom. Hence all other factors being equal one would expect the resistivity to vary as $\left(\frac{S_{f.e.}}{S}\right)^2$

Ziman (58) has evaluated equation 1.99 using measured values of the parameters M, Θ_D, n_c and also S (from anomalous skin effect measurements) for several metals in groups 1, 11, 111, and 1V of the periodic table and obtains agreement with the experimentally measured resistivities within a factor of two.

Transition Metals and Inter-band Scattering

The inter-band scattering model was first proposed by Mott (59) to explain the high phonon resistivities of transition metals. Because the narrow d-band width and high density of states

in these metals leads to a large d electron effective mass, the majority of the electric current is carried by s electrons. However the vacant d states are still available to act as a "trap" for s electrons which are scattered by phonons. It turns out that the ratio of the resistivity contributions from $s \rightarrow s$ and $s \rightarrow d$ phonon scatterings are proportional to the densities of states in the s and d bands respectively.

$$\text{i.e.} \quad \frac{\rho_{s \rightarrow d}}{\rho_{s \rightarrow s}} = \frac{n_d(E_F)}{n_s(E_F)}$$

Electron-electron Scattering

In a simple free-electron-like metal, electron-electron collisions are not expected to contribute to the electrical resistivity because the average electron momentum in the direction of the electric field is conserved at each collision. However, as Baber (60) first pointed out, collisions between s and d electrons in a transition metal may give rise to an important contribution to the resistivity. This arises from the large effective mass of the d electrons, which enables s electrons, the predominant current carriers, to lose drift momentum at collisions. The predicted temperature dependence for this resistivity contribution is T^2 and it arises because both the numbers of scattering electrons of available empty states are proportional to kT. The final expression for the resistivity is (61)

$$\rho_{el\text{-}el} \approx \frac{\pi^4}{16} \frac{e^2}{v_s E_F} \left(\frac{k_F}{q}\right)\left(\frac{v_s - v_d}{v_d}\right)^2 \left(\frac{kT}{E_F}\right)^2 \qquad 1.100$$

where q is the electronic screening length and v_s and v_d the Fermi velocities for s and d electrons respectively. A term of this type would be expected to dominate the electrical resistivity at low temperatures where the phonon contribution drops as T^5. A T^2 low temperature term is in fact observed in the transition metals Pd, Pt, Rh and W (62). A T^2 term is also observed in the ferro-magnetic transition metals Co, Ni and Fe but a part of this is attributable to scattering by spin excitations.

Spin Disorder Resistivity

For a magnetic material, the departure from translational symmetry due to spin disorder gives rise to a contribution to the electrical resistivity. In the region well above the magnetic ordering temperature, where there is no correlation between spin directions on different atomic sites, this contribution is temperature independent. As the material is cooled below the magnetic ordering temperature the degree of long range order grows and the spin disorder resistivity falls, until at T = 0, where perfect order exists, it is zero.

At temperatures well below the magnetic ordering temperature, where spin-disorder is best described in terms of spin waves, Mannari (63) has investigated the scattering of conduction electrons through the s - d exchange interaction. He finds a resistivity contribution which goes as T^2 for a ferro-magnet and as T^4 for an anti-ferro-magnet. Liu (64) has pointed out that the s - d interaction should not be regarded as a small perturbation on a system of magnetically coupled spins, and free electrons. He takes a model in which the d-spin coupling arises entirely from the indirect s - d exchange and, for a ferro-magnet,

finds an additional term proportional to $T^{\frac{3}{2}}$ in the resistivity which dominates at low temperatures.

Friedel and de Gennes (65) have shown that an additional resistivity contribution may arise from critical phenomena, and particularly from the short range order which may exist at temperatures above the critical temperature for long range magnetic order.

Impurity Resistivity

In the absence of impurity-impurity interactions it is possible to separate the impurity resistivity into three contributions

$$\rho_{imp} = \rho_n + \rho_{res} + \rho_{exch}$$

where ρ_{res} represents resonant scattering by the impurity virtual bound state, ρ_{exch} exchange scattering and ρ_n non-resonant and spin-independent contributions. Abrikosov (66) has shown that interference terms between ρ_{exch} and $\rho_{res}+\rho_n$ vanish.

The resonant scattering contributions ρ_{res} may be calculated using a Friedel phase shift analysis for a free-electron like solvent (5,67).

$$\rho_{res} = \frac{ch(2\ell + 1)}{ze^2 k_F}\left[\sin^2\eta_{\ell\uparrow} + \sin^2\eta_{\ell\downarrow}\right] \qquad 1.101$$

where c is the impurity concentration, z the number of conduction electrons per solvent atom. For a virtual d state $\ell = 2$ and the phase shifts $\eta_{\ell\uparrow}$ and $\eta_{\ell\downarrow}$ are related to the number of d electrons of spin $\uparrow$ and $\downarrow$ by the Friedel Sum Rule.

i.e. $\eta_{\ell\uparrow} = \frac{\pi}{5} n_{d\uparrow}$ and $\eta_{\ell\downarrow} = \frac{\pi}{5} n_{d\downarrow}$

For an unsplit virtual bound state $n_{d\uparrow} = n_{d\downarrow} = \frac{Z_d}{2}$, where Z_d is the total number of localised d electrons per impurity, and

$$\rho_{res} = \frac{10\ c\ h}{Ze^2 k_F} \sin^2\left(\frac{\pi Z_d}{10}\right) \qquad 1.102$$

1.5 REVIEW OF THE PROPERTIES OF DILUTE SOLUTIONS OF TRANSITION METAL ATOMS DISSOLVED IN ZINC

As it is our intention to compare the properties of transition atoms in the ζ-phase intermetallic compounds with those of the corresponding dilute solid solutions in zinc, it is first necessary to review the properties of the latter.

Zn-Mn System

Resistivity

Measurements (68,69,70) show a Kondo effect, (i.e. a resistance minimum and an impurity resistivity varying logarithmically with temperature) with concentration dependent effects occuring above 20 p.p.m. of Mn. In a recent study on alloys with concentrations below 20 p.p.m. Ford et.al. (71) found deviations from a pure logarithmic behaviour below 0.5 K - in fact a T^2 dependence is observed. They were able to fit their data to Hammann's equation based on the s.S exchange model:

$$\rho(T) = A + B\left[1 - \frac{\ln\left(\frac{T}{T_k}\right)}{\left(\ln^2\left(\frac{T}{T_k}\right) + \pi^2 S(S+1)\right)^{\frac{1}{2}}}\right] \qquad 1.103$$

with $S = \frac{3}{2}$ and $T_k = 1$ K.

If the low temperature data is fitted to the expression

$$\rho(T) = \rho_o \left(1 - \left(\frac{T}{\theta}\right)^2\right) \text{ then } \theta = 2.5 \text{ K}$$

Magnetic Susceptibility

Measurements in the concentration range 0.04 - 0.4 at.% Mn indicate $S = \frac{3}{2}$ for the high temperature spin. (72). ($p_{eff} = 4.1\ \mu_B$)

Specific Heat

In two series of investigations on dilute alloys in the concentration range 0.02 to 0.2 at.% Mn, and at temperatures above 0.4 K, Martin (73,74) finds a maximum in the impurity contribution to the specific heat whose temperature increases linearly with concentration and that the associated entropy indicates a spin value $S = \frac{3}{2}$. There was no evidence for the concentration independant maximum predicted for a spin compensated state at $T \approx \frac{T_k}{3}$

Thermo-power

A "giant" negative thermo-power, characteristic of localised magnetic moments, has been found in various measurements on dilute alloys. (68,75).

Superconductivity

An investigation into the rate of depression of the superconducting transition temperature, T_c, of zinc by Mn impurities gives $-\frac{dT_c}{dc} = 315$ K/at.%. (76)

The Zn-Fe System

Resistivity

Measurements on Zn-Fe samples in the temperature range

1.5 - 4.2 K (77) indicate the presence of a very weak ln(T) term varying linearly with concentration for concentrations below 200 p.p.m. The quantity $\frac{1}{C}\frac{d\rho}{d(\ln T)}$ for Zn-Fe is about 1000 times smaller than for Zn-Mn alloys, where the Mn atoms definitely possess a localised magnetic moment at high temperatures.

In recent preliminary measurements (71) on samples in the same concentration range but at temperatures down to 0.3 K, it appears that the impurity resistivity shows a T^2 behaviour in the low temperature limit. Fitting the data to $\rho(T) = \rho_0\left(1 - \left(\frac{T}{\theta}\right)^2\right)$ gives θ = 80 K.

Magnetic Susceptibilty

Measurements on a sample of Zn-0.1 at.% Fe (1.78) show no evidence for the presence of a localised magnetic moment on the Fe atoms. The evidence for an additional temperature independent Pauli term is inconclusive.

Superconductivity

(76) finds $-\left(\frac{dT_c}{dc}\right)$ = 10 K/at.%, similar to that for Mn impurities in Al, the original localised spin fluctuation system.

The Zn-Co System

Few measurements exist on this system apart from residual resistivity measurements (67) and the superconductivity results of (76) indicating that the Co atoms are non-magnetic.

Residual Resistivities of 3d Impurities in Zinc

In figure 1.8 the impurity resistivity at 4.2 K is plotted as a function of the impurity atomic number. The data comes from two sources - Boato et.al. (67) and Ford et.al.'s (71) recent work on alloy concentrations below 20 p.p.m. In the case of

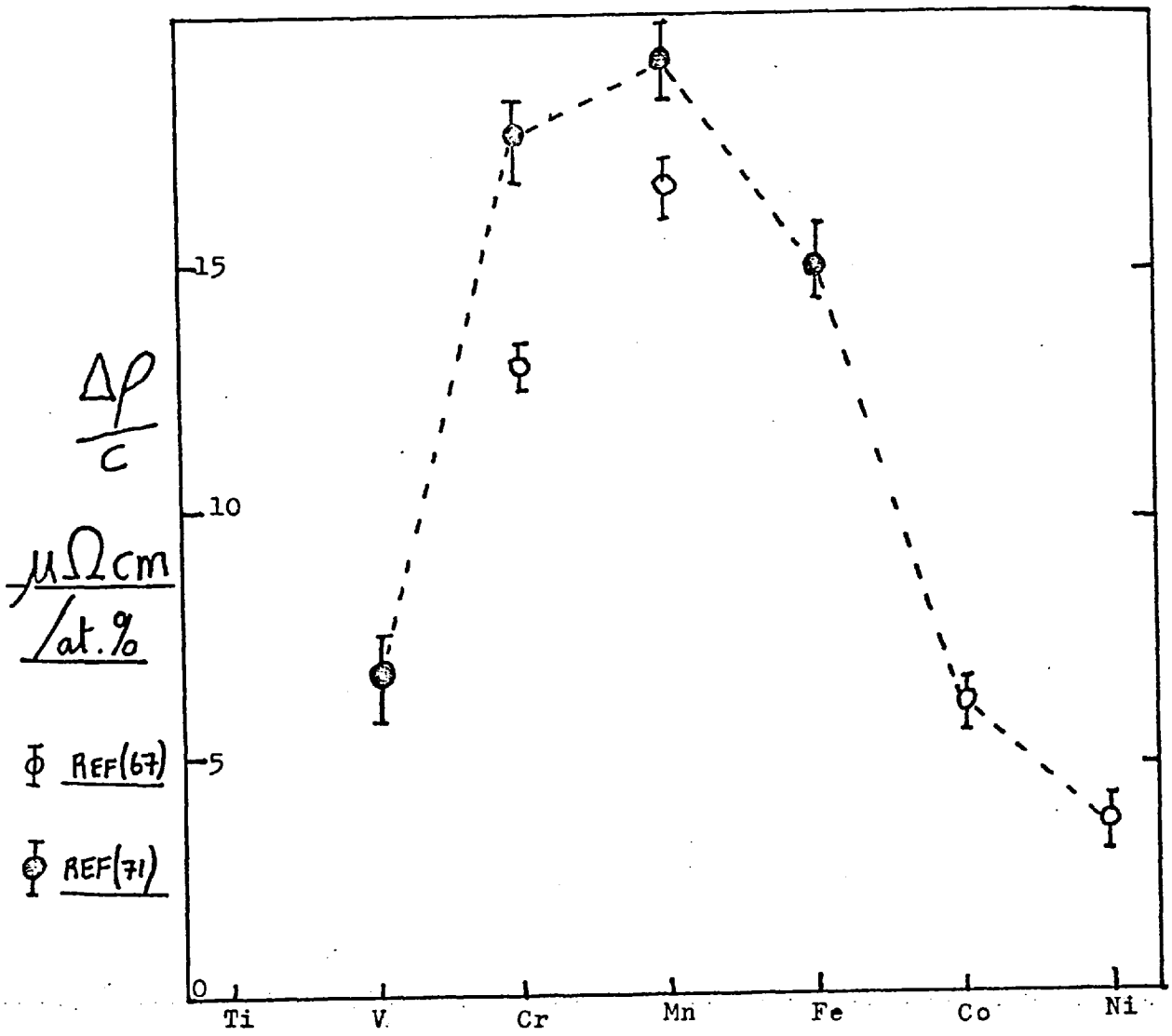


FIG 1.8 RESIDUAL RESISTIVITY (AT 4.2 K) FOR 3d METALS IN ZINC

ALLOY	Z_d	$\left(\frac{\rho_d}{c}\right)_{EXP}$ μΩcm/at%	$\left(\frac{\rho_d}{c}\right)_{FRIEDEL}$ μΩcm/at%	$\alpha = \frac{EXP}{THEORY}$
ZnV	2	6.5±1.0	2.84	2.29
ZnCr	4	18.5±1.0	7.45	2.5
ZnMn	5	23.5±1.0	8.24	2.85
ZnFe	7	14.8±1.0	5.38	2.75
ZnCo	8	6.2±1.0	2.84	2.18
ZnNi	9	1.9±1.0	0.78	2.44

TABLE 1.1 RESIDUAL RESISTIVITY OF 3d TRANSITION ATOMS IN ZINC

AT T=0 K AFTER REF(7 1)

Cr and Mn impurities the residual resistivity (at T = 0) will be different due to the temperature dependent spin scattering. Ford et.al. have been able to estimate the magnitude of this correction by fitting their low temperature data to Hammans expression (equation 1.103). The overall shape of the curve in figure 1.8 is unaltered by correcting for the spin resistivity and the corrected residual resistivities are shown in table 1.1.

Ford et.al. have calculated the residual resistivities for 3d impurities from the Friedel model, assuming non-magnetic virtual bound states and a free electron conduction band. The additional resistivity is proportional to $\sin^2\left(\frac{\pi Z_d}{10}\right)$ (c.f. equation 1.102). Their calculated values for the 3d impurity residual resistivities are also tabulated in table 1.1, assuming that Z_d is 2, 4, 5, 7, 8, and 9 for V, Cr, Mn, Fe, Co and Ni respectively.

The ratio between the experimental and calculated values is approximately constant $\approx 2.5 \pm 0.4$ and is probably due to the use of the free electron model for the zinc host metal. A somewhat better fit for the ZnCo system would be obtained if the number of d electrons on each cobalt atom was slightly greater than 8.

To summarise the behaviour of Mn, Fe and Co in dilute solution in zinc:- Mn is magnetic, Fe on the borderline and Co non-magnetic. The susceptibility measurements on dilute Zn-Mn indicate a certain amount of overlap is necessary between spin↑ and spin↓ virtual bound states to explain the p_{eff} value

1.6 PREVIOUS WORK ON DILUTE TRANSITION METAL COMPOUNDS

Previous Work on Zinc-rich Transition Metal Compounds

No references to electrical resistivity or low temperature specific heat measurements could be traced. However

magnetic investigations have been reported on the Zn-Co, Zn-Fe and Zn-Mn systems. Binary phase diagrams for these systems may be found on pages 86 to 88 .

Zn-Co System

Schramm (79) has reported magnetic susceptibility measurements at room temperature and above on alloys in the composition region 0 to 15 at.% Co. The ζ and γ_1 phases, at 7.2 at.% and 13 at.% Co respectively, show no evidence for the existence of localised magnetic moments. In fact the measured susceptibilities increase slowly as the temperature is raised.

Measurements on alloys containing $\approx$ 15% Co, just inside the γ-phase field (14 - 25% Co), show clear evidence of a Curie-Weiss like susceptibility, but no effective moment is quoted.

Zn-Fe System

Schramm (79) has measured the high temperature susceptibilities of alloys containing up to 30 at.% Fe. The ζ-phase (7.2 at.% Fe) has a temperature independent susceptibility. Both the δ_1 phase (8 to 13 at.% Fe) and the Γ phase (23 to 31 at.% Fe) have Curie-Weiss like susceptibilities, the magnitude of which increases as the concentration of Fe is raised within each phase field. Again no effective moments are quoted.

Zn-Mn System

Nakagawa et.al. (80) have reported susceptibility measurements on the intermetallic phases with compositions less than 40 at.% Mn but excluding the δ_1 phase (at 10 at.% Mn) and the ζ-phase (7.2 at.% Mn).

The ϵ phase has a hexagonal close-packed structure and it is stable at temperatures greater than 400°C and over a

composition range 15 to 60 at.% Mn. Five different compositions were measured and the results fitted to a Curie-Weiss law. The fitted parameters are shown in table 1.2. The Curie Temperature is 260 K at 15% Mn.

% Mn	Temp. Range of C.-W. Fit (K)	θ_p K	p_{eff} μ_B
15	660 - 770	150	3.6
20	670 - 830	50	4.0
25	650 - 870	-50	4.3
30	590 - 930	-120	4.3
35	570 - 960	-190	4.3

Table 1.2 ϵ-phase Zn-Mn C.- W. Parameters

The α' phase is face centred cubic with an ordered Cu_3Au type of structure. The fitted Curie-Weiss parameters are θ_p = 110 K and p_{eff} = 3.7 μ_B. The Néel temperature is 150 K.

The γ phase, centred on the composition 20 at.% Mn, has a Curie-Weiss susceptibility with θ_p = 70 K and p_{eff} = 5.4 μ_B.

Previous work on Beryllium-rich Transition Metal Intermetallic Compounds

Herr (81) has measured the magnetic susceptibility of $FeBe_{12}$, $MnBe_{12}$ and $CrBe_{12}$. $FeBe_{12}$ has a temperature independent susceptibility of $\chi = -0.8 \times 10^{-6}$ e.m.u./gm. The susceptibility of $MnBe_{12}$ is only quoted at two temperatures, $\chi = 2.8 \times 10^{-5}$ e.m.u./gm. at 4.2 K and $\chi = 3.2 \times 10^{-5}$ e.m.u./gm. at 1.8 K. The susceptibility of $CrBe_{12}$ was fitted to a Curie-Weiss law with p_{eff} = 2.22 μ_B (per Cr atom). The compound orders magnetically at $\approx$ 50K with an

effective moment per Cr atom of 0.3 μ_B. These measurements are in agreement with those of Wolcott and Falge. (82).

Some results of low temperature specific heat measurements are reported also. For $FeBe_{12}$ the electronic specific heat coefficient γ= 0.84 mJ/mole, for $FeBe_5$ γ=8.5 mJ/mole, while for $CrBe_{12}$ γ= 1.79 mJ/mole.

The susceptibility of pure Be is $\chi = -1.0 \times 10^{-6}$ e.m.u./gm. while its electronic specific heat coefficient is γ = 0.226 mJ/mole.

Aluminium-rich Transition Metal Intermetallic Compounds

Foex and Wucher (83) have reported that $CrAl_7$, $CrAl_4$, $MnAl_6$, $CoAl_4$, Co_4Al_{13}, Co_2Al_5 and $NiAl_3$ have small temperature independent para- or dia-magnetic susceptibilities, while $FeAl_3$ followed a Curie-Weiss law with p_{eff} = 1.67 u_b and θ = -103 K.

Taylor (84) has measured the susceptibilities of a large number of aluminium-rich compounds between 77 K and 300 K. He finds that the majority (all in the case of V, Cr and Co compounds) show a small approximately temperature independent paramagnetism - these are reproduced in figure 1.9.

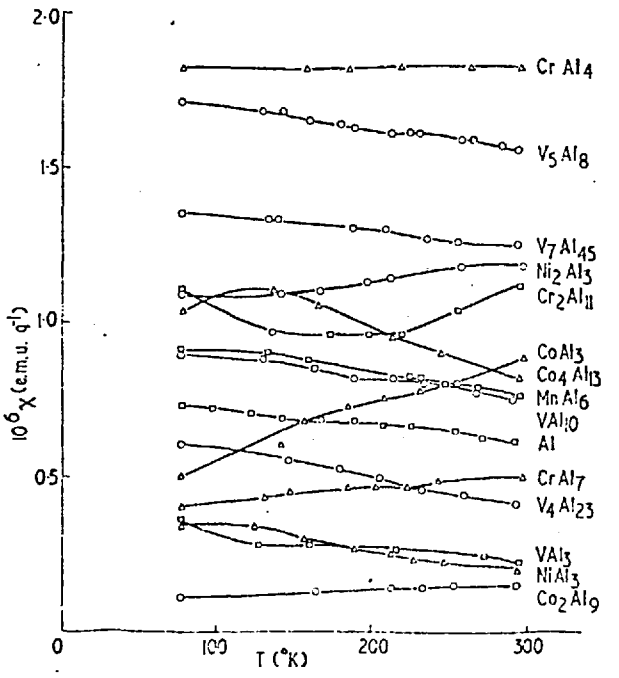


Fig. 1.9 Susceptibilities of some Intermetallic Compounds. Ref.(84)

A smaller group of compounds have susceptibilities obeying a Curie-Weiss law. The fitted values of p_{eff} and θ are shown in table 1.3 .

Alloy	p_{eff} (μ_B)	θ (K)
$MnAl_4$	1.77	-163
Mn_3Al_{10}	1.66	-120
Mn_4Al_{11}	1.59	--50
Fe_4Al_{13}	2.37	-300
Fe_2Al_5	2.47	-103
$FeAl_2$	1.32	-80

TABLE 1.3 C-W PARAMETERS FOR Al-RICH COMPOUNDS AFTER REF(84)

Charge Transfer

At one time a temperature independent susceptibility was interpreted as the result of a full 3d shell. This interpretation would have fitted in with Raynor's suggestion (85) that transition metal atoms in aluminium-rich compounds absorb electrons to the "maximum extent" i.e. until the 3d shell is full.

Hume-Rothery and Coles (86) have suggested that Raynor's "negative valency" scheme is physically improbable - at least to the extent that a Mn atom in say the $MnAl_6$ compound has completely filled its d-shell. After analysing the congruent melting points of aluminium-rich transition metal compounds they suggested that the high cohesion observed may be the result of increasing ionicity in the bonding due to a limited charge transfer of electrons onto the transition atoms, and that this should be a maximum for Co-Al alloys.

Wenger et.al. (87) have attempted to measure the amount of charge transferred onto the transition atom, Δn_d, by soft X-ray spectroscopy. The magnitude of the change Δn_d for various binary alloys is shown in figure1.10, where n_d for the pure metal has been taken as 6 for Mn, 7 for Fe, 8.3 for Co and 9.5 for Ni.

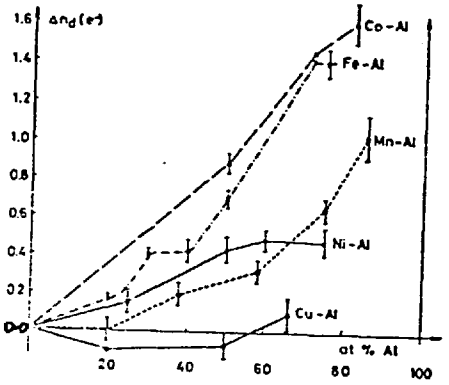


Figure1.10. Change of the Number n_d of 3d Electrons on Mn, Fe, Co, Ni or Cu atoms in the Binary Alloys of these Metals with Al. Ref. (87)

Figure 1.11shows the change Δn_d of the number of 3d electrons as a function of the element alloyed to aluminium for different aluminium concentrations. The maximum value of Δn_d, $\approx$ 1.6 electrons, occurs for Co-Al compounds.

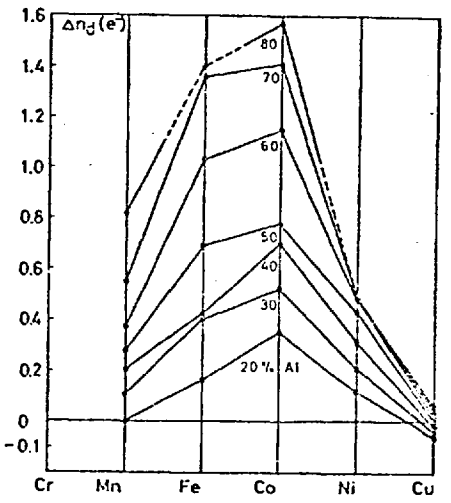


Fig.1.11 Δn_d as a function of the Element Alloyed to Al. After Ref(87)

CHAPTER 2

THE ζ -PHASE COMPOUNDS

PHASE DIAGRAMS AND CRYSTAL STRUCTURE

The binary alloy systems of zinc with the transition elements manganese, iron and cobalt have been the subject of numerous metallurgical investigations and the combined findings have been used to construct the "most probable" phase diagrams in Hansen's book the "Constitution of Binary Alloys" (88). These are reproduced in figures 2.1 to 2.5

In all three binary alloy systems Mn-Zn, Fe-Zn and Co-Zn Schramm (89,90,91) showed that the intermetallic compounds most rich in zinc (the ζ-phases) form peritectically at an approximate composition of 93 at.% zinc i.e. MZn_{13}. Gotzl et.al.(92) showed them to be isomorphous (with a monoclinic structure), confirmed the stoichiometric composition MZn_{13} and determined the lattice parameters and possible space groups. Brown (93) has carried out a more detailed X-ray investigation using single crystals extracted electrolytically from slowly cooled dilute (approximately 1%) alloys. She showed that the correct space group for the structure is C2/m, and determined the positions of all the atoms in the unit cell. All relevant information about the structure, including a schematic view down the [001] direction, is reproduced in figures 2.6 and 2.7 and tables 2.1 to 2.4

The simplest way of visualising the structure is to picture each transition metal atom surrounded by twelve zinc atoms at the vertices of a slightly distorted icosahedron; these icosahedra then link together by sharing a pair of opposite vertices to form chains parallel to the c-axis. These chains are packed together

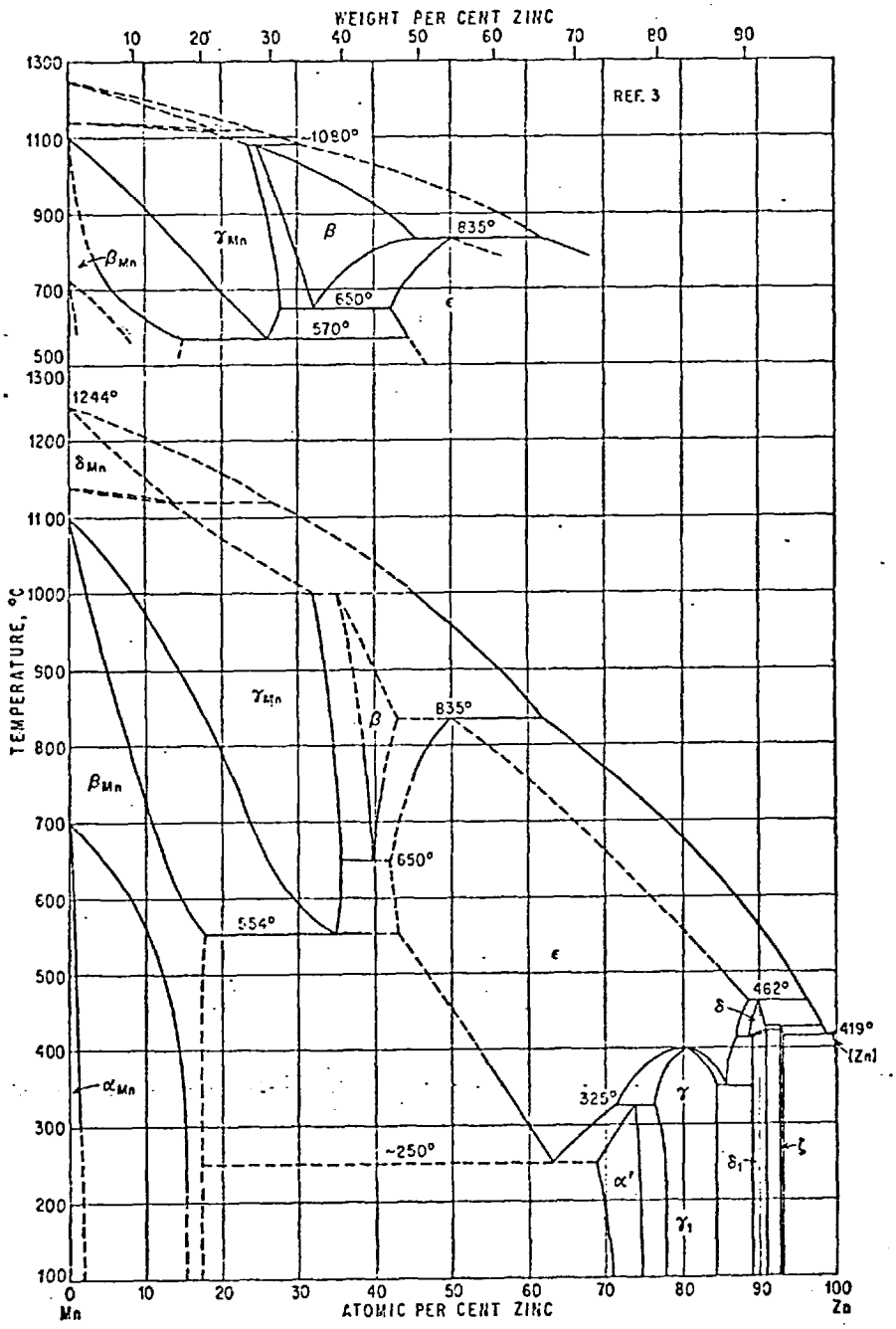


FIG.2.1 THE MANGANESE-ZINC PHASE DIAGRAM

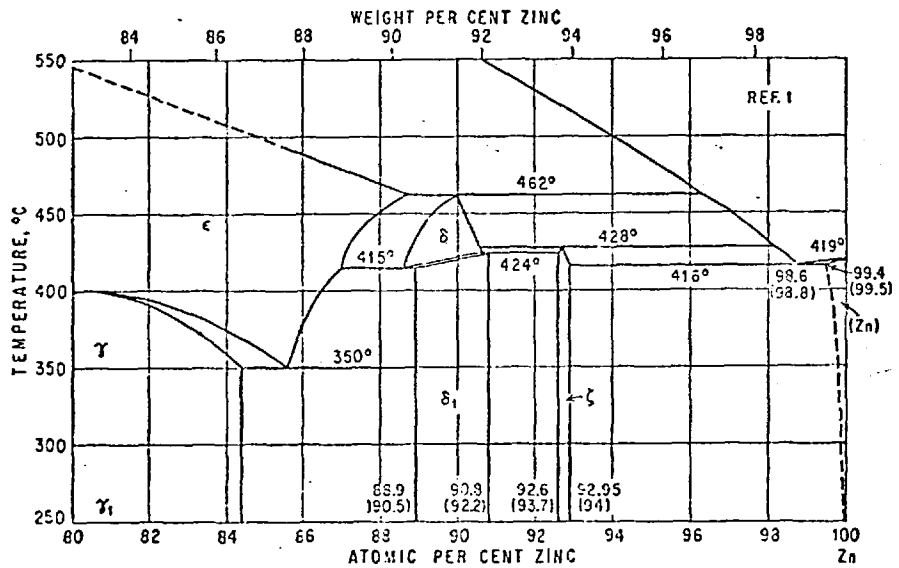


FIG.2.2 DETAIL FROM THE MANGANESE-ZINC PHASE DIAGRAM

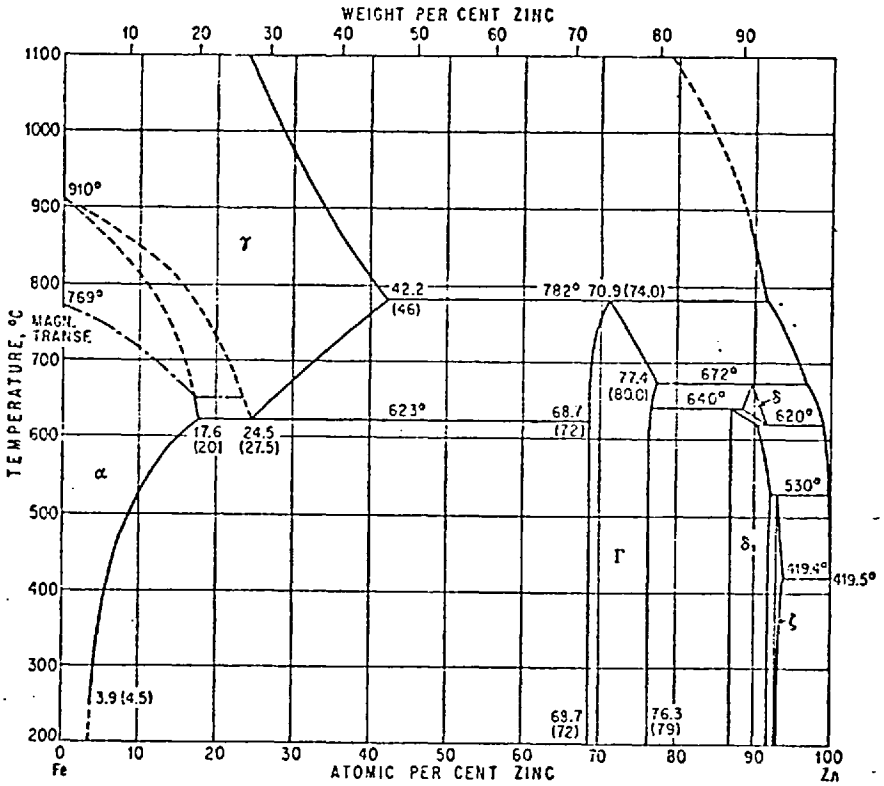


FIG. 2.3 THE IRON-ZINC PHASE DIAGRAM

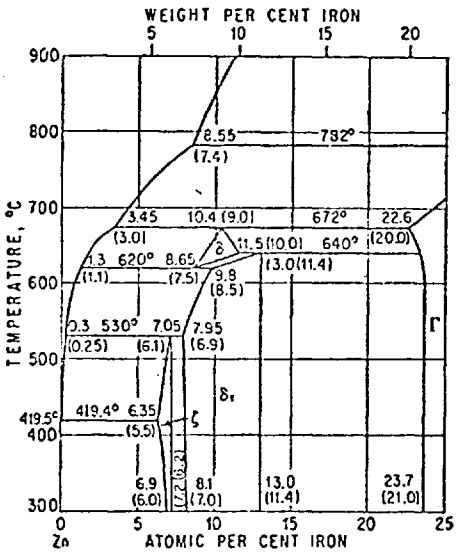


FIG. 2.4 DETAIL FROM THE IRON-ZINC PHASE DIAGRAM

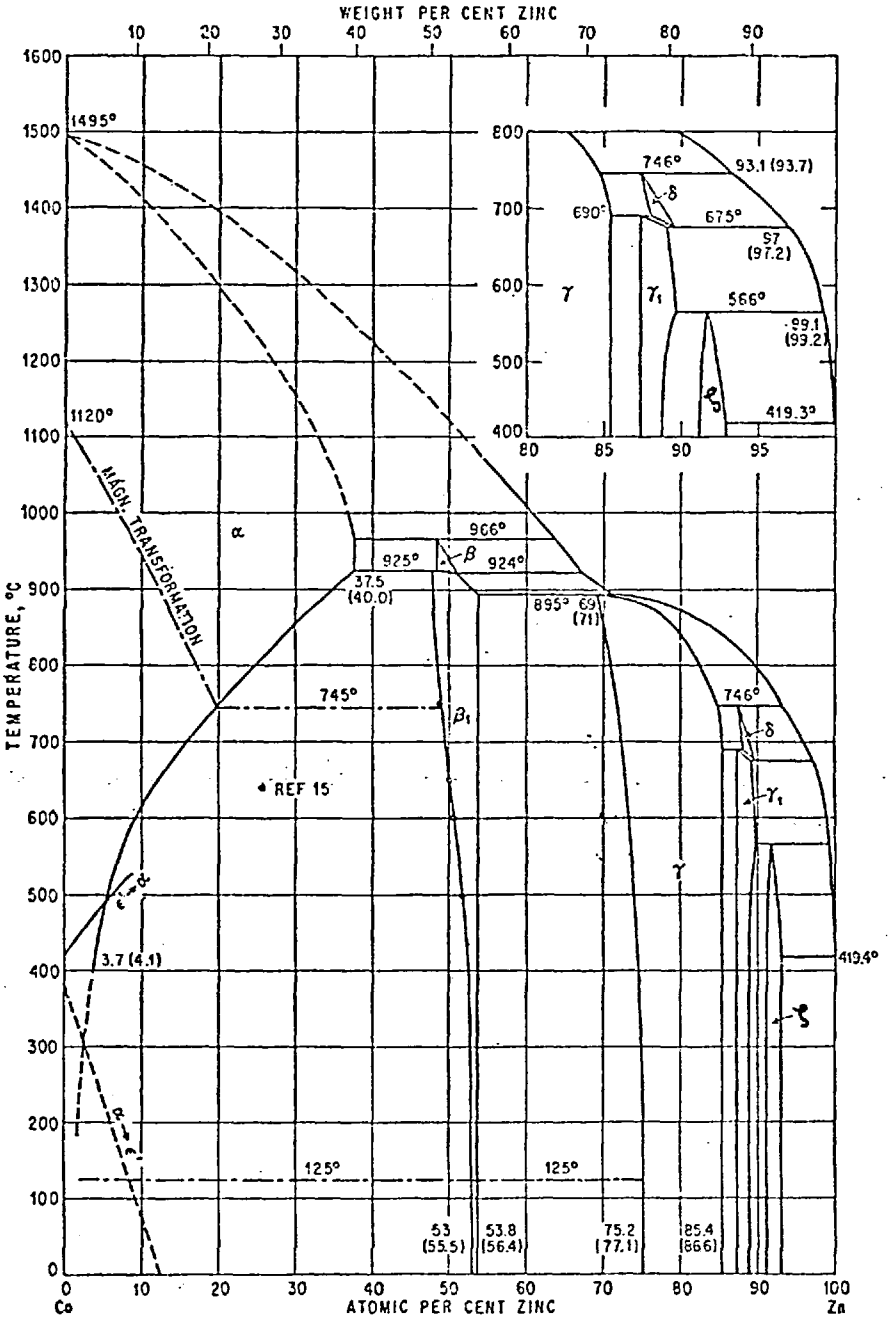


FIG.2.5 THE COBALT-ZINC PHASE DIAGRAM

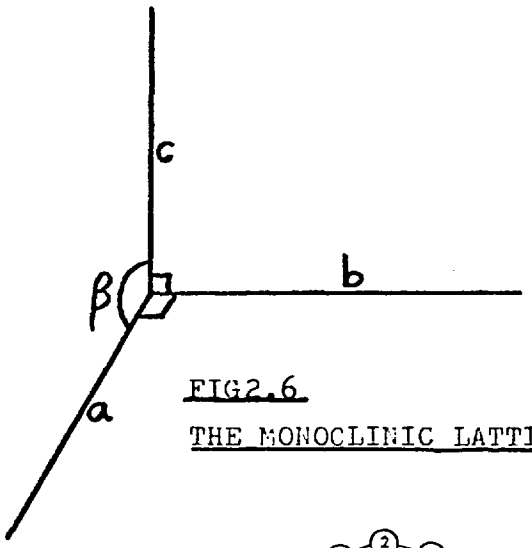


FIG 2.6

THE MONOCLINIC LATTICE

	$CoZn_{13}$ (Å)	$FeZn_{13}$ (Å)	$MnZn_{13}$ (Å)
a	13·306 ± 0·033	13·424 ± 0·005	13·483 ± 0·005
b	7·535 ± 0·002	7·6080 ± 0·001	7·6626 ± 0·001
c	4·992 ± 0·012	5·061 ± 0·003	5·134 ± 0·003
β	126° 47′ ± 15′	127° 18′ ± 2′	127° 47′ ± 2′

TABLE 2.1 THE ζ-PHASE LATTICE PARAMETERS

A	2 Zn_0	in 2(a)	(0, 0, 0)
C	2 T.M.	in 2(c)	(0, 0, ½)
I_1	4 Zn_1	in 4(i)	(x_1, 0, z_1)
I_2	4 Zn_2	in 4(i)	(x_2, 0, z_2)
J_3	8 Zn_3	in 8(j)	(x_3, y_3, z_3)
J_4	8 Zn_4	in 8(j)	(x_4, y_4, z_4)

TABLE 2.2 POSITIONS OF THE ATOMS

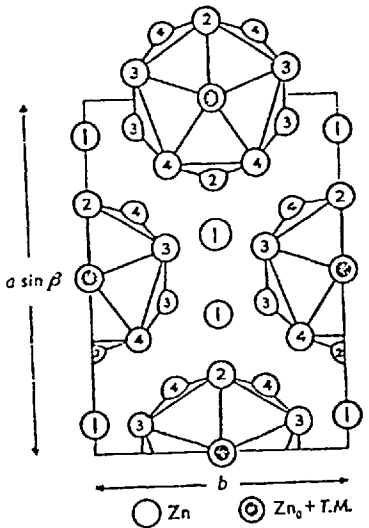


FIG 2.7 SCHEMATIC VIEW OF THE STRUCTURE DOWN [001]

Parameter	$CoZn_{13}$	$FeZn_{13}$	$MnZn_{13}$	Standard deviation
x_1	0·b110	0·b120	0·b155	0·0005
z_1	0·2920	0·2920	0·2910	0·002
x_2	0·2190	0·2195	0·2232	0·0005
z_2	0·0770	0·0730	0·0735	0·002
x_3	0·0780	0·0770	0·0750	0·0005
y_3	0·2975	0·2920	0·2920	0·0007
z_3	0·8340	0·8350	0·8330	0·001
x_4	0·1765	0·1760	0·1744	0·0005
y_4	0·1765	0·1780	0·1810	0·0007
z_4	0·5530	0·5450	0·5485	0·001

TABLE 2.3 ATOMIC PARAMETERS OF THE ζ-PHASES

Atom	Neighbour	$CoZn_{13}$	$FeZn_{13}$	$MnZn_{13}$	Standard deviation	Other neighbours
T.M.	2 Zn_0	2·496	2·530	2·567	0·006	
	2 Zn_2	2·594	2·595	2·620	0·011	
	4 Zn_3	2·609	2·599	2·614	0·009	
	4 Zn_4	2·571	2·610	2·607	0·009	
Zn_0	2 Zn_2	2·701	2·738	2·794	0·011	2 T.M.
	4 Zn_3	2·796	2·783	2·797	0·009	
	4 Zn_4	2·671	2·669	2·695	0·009	
Zn_1	1 Zn_1	2·628	2·647	2·687	0·022	
	1 Zn_2	2·550	2·576	2·584	0·016	
	2 Zn_3	2·674	2·716	2·745	0·012	
	2 Zn_3	2·558	2·591	2·606	0·012	
	2 Zn_4	2·782	2·787	2·787	0·012	
	2 Zn_4	2·653	2·654	2·658	0·012	
Zn_2	2 Zn_3	2·895	2·940	2·928	0·012	1 T.M., 1 Zn_0,
	2 Zn_3	2·700	2·693	2·738	0·012	1 Zn_1
	2 Zn_4	2·865	2·902	2·892	0·012	
	2 Zn_4	2·675	2·725	2·729	0·012	
	2 Zn_4	3·057	3·094	> 3·2	0·012	
Zn_3	1 Zn_3	2·671	2·697	2·703	0·014	1 T.M., 1 Zn_0,
	1 Zn_3	3·052	3·165	3·187	0·014	2 Zn_1, 2 Zn_2
	1 Zn_4	2·845	2·878	2·896	0·010	
	1 Zn_4	2·862	2·840	2·792	0·010	
	1 Zn_4	3·130	3·105	3·159	0·010	
	1 Zn_4	2·592	2·652	2·655	0·010	
Zn_4	1 Zn_4	2·564	2·540	2·601	0·014	1 T.M., 1 Zn_0, 2 Zn_1,
	1 Zn_4	2·660	2·709	2·774	0·014	3 Zn_2, 4 Zn_3

Values are in Ångström units; T.M. stands for transition metal: Mn, Fe or Co.

TABLE 2.4 INTERATOMIC DISTANCES IN THE ζ-PHASES

in an approximately hexagonal array with the extra zinc atoms in the interstices between the chains. There are no nearest neighbour transition metal atoms in the ζ-phase compounds and the shortest distance between any two is 5A° (along the c direction).

SPECIMEN PREPARATION

The starting materials for our compounds were supplied by Koch Light Laboratories in the following forms and purities:- 8 mm. diameter zinc rods (5N), manganese flake (4N5), 1mm. diameter cobalt wire (4N8) and 1mm. diameter iron wire (4N8).

The zinc rods were cut to the required length using a hacksaw blade kept specifically for that purpose and then etched in a 20% aqueous solution of hydrochloric acid for 5 minutes followed by rinses in distilled water and ether. The iron and cobalt wires were cut using side-cutters, again each metal having its own labelled cutter, then etched in concentrated hydrochloric acid for 10 to 15 minutes before rinsing as for the zinc. The manganese had to be cleaned by a different method as the oxide film rapidly re-forms after etching in hydrochloric acid. This problem was overcome by giving a short but rapid etch in a 20% aqueous solution of nitric acid for a couple of seconds before rinsing in ether. The resulting shiny surface appeared to be passivated and remained un-tarnished for several hours.

The cleaned and weighed starting materials were placed in 8 mm.I.D. quartz tubes which had previously been etched for several hours in aqua-regia (3:1; $HCl:HNO_3$) followed by rinsing in distilled water. The tubes were then evacuated to a pressure of 10^{-5} torr, heated to 150°C to drive off any volatile contaminant and finally sealed off.

The transition metal constituents were completely dissolved in the liquid zinc by holding at a temperature 50°C above the relevant liquidus temperature accompanied by frequent vigorous shaking. Iron and cobalt alloys received from two to three hours of this treatment, and the manganese one hour, before quenching into cold water - more than three-quarters of the quartz tubes survived this proceedure without cracking.

Typical specimens examined microscopically in the "as quenched" condition were observed to consist of very fine grained intermetallic phases surrounded by material of the eutectic composition. Inspection of the binary phase diagrams indicates that the first intermetallics to be precipitated on cooling should lie on the transition metal rich side of the ζ-phase composition. For example in the case of an alloy of the $CoZn_{13}$ composition quenched from 800°C intermetallic phases will appear in the following order γ, δ, γ_1, then, below 566°C, ζ. In rapidly cooled alloys peritectic reactions i.e. of the form 'solid' + 'liquid' → 'solid' are unable to proceed very far. In fact it has been reported by Schramm (94) that the peritectic formation of the ζ-phases is almost completely suppressed in a rapidly cooled alloy.

Annealing the quenched alloy below the relevant ζ-phase peritectic temperature will lead to the formation of the thermodynamically stable ζ-phase via a 'solid' + 'liquid' → 'solid' peritectic reaction e.g. for a $CoZn_{13}$ composition γ_1 + liquid → ζ. The speed at which this type of reaction proceeds to completion is principally limited by the rates of diffusion of the two atomic species within the transition metal rich phases formed during the quenching process and hence depends upon both the grain size (dependent on quenching speed) and the annealing temperature.

$FeZn_{13}$ and $CoZn_{13}$ alloys were annealed at a temperature 30°C below the peritectic, i.e. at 500°C and 530°C respectively, for three weeks before slowly cooling to room temperature over a period of several days. In the case of $MnZn_{13}$ the temperature interval between the eutectic (at 416°C), and the peritectic (at 428°C) is smaller and these alloys were annealed at 420°C for four weeks. When possible, samples were annealed in their original unbroken quartz tubes loosely sealed inside copper tubes with "rock-wool" end plugs. Furnace temperatures were held constant to within ± 1°C by either "Perram" (type "three star") or "Eurotherm" (type "PID/SCR10") controllers, calibrated against a chromel-alumel thermocouple. The thermocouple was regularly calibrated at the freezing point of zinc (419.5°C) by the standard cooling curve technique.

A certain proportion (about 20%) of quartz tubes cracked during the initial quench and the specimens had to be re-sealed in new tubes. An unusual effect was observed on increasing the temperature above the eutectic; the specimens developed numerous cracks from some of which "cauliflower-like" growths emerged making them completely useless for any type of measurements. A possible explanation is the following; on re-heating the alloy above the eutectic the material between the grains of precipitated intermetallic will melt and, as the sample is no longer constrained by a tightly fitting quartz envelope, may be extruded from between the grains before the peritectic reaction is completed.

METALLURGICAL EXAMINATION

The annealed alloys were examined by several techniques.

(a) MICROSCOPIC

Every sample had pieces removed from each end and a flat surface ground and polished along its whole length. These were examined microscopically both before and after etching with a 5% solution of hydrochloric acid in alcohol.

The γ-phase compounds $FeZn_{13}$ and $CoZn_{13}$ appeared fine grained and single phase along their entire length.

The γ-phase $MnZn_{13}$ specimens had a small variable concentration of a second phase (never greater than 5%) uniformly distributed, which by its etching characteristics appeared to be the ZnMn terminal solid solution. Increasing the manganese concentration by 0.2at.% produced an alloy which appeared single phase under the microscope. It is a possibility that manganese attacks the surface of the quartz tubes during the melting process and is lost from the solution - this is consistent with a small observed specimen weight loss.

(b) ELECTRON MICRO-PROBE ANALYSIS

Three representative samples, one each of $CoZn_{13}$, $FeZn_{13}$ and $MnZn_{13}$ were sent to the Analytical Services Laboratory at Imperial College for electron micro-probe analysis. In this technique a narrow beam of electrons is directed at a polished surface of the sample and the resulting X-rays are subject to energy analysis, each element present produces its own characteristic lines. It is possible to see variations in the alloy composition of less than 1% over distances of the order of 2 microns.

The results indicated a uniform composition throughout the $CoZn_{13}$ and $FeZn_{13}$ compounds and a constant manganese concentration within the majority phase of the $MnZn_{13}$ alloy, but a much lower

concentration in the second phase regions confirming that these consist of the ZnMn solid solution.

(c) X-RAY POWDER SPECTRA

X-ray powder patterns were obtained for typical samples of all three ζ-phase compounds using a 5.8 cm radius camera in the Material Science group of the Electrical Engineering Department at Imperial College. There was no discernible difference between the three compounds either in the relative amplitudes or positions of the X-ray lines. Figure2.8shows the powder pattern schematically. Unfortunately no published powder pattern data for the ζ-phases could be found, making an "instant" indentification impossible.

For a line to appear in a powder pattern at an angle corresponding to scattering by planes of atoms defined by the Miller Indices (h,k,l) two sets of conditions have to be satisfied. The first of these is simply the Bragg condition.

$$\lambda = 2d_{hkl} \sin\theta \qquad 2.1$$

where λ is the X-ray wavelength, θ the angle between the parallel planes of atoms and the incident X-ray beam (i.e. half the angle through which the beam is scattered) and d_{hkl} is the spacing between planes.

For a general lattice, d_{hkl} is given by the expression

$$\frac{1}{d^2_{hkl}} = h^2a^{*2} + k^2b^{*2} + l^2c^{*2} + 2hka^*b^*\cos\gamma^* + 2hla^*c^*\cos\beta^* + 2klb^*c^*\cos\alpha^* \qquad 2.2.$$

a^*, b^* and c^* are the reciprocal lattice vectors and α^*, β^*, γ^* the angles between reciprocal lattice vectors. For the monoclinic lattice of the ζ-phases these may be expressed in terms of the real space lattice vectors as

$$a^* = \frac{1}{a \sin\beta} , \quad b^* = \frac{1}{b} , \quad c^* = \frac{1}{c \sin\beta}$$

$$\alpha^* = 90^\circ, \quad \beta^* = 180^\circ - \beta, \quad \gamma^* = 90^\circ$$

Equation (2.2) becomes

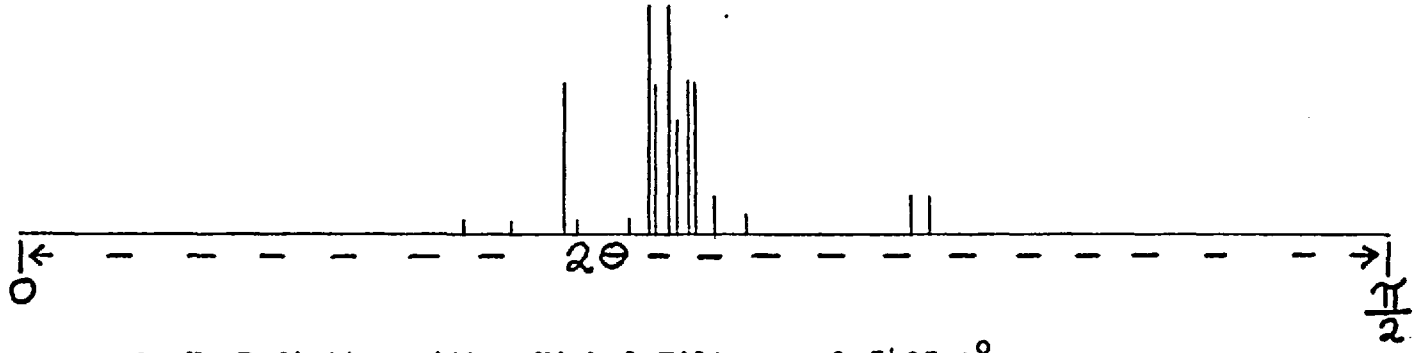
$$\frac{1}{d^2_{hkl}} = \frac{h^2}{a^2 \sin^2\beta} + \frac{k^2}{b^2} + \frac{l^2}{c^2 \sin^2\beta} - \frac{2hl \cos\beta}{ca \sin^2\beta} \qquad 2.3$$

The second condition is that the structure factor F_{hkl} be non zero. F_{hkl} gives a measure of the interference between the scattered waves from each atom within the unit cell and may be written as

$$F_{hkl} = \sum_n f_n \exp\left\{2\pi i \left(\frac{hx_n}{a} + \frac{ky_n}{b} + \frac{lz_n}{c} \right) \right\} \qquad 2.4$$

where f_n is the X-ray scattering length for the n^{th} atom and (x_n, y_n, z_n) the position of the n^{th} atom in the unit cell expressed as fractions of (a,b,c) the lattice parameters. For centrosymmetric crystals, as are the ζ-phases, equation (2.4) becomes

$$F_{hkl} = 2\sum_n f_n \cos 2\pi \left(\frac{h\, x_n}{a} + \frac{k\, y_n}{b} + \frac{l\, z_n}{c} \right) \qquad 2.5$$



Cu K_α Radiation with a Nickel Filter = 1.5405 A°

Figure2,8 Schematic Powder Spectrum of $MnZn_{13}$ —

Expected Strong Lines (h,k,l)	Calculated F_{hkl}	Calculated $(\frac{1}{d}_{hkl})$	Measured $(\frac{1}{d})$ for Strongest Lines in the Powder Pattern
$42\bar{1}$	14.3 f_{Zn} - 2 f_{TM}	0.396	0.398
$60\bar{1}$	18.4 f_{Zn} - 2 f_{TM}	0.456	0.459
$11\bar{2}$	10.3 f_{Zn} + 2 f_{TM}	0.461	0.462
$60\bar{2}$	17.3 f_{Zn} + 2 f_{TM}	0.469	0.472
$42\bar{2}$	12.4 f_{Zn} + 2 f_{TM}	0.475	0.477
330	12.3 f_{Zn} + 2 f_{TM}	0.482	0.485
510	13.1 f_{Zn} + 2 f_{TM}	0.487	0.489

Table2.5 Calculated and Measured Parameters for $MnZn_{13}$—

Metal	$\frac{2\sin\theta}{\lambda}$ = 0.0	$\frac{2\sin\theta}{\lambda}$ = 1.0	$\frac{2\sin\theta}{\lambda}$ = 2.0
Zn^{+2}	28	14.5	7.36
Co^{+2}	25	12.2	6.71
Fe^{+2}	24	11.5	6.51
Mn^{+2}	23	10.8	6.33

Table 2.6 Atomic Scattering Factors f_n after Reference (95)

The actual intensity (I) of a powder pattern line is given by (96) as

$$I \propto j_{hkl} \left|F_{hkl}\right|^2 \left(\frac{1 + \cos^2 2\theta}{2 \sin\theta \sin 2\theta}\right) \qquad 2.6$$

where j_{hkl}, the degeneracy factor, gives the number of families of planes having the same value of the d spacing.

For the γ-phase compounds (with space group C2/m) the structure factor F_{hkl} is zero for planes (h,k,l) whenever h + k is odd, and the maximum value it can take is $26\ f_{Zn} + 2\ f_{TM}$. Calculations of the structure factor have been made for all planes having $\frac{1}{d_{hkl}}$ values $\left(= \frac{2 \sin\theta}{\lambda}\right)$ up to 0.500. Those planes having structure factors greater than one third of the maximum allowed value are listed in the first column of table 2.5, together with the calculated values for the structure factors, expressed in terms of f_{Zn} and f_{TM}, and calculated values of $\frac{1}{d_{hkl}}$. The final column of the table lists the measured $\frac{1}{d}$ parameters of the strong lines in the powder pattern of figure 2.8. Apart from a small systematic difference of 0.5% the correspondence is good.

Values for the X-ray atomic scattering factors, taken from reference (95), are shown in table 2.6.

A notable feature of the powder spectrum of the γ-phase structure is the "bunching" of strong lines between $\frac{1}{d}$ values of 0.45 and 0.49. For larger $\frac{1}{d}$ values the paucity of strong lines is accounted for by the "fall off" with scattering angle of both the final term in equation 2.6 and the individual scattering amplitudes f_n, whereas for smaller $\frac{1}{d}$ the explanation lies in small structure factors (F_{hkl}). This point will be referred to again later.

MACHINING OF RESISTIVITY SPECIMENS

Cylindrical resistivity specimens were cut from annealed ingots measuring 8 mm. in diameter and 4 to 5 cms. in length using a "Servomet" Spark Machiner manufactured by Metals Research Limited. This utilises the technique of spark erosion. A tool to match the shape of the finished specimen is held at a fixed distance, normally 5 thousandths of an inch, from the ingot by a servo-mechanism and a series of D.C. voltage pulses are applied to the tool. Both the tool and specimen are immersed in a dielectric (paraffin) and the sparks form across the narrowest gap.

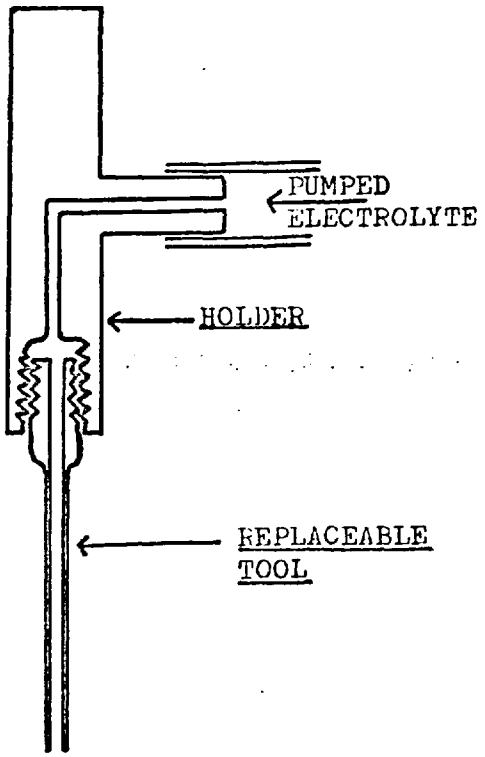


FIG.2.9 TREPANNING TOOL

For cuts deeper than a couple of millimetres, provision has to be made to supply clean dielectric continuously to the cutting (sparking) edge to sweep away the debris of fine metal particles and gas bubbles produced during the erosion process.

The form of the tool-holder and replaceable tool is shown in fig.2.9. Both were made of brass studding, drilled out to the required inside diameter and the outside turned down to remove the threading.

Due to the extreme brittleness of all the γ-phase compounds great care had to be taken in their handling after cutting to the resistivity specimen size of 1½ to 2 mm. diameter by 3 cm. long.

MACHINING OF SUSCEPTIBILITY SPECIMENS

Again these were cut from annealed ingots using the spark machiner. Early specimens which had to fit inside the quartz bucket of the magnetic susceptibility balance were trepanned using the "resistivity tool". Later specimens, of 6 mm. diameter were turned down from the ingot using the "spark-lathe" attachment. The ingot is held in a lathe chuck rotating in the paraffin dielectric while the tool, a brass straight-edge, is brought down under servo control as shown in figure 2.10.

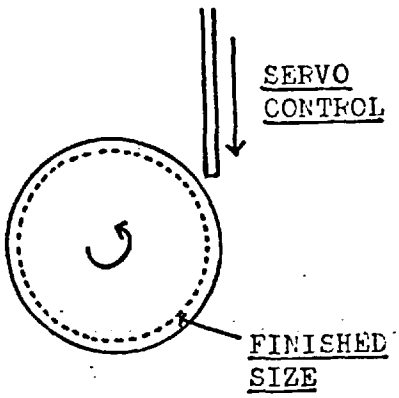


FIG. 2.10

A fine groove to locate an aluminium wire loop was machined close to one end. using a razor-blade as a tool. The specimens were finally "parted-off" to the required length, 12 mm., using the razor-blade, etched for a couple of seconds in a 20% aqueous solution of HNO_3 and finally rinsed in distilled water.

Specimens of $MnZn_{13}$ for low temperature magnetization measurements using the vibration magnetometer had to be accurately machined into cylinders 0.055 inches in diameter by 0.550 inches long. This was achieved in a three stage process. Initial trepanning from the ingot to approximately 0.1 inch diameter, turning in the "spark-lathe" to 0.060 inches in diameter and finally etching in a 20% aqueous solution of HNO_3 to the final diameter.

SPECIFIC HEAT SPECIMENS

Either the larger form of the susceptibility specimen or the annealed ingot itself were used. The only preparation required before the standard etching proceedure was to ~~rub on~~ produce a flat surface with emery-paper.

SINGLE CRYSTALS OF $MnZn_{13}$

It had been hoped to perform a neutron diffraction study on a single crystal of $MnZn_{13}$, which would require a crystal of minimum dimensions 4 mm. cubed due to the dilution of the transition metal constituent. An attempt was made to grow a suitably sized crystal using a combined concentration and temperature gradient technique.

A two-constituent starting material was firstly prepared by sealing two approximately equal length rods, one of pure zinc and the other of polycrystalline ζ-phase $MnZn_{13}$, end to end inside an evacuated pyrex tube. The pyrex tube was then sealed inside a copper tube with loosely fitting copper end plugs (figure 2.11) itself contained within a horizontal wire wound furnace. The exact position of the copper tube within the furnace tube and the furnace temperature had previously been carefully adjusted to give the internal temperature profile of figure 2.12. With the help of the partial phase diagram of figure 2.13 it can be seen that single crystals may grow in the following way.

On first introducing the composite specimen into the temperature gradient the pure zinc will melt and the interface between it and the solid ζ-phase $MnZn_{13}$ will be at some temperature T_x. ζ-phase will dissociate at the interface and

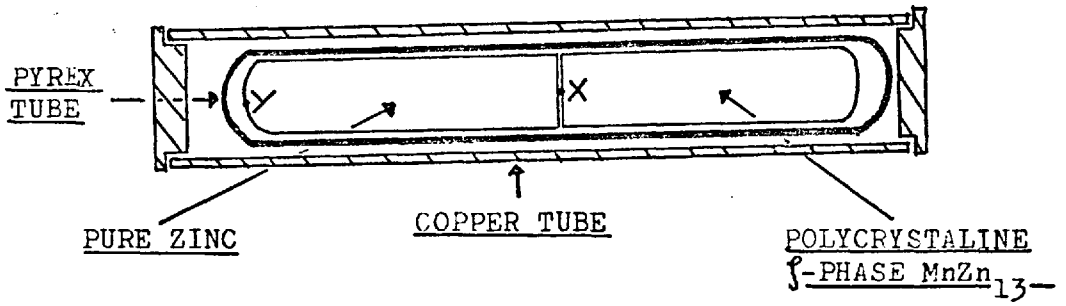
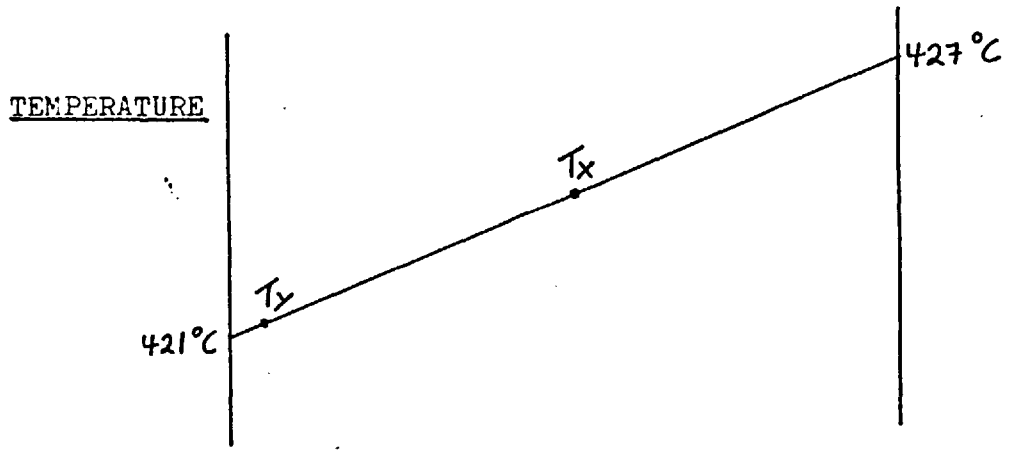


FIGURE 2.11



TEMPERATURE PROFILE INSIDE Cu TUBE

FIGURE 2.12

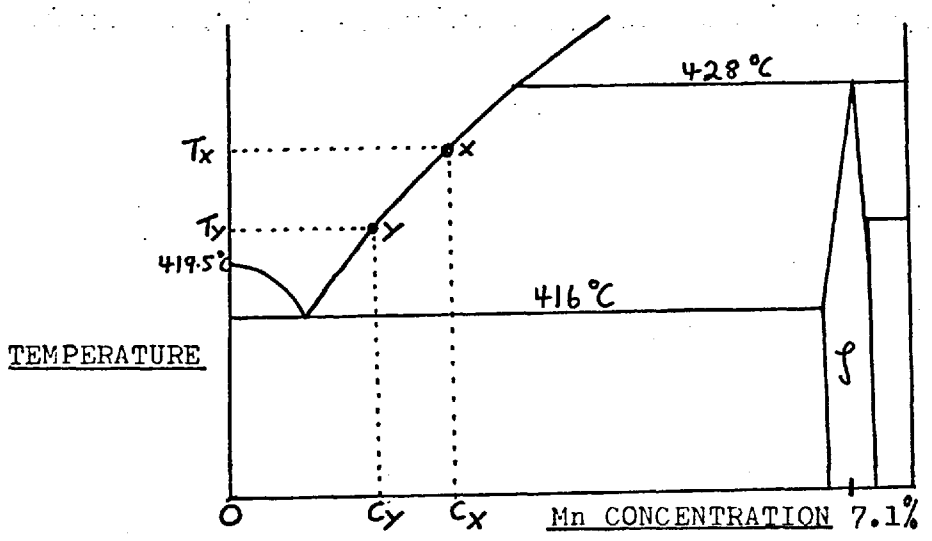


FIGURE 2.13

PART OF Mn-Zn PHASE DIAGRAM

manganese will diffuse into the liquid zinc in an attempt to raise the manganese concentration to c_Y, the local thermal equilibrium value at temperature T_X. However if the cold end of the tube is maintained at some intermediate temperature between T_X and the melting point of pure zinc (419.5 °C), say T_Y, then the manganese concentration can only rise to the concentration c_Y at position Y on the phase diagram, at which stage ζ-phase will be deposited at the cold end of the tube. As time progresses the net effect is to transport manganese atoms via a concentration gradient towards the cold end of the tube where crystals of ζ-phase $MnZn_{13}$ may nucleate and grow. A disadvantage with this technique in the particular case of $MnZn_{13}$ is the very restricted allowed temperature interval between the cold end, which must be held above the melting point of pure zinc (419.5 °C), and the hot end, which it is preferable to keep below the ζ-phase peritectic of 428 °C to exclude the possibility of higher manganese concentration phases, such as the δ-phase, from precipitating at intermediate points along the tube. Also there is the additional problem that the actual temperature gradient along the metallic specimen will be smaller than that along the copper tube due to the effect of the low pyrex thermal conductivity compared with that of the metal.

After five days the pyrex tube was removed from the furnace and quenched. An electrolytic method was used to extract crystals of ζ-phase from the surrounding matrix using a similar experimental arrangement to Raynor et al. (97) and Clare (98) and this is shown in figure 2.14.

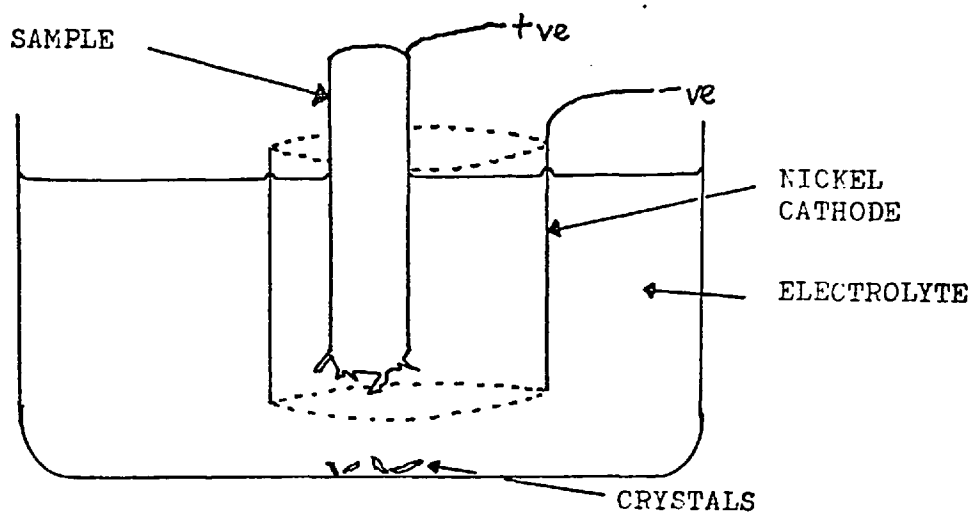


FIGURE 2.14 ELECTROLYTIC EXTRACTION OF CRYSTALS

A variety of electrolytes were tried, including dilute solutions of zinc chloride, acetic acid, sodium hydroxide, nitric acid and hydrochloric acid and none proved to be entirely satisfactory. Although small crystals (of dimensions less than 0.5 mm.) were uncovered, released and fell to the bottom with very little attack, whenever larger crystals became partially exposed then they also were electro-chemically attacked. Presumably the difference in electro-chemical potential between the ζ-phase $MnZn_{13}$ and the eutectic composition matrix is rather small. This difficulty was partially overcome by painting an electrically insulating layer of G.E. varnish over the exposed surface of any large crystal, and using a very dilute solution of hydrochloric acid as the electrolyte. The largest crystal extracted had dimensions of only 5 mm. x 2 mm. x 0.5 mm., had rather poorly developed faces and suffered from some cracking, suggesting that further refinements of the crystal

growing and extraction techniques are required before a single crystal neutron diffractron study is possible.

ζ-PHASE $CrZn_{13}$ (?)

The phase diagram of the CrZn system has been investigated by a number of workers (88). The majority observed only one intermetallic compound in the system, designated θ, located at 5.6 at. % chromium and having a complex hexagonal unit cell containing about 288 atoms. However (99) has observed needles of a second intermediate phase at a composition of approximately 8 at. % Cr. Brown (93) made a slowly cooled dilute alloy of chromium in zinc and electrolytically extracted crystals of intermetallic compounds. The majority turned out to be the θ-phase, however a few very thin needle-shaped crystals were also found and these proved to be isomorphous with the other ζ-phases. Because of their small size a complete analysis of the structure was impossible. There are still doubts as to whether or not this is a true equilibrium binary phase.

An attempt was made to prepare a specimen of ζ-phase $CrZn_{13}$ by the standard proceedure described earlier of dissolving the chromium at a high temperature followed by quenching and a lower temperature annealing treatment. However even after holding at temperatures close to the boiling point of zinc (902 °C at atmospheric pressure) for a week a substantial proportion of undissolved chromium remained. Following a suggestion by Stone (100) that the tenacious oxide film (Cr_2O_3) usually present on chromium may undergo a sintering type of transition around 1050 C thus allowing liquid zinc to react with the clean

chromium metal surface, the initial melting temperature was raised to 1100 C. At this temperature the vapour pressure above the zinc before any chromium enters solution is ten atmospheres, just within the strength limitations of the sealed quartz tubes. After three days a specimen was removed from the furnace and quenched into water and the quartz tube cracked and its surface appeared to have been attacked by the melt. The quenched ingot was examined microscopically and showed a three-phase structure :- Zn-Cr terminal solid solution, large areas of an unevenly shaped constituent (perhaps θ) and a small amount of a needle shaped phase (perhaps ζ), no undissolved or precipated chromium could be observed. After examination the specimen was divided into three pieces, each sealed in individual pyrex tubes and annealed for five days at different temperatures. (A) at 350°C , (B) at 416°C and (C) at 500°C. After annealing, all three specimens were again examined microscopically and the following observations made:-

(A) Showed a small amount (5 to 10%) of a second phase.

(B) Almost completely single phased. (Less than 1% of a second phase).

(C) This sample had been liquid on removal from the furnace at 500 C and when cooled consisted of Zn-Cr terminal solid solution and chromium only.

An X-ray powder pattern was obtained for specimen (B) and proved that the intermetallic phase did NOT have the ζ-phase structure. Probably it is the θ-phase previously observed in the chromium-zinc system

In conclusion there is still a doubt as to whether there exists a ζ-phase as a true equilibrium binary phase in the chromium-zinc system.

Additional Specimens

$Mn_{0.05}Fe_{0.95}Zn_{13}$

This composition represents the random substitution of 5% of the iron atoms in an $FeZn_{13}$ compound by manganese atoms, or alternatively a 5% solid solution of $MnZn_{13}$ in $FeZn_{13}$. After weighing out the cleaned starting materials, the alloy was prepared using exactly the same proceedure as for pure ζ-phase $FeZn_{13}$. The annealing temperature of 500°C is ~70°C above the ζ-phase $MnZn_{13}$ peritectic, with the probability that the manganese atoms will randomly occupy iron sites in the ζ-phase $FeZn_{13}$. A microscopic examination of the annealed alloy showed it to be entirely single phased.

The δ_1-phase in the MnZn system

After the difficulties encountered in producing purely single phased ζ-phase $MnZn_{13}$, and before proving that the 5% of second phase was the dilute Zn-Mn solid solution, it was decided to check some of the properties of the δ_1-phase. This phase lies on the manganese rich side of the ζ-phase composition and occurs between 89 and 91 at.% manganese (88) (see figure 2.2). Schramm (101) has performed an X-ray diffraction investigation on the δ_1-phase and showed that it has a complex hexagonal unit cell containing ~550 atoms. Several specimens of the δ_1-phase were prepared by the same technique as for ζ-phase $MnZn_{13}$, with a final annealing temperature of 420°C. Microscopic

examination revealed single phase structures.

CHAPTER 3

EXPERIMENTAL METHODS AND APPARATUS

MAGNETIC SUSCEPTIBILITY

The majority of susceptibility measurements were taken using a magnetic balance, the exceptions being measurements on $MnZn_{13}$ specimens in the temperature region below 77 K for which a vibration magnetometer was used.

The Magnetic Susceptibility Balance

The magnetic balance used in our measurements was originally designed and constructed by D. Griffiths (102), and has since been modified by Waszink (1) and Williams (103) It is based on the Faraday method, which utilises the fact that a magnetic material (possessing either an induced or permanent magnetic moment) experiences a translational force when placed in a spatially varying magnetic field. The force is given by the expression (104)

$$\underline{F} = (\underline{M}.\nabla)\underline{H} \qquad 3.1$$

where $\underline{M}$ is the specimen magnetization and $\underline{H}$ that part of the magnetic field not produced by the specimen itself. In the co-ordinate system of figure 3.1.

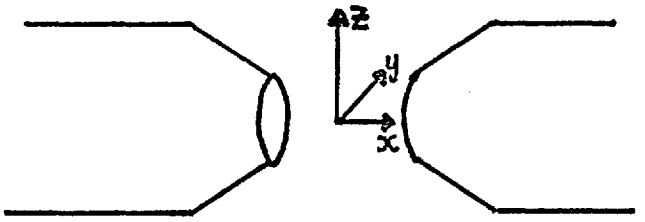


FIGURE 3.1

and for a specimen positioned on the z-axis, then equation (3.1) simplifies to:

$$F_z = M_x \frac{\partial H_x}{\partial z} \qquad 3.2$$

and if M_x is expressible as:

$$M_x = m\chi H_x$$

where m is the specimen mass and χ the magnetic susceptibility per unit mass, then:

$$F_z = m\chi H_x \frac{\partial H_x}{\partial z} \qquad 3.3$$

A schematic diagram of the apparatus is shown in figure 3.2. The balance consists of a helical elinvar spring held firmly at its upper end. From its lower end are supported three weighted arms and a torsional mode damping mechanism consisting of three copper discs suspended over small button magnets to produce eddy-current (i.e. velocity dependent) damping.

Below the three arms is a perspex scale pan, onto which a known calibrating weight can be lowered by an electromagnetic relay during the calibration proceedure. Below this is a small coil (labelled "restoring coil" in figure 3.2) wound onto a cylindrical copper former which hangs freely inside the radial gap of a loudspeaker magnet attached to the balance base plate.

The suspension is continued as a copper wire through the centre of the loudspeaker magnet and the base plate and then as a quartz rod. The quartz sample holder locates onto the bottom of the quartz rod by means of a J-shaped slit and pip arrangement.

During the series of measurements two other users of the magnetic balance, D. C. Golibersuch and A. E. Bell, carried

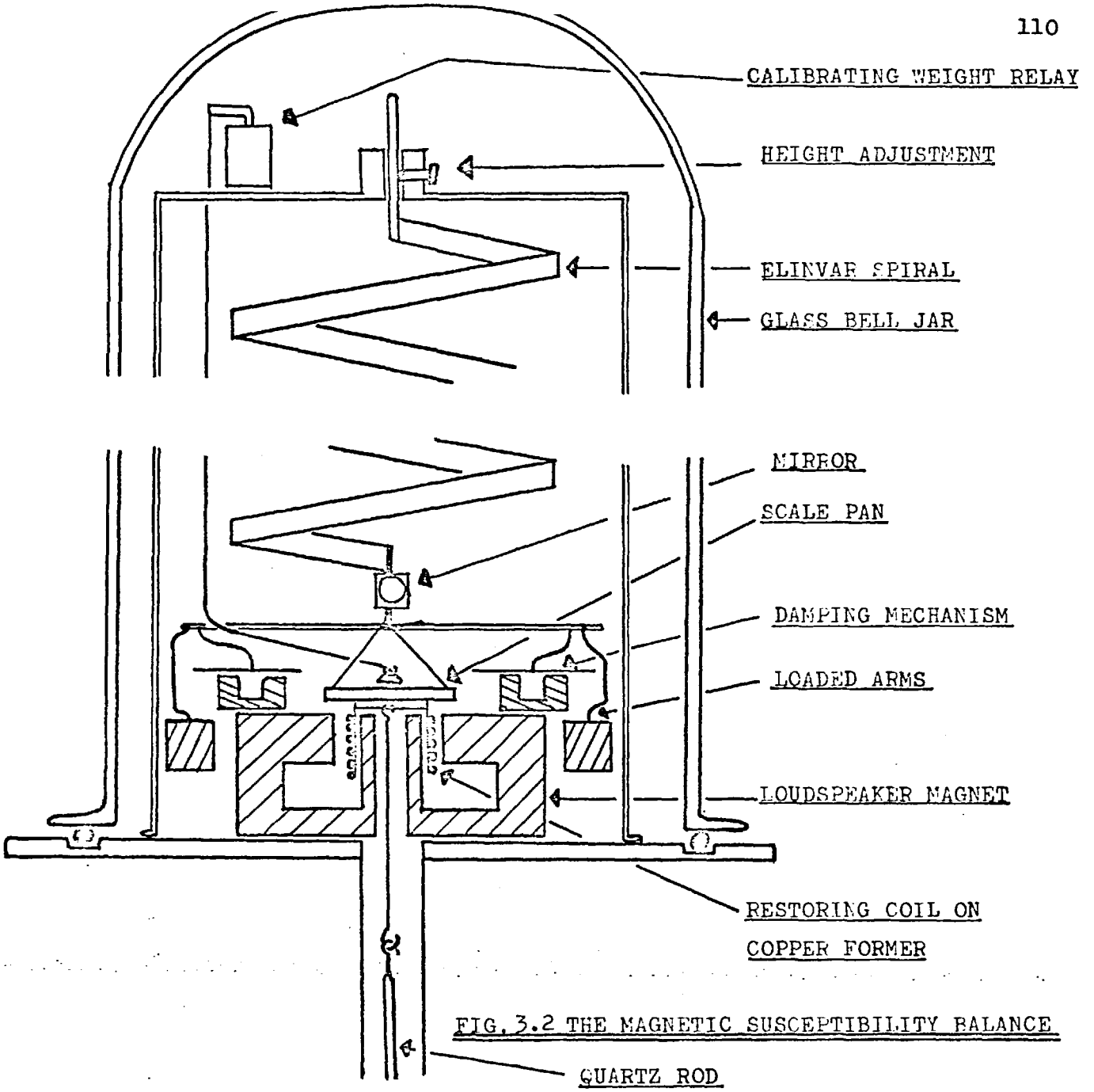
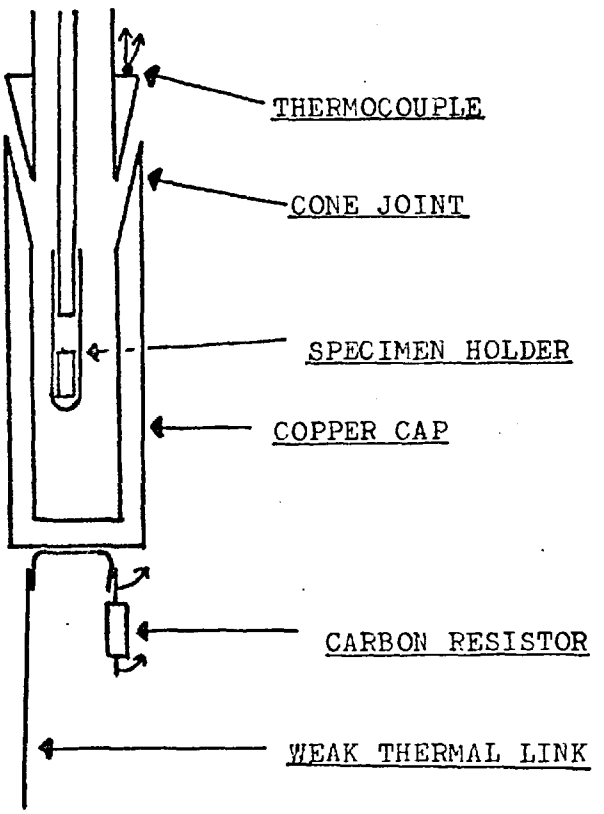


FIG. 3.2 THE MAGNETIC SUSCEPTIBILITY BALANCE



out a modification to enable samples of a greatly increased size to be measured. The inside diameter of the quartz bucket is only 2.7 mm., whereas the inside diameter of the copper cap is 8 mm., so with an alternative method of attachment the specimen diameter could be increased to approximately 6 mm. The modification involved shortening by 10 cms. the copper wire from which the quartz rod hangs and then adding 10 cms. of aluminium wire and an aluminium hook to the bottom of the quartz rod. The specimen is machined into the form of a cylinder with a small groove cut approximately 1 mm. from one end to help fasten an aluminium wire loop to the specimen. The old and new methods of specimen attachment are compared in figure 3.3.

Any change in the vertical force acting upon the balance produces a rotation of the lower end of the helical spring. A simple optical-lever converts this into the movement of a lamp filament image across a split differential selenium photo-cell, resulting in a change in output observable on a galvanometer. The system ismade null detecting by changing the current through the restoring coil so as to produce an equal and opposite vertical force on the balance and return the photo-cell output to its original value. The original change in the vertical force is then directly proportional to the change in restoring coil current.

The upper part of the balance, above the base plate, is enclosed within a glass bell-jar which rests on a rubber O-ring located within a groove. The suspension below the base plate is enclosed within a German-silver tube which ends with

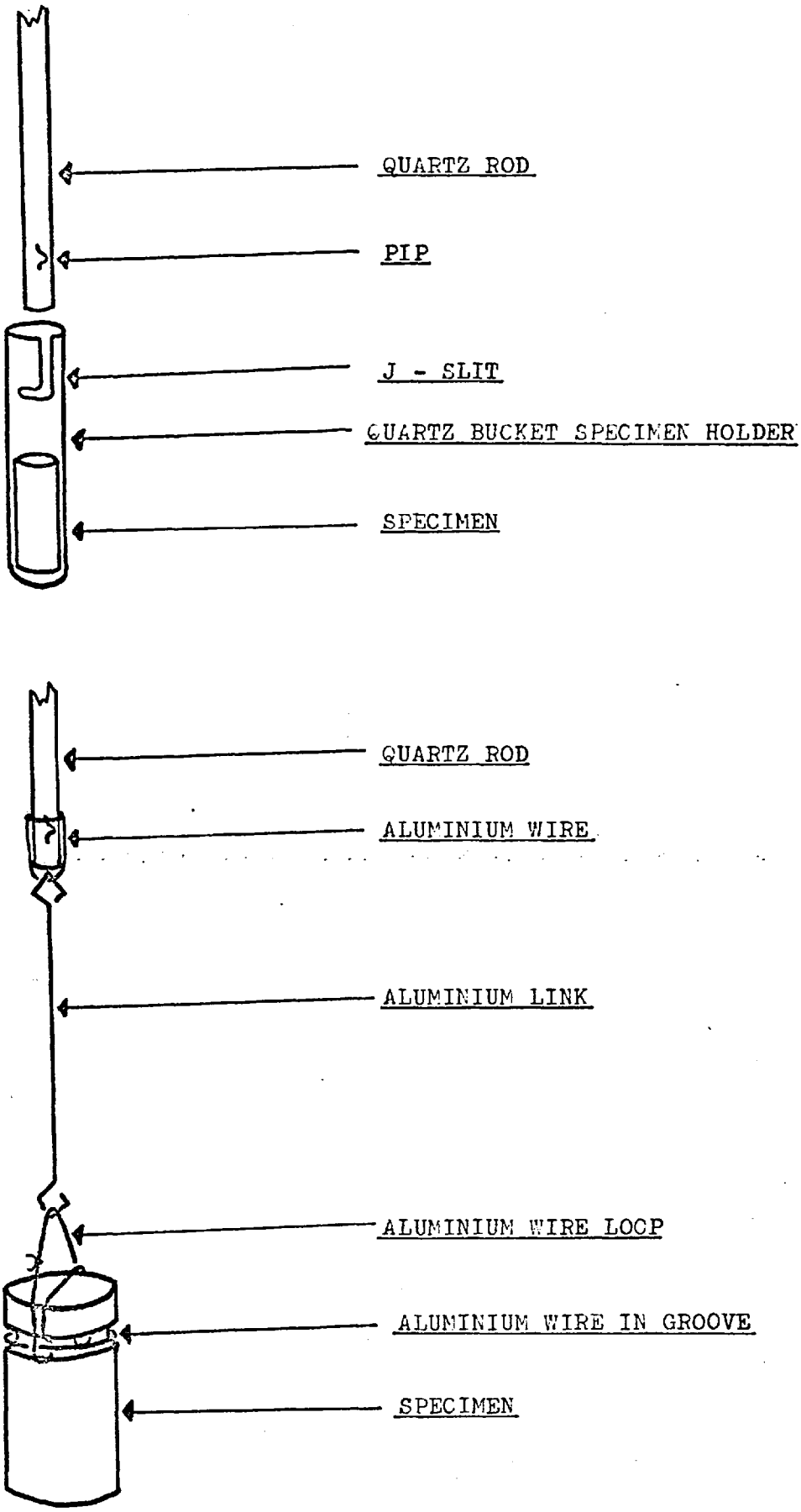


FIG.3.3 ALTERNATIVE SPECIMEN HOLDERS

a copper cone-joint and demountable copper cap to facilitate specimen changing.

Thermometry

The direct measurement of specimen temperature is a problem with any magnetic balance as to attach a thermometer, and its associated leads, to the specimen itself would considerable reduce the force sensitivity. In practice the simplest solution is to attach the thermometers to the thick walled copper cap and rely on heat transfer via 1 or 2 mm/Hg. pressure of helium exchange gas in the balance space to maintain thermal contact with the specimen.

Initially two separate thermometers were used.

(1) An Au-2 at.% Co versus Ag thermo-couple with one junction buried in solder on the upper part of the copper cone joint and the reference junction in an ice bath. This thermocouple has a useable range from room temperature down to 20 K, below which the differential thermopower drops rapidly.

(2) A 39 Ω (nominal) Allen-Bradley carbon resistor hanging below the copper cap and with a useful operating range from 1.7 K to 30 K.

A disadvantage with the original positioning of the carbon-resistor was that after the liquid helium level had just dropped below the bottom of the copper cap the resistor was still immersed and hence indicated too low a temperature. This situation persisted until the liquid level dropped below the resistor and led to a systematic error in the measured

temperature of approximately 0.5 K between 4.2 K and 10 K. This problem was overcome by soldering a small copper block 3 mm. square by 5 mm. long to the base of the copper cap with the long axis in a horizontal plane. A hole was drilled along the axis of the block in which was positioned a miniature $\frac{1}{10}$ watt 39 Ω (nominal) Allen-Bradley resistor sealed in with G.E. varnish. At the same time as this modification the original thermo-couple was replaced with one of Au-0.03 at.% Fe versus Chromel which retains a differential thermopower of approximately 15μV/K down to 4.2 K. More recently the cold junction of this thermo-couple has been moved from the upper section of the cone joint onto the cap itself, at the same level as the specimen, where it is physically and thermally attached by G.E. varnish.

Thermometer Calibrations

The Au-0.03 at.% Fe versus Chromel thermo-couple was calibrated by measuring its e.m.f.s at 4.2 K and at 77 K relative to the ice-point and comparing with a table, which had been supplied by Dr. R. Berman to A. Stewart of the Electrical Engineering Department of Imperial College, and applying a small linear interpolation on the differences. The carbon resistor was calibrated by measuring its resistance versus temperature between 1.7 K and 4.2 K (using helium vapour pressure tables) and again at the boiling point of liquid nitrogen, 77.4 K, and then fitting graphically to the equation:

$$\log R + \frac{A}{\log R} = \frac{B}{T} + C \qquad 3.4$$

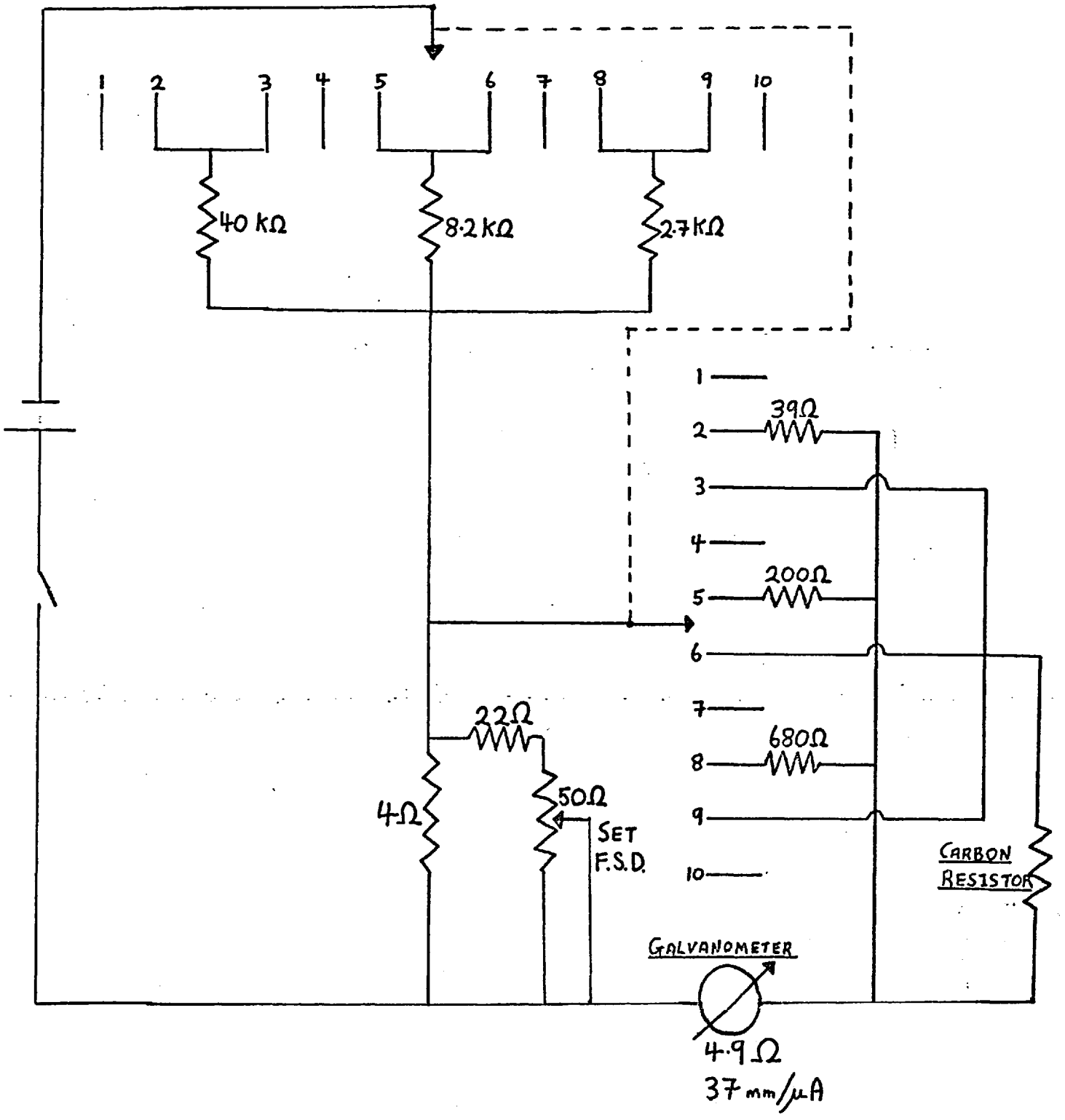


FIG 3.4 CARBON THERMOMETER CIRCUIT DIAGRAM

$\log R + A(\log R)^{-1}$ was plotted against T^{-1} using the measured values between 1.7 K and 4.2 K for various values of A. The quality of the fit, as judged by eye, appeared to be very weakly dependent upon A. For example no difference was detectable for values between 2 and 3 for the particular resistor used. However taking the A, B and C values from the sub 4.2 K fit and calculating the apparent temperature, T_{calc}, of the carbon resistor from the value of its measured resistance when immersed in boiling nitrogen gave widely varying values for different A's. For example, T_{calc} = 87 K for A = 2.40 and T_{calc} = 67 K for A = 2.42. A was then chosen to give a perfect agreement at the nitrogen point i.e. that T_{calc} = 77.4 K.

The carbon thermometer resistance is measured by a two terminal method and the circuit diagram is shown in figure 3.4. The galvanometer deflection was calibrated in terms of resistance by replacing the carbon thermometer by a resistance box and recording the deflection as a function of resistance. This was then converted into galvanometer deflection versus temperature using the fitted parameters of equation 3.4.

The resolution of the carbon thermometer drops rapidly with increasing temperature from about $\pm$ 0.02 K at 4.2 K to $\pm$ 0.2 K at 20 K, while that of the thermo-couple remains constant at $\pm$ 0.2 K from 4.2 K up to room temperature. The indicated temperatures of the thermometers were found to agree to within the accuracy of measurement up to 20 K, although it must be remembered that it is the temperature of the copper cap that is being measured and <u>not</u> that of the specimen directly.

To check the possibility of the specimen being warmer than the copper cap due to absorption of thermal radiation from the warmer upper part of the suspension tube, it was decided to perform an experimental run on a dilute alloy specimen known to obey the Curie Law. Murani(105) has measured the susceptibility of a Au 0.3 at.% Gd alloy and found that it obeys the Curie Law (with a maximum Curie-Weiss θ within the limits $\pm$ 0.05 K). A specimen was obtained from his original ingot and the results of our susceptibility measurements are shown in figure 3.5 plotted in the form $\frac{1}{\chi_{alloy} - \chi_{Au}}$ versus measured copper cap temperature. The intercept of 0.3 K on the temperature axis indicates that there is a temperature difference between specimen and cap of 0.3 K.

Magnetic Field Constants

In order to calculate the specimen magnetization and magnetic susceptibility from the measured specimen force, the quantities H_x, $\frac{\partial H_x}{\partial z}$ and $H_x \frac{\partial H_x}{\partial z}$ must be known. In principle all three could be deduced from a profile of H_x versus z, however it is easier to measure $H_x \frac{\partial H_x}{\partial z}$ and H_x separately, and then to calculate $\frac{\partial H_x}{\partial z}$. $H_x \frac{\partial H_x}{\partial z}$ was determined by measuring the force on a pure palladium specimen of known susceptibility (5.23×10^{-6} e.m.u./grm. at 295 K) (106) and then substituting into equation 3.3. The specimen was initially traversed along the z-axis to determine the position of maximum force and hence of $H_x \frac{\partial H_x}{\partial z}$.

The magnetic field H_x at the position of the specimen

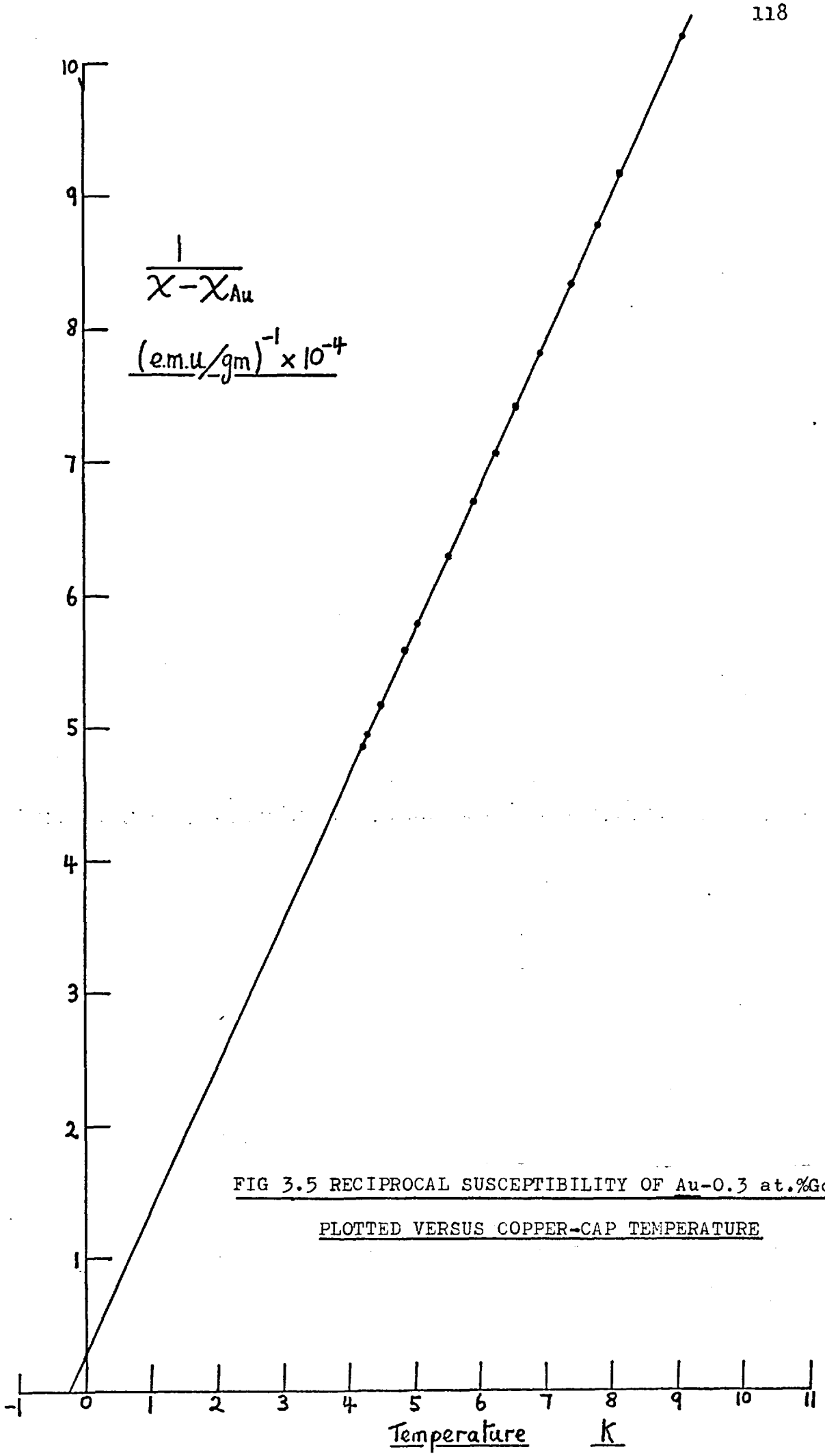


FIG 3.5 RECIPROCAL SUSCEPTIBILITY OF Au-0.3 at.%Gd PLOTTED VERSUS COPPER-CAP TEMPERATURE

centre was measured using a Hall probe gaussmeter (Bell Type 620) which had been previously checked against an N.M.R. probe($\pm$0.1%error) The sensitive area of the Hall probe, measuring 2 mm. by 2 mm. was positioned with the aid of a travelling microscope.

Balance Calibration and Sensitivity

As has already been noted, the change in force acting on the balance is directly proportional to the change in restoring current. In actual use the voltage across a wire-wound resistor in the restoring coil current circuit is measured rather than the current itself, and the proportionality constant between this voltage and the balance force is determined during the course of each experimental run by lowering a platinum calibrating weight on to the scale pan. (see figure 3.2).

Under ideal operating conditions the vibrational noise of the balance, as observable on the photo-cell galvanometer, is equivalent to $\pm$ 0.002 dynes. Under the usual operating conditions when zero drifting is present (this is discussed later) the balance force is measurable to $\pm$ 0.01 dynes. The dominant source of uncertainty in the eventual absolute value of the specimen susceptibility or magnetisation of $\pm$ 5% arises from inaccuracies of the specimen positioning. This estimate was made after investigating the change in force on traversing the specimen along the x and y axes.

Experimental Proceedure

Specimen Replacement and Positioning

Access to the specimen is achieved by wheeling away the magnet, removing the double dewar system, letting the balance

space up to atmospheric pressure and then removing the copper cap to expose the lower part of the suspension. Under the old system, the quartz bucket was untwisted and the specimen tipped out. Before replacing with a new specimen the bucket was cleaned in hydrochloric acid, distilled water and finally carbon tetra-chloride to remove any dust or grease contamination. Under the new system, the specimen is simply detached from the aluminium hook and replaced by a new one complete with its own attached aluminium wire loop. After specimen replacement the magnet is wheeled back into position and its height adjusted until the specimen centre coincides with the position of maximum $H_x \frac{\partial H_x}{\partial z}$. This is checked by means of a travelling microscope.

The two cone-joint surfaces are cleaned with carbon tetra-chloride and regreased with Edwards silicone high vacuum grease before replacing the copper cap. Next the balance space is evacuated to a pressure of 0.05 mm./Hg. using a rotary pump, before letting in 1 to 2 mm./Hg. pressure of pure helium exchange gas taken from the boil-off of a liquid helium transport vessel.

After checking that the balance is swinging freely, by observing its response to a small vertical force, the dewars are replaced and the magnet again moved into position.

Force Measurement

The positioning of the light bulb filament image exactly between the split photo-cells to give a zero output generally involves passing a finite current through the restoring coil even in zero applied magnetic field. The zero tends to drift around due to the influence of temperature fluctuations on the

elinvar spiral spring, and also due to changes in the thermo-molecular forces acting on the balance as the temperature around the specimen position changes.

The measurement of the "field induced" force acting upon the balance and the specimen involves taking three sets of readings:

(1) the restoring current in zero field

(2) the restoring current after re-balancing with the field on

(3) again in zero field.

Assuming a steady zero drift, the "field induced" force is then reading (2) minus the average of (1) and (3).

The total force acting on the balance is the sum of the force on the specimen plus the force on the balance with the specimen removed. Thus to obtain the specimen force alone, the force on the empty balance has to be known, both as a function of field and of temperature. The "empty-balance" force is made up of several contributions e.g. taking the case of the original specimen holder:-

(1) The force on the quartz bucket which is weakly temperature dependant due to paramagnetic impurities.

(2) The force on the quartz rod which acts as a Gouy specimen - again this is weakly temperature dependent.

(3) The stray magnet field on the upper part of the balance, as several parts are magnetic. This stray field was measured as 0.1 Gauss at maximum current. As the balance is sensitive to torques in addition to direct vertical forces, part of this apparent force could be due to torques on the upper part of the balance.

After the suspension had been modified the apparent empty balance force was reduced by a factor of five and was temperature independant within the accuracy of measurement, making the empty balance correction simpler.

Temperature Control

Below 4.2 K the temperature is controlled by maintaining a constant pressure above the boiling liquid helium in the dewar using a rubber diaphram type of manostat. The pressure can be held steady to 0.5 cms./Hg over a period of 30 minutes.

Between 4.2 K and 77 K there is no method of controlling the temperature - measurements have to be taken while the apparatus slowly warms . While helium remains in the tail of the dewar, the temperature rise is slowed down by the evaporating cold gas passing between the copper-cap and the closely fitting dewar tail and also by heat leaking down a 18 s.w.g. copper wire hanging into the remaining liquid from the copper-cap. Typically the warm-up from 4.2 K to 77 K takes 90 minutes.

Between 77 K and 300 K the temperature may be held constant by controlling the pressure in the helium dewar interspace with liquid nitrogen in the surrounding jacket. A diffusion pump is connected to the helium dewar interspace via two feet of plastic line. On isolating the diffusion pump the pressure rises due to outgasing of the plastic tube, the thermal conductivity increases and the temperature falls. Opening up the pump again reduces the heat leak , the rate of temperature change drops and a"plateau" is reached before the temperature eventually rises. The temperature on the "plateau" region is constant to within $\pm$ 0.1 K for one minute, a sufficient time to take a reading.

Generally measurements of magnetisation were taken for nine different field values at the fixed temperatures 1.7 K, 4.2 K, 77 K and 300 K, while at intermediate temperatures readings were taken at one fixed field.

The Vibration Magnetometer

Certain magnetic measurements on specimens of $MnZn_{13}$ were taken using the vibration magnetometer built in this laboratory by A. P. Murani (105). This apparatus has the advantages that measurements may be made in zero applied magnetic field and that the natural warm-up rate from 4.2 K to 77 K is an order of magnitude slower than that of the balance; also it is possible to manually control the specimen temperature in this region to within $\pm$ 0.1K for periods of several minutes, thus allowing measurements of magnetisation as a function of field to be made for an "Arrot plot" determination (107) of the magnetic ordering temperature.

The arrangement of the vibration magnetometer is shown in figure 3.6. The specimen, machined into the form of a cylinder 0.055 inches in diameter by 0.55 inches long, is pushed into a thin walled pyrex holder and held in place by a dab of G.E. varnish at the outer end. Wound round the outside of the holder is a "nulling coil" consisting of two layers of 49 s.w.g. varnished copper wire. The specimen is vibrated axially in a pick-up coil by means of a balanced piezo-electric bimorph tuning fork driven electrically by an audio oscillator. A block diagram of the detection system is shown in figure 3.8. The signal from the pick-up coil is amplified and fed into a phase sensitive detector, and by adjusting the D.C. current through the nulling coil the

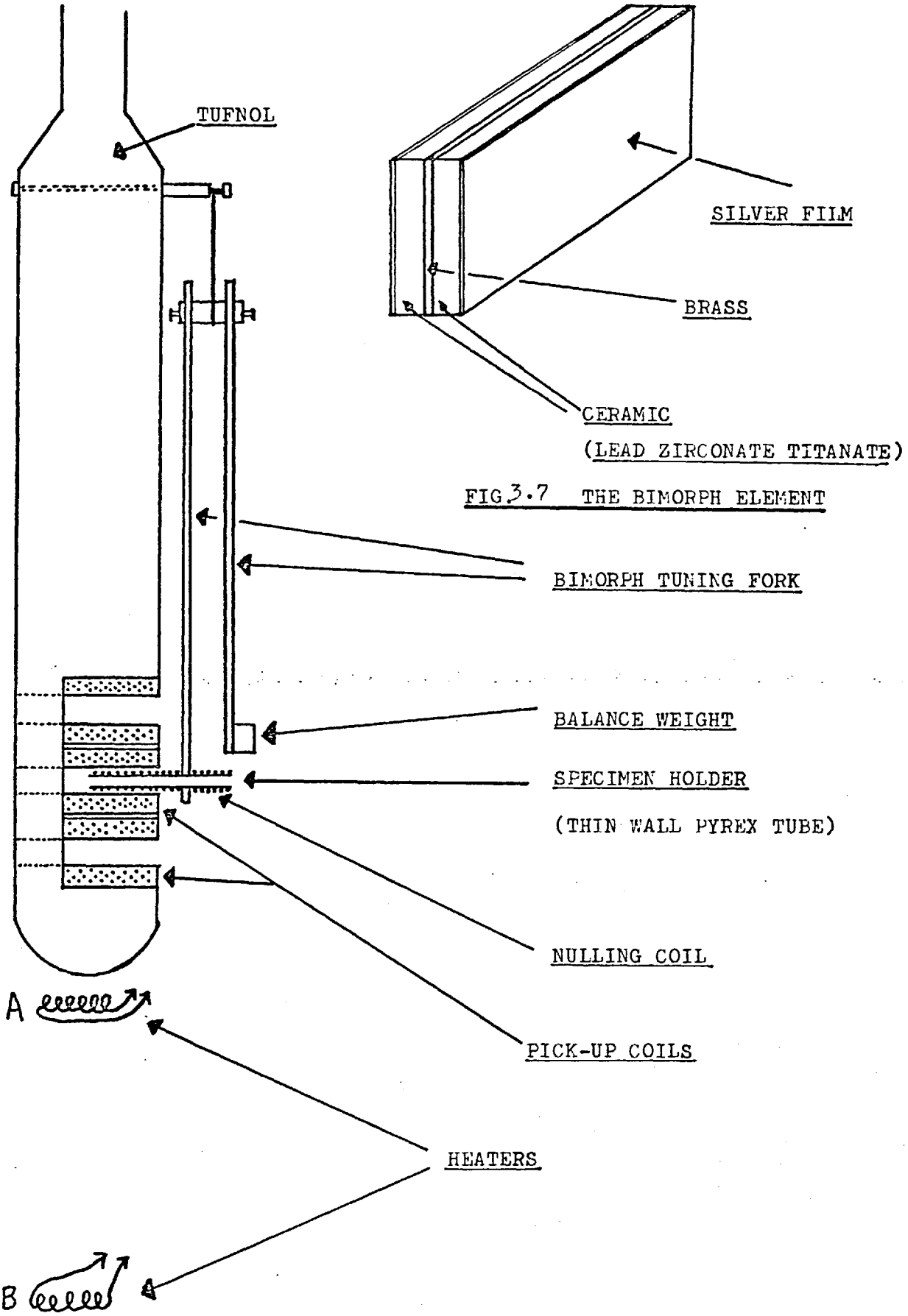


FIG.3.7 THE BIMORPH ELEMENT

FIG.36 SPECIMEN VIBRATOR AND PICK-UP COILS

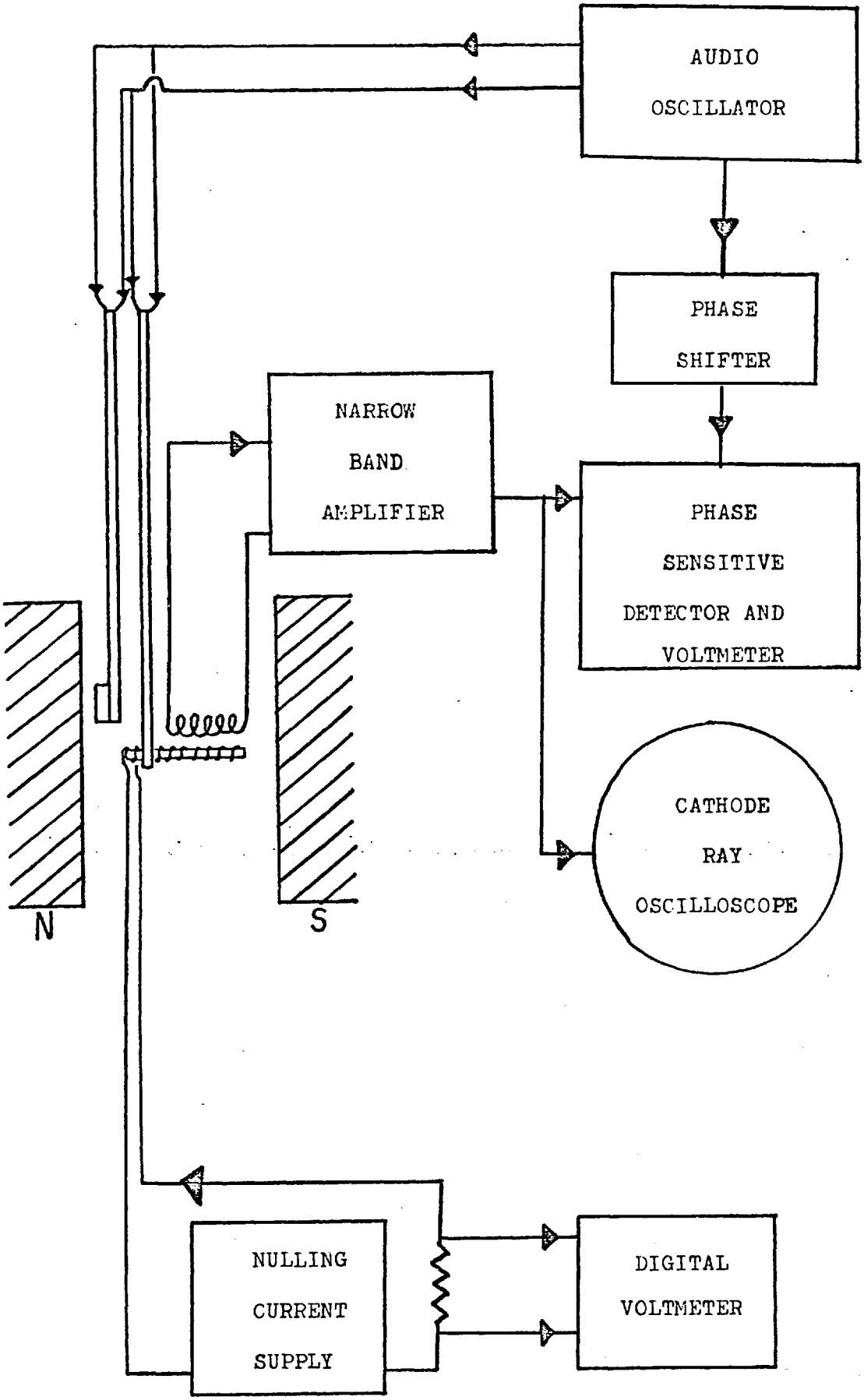


FIG.3.8 BLOCK DIAGRAM OF VIBRATION MAGNETOMETER

magnetisation of the specimen may be compensated so as to give zero output. The specimen magnetisation is directly proportional to the nulling current.

The specimen, vibrator and pick-up coils are enclosed within a standard glass two-dewar cryogenic system and the dewar tails fit inside the 6 cm. gap of a Newport type D water-cooled electro-magnet, energized by a 15 amp Wareham power supply. The maximum magnetic field available is 8 kilo-gauss.

Thermometers and Their Calibration

Specimen temperature is measured by two separate thermometers having an overlap of 10 K between 20 K and 30 K.

(1) A miniature 47 Ω (nominal) Allen-Bradley carbon resistor positioned on the pick-up coil holder alongside the specimen. This thermometer has a useful range from 1.6 K up to 30 K and its resistance is measured by a two terminal method similar to that of the magnetic balance (shown in figure 3.4). The thermometer was calibrated against helium vapour pressure tables below 4.2 K and at the boiling point of oxygen (90.18 K), and the data fitted graphically to the empirical expression

$$\log R + \frac{A}{\log R} = \frac{B}{T} + C$$

as for the magnetic balance carbon thermometer.

(2) Above 20 K the copper resistor formed by the nulling coil itself is used as a thermometer, and this has the advantage of being in excellent thermal contact with the specimen. As its resistance is only 1.6 Ω at 4.2 K a four terminal method of measurement is used. The voltage across the nulling coil is measured by a digital voltmeter and the current is determined

by measuring the voltage across a standard 1 Ω resistor in the nulling current circuit using the same digital voltmeter. For commercial copper wire White (108) has tabulated the resistivity, in the form $Z = \frac{R_T - R_{4.2}}{R_{273} - R_{4.2}}$ versus temperature.

As the majority of measurements are taken in a magnetic field, the magneto-resistance of the nulling coil must be corrected for. Murani (105) measured the magneto-resistance at 4.2 K and at 20 K and found that it obeyed the same dependence

$$R \times \Delta R_H = f(H)$$

at both fixed points. He assumed that it would show the same dependance at any temperature T. Murani has written a computer program which takes the measured value of the resistance and, after correcting for the magneto-resistance, uses an interpolation formula to calculate the temperature from White's tabulated values.

The agreement between the two thermometers in the temperature interval 20 to 25 K is within 0.1 K.

Temperature Control

Below 4.2 K the temperature is controlled by the standard technique of pumping on the liquid helium via a manostat. After the helium level has dropped below the specimen and pick-up coils, the apparatus begins a slow warm-up, and the rate is limited to approximately 10 K per hour by evaporating gas from the residual pool of liquid helium in the dewar tail. The warm-up rate may be increased by using heater (A), positioned just below the pick-up coil holder, to heat the rising gas stream. Alternatively the temperature may be held constant to $\pm$ 0.1 K for several minutes by using heater (B), positioned in the residual

liquid helium at the bottom of the dewar tail, to increase the boil-off rate.

In the temperature region between 77 K and 300 K no attempt is made at temperature stabilisation. The helium dewar interspace is carefully flushed with dry nitrogen gas and then pumped out using a rotary pump, and the nitrogen dewar filled right up. The cool-down to 77 K then takes about six hours and measurements are taken as it proceeds.

Magnetic Field Calibration

The Wareham power supply is equipped with a ten turn heli-pot and using this alone it is possible to re-set the magnetic field within $\pm$ 1 Oe over any part of the range. The magnetic field was calibrated in terms of heli-pot setting using an N.M.R. probe with 0.1% accuracy.

Nulling-Coil Calibration

Calibration of the nulling-coil in terms of magnetic moment per unit current was performed by measurements on a pure palladium specimen of known susceptibility (106).

Nulling-Coil Heating Effects

Heating effects put an upper limit on the current which may be passed through the nulling-coil and hence on the maximum specimen magnetization for which the nulling-coil method of measurement may be used. When the specimen and holder are totally immersed in liquid helium the maximum allowed current is around 120 mA, which corresponds to a specimen magnetic moment of $\sim 10^{-1}$ e.m.u. and a heat dissipation of 10^{-2} watts. When the specimen is in the gas above the liquid helium the maximum

permissible current drops to 10 mA, with a corresponding specimen magnetic moment of $\sim 10^{-2}$ e.m.u.

Experimental Proceedure

The experimental proceedure followed was essentially the same as that of Murani and it has been described in great detail in his thesis (105). After specimen replacement a check is made to ensure that the specimen holder is vibrating freely, as any "touching" greatly increases the amount of synchronous noise from the pick-up coils. By passing a steady current through the nulling-coil and observing the amplified pick-up coil signal on a cathode ray oscilloscope, any touching shows up clearly as a grossly distorted sine wave.

The other main area in which great care has to be exercised lies in the minimisation of synchronous noise due to vibration of the pick-up coils at the same frequency as the specimen. If the pick-up coil axis is at an angle to the magnetic field, then any torsional oscillation of the pick-up coil assembly may lead to a synchronous noise signal having a component in phase with the "wanted" signal. This may be minimised by setting the pick-up coil axis accurately parallel to the magnetic field. For a particular driving frequency the specimen signal, in terms of the nulling current, is measured as a function of the magnetic field orientation θ by rotating the magnet within a couple of degrees of the estimated parallel position. This proceedure is repeated for another two or more values of the driving frequency and a graph of nulling current versus θ plotted for the various frequencies. A family of curves is obtained having a common intersection point, which is the optimum setting for minimum synchronous pick-up.

Magnetization versus field measurements were taken at the fixed temperatures 1.6, 4.2, 77 and 300 K using the nulling current method. In the temperature region between 4.2 K and approximately 50 K the nulling current method could not be used for specimens of $MnZn_{13}$ due to the heating effects mentioned earlier. This difficulty was overcome by first measuring the amplified pick-up coil signal after phase sensitive detection (S) with no current flowing through the nulling-coil, and then with 10 mA. flowing (S + 10). Thus the specimen magnetization could be calculated in terms of effective mA. of nulling current providing that the output from the amplifier and phase sensitive detector is linear. The accuracy of this method was checked at 4.2 K with the specimen still immersed in liquid helium before the warm-up started, as under these conditions the magnetization may also be measured by the nulling current method. This was done for increasing amplifier gain until the linearity limit was reached, typical results are shown in table 3.1

	Amplified Signal (S). Volts	Amplified Signal (S + 10) Volts	Specimen Signal in Effective mA. of Nulling Current
Increasing Amplifier Gain ↓	0.196 volts	0.162 volts	115
	0.440 "	0.402 "	116
	0.578 "	0.528 "	116
Linearity Limit →	0.645 "	0.592 "	122

TABLE 3.1

The specimen magnetization measured by the nulling-coil method is 114.8 mA.

Magnetization measurements were taken at three magnetic fields between 4.2 K and 30 K , and otherwise at one field only. In calculating the results the magnetic moment of the specimen holder has to be taken into account, this is checked in separate runs at intervals.

THE SPECIFIC HEAT APPARATUS

The specific heat measurements were made by the writer and Dr. J. R. Cooper using an apparatus at the Instituto di Fisica of the University of Genoa in Italy. The specific heat apparatus had been originally designed for measurements on small arc-melted buttons of intermetallic compounds and the total mass of the specimen holder, thermometer and heater has been kept as low as possible. A diagram of the apparatus is shown in figure 3.9.

The specimen holder consists of a thin sheet of mylar 10 mm. long by 5 mm. wide supported between two copper posts by tensioned loops of nylon thread and the specimen is physically and thermally attached to it by a small quantity of G.E. varnish. The specimen heater consists of a thin film of nichrome evaporated onto the under surface of the mylar sheet. Electrical connection to the heater is made via two fine niobium wires leading to insulated terminals on the copper posts, and the current and potential leads are taken from this point. The total mass of the specimen holder and heater is approximately 50 milligrams .

The posts are fixed onto a copper plate which forms the base of the inner can. The copper cylinder forming the inner can is simply screwed onto the base plate with a liberal application of silicone vacuum grease to ensure good thermal contact. There

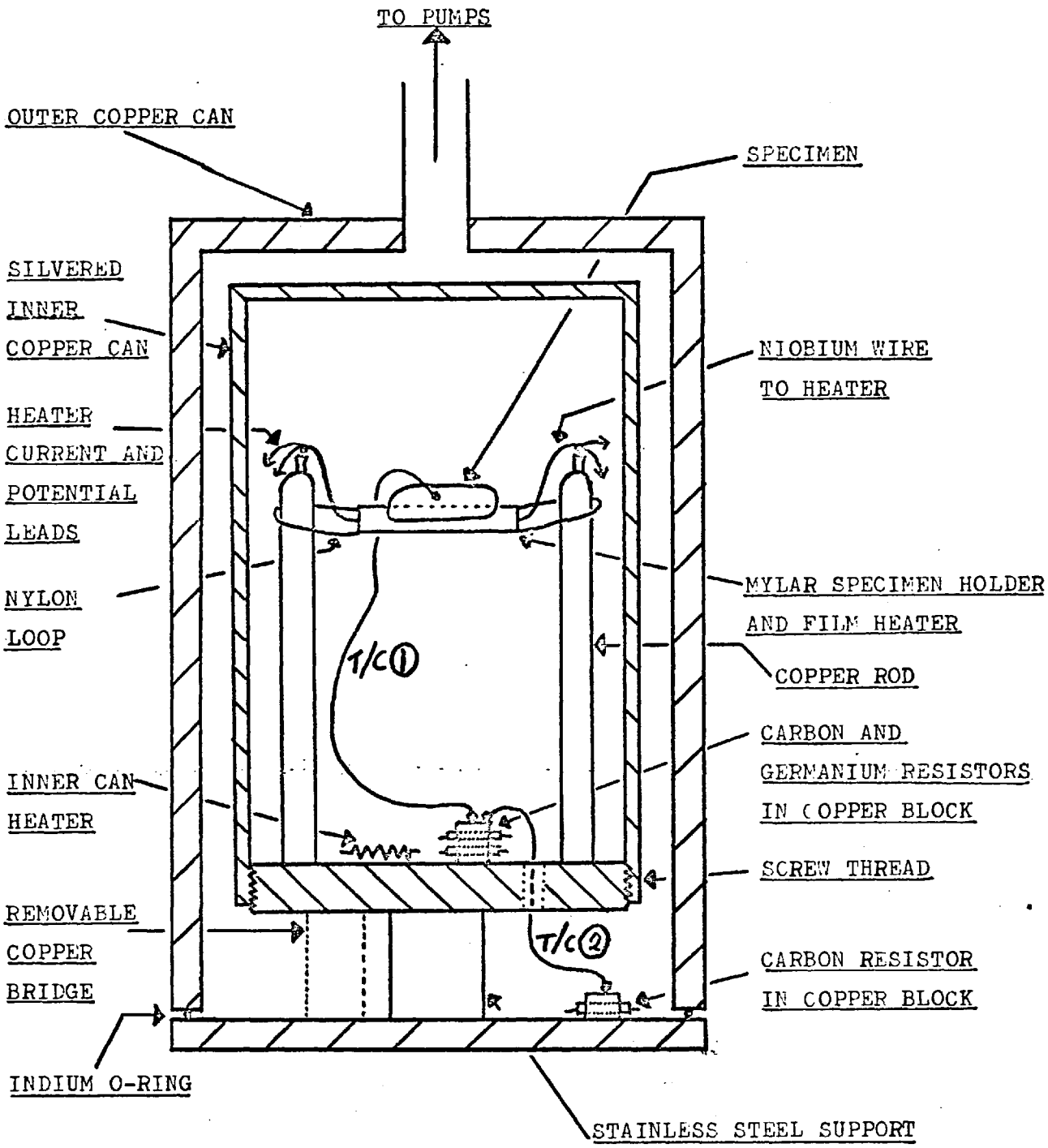


FIG.3.9 THE SPECIFIC HEAT APPARATUS

is no intention of forming a vacuum seal, in fact the can is perforated in several places to equalize the pressure inside and out. Also mounted on the inner can base plate are a heater and a copper block, drilled to accept carbon and germanium resistance thermometers and therm-couple junctions. The inner and outer can base plates are connected by a stainless steel tube which forms a relatively weak thermal link, although when necessary a copper bridge may be fixed in position to improve the thermal link. The apparatus is enclosed within a standard double glass dewar system.

Thermometers

The temperature difference between the specimen and the inner can is measured by a Au-0.03 at.% Fe versus Chromel thermo-couple, labelled T.C.(1) in figure 3.9. This thermo-couple is physically and thermally anchored to the specimen by a small quantity of G.E. varnish and the reference junction is situated on the inner can base plate. A calibration of e.m.f. versus termperature for the actual thermo-couple used has been determined using a thermo-power apparatus at Genoa, with an accuracy of 5%.

For measurements below 4.2 K, the temperature of the inner can is measured by either a carbon resistance thermometer or a germanium resistance thermometer. If measurements much above 4.2 K are required the temperature difference between the inner can and the outer can (which is surrounded by liquid helium) is determined by a second Au-0.03 at.% Fe thermo-couple T.C.(2).

Experimental Proceedure

As all our measurements were taken in the temperature

region below 4.2 K, the copper bridge was left in position in order to minimise the temperature difference between the inner and outer cans. After replacing a specimen, attaching the specimen thermo-couple T.C.(1) and remaking the can joints, the apparatus is flushed with pure dry nitrogen gas before pumping out with a diffusion pump. Before commencing the cool down to 77 K a couple of mm/Hg pressure of pure hydrogen exchange gas is admitted into the apparatus. After the pre-cool to 77 K and during the initial slow transfer of cold helium gas into the helium dewar the specimen temperature is continuously monitored to ensure that it cools at the same rate as the cans down to $\sim$ 15 K. Below this temperature the hydrogen exchange gas freezes out, so that if the initial transfer is too fast the cans rapidly cool below 15 K leaving the specimen thermally isolated at a much high temperature, from which it takes hours to cool.

To determine the specimen specific heat, the temperature rise of the specimen is measured for a known heat pulse. In a true adiabatic method the specimen is cooled to the lowest attainable temperature and then thermally isolated by using some type of heat switch. The temperature is then raised in a series of small steps by known heat pulses, while slowly increasing the temperature of the specimen can, or more usually an intermediate shield, to maintain it as close as possible to the specimen temperature, thus minimising extraneous heat leaks. For the sake of convenience an alternative technique is followed here. A small amount of helium exchange gas is admitted into the apparatus and its pressure is adjusted by use of the diffusion pump until the

time constant τ for the return of the specimen temperature to its original value after a heat pulse is around 30 seconds. By using this technique the temperature of the specimen may easily be varied either up or down (by pumping on the liquid helium bath via a manostat) between individual measurements, and several measurements may be taken at each temperature. However it does mean that a correction has to be made to the observed temperature rise, depending upon the ratio between the heat pulse length and τ.

The temperature difference between the specimen and the inner can is measured by T.C.(1) and the e.m.f. is detected by a Keithley nano-voltmeter whose output is displayed on an x - t chart recorder. A typical recorder trace is shown in figure 3.10.

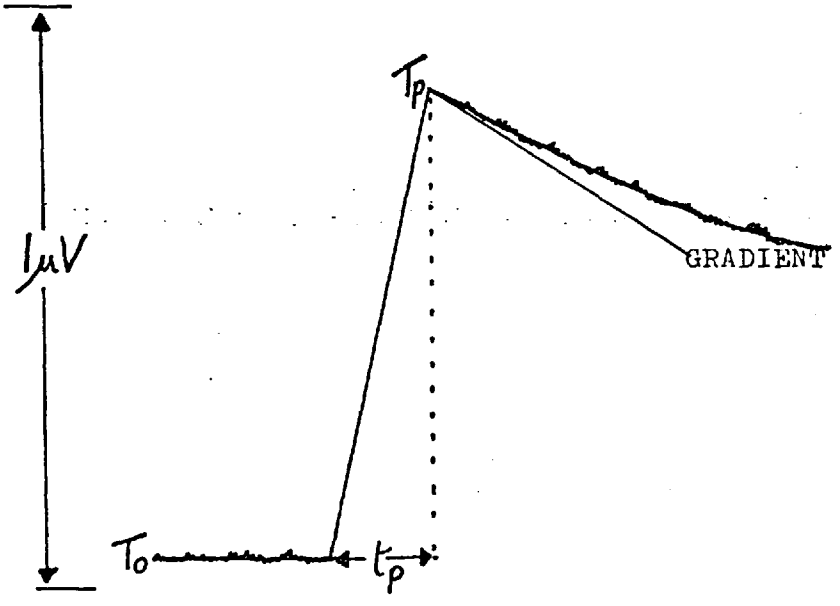


FIGURE 3.10

T_o is the original equilibrium specimen temperature, T_p the final temperature after a heat pulse of power P and duration t_p seconds, C the specific heat and τ the time constant.

During the heat pulse the rate of temperature rise is given by

$$\frac{dT}{dt} = \frac{P}{C} - \frac{(T - T_o)}{\tau}$$

then $$\int_{T_o}^{T_p} \frac{dT}{\frac{P}{C} - \frac{(T - T_o)}{\tau}} = \int_0^{t_p} dt$$

giving $$\left[-\tau \log\left(\frac{P}{C} - \frac{(T - T_o)}{\tau} \right) \right]_{T_o}^{T_p} = t_p$$

and $$1 - \frac{C}{P} \frac{(T_p - T_o)}{\tau} = e^{-\frac{t_p}{\tau}} = 1 - \frac{t_p}{\tau} + \frac{t_p^2}{2\tau^2} - \ldots\ldots$$

finally $$C = \frac{P\, t_p}{T_p - T_o} \left(1 - \frac{t_p}{2\tau}\right)$$

τ may also be calculated from the trace, as the initial rate of decay $= -\frac{(T_p - T_o)}{\tau}$. The pulse length usually used is two seconds and the time constant τ around 30 seconds, hence the correction factor $\frac{t_p}{2\tau}$ is $\sim 3\%$.

The heater voltage and current are measured on alternate pulses. A typical temperature rise during a heat pulse is 0.05 K and when calculating the specific heat from the traces $\frac{T_p - T_o}{2}$ is taken to be the average specimen temperature. At the end of each run a few cms./Hg pressure of helium exchange gas is introduced into the apparatus ensuring that both inner and outer cans are at the same temperature. Any standing thermal e.m.f.s on the thermo-couple are noted and these are corrected for when calculating the specimen temperature. At this time the carbon and germanium thermometers are calibrated by measuring their resistances

as a function of temperature from helium vapour pressure tables.

The specific heat of the specimen holder, heater etc has to be taken into account when calculating the results and this was measured in a separate experiment and is shown in figure 3.11.

The major source of systematic error in calculating the total specific heat of the specimen and addenda arises from uncertainties in the calibration of the Au-0.03 at.%Fe versus Chromel T/C (1) and this is estimated as $\pm$ 5%. The specimen temperature before each heat pulse may be determined to $\pm$ 0.01 K in the temperature range 1 - 4 K using the carbon and germanium thermometers on the inner can and T/C (1) (after correcting for standing thermal e.m.f.s). The noise on the T/C (1) amplified output which is displayed on the x - t chart recorder leads to a scatter of $\pm$ 3% in the measured temperature rise.

To check the accuracy of the apparatus measurements were taken on a specimen of pure zinc and the results are shown in figure 3.12 and compared to the data of D. L. Martin (74). The γ values agree to within the accuracy of measurement ($\pm$ 5%) but the lattice specific heat coefficients (β) disagree by 20%. Also shown in figure 3.12 is the measured addenda specific heat plotted on the same scale as the zinc data. It can be seen that the discrepancy in the β values for zinc could be accounted for by a factor 2 error in the lattice term of the addenda. As the total weight of the specimen holder and heater is only 50 mg. its specific heat may easily be changed by using variable amounts of G.E. varnish in attaching the specimen and thermo-couple.

FIG 3.11 SPECIFIC HEAT OF THE ADDENDA

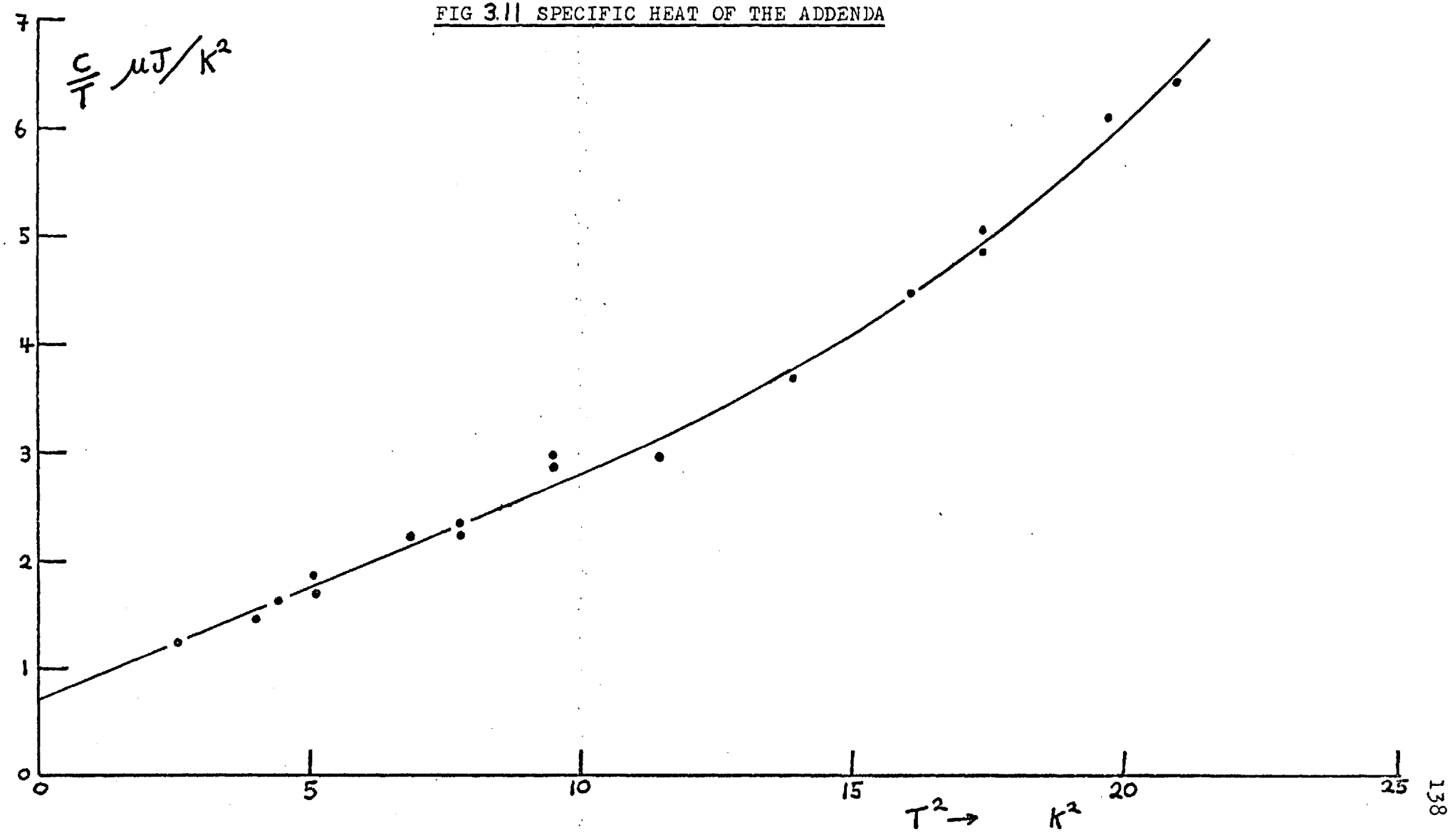
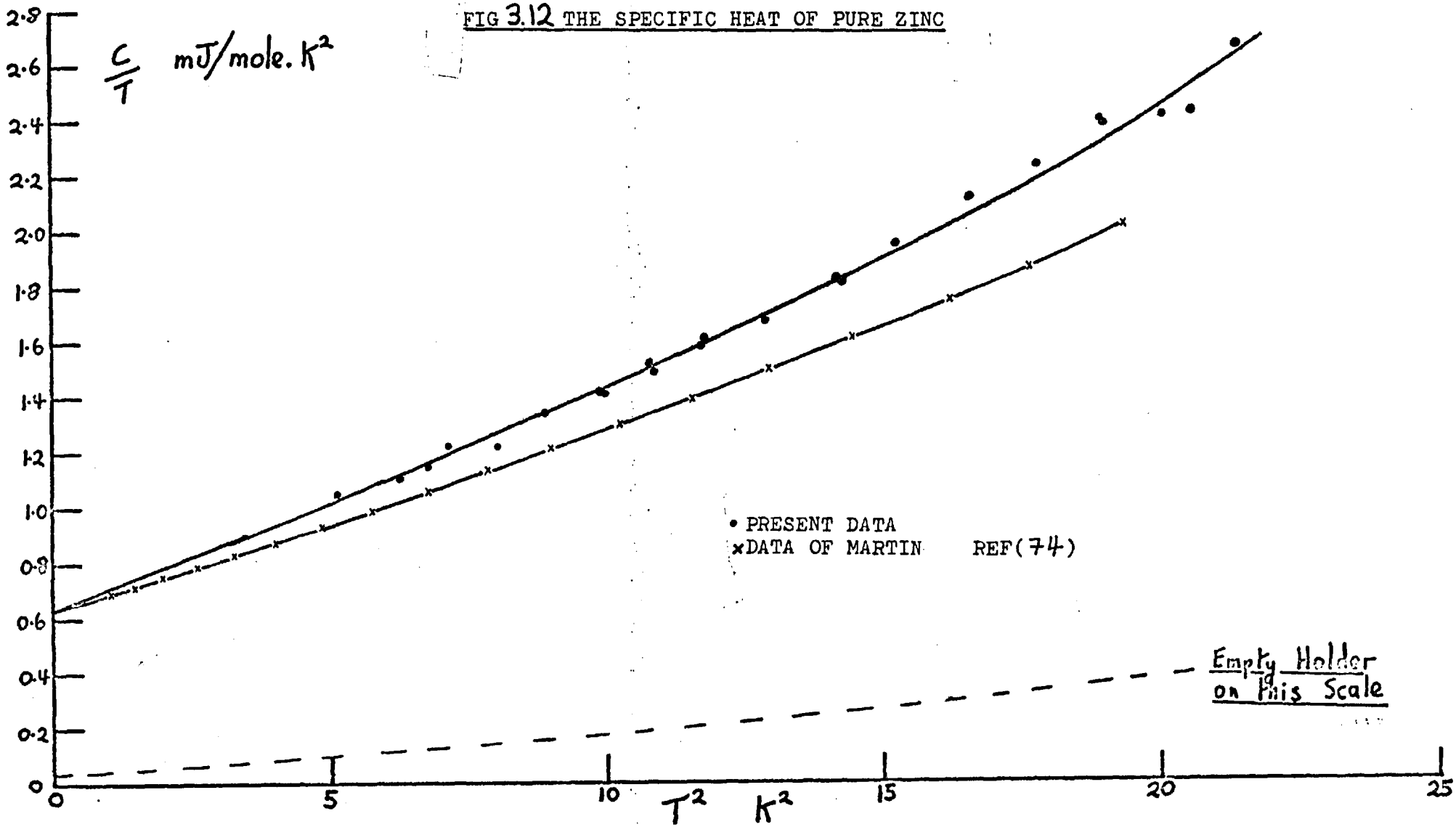


FIG 3.12 THE SPECIFIC HEAT OF PURE ZINC



This would also have the effect of changing the lattice contribution while not altering the electronic coefficient γ. The error which this introduces into the lattice specific heat depends upon the specimen mass. The pure zinc specimen weighed 10 gms., while the ζ-phase specimens weighed $\approx$ 2 gms. The estimated error in the calculated Debye temperatures θ_D is $\pm$ 7% and in the electronic coefficient γ is $\pm$ 5%.

ELECTRICAL RESISTIVITY APPARATUS

Electrical resistivities were measured by the conventional four terminal method using an apparatus designed and constructed by Dr. A. D. Caplin. The specimen resistance is determined by comparing the potential drop along the specimen with that across a standard resistance in the same current circuit using a Tinsley Stabaumatic potentiometer type 5545. The null detector is a Tinsley galvanometer amplifier in conjunction with a galvanometer. Current is provided by a Tinsley regulated supply type 5753 and the standard resistors in the current circuit are situated in a thermostatically controlled water bath held $\sim 2^{\circ}C$ above the highest temperature encountered in the laboratory. The current is stable to 1 part in 10^5 over a period of several hours. Thermal e.m.f.s. are compensated by reversing the current, and the potential drop across the specimen may be measured with a resolution of 2×10^{-9} volts. A typical specimen resistance is $10^{-4}\Omega$'s and a current of 200 mA, which means that the resistivity may be measured to a relative accuracy of 1 part in 10^4. The absolute accuracy of the resistivity is limited in the first instance by the accuracy of measurement of the specimen dimensions estimated at $\pm$ 5%, and in addition by the possibility of internal cracking of the brittle materials.

The specimen can holds four specimens and is shown in figure 3.12. The upper and lower ends are tufnol discs separated by three copper-nickel supporting tubes and the specimens are enclosed within a cylindrical copper shield, which slides upwards for ease of access and provides an isothermal environment. The specimen can is situated in the tails of a conventional glass double dewar system and between the poles of a Newport water cooled electromagnet capable of producing a maximum field of 20 kilo Gauss.

Potential leads, of annealed platinum wire, were attached to the specimens by spot welding. The current leads, of tinned copper wire, were twisted around the extreme ends of the specimens before soldering with a low melting point indium-tin eutectic solder using a cool iron. A complete cap of solder formed over the specimen ends and, apart from imparting mechanical strength, it allowed the potential leads to be attached closer to the ends than would otherwise have been possible. No discontinuities in the data were detected such as may be caused by current redistribution in the specimen due to superconducting transition of the solder. Great care had to be taken at all times in handling the cylindrical resistivity specimens due to the extremely brittle nature of the intermetallic compounds.

Thermometers and Temperature Control

Below 4.2 K, when the specimens and the can are completely immersed in liquid helium the temperature is stabilised by the standard technique of pumping on the helium via a rubber diaphragm manostat, and the temperature is determined by reference to helium vapour pressure tables.

Temperature measurement above 4.2 K, after the liquid helium level has dropped below the specimen can, is by two

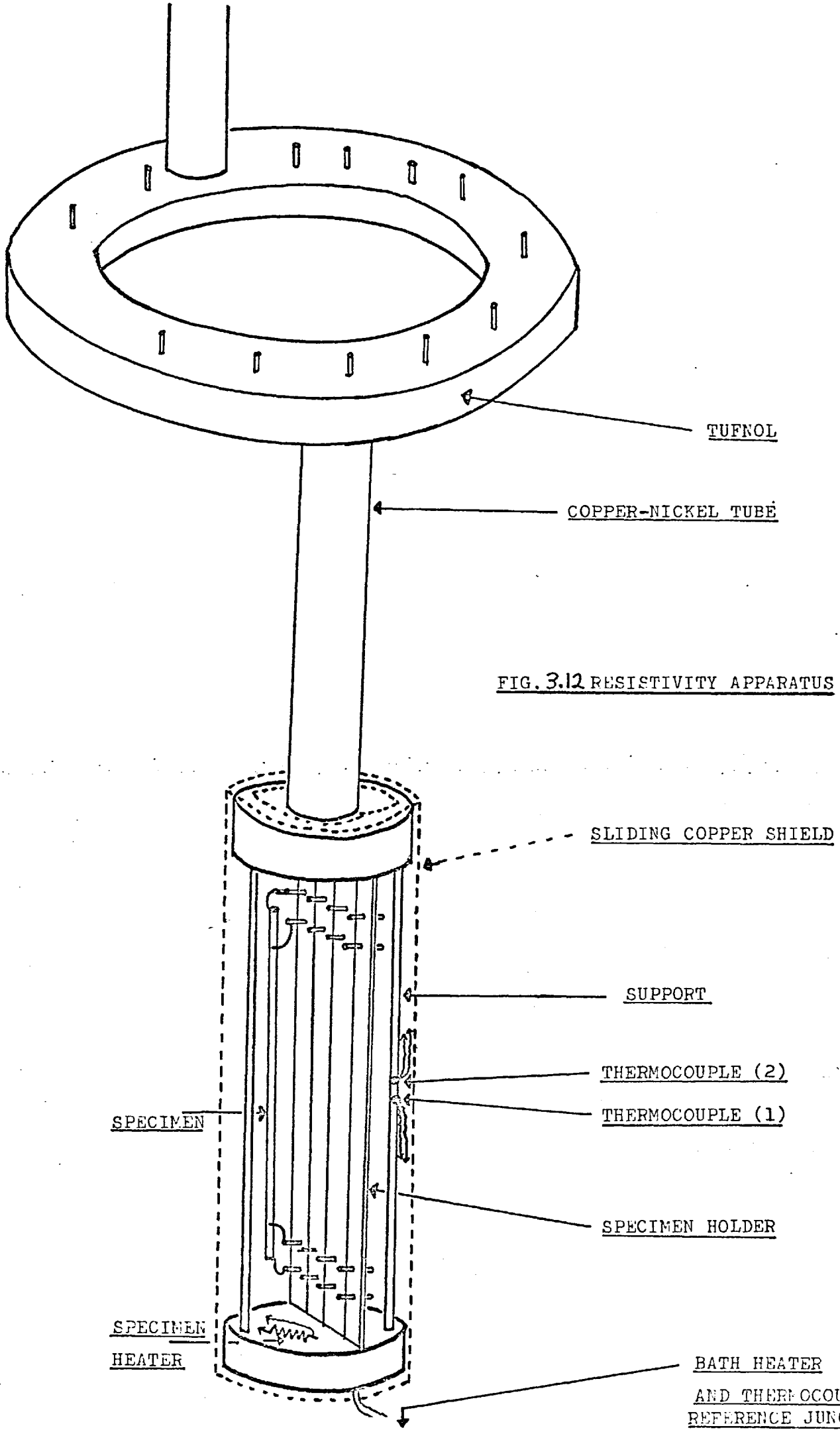


FIG. 3.12 RESISTIVITY APPARATUS

thermo-couples sited on one of the supporting tubes in the specimen can. (1) is a Au-0.03at.% Fe versus Chromel thermo-couple with its reference junction at the bottom of the dewar tail in the residual liquid helium. (2) is a copper versus constantan couple with its reference junction in a small dewar containing either liquid nitrogen or oxygen. The thermo-couple e.m.f.s are amplified by a D.C. amplifier with input impedance greater than $10^4 \Omega$'s and measured on a digital voltmeter. Rosenbaum's calibration (109) was used for the Au-0.03 at.% Fe versus Chromel thermo-couple and Powell's for the copper-constantan. (110). The error in the measured temperature increases from $\pm$ 0.05 K just above 4.2 K to $\pm$ 0.3 K above 25 K. Temperature control is made possible by the use of two heaters:- one at the bottom of the specimen can to increase the warm-up rate and a second in the residual liquid helium in the dewar tail to increase the evaporation rate and hence cool the specimen can.

To check for specimen self-heating, the current was occasionally halved, thus reducing the power dissipation by a factor of four, and the resistivity re-measured.

CHAPTER 4

EXPERIMENTAL RESULTS

Introduction

In this chapter the results of electrical resistivity, low temperature specific heat and magnetic susceptibility measurements on the ζ-phase compounds $CoZn_{13}$, $FeZn_{13}$ and $MnZn_{13}$ are presented.

Also reported are the results of E.S.R. measurements made by Mr. R. H. Taylor of the Solid State Group at Imperial College on our specimens of $MnZn_{13}$, and a neutron diffraction experiment carried out by Dr. J. B. Forsyth at the U.K.A.E.A. Harwell, on a specimen of $MnZn_{13}$.

Specific Heat Measurements

$CoZn_{13}$

Measurements were made on the same sample of $CoZn_{13}$ (149), weighing 2.4 gms., that was used for the susceptibility measurements. The results, plotted in the form $\frac{C}{T}$ versus T^2, are shown in figure 4.1. One immediately obvious feature of the results is the rapid break-away from a linear dependence at temperatures above 3 K. Below 3K the fit to the relation $C = \gamma T + \beta T^3$ gives

$$\gamma = 8.1 \text{ mJ/mole(formula unit).K}^2$$

and $$\beta = 1.10 \text{ mJ/mole(formula unit).K}^4$$

This value of β corresponds to a Debye temperature of $\theta_D = 292$ K, however at 4K the β value has already increased to 2.26 mJ/mole.K^4 and the Debye temperature has dropped to $\theta_D = 230$ K.

$\underline{FeZn_{13}}$

Measurements were taken on two specimens of $FeZn_{13}$.

The specific heat of a 1.8 gm sample of $FeZn_{13}$ (12-14) (again the same sample as used for the susceptibility measurements) was measured below 3.5 K and the results are shown in figure 4.2. The fitted line gives

$\gamma = 17.7$ mJ/mole(formula unit).K^2

and $\beta = 3.21$ mJ/mole(formula unit).K^4, giving a Debye temperature $\theta_D = 204$ K.

Specimen (126), weighing 1.4 gms., consisted of the remainder of the ingot from which the resistivity and susceptibility specimens were cut. The results of specific heat measurements below 4.5 K are shown in figure 4.3. The fitted line gives

$\gamma = 17.4$ mJ/mole(formula unit).K^2

and $\beta = 3.22$ mJ/mole(formula unit).K^4, hence the Debye temperature $\theta_D = 204$ K.

$\underline{MnZn_{13}}$

Measurements were made on a 1.24 gms. specimen of $MnZn_{13}$ (13-34) and, although the compound is magnetically ordered with the possibility of a spin-wave contribution to the specific heat, the results have been plotted in the form $\frac{C}{T}$ versus T^2 (figure 4.4). A linear fit to the data below 3.5 K gives

$\gamma = 62.3$ mJ/mole(formula unit).K^2

and $\beta = 3.09$ mJ/mole(formula unit).K^4

The results of all the specific heat measurements for the ζ-phase compounds are summarised in Table 4.1.

ζ-phase	γ ± 5% mJ/mole (formula unit). K^2	θ_D ± 7% (K)
$CoZn_{13}$ (149)	8.1	292 below 3K 230 at 4K
$FeZn_{13}$ (12-14) $FeZn_{13}$ (126)	17.7 17.4	204 K 204 K
$MnZn_{13}$ (13-34)	62.3	206 K

TABLE 4.1

FIG 4.1 THE SPECIFIC HEAT OF ζ-PHASE $CoZn_{13}$ — (14-9)

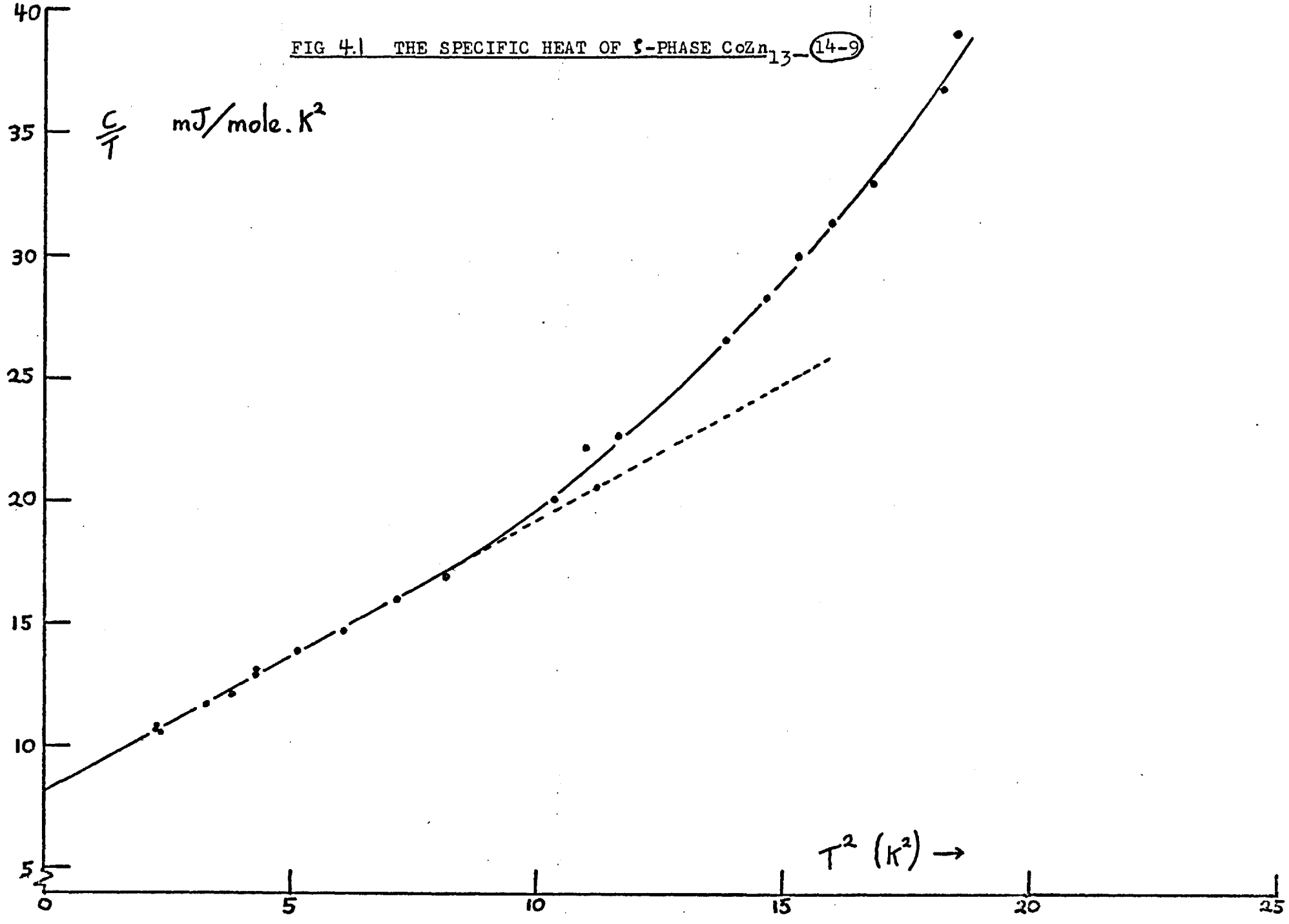


FIG 4.2 THE SPECIFIC HEAT OF ζ-PHASE $FeZn_{13}$ - (12-14)

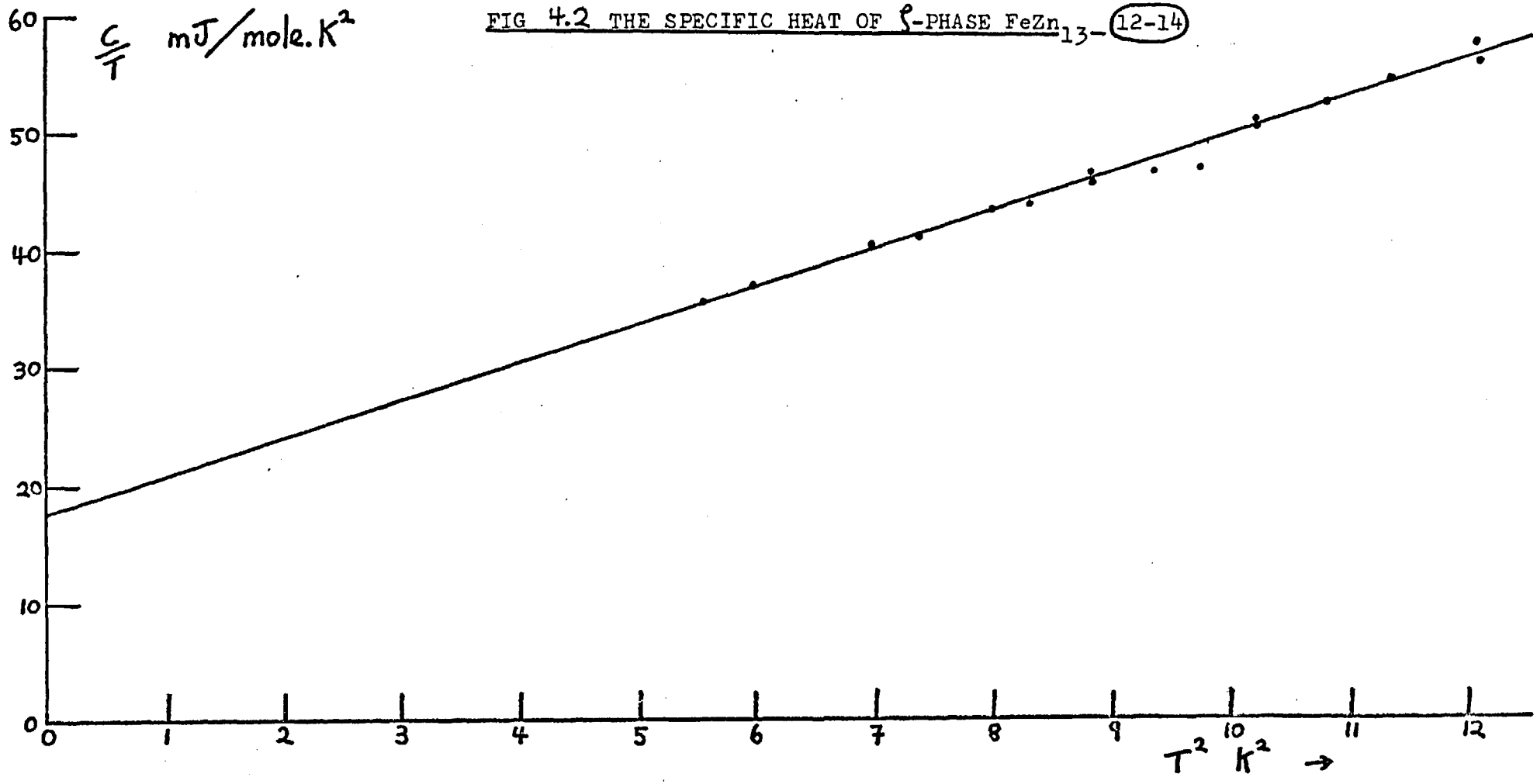
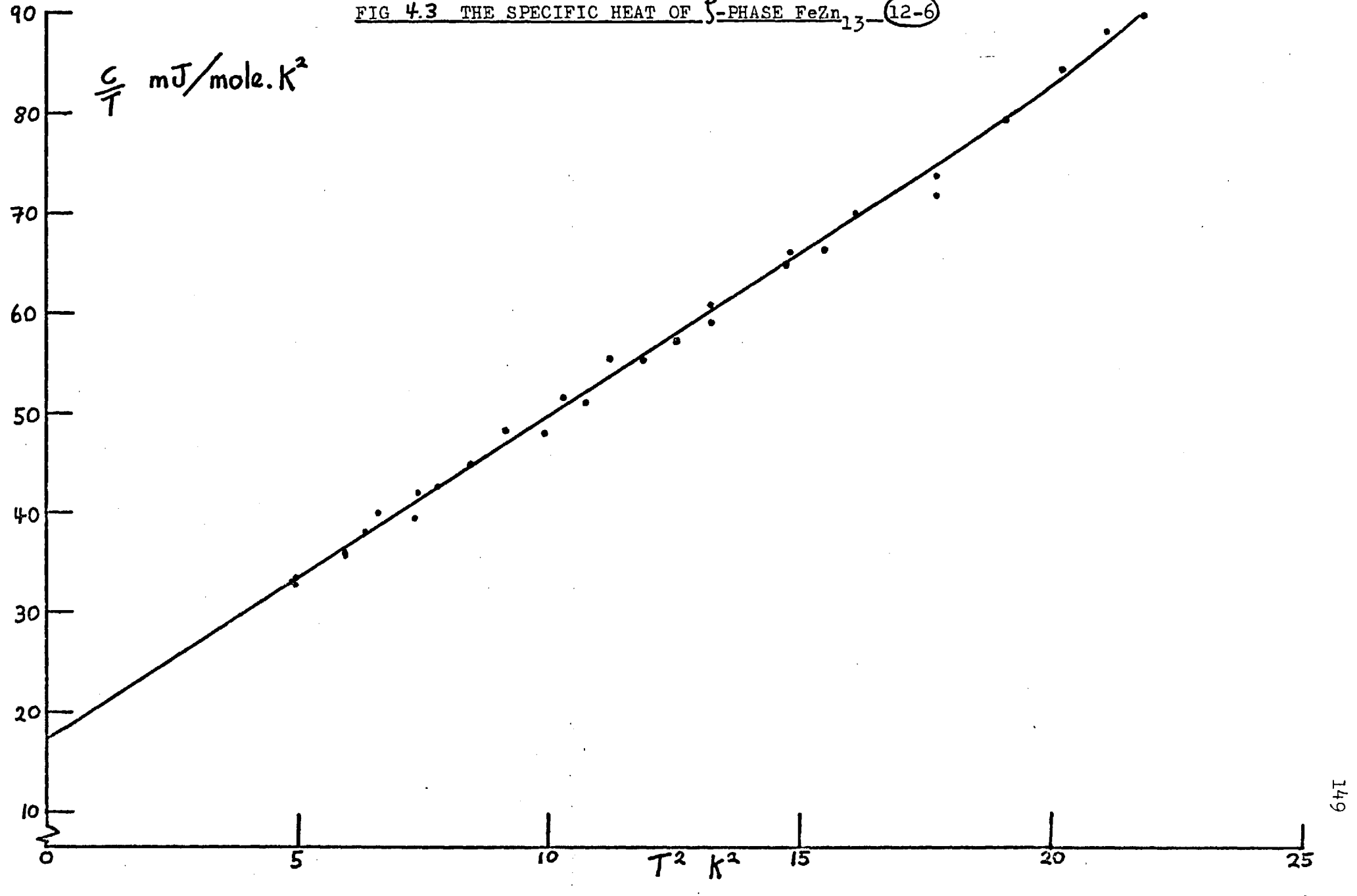


FIG 4.3 THE SPECIFIC HEAT OF ζ-PHASE $FeZn_{13}$ (12-6)



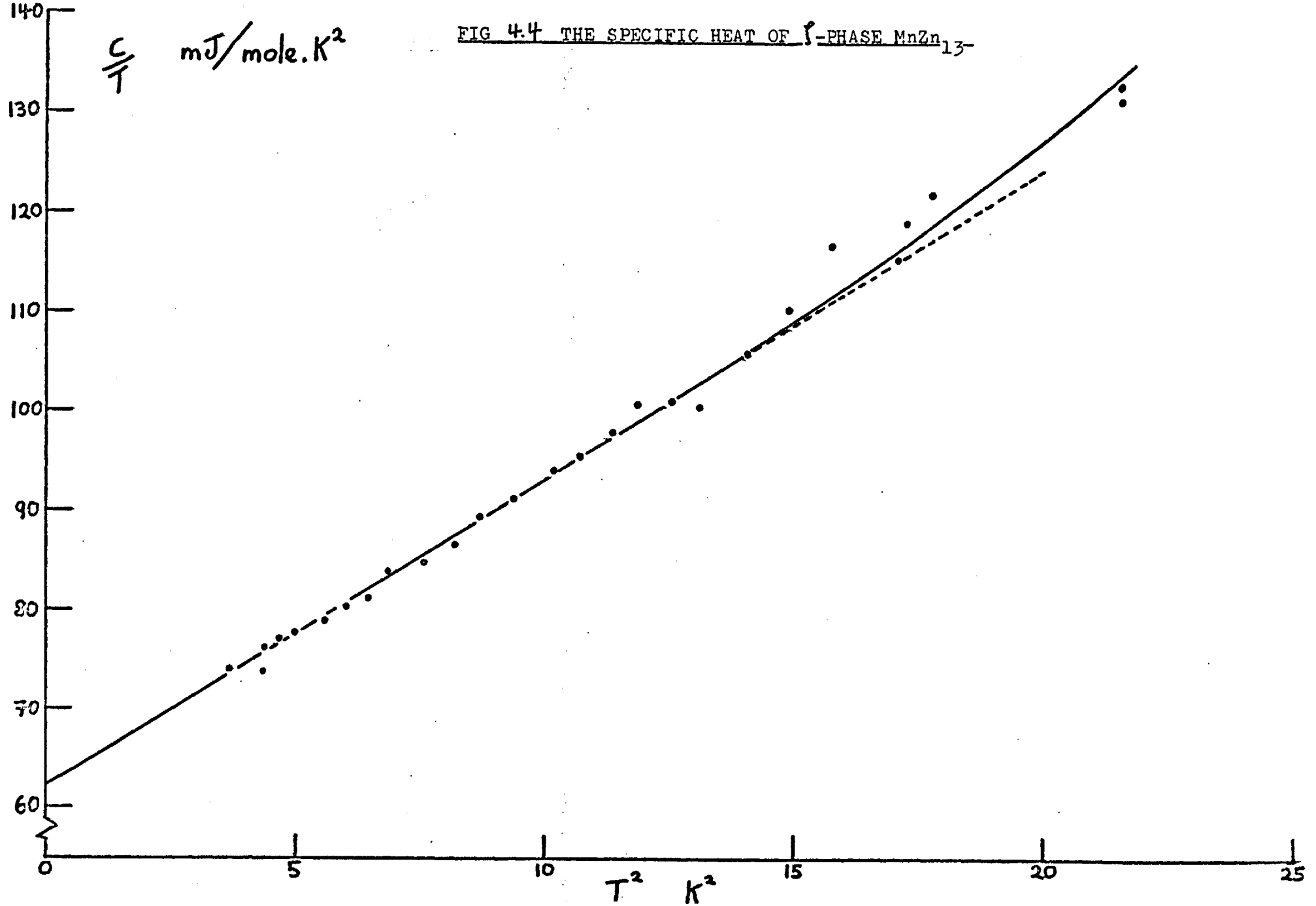


FIG 4.4 THE SPECIFIC HEAT OF ζ-PHASE $MnZn_{13}$

Magnetic Susceptibility

$CoZn_{13}$

The susceptibility of $CoZn_{13}$ (145) was measured in the magnetic balance before the suspension modification had been carried out (see page 111) and the largest specimen mass that could be used was 165 milligrams. At the maximum value of $\frac{H\ dH}{dx}$ the total force on the sample and balance was 1.65 dynes of which only 0.20 dynes was due to the specimen force. The estimated error in the susceptibility of this specimen is $\pm$ 20%.

Figures 4.5 and 4.6 show the specimen magnetization versus field at 1.8 K, 4.2 K, 77 K and 299 K. The zero field intercept in each case is 0.85×10^{-4} e.m.u./gm and is probably due to small particles of a ferromagnetic contaminant whose magnetization is saturating at field below 1 or 2 K. Gauss. It would only require 0.5 micro-grams of undissolved cobalt per gram of $CoZn_{13}$ to produce this magnetization!

The susceptibilities calculated from the high field slope of the magnetization versus field plot are shown in Table 4.2

Temperature K	$\chi \times 10^6$ e.m.u./gram
299	-0.15
77	-0.10
4.2	-0.09
1.8	-0.11

TABLE 4.2

$CoZn_{13}$ (149) was measured after the balance suspension modification and the specimen mass used was 2.44 grams, an increase by a factor of 15.

Magnetization versus field measurements are shown in figures 4.7 and 4.8. The susceptibilities calculated from the high field slope of the M versus H curve, and the extrapolated zero field magnetization M_o are tabulated below.

Temperature	Susceptibility $\chi \times 10^6$ e.m.u./gram	M_o e.m.u./gram
300	-0.164	1.5×10^{-4}
77	-0.140	1.6×10^{-4}
4.2	-0.116	1.8×10^{-4}
1.7	-0.112	1.8×10^{-4}

TABLE 4.3

Again the extrapolated zero field magnetization could be accounted for by 1 micro-gram of undissolved cobalt.

Measurements of susceptibility were taken at intermediate temperatures and these showed a monotonic decrease between 300 K and 1.7 K. They have been included in figure 4.20, which compares the susceptibilities of all three γ-phases, but have not been plotted separately.

$FeZn_{13}$

Measurements were taken on a 164 milli-gram of $FeZn_{13}$ (126) using the old quartz bucket method of specimen attachment and the force on the specimen was approximately a

half of that on the "empty balance". The estimated error in the susceptibilities is ± 10%.

Magnetization versus field measurements at 299 K, and 77 K and 4.2 K are shown in figure 4.9. The extrapolated zero field magnetization, M_o, is 6.4×10^{-4} e.m.u./gram and this would correspond to 3 micro-grams of particulate undissolved Fe per gram of $FeZn_{13}$.

Susceptibilities at the three fixed points calculated from the high field slope of the magnetization versus field curve are shown below.

Temperature K	$\chi \times 10^6$ e.m.u./gram
299	0.27
77	0.32
4.2	0.63

TABLE 4.4

Susceptibilities, corrected for M_o, are shown as a function of temperature in figure 4.10. Between 170 K and 300 K the susceptibility is temperature independent, while at lower temperatures an upturn is observed. Over a limited temperature range this may be fitted to a Curie-Weiss law as is shown in figure 4.11 where the fit is between 1.8 K and 10 K. It can be seen that the χ_o of the Curie-Weiss fit, $\chi_o = 0.35 \times 10^{-6}$ e.m.u./gram, is larger than the observed temperature independent

susceptibility between 170 K and 300 K. The susceptibility cannot be fitted to a Curie-Weiss law with constant values of the parameters θ and χ_o over a wider temperature range. If this low temperature Curie-Weiss behaviour is attributed to a small moment on each Fe atom then p_{eff} per Fe atom = $\underline{0.14\ u_B}$.

Magnetization versus field curves for $FeZn_{13}$ (12-14) are shown in figure 4.12. The extrapolated zero field magnetizations, M_o, are much larger for this specimen and would correspond to approximately 20 micro-grams of undissolved Fe per gram of specimen. However, the resistance ratio was still greater that 30 indicating that the bulk of the specimen was crystallographically well ordered. The susceptibilities calculated from the high field slopes of the magnetization versus field curves are shown in table 4.5.

Temperature K	$\chi \times 10^6 \pm 5\%$ e.m.u./gm.	$M_o \times 10^3$ e.m.u.
300	0.31	3.0
77	0.32	3.7
4.2	0.59	4.2

TABLE 4.5

The susceptibilities of specimens number (126) and (12-14) agree to within the accuracy of measurement at the fixed temperatures, however no attempt has been made to fit the susceptibility of (12-14) to a Curie-Weiss law at intermediate

temperatures because of the large temperature variation of the zero field magnetization.

Measurements were taken on a third specimen of $FeZn_{13}$ 12-16 and the susceptibilities were considerably different to the previous specimens:- 1.06×10^{-6} e.m.u./gm. at 4.2 K and 0.58×10^{-6} e.m.u./gm. at 300 K. A resistance ratio check on this specimen gave the low value of 7 with a resistivity at 4.2 K of 6 $\mu\Omega$cm. If this high residual resistivity is attributed to Fe atoms accupying wrong sites in the structure and such atoms produce the same impurity resistivity contribution as found in dilute Zn-Fe alloys ($\sim$15 $\mu\Omega$/at.% (71)) then it required the order of a 0.3 at.% occupation of incorrect sites. In addition such Fe atoms, because of the form of the crystal structure, would have as a nearest neighbour an Fe atom on its correct site with a resulting modification of the magnetic character. A considerable variation of the properties of dilute Zn-Fe alloys depending on the sample treatment has been observed (77) and this would appear to be mirrored in the ζ-phase $FeZn_{13}$.

$MnZn_{13}$

The high temperature (above 77 K) susceptibility of $MnZn_{13}$ (135) was measured using the magnetic balance. Magnetization versus field plots at 300 K and 77 K are shown in figures 4.13 and 4.14, in neither case is there a zero field intercept. The susceptibility was measured a a function of temperature and fitted to a Curie-Weiss law (figure 4.15). This can only be done successfully using the data points above 120 K. Attempting to include the points below 120 K leads to a deterioration in the

quality of the fit - in fact it produces an S-shaped curve. The best fit to the data above 120 K is

$$\chi = \left(0.53 + \frac{461}{T-36.5}\right) \times 10^{-6} \text{ e.m.u./gm.}$$

This corresponds to an effective moment on each Mn atom of

$$p_{eff} = 1.82 \pm 0.05 \ \mu_B$$

Figure 4.16 shows the magnetization in a field of 7 K. Gauss plotted versus temperature - the data below 77 K was taken using the vibration magnetometer and above 77 K using the balance. The form of the curve indicates that the specimen undergoes a magnetic ordering transition but does not fix the ordering temperature itself.

Figure 4.17 shows a magnetization versus field curve at 4.2 K, below the ordering temperature. Although the magnetization is not completely saturated at the highest available field, taking it to be 2 e.m.u./gm. the corresponding ordered moment per manganese atom is

$$n_{eff} = 0.3 \ \mu_B$$

To determine the magnetic ordering temperature, magnetization versus field measurements were taken at fixed temperatures (manually controlled to $\pm$ 0.2 K) between 4.2 K and 30 K and, following a similar proceedure to that of Arrott (107), plotted in the form $\frac{H}{M}$ versus M^2 (see figure 4.18). This indicates a magnetic ordering temperature of 22.9 $\pm$ 0.3 K.

$Mn_{0.05}Fe_{0.95}Zn_{13}$

The susceptibility of this specimen was measured in the magnetic balance between 4.2 K and 77 K. A Curie law is obeyed down to 20 K and figure 4.19 shows χ versus $\frac{1}{T}$. The fitted value of the Curie constant corresponds to a magnetic moment per Mn atom of $p_{eff} = 4.0\ \mu_B$

The magnetic susceptibilities of all three J-phases are compared in figure 4.20.

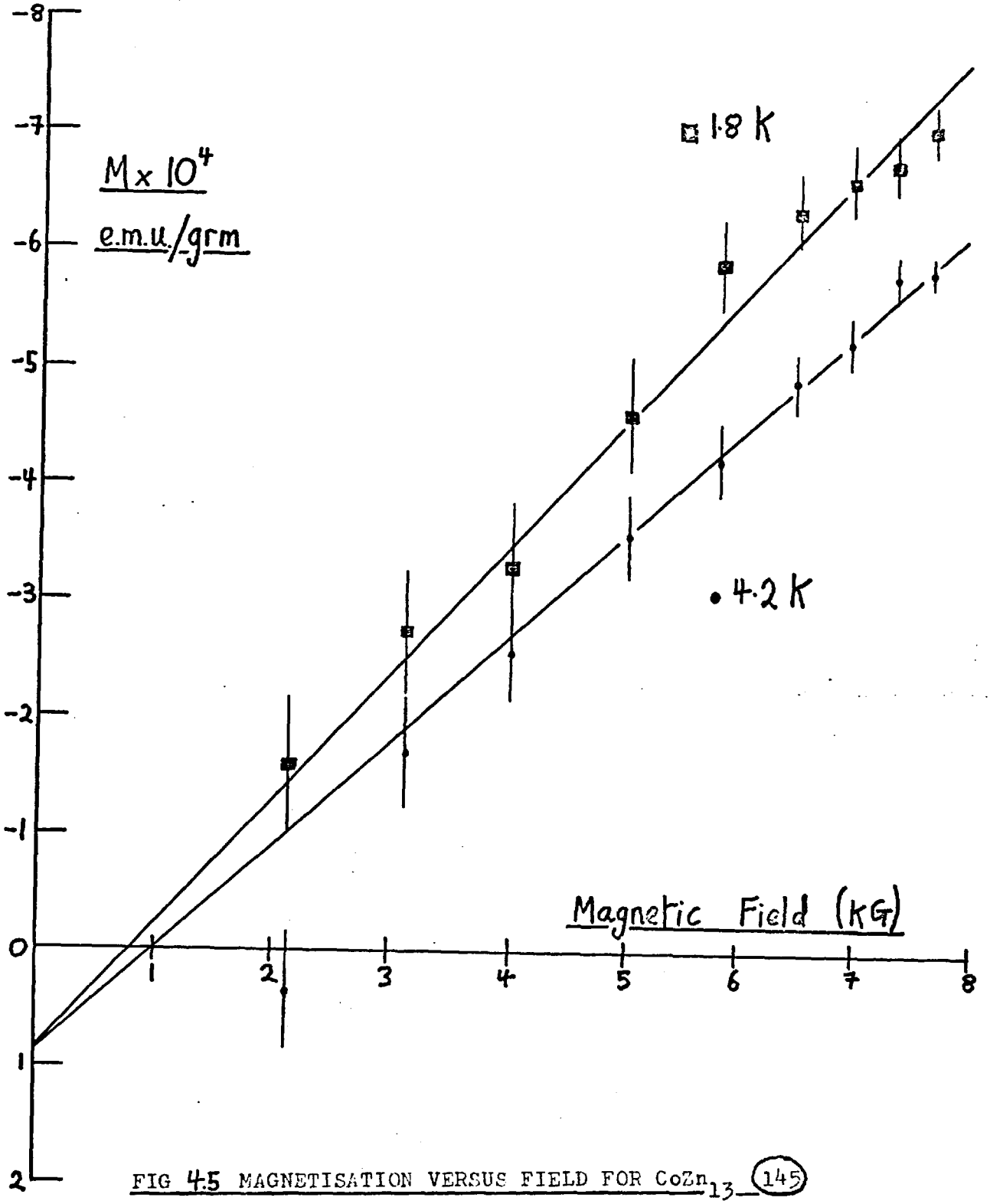


FIG 4.5 MAGNETISATION VERSUS FIELD FOR $CoZn_{13}$ (145)

AT 4.2 K AND 1.8 K

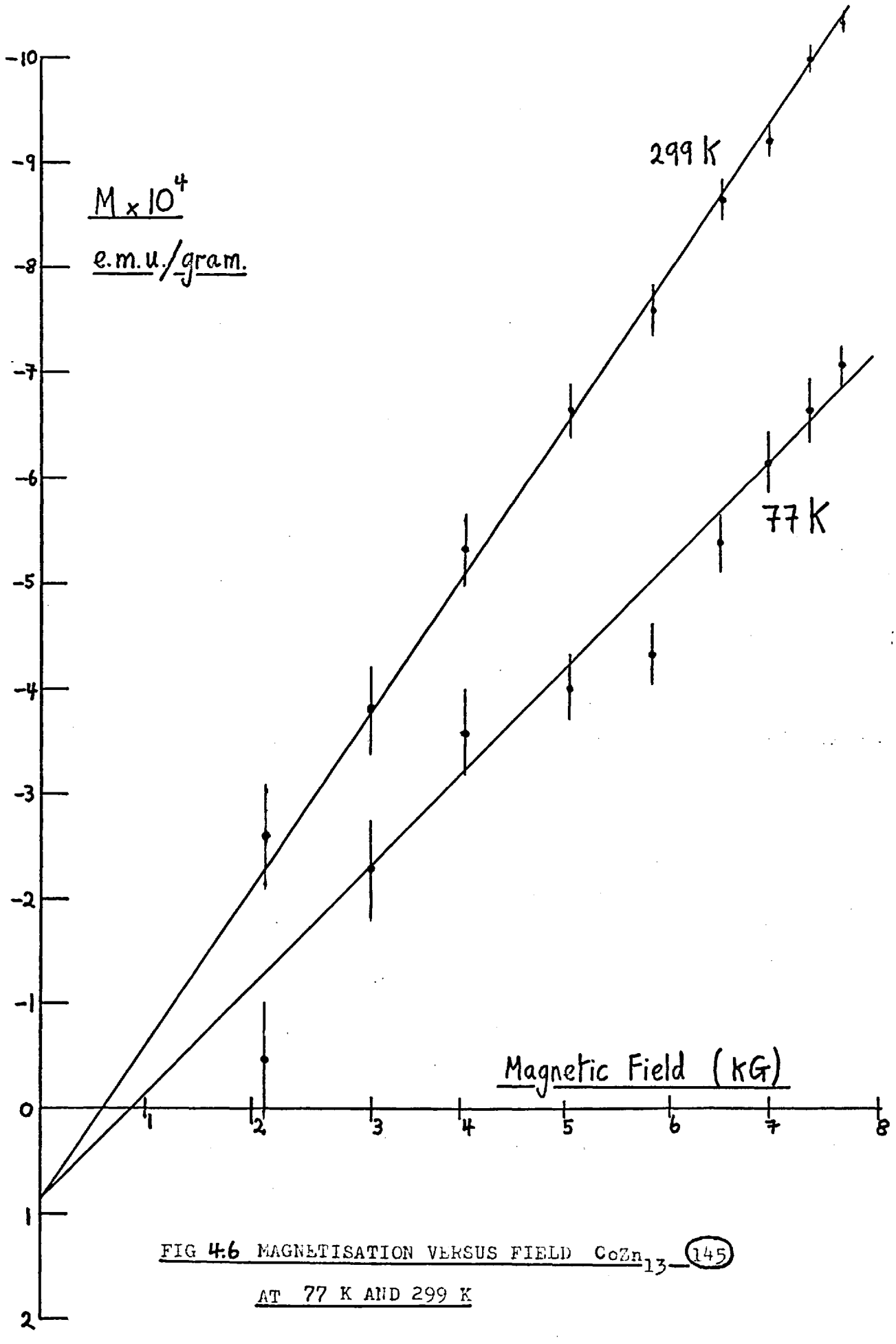


FIG 4.6 MAGNETISATION VERSUS FIELD $CoZn_{13}$ (145)

AT 77 K AND 299 K

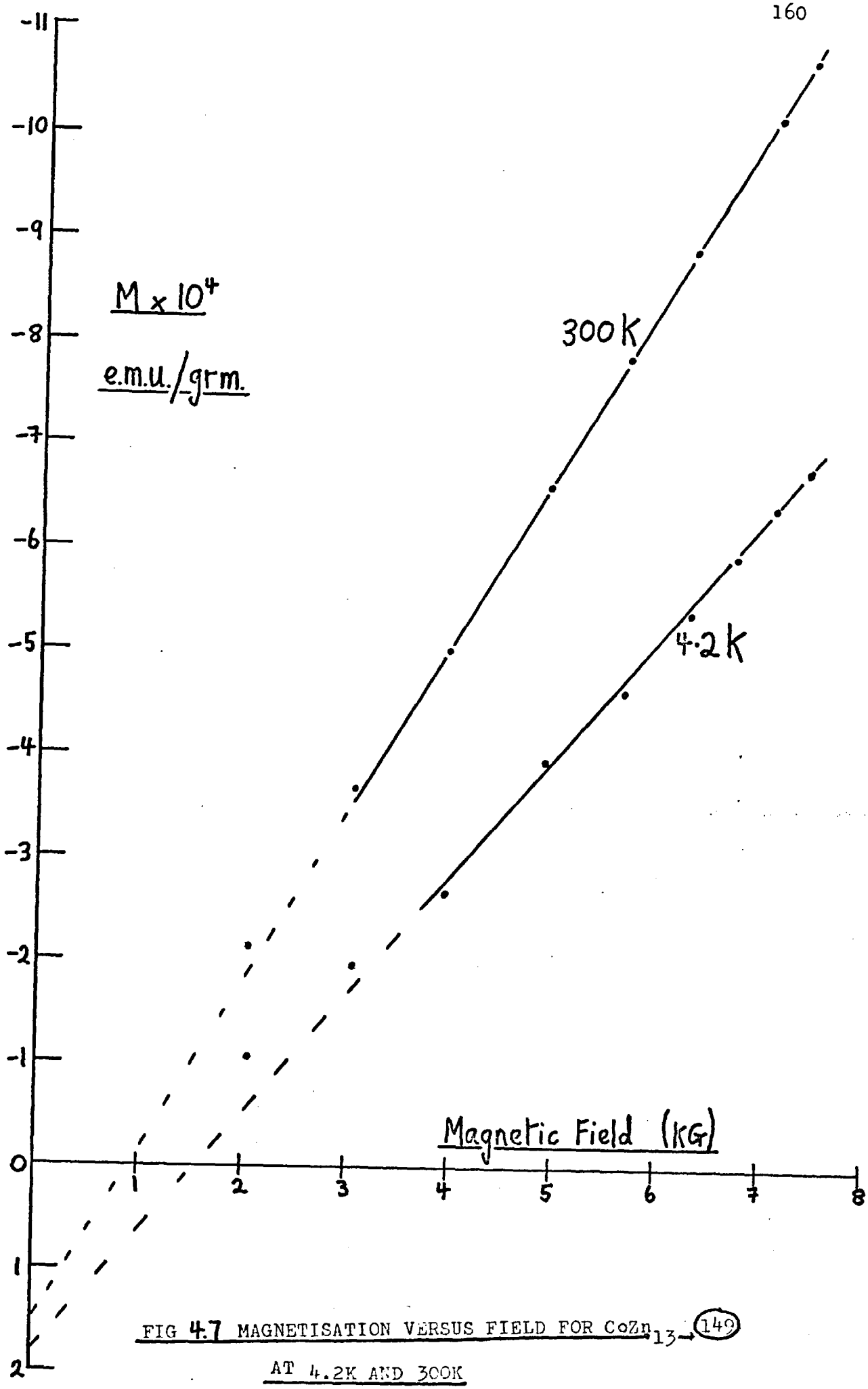


FIG 4.7 MAGNETISATION VERSUS FIELD FOR $CoZn_{13}$ → (149)

AT 4.2K AND 300K

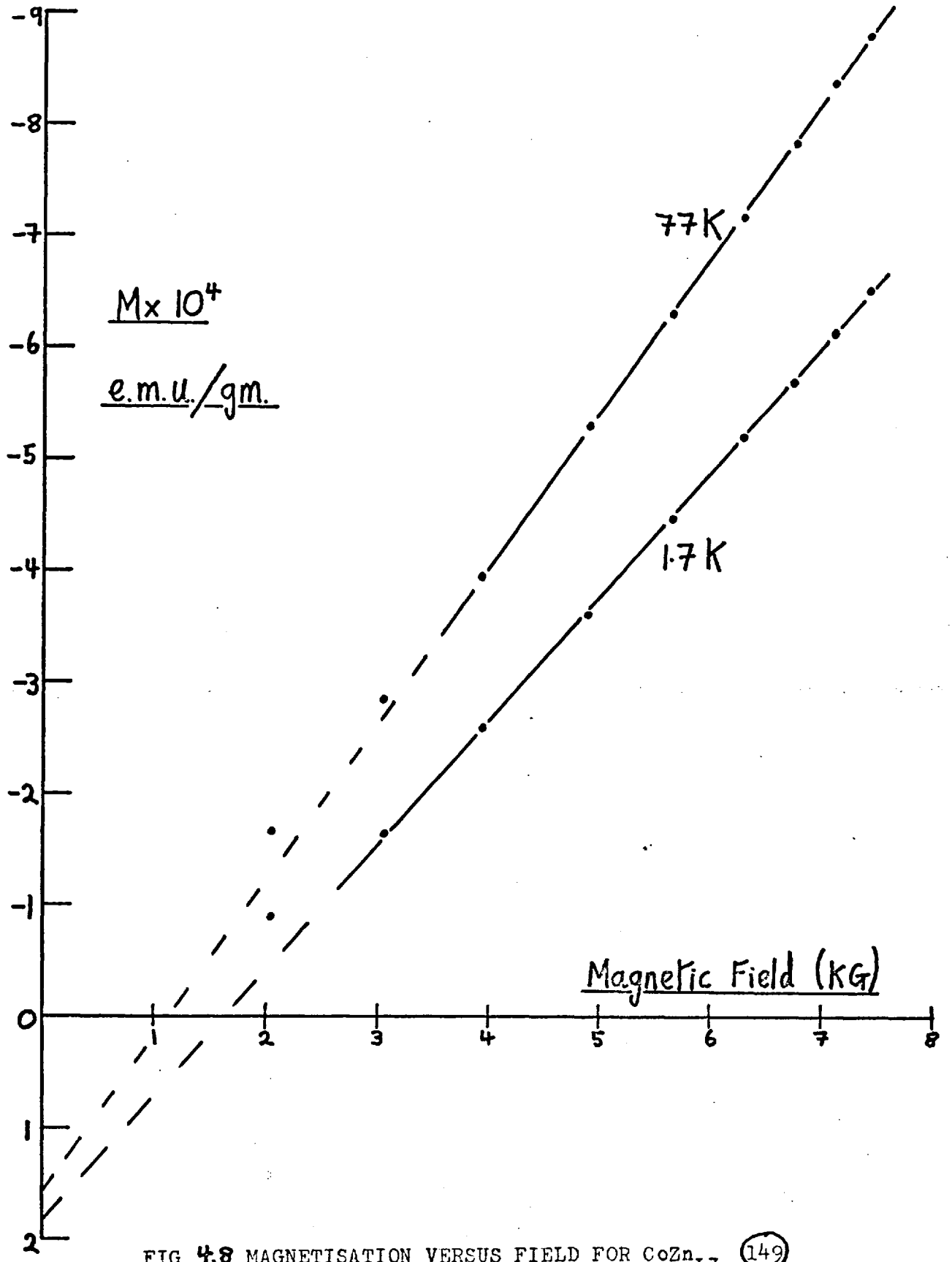
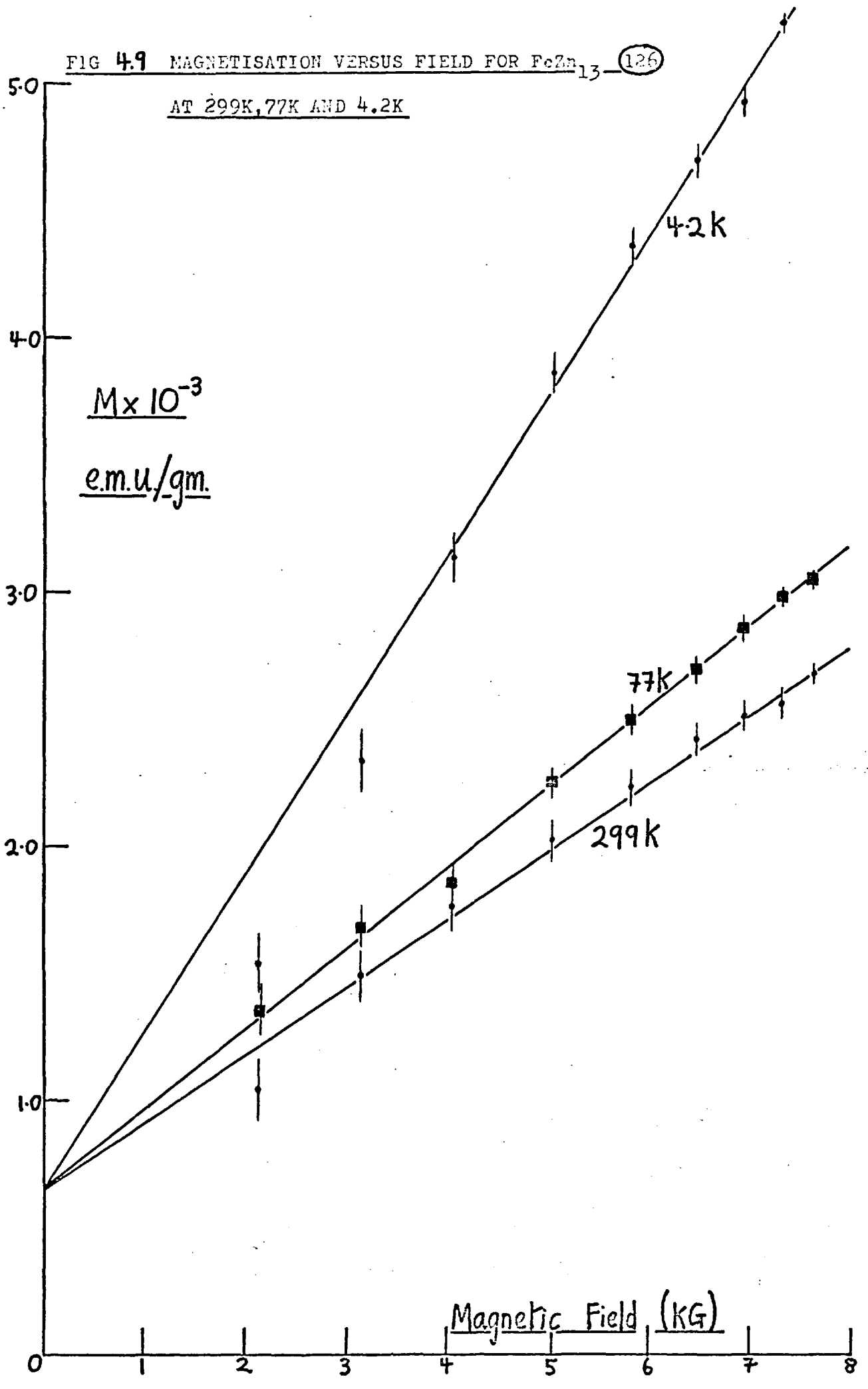


FIG 4.8 MAGNETISATION VERSUS FIELD FOR $CoZn_{13}$ (149)

AT 1.7K AND 77K

FIG 4.9 MAGNETISATION VERSUS FIELD FOR $FeZn_{13}$ (126)

AT 299K, 77K AND 4.2K



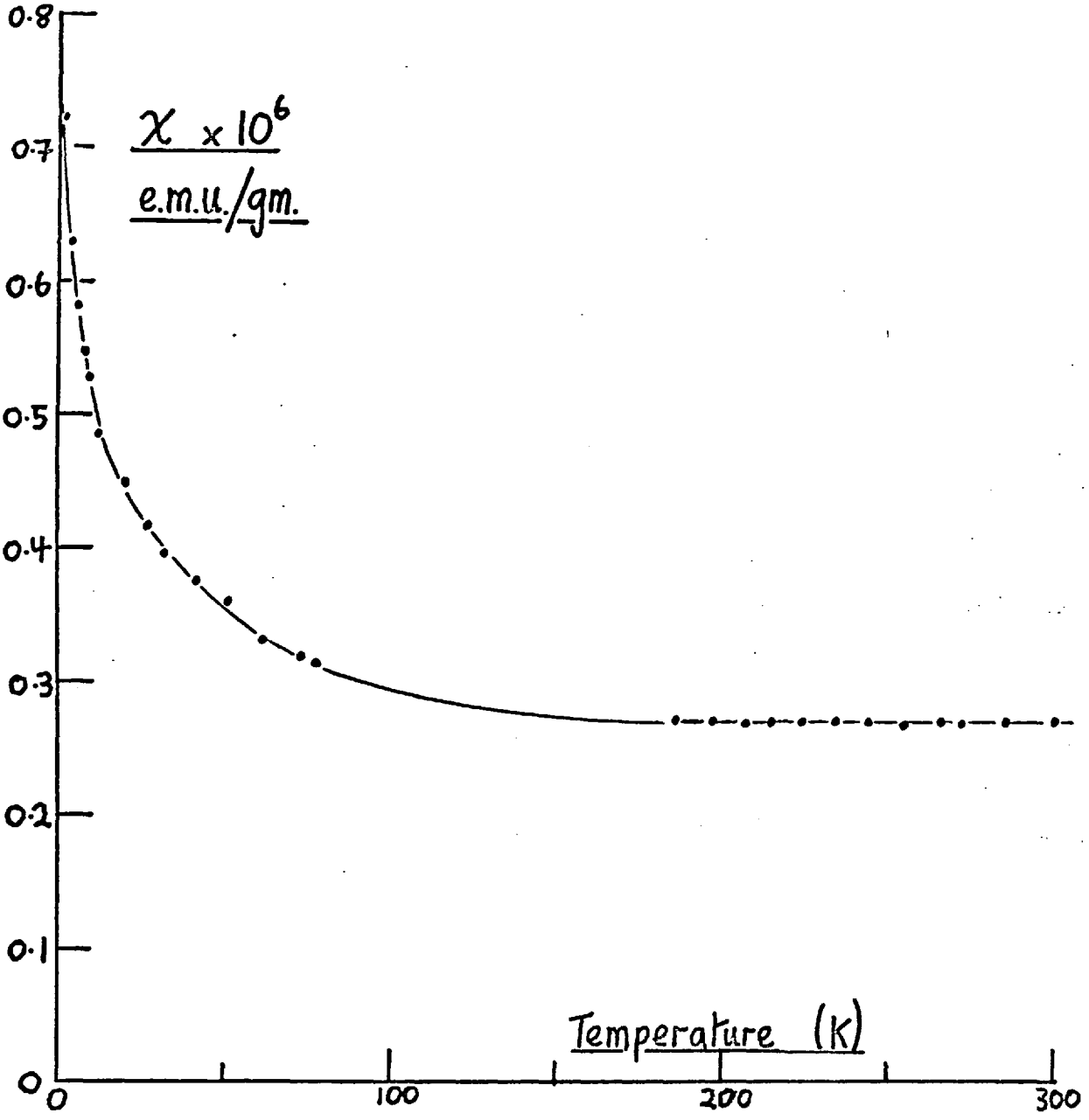
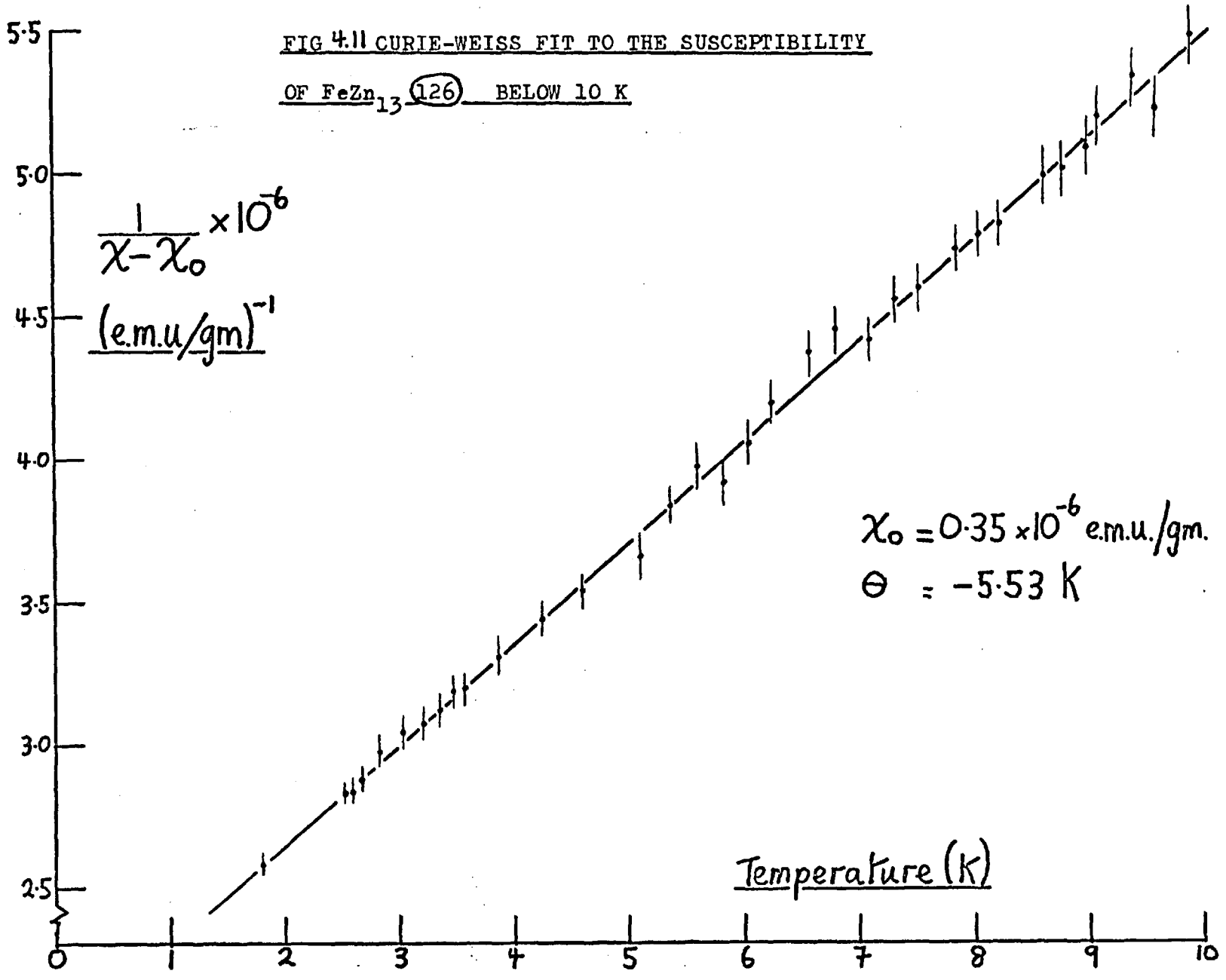


FIG 4.10 MAGNETIC SUSCEPTIBILITY OF $FeZn_{13}$ (126)

FIG 4.11 CURIE-WEISS FIT TO THE SUSCEPTIBILITY OF $FeZn_{13}$ (126) BELOW 10 K



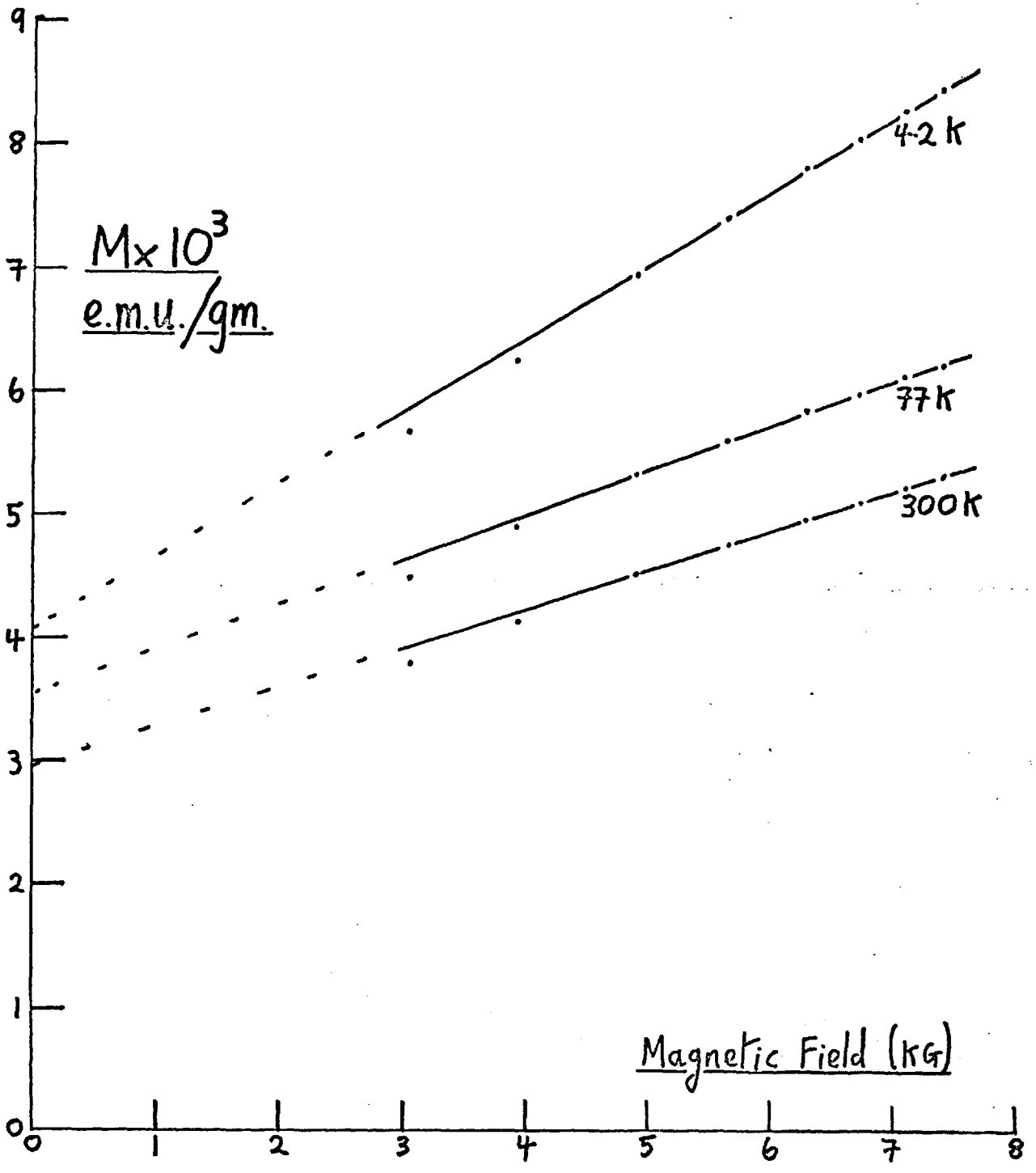


FIG 4.12 MAGNETISATION VERSUS FIELD FOR $FeZn_{13}$ (12-14)

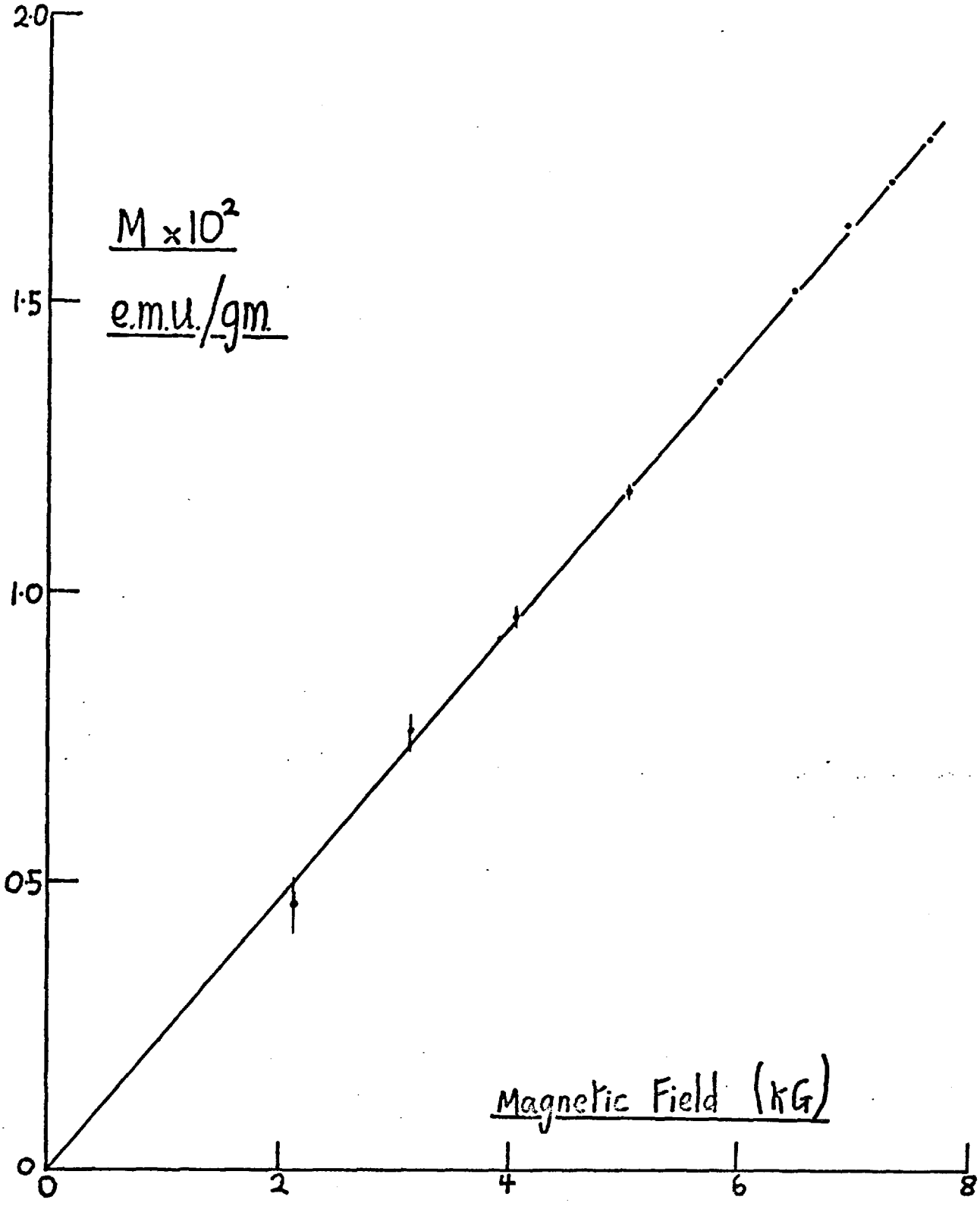


FIG 4.13 MAGNETISATION VERSUS FIELD FOR $MnZn_{13}$ (135) AT 300K

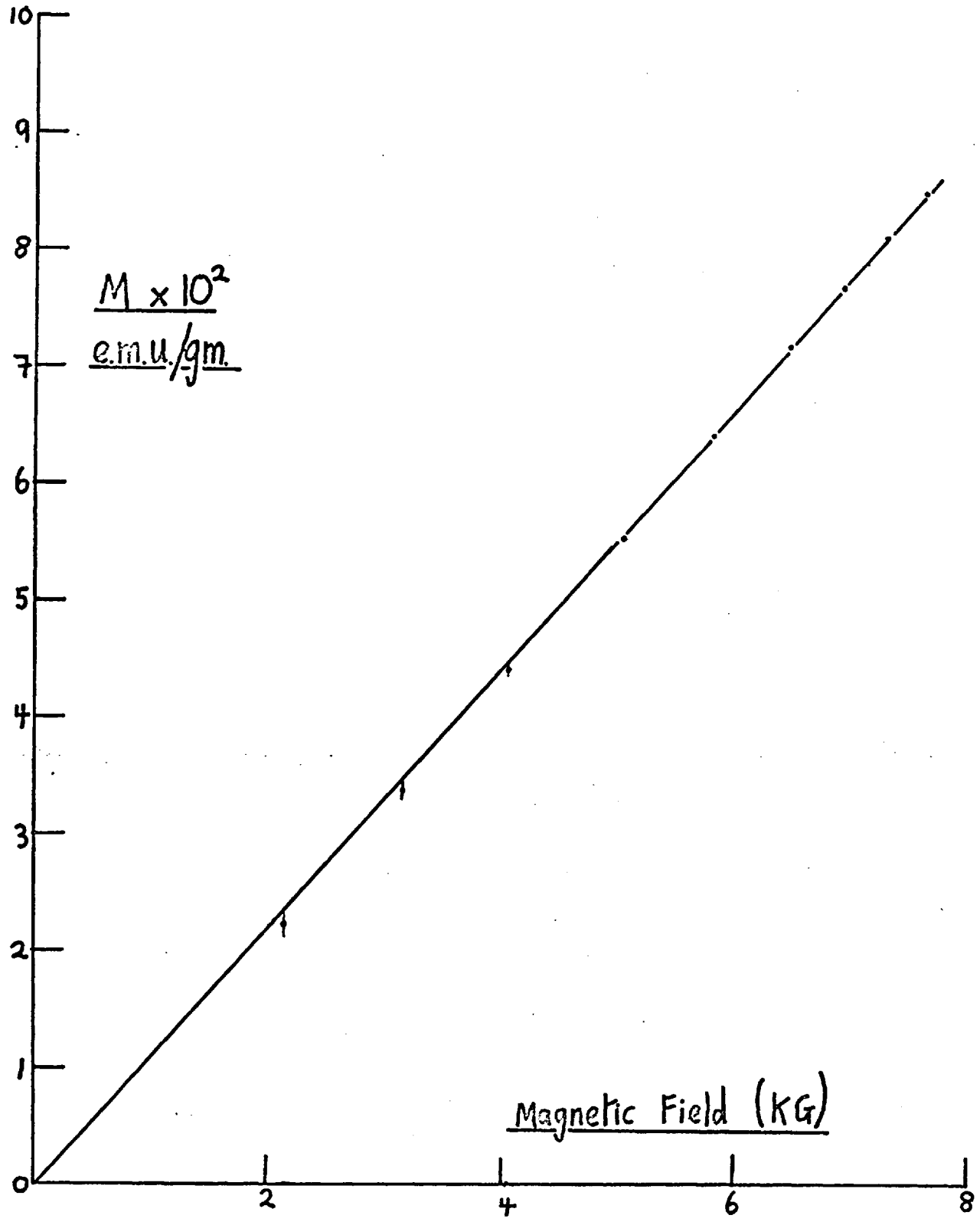
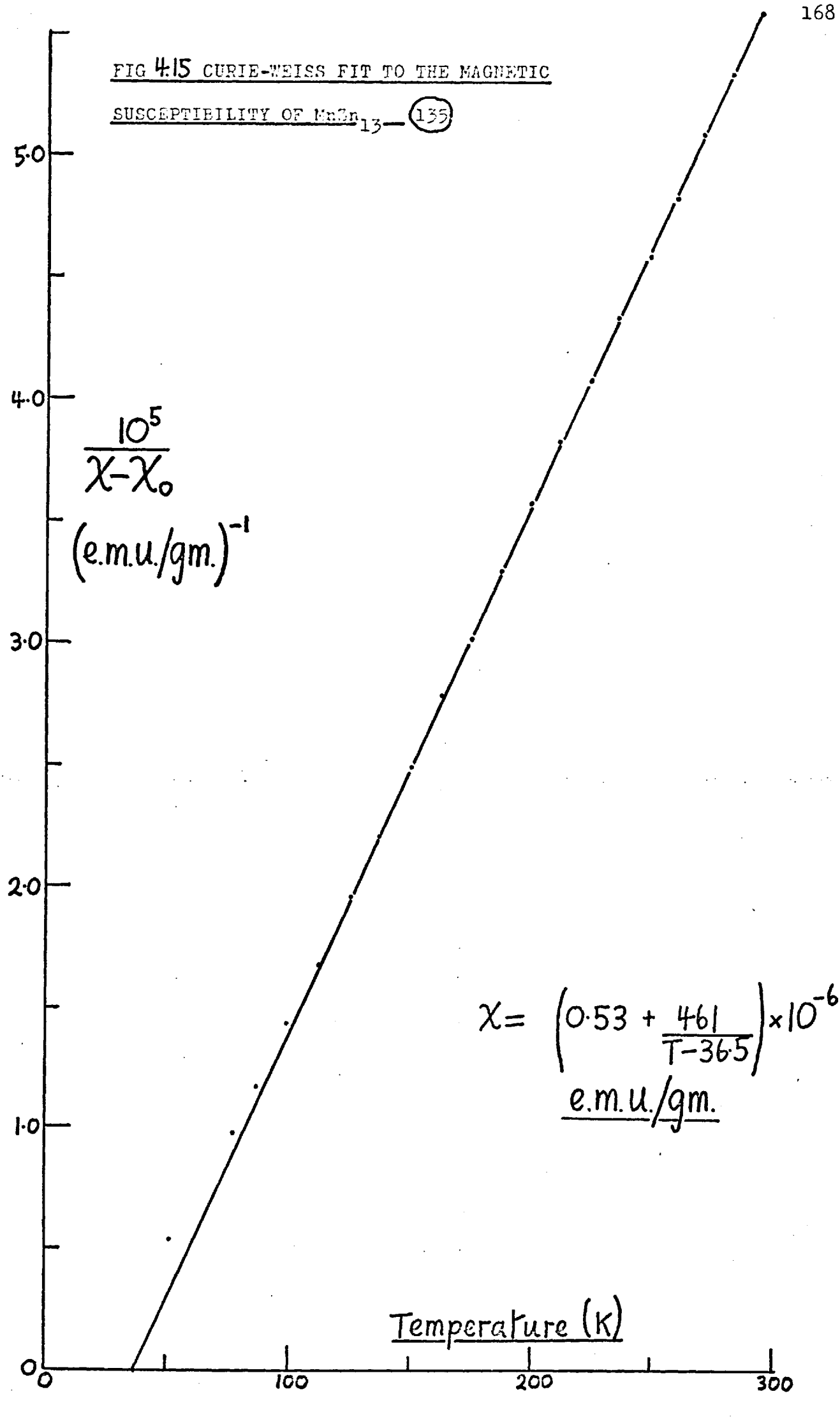


FIG 4.14 MAGNETISATION VERSUS FIELD FOR $MnZn_{13}$ (135) AT 77K

FIG 4.15 CURIE-WEISS FIT TO THE MAGNETIC SUSCEPTIBILITY OF $MnZn_{13}$ — (135)



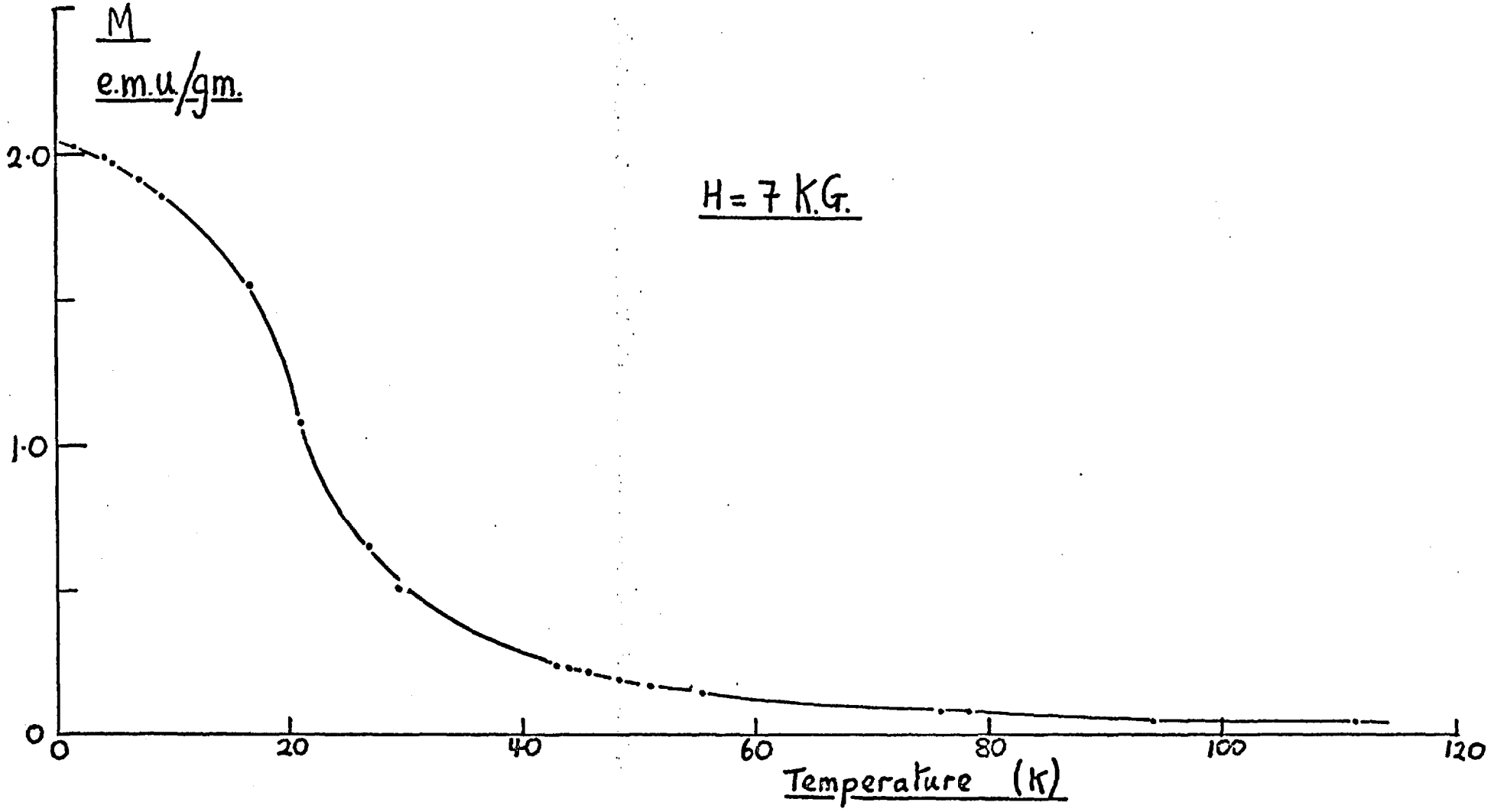


FIGURE 4.16 MAGNETISATION IN A FIELD OF 7 KG. VERSUS TEMPERATURE FOR $MnZn_{13}$ (135)

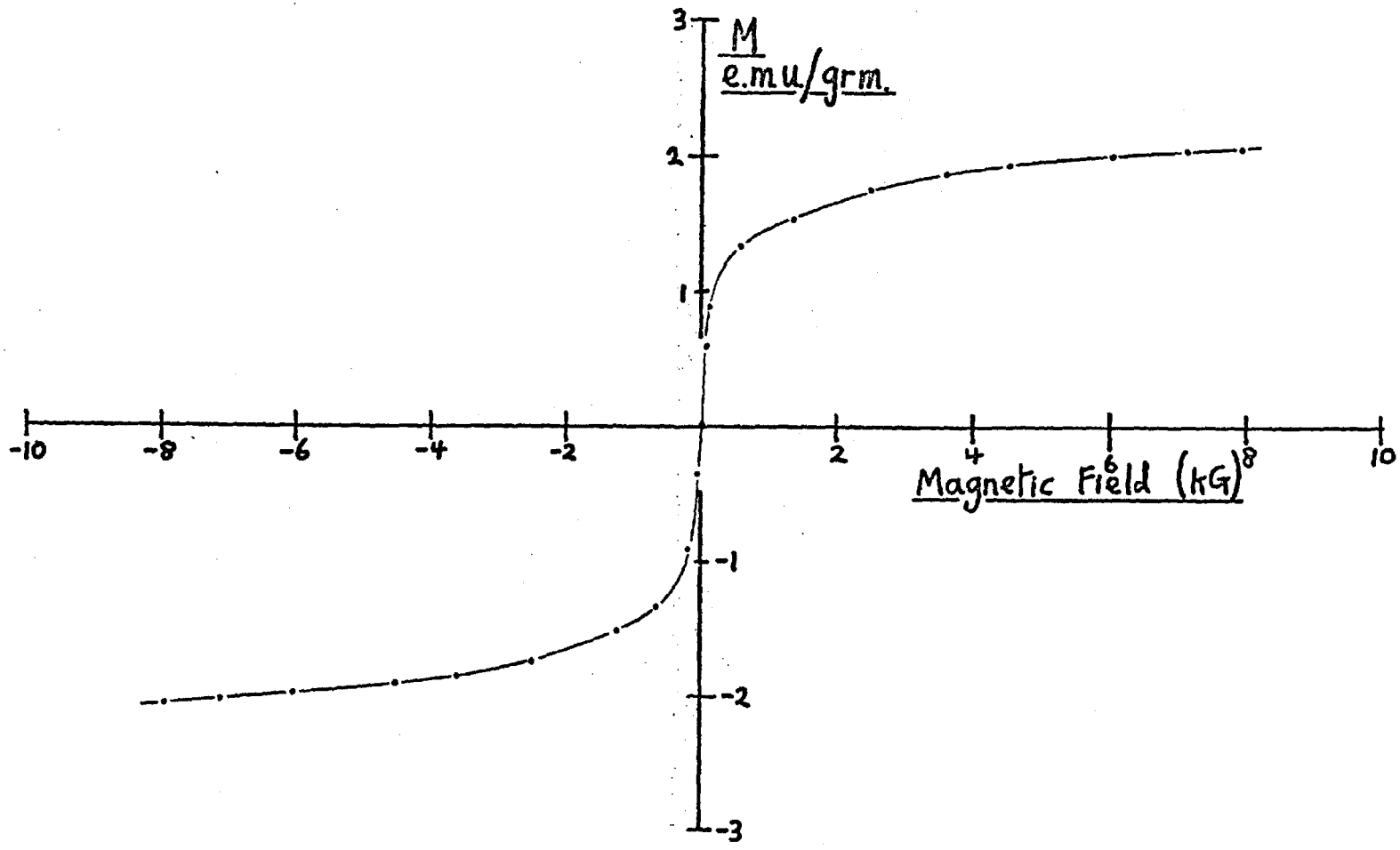


FIG 4.17 MAGNETISATION CURVE FOR $MnZn_{13}$ (135) AT 4.2K

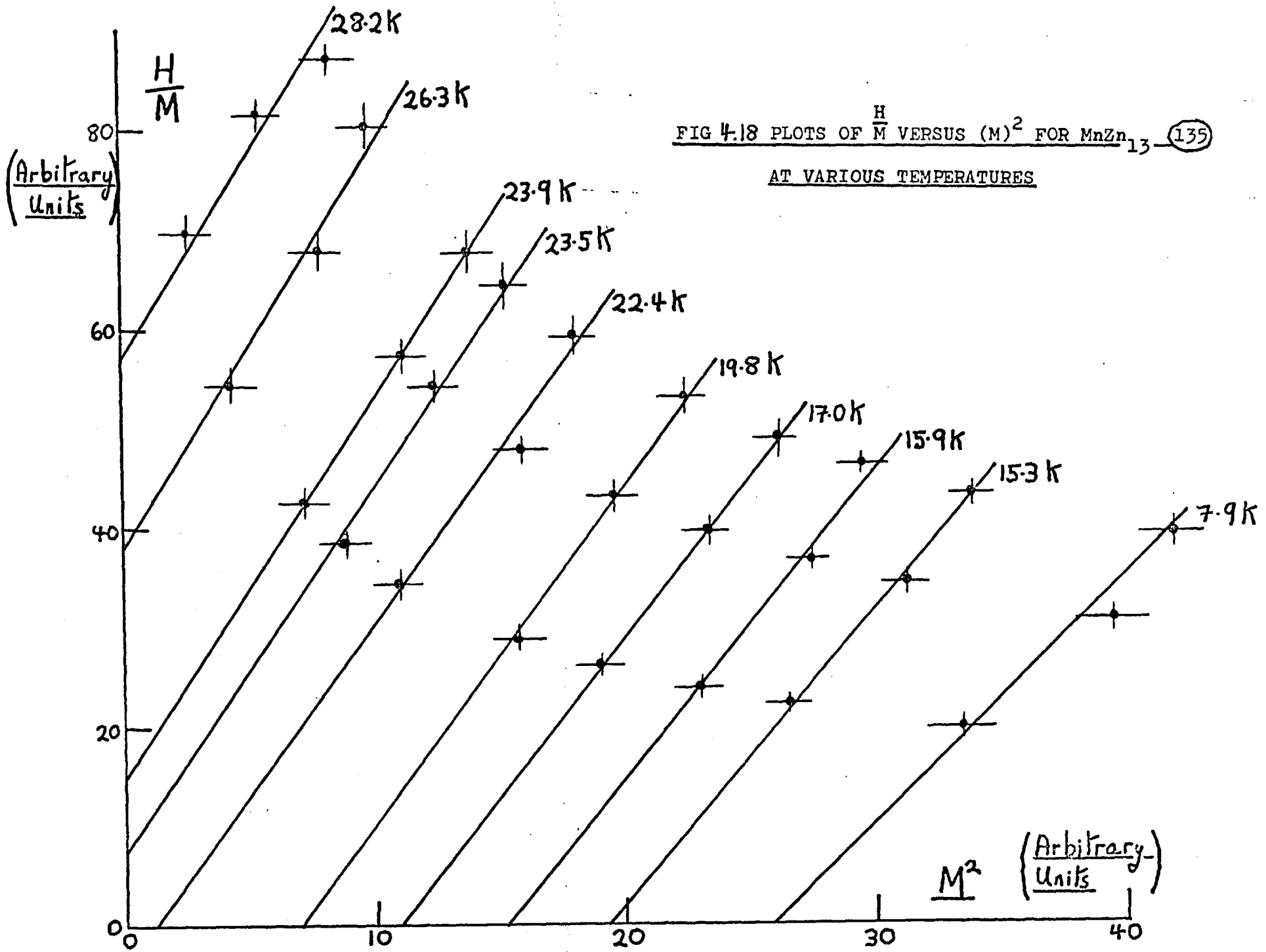
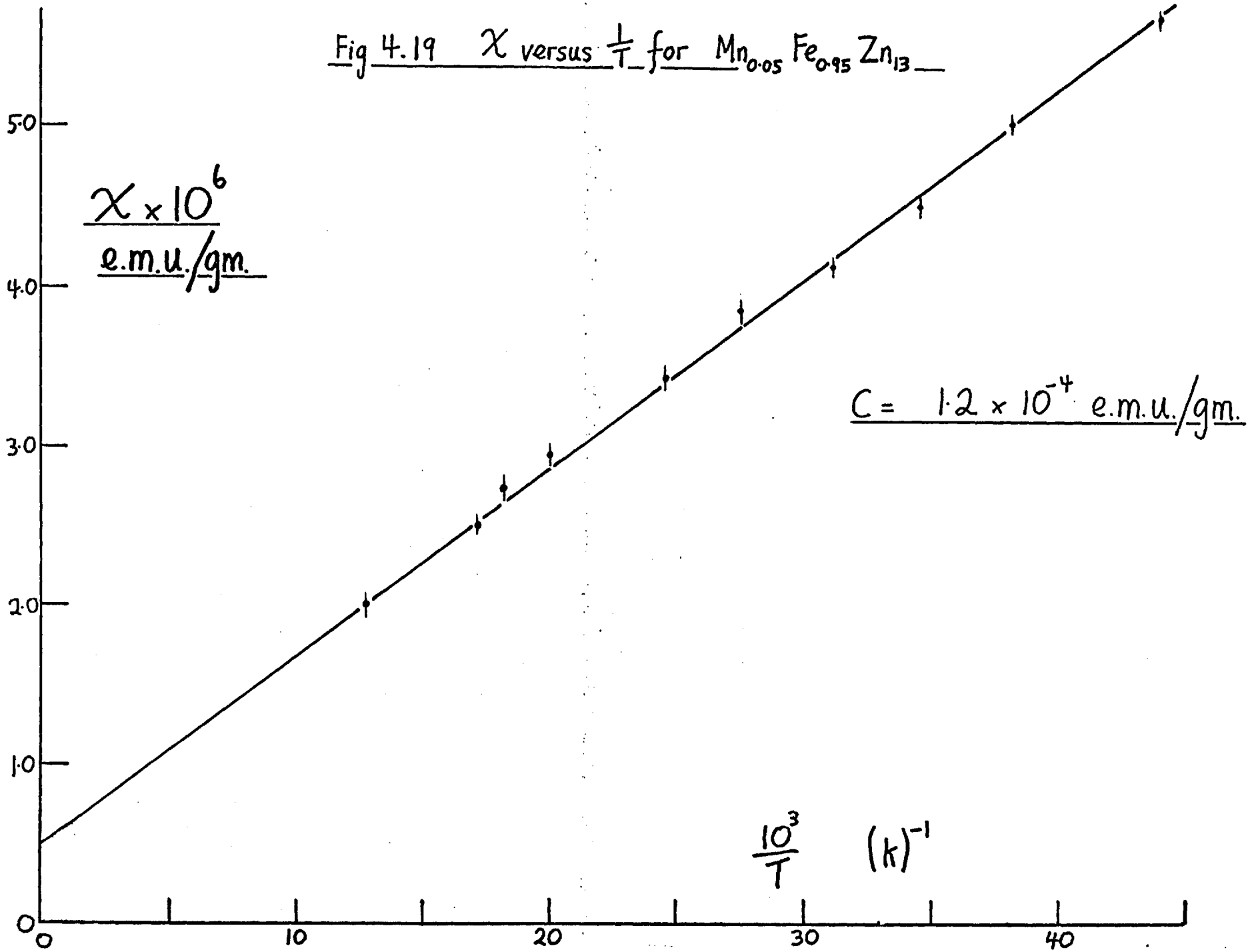


FIG 4.18 PLOTS OF $\frac{H}{M}$ VERSUS $(M)^2$ FOR $MnZn_{13}$ (135)

AT VARIOUS TEMPERATURES

Fig 4.19 χ versus $\frac{1}{T}$ for $Mn_{0.05}Fe_{0.95}Zn_{13}$



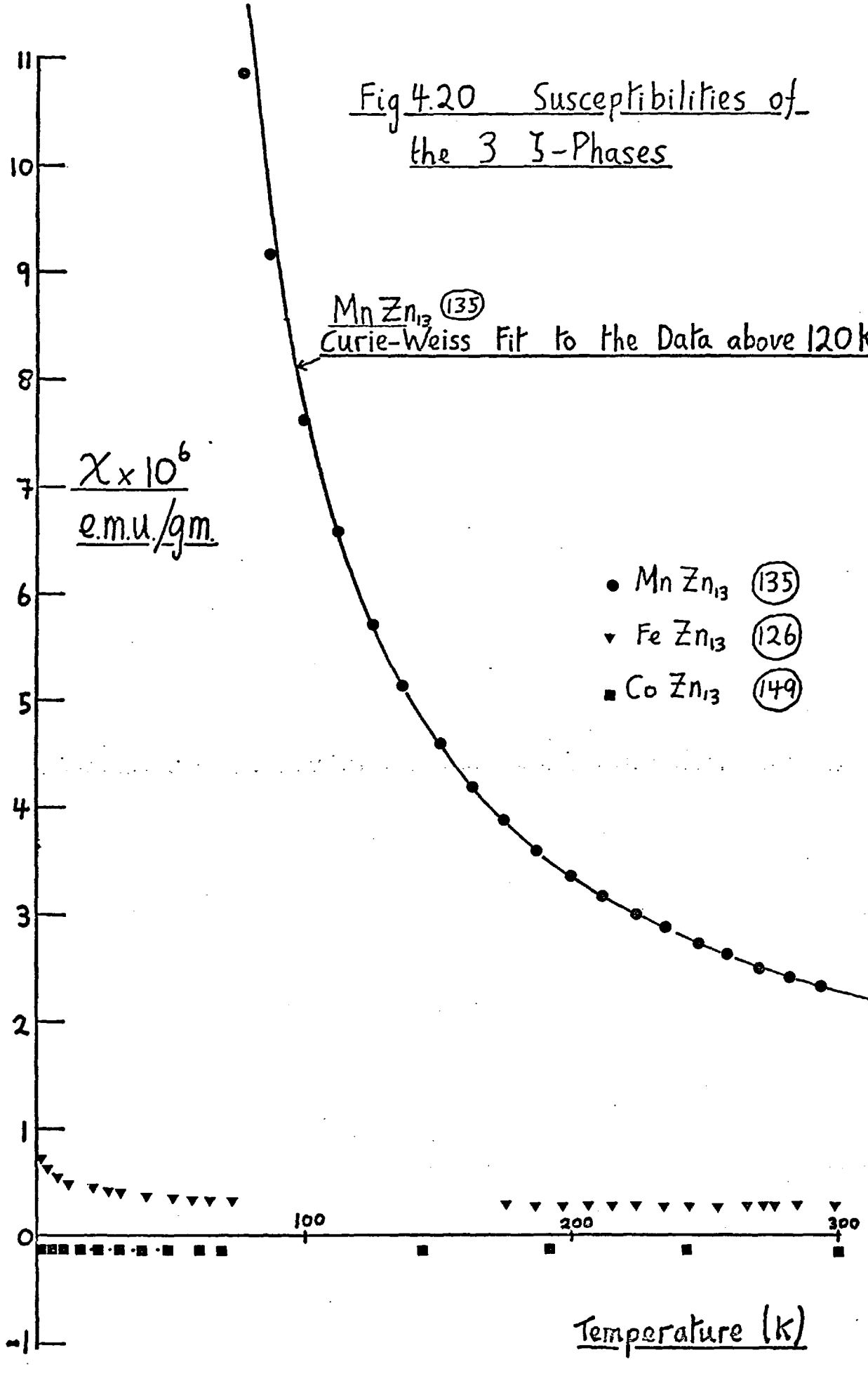


Fig 4.20 Susceptibilities of the 3 Σ-Phases

Electrical Resistivity

$CoZn_{13}$

Measurements were made on two separate samples.

$CoZn_{13}$ (145) had an ice point resistivity of $\rho_{273} = 20.4\ \mu\Omega$cm. and a residual resistivity of $\rho_o = 2.9\ \mu\Omega$cm. Figure 4.21 shows the temperature dependent part of the resistivity, $\rho_T - \rho_o$, plotted versus T on log-log scales. Below about 8 K the resistivity, $\rho_T - \rho_o$, appears to be proportional to T^4, although a T^5 or even T^3 dependence would not be inconsistent with the accuracy of measurement in this temperature region.

$CoZn_{13}$ (149) had a room temperature resistivity of 20.6 $\mu\Omega$cm. and a residual resistivity of $\rho_o = 2.7$ uΩcm. Figure 4.22 shows the temperature dependent part of the resistivity plotted versus T on a log-log scale. Again a low temperature dependence of approximately T^4 is observed.

$FeZn_{13}$

One specimen was measured, number (126), although we also present the previously unpublished data of A. D. Caplin on his specimen of $FeZn_{13}$ number (124).

The temperature dependent part of the resistivity, $\rho_T - \rho_o$, of $FeZn_{13}$ number (124) is shown in figure 4.23 $\rho_T - \rho_o$ is plotted versus T on a log-log scales. From the graph, the limiting low temperature dependence appears to be T^2, and this increases to about a $T^{2.3}$ dependence in the temperature range 10 - 20 K.

Figure 4.24 shows $\rho_T - \rho_o$ plotted versus T^2. A T^2 law fits the measured resistivities very well up to about 8 K,

above which a positive deviation is observed. The best fit to the data below 8 K is

$$\rho_T = \rho_o + 0.705 \times 10^{-3}\ T^2\ \mu\Omega\,cm.$$

Figure 4.25 shows the resistivity of $FeZn_{13}$ (126) plotted versus temperature between 1.5 and 8 K. A shallow minimum is observed below 4 K, and in the limited temperature range 1.5 - 3.0 K a log(T) dependence is followed.

After correction for the log(T) term, the resistivity is re-plotted in figure 4.26. Again the resistivity is well described by a T^2 dependence below about 8 K and with a positive deviation (i.e. a faster dependence that T^2) occurring above 8 K.

$MnZn_{13}$

The room temperature resistivity of $MnZn_{13}$ (136) is $\rho_{300} = 99.5\ \mu\Omega cm$. and the residual resistivity $\rho_o = 4.65\ \mu\Omega cm$.

Figure 4.27 shows the temperature dependent part of the resistivity, $\rho_T - \rho_o$, plotted versus temperature on log-log scales. The resistivity appears to follow a $T^{\frac{3}{2}}$ behaviour at low temperatures with an additional term coming in as the magnetic transition temperature is approached.

The resistivity of $MnZn_{13}$ (136) is re-plotted against $T^{\frac{3}{2}}$ for temperatures below 4.2 K in figure 4.28. This indicates that the resistivity is very exactly proportional to $T^{\frac{3}{2}}$ in this temperature region. The best fit to the data is

$$\rho = \rho_o + 32.2 \times 10^{-3}\ T^{\frac{3}{2}}\ \mu\Omega\,cm.$$

In an attempt to determine the temperature dependence of the additional term which appears in the resistivity at higher temperatures, the quantity $\frac{\rho_T - \rho_o}{T^{\frac{3}{2}}}$ was plotted versus various powers of T. The plot of $\frac{\rho_T - \rho_o}{T^{\frac{3}{2}}}$ versus T^2 for temperatures up to 19 K is shown in figure 4.29. The data is well described by a power law of the form

$$\rho = \rho_o + 32.2 \times 10^{-3} T^{\frac{3}{2}} + 28 \times 10^{-6} T^{\frac{7}{2}} \ \mu\Omega cm.$$

The resistivities of all three ζ-phase compounds, $CoZn_{13}$, $FeZn_{13}$ and $MnZn_{13}$ are compared in figure 4.30. The resistivity of pure zinc has also been included.

$\underline{Mn_{0.05}\ Fe_{0.95}\ Zn_{13}}$

The resistivity of this specimen is shown in figure 4.31, plotted against log(T). A resistance minimum occurs at 19 K and a maximum at 3.8 K, and between 7 K and 14 K a logarithmic dependence is observed.

Magneto-Resistance

$\underline{CoZn_{13}}$

The magneto-resistance of $CoZn_{13}$ (145) was measured at one fixed temperature, 4.2 K. Figure 4.32 shows $\rho_H - \rho_{H=0}$ versus magnetic field H on a log-log plot. The solid line on the graph represents a dependence of $H^{\frac{3}{2}}$ and provides a good fit to the data over the whole range of magnetic fields.

$\underline{FeZn_{13}}$

The magneto-resistance of $FeZn_{13}$ (126) at 4.2 K is shown in figure 4.33. No simple power law dependence upon the magnetic field is observed.

$\underline{MnZn_{13}}$

The magneto-resistance of $MnZn_{13}$ (136) at 4.2 K, shown in figure 4.34, is large and negative. The initial dependence upon magnetic field H is approximately $\rho_H \propto - T^{1.2}$, but it eventually saturates at H = 15 K.Gauss and then begins to decrease.

The magneto-resistance of this specimen in a field of 18 K.Gauss was measured as a function of temperature and the results are shown in figure 4.35. A sharp peak is observed around 20 K, and this gives a much clearer indication of the position of the magnetic ordering temperature than either the resistivity or a straight plot of magnetization versus temperature.

RESISTIVITY OF $CoZn_{13}$ - (145) FIG 4.21

$-(\rho-\rho_0)$ VERSUS TEMPERATURE

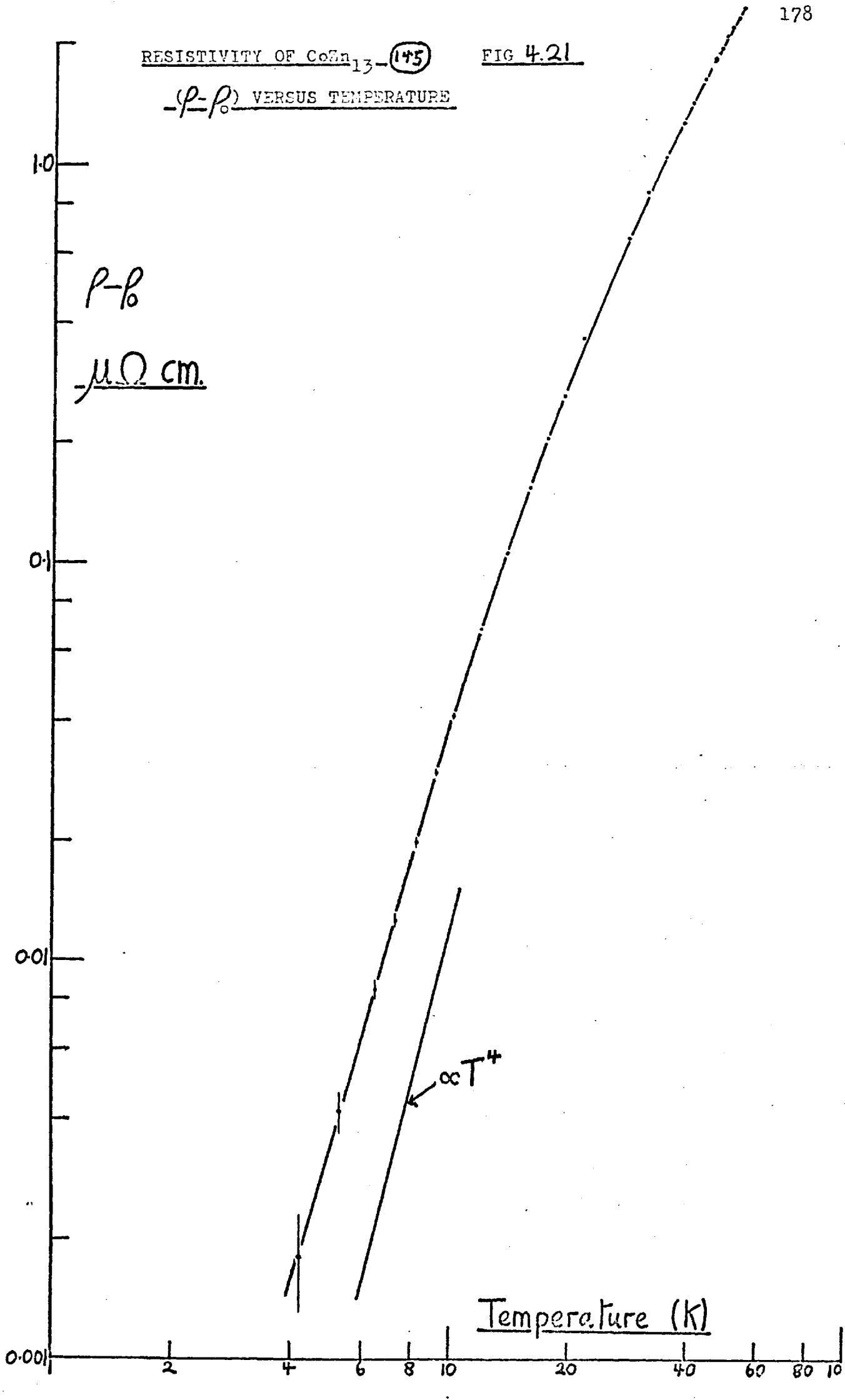


FIG 4.22 RESISTIVITY OF $CoZn_{13}$ (149)

$(\rho_T - \rho_0)$ VERSUS TEMPERATURE

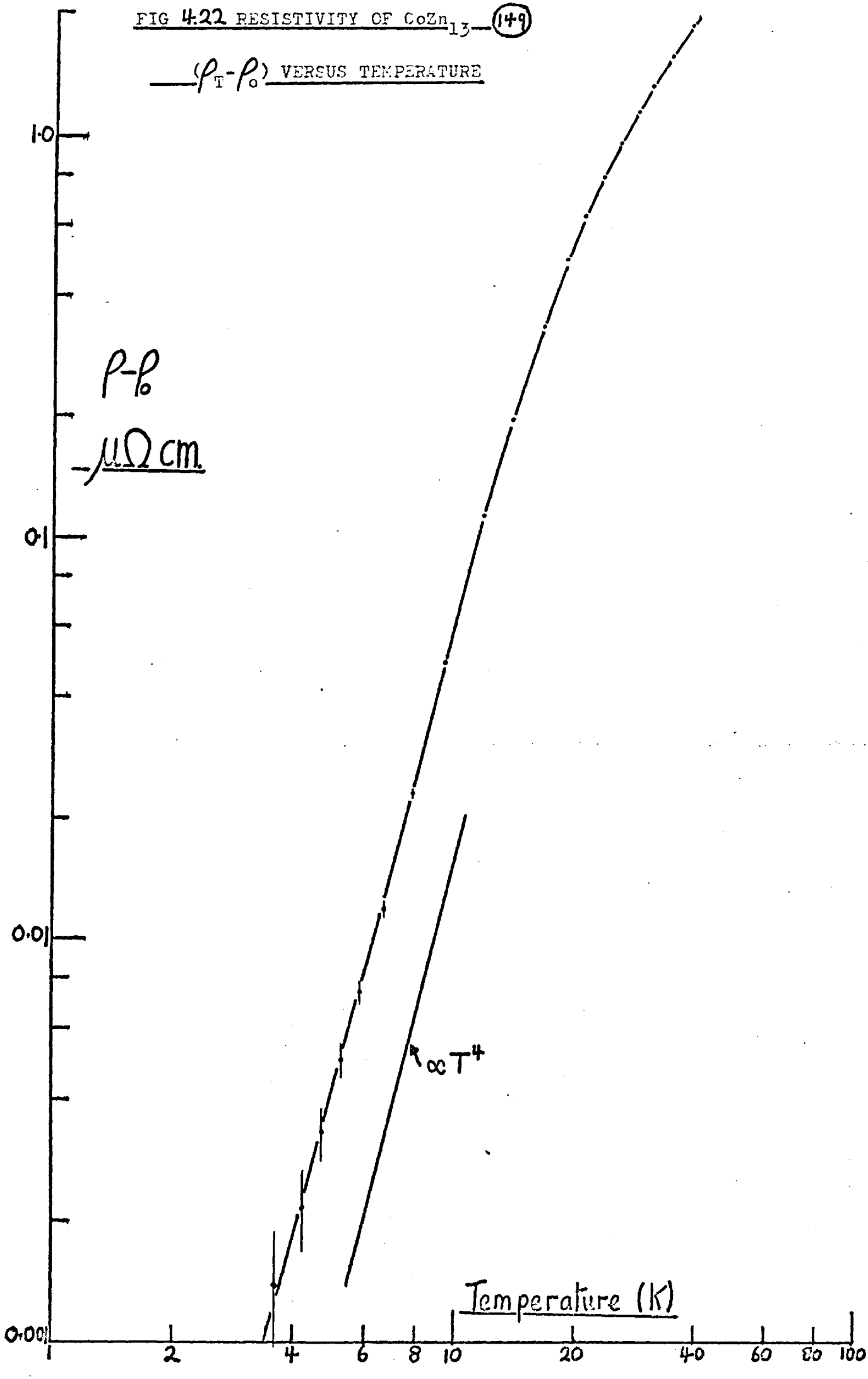
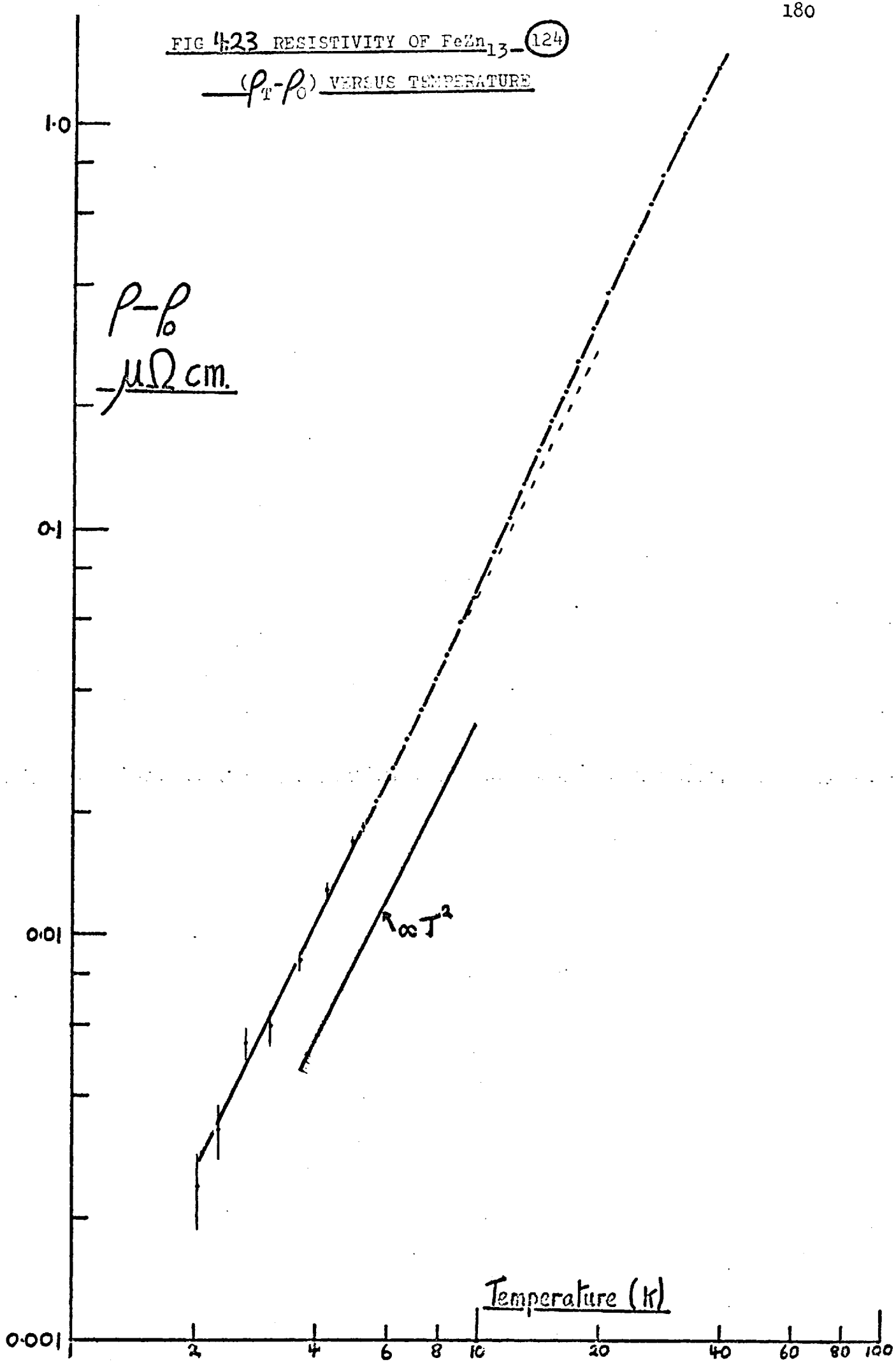


FIG 4.23 RESISTIVITY OF $FeZn_{13}$ - (124)

$(\rho_T - \rho_0)$ VERSUS TEMPERATURE



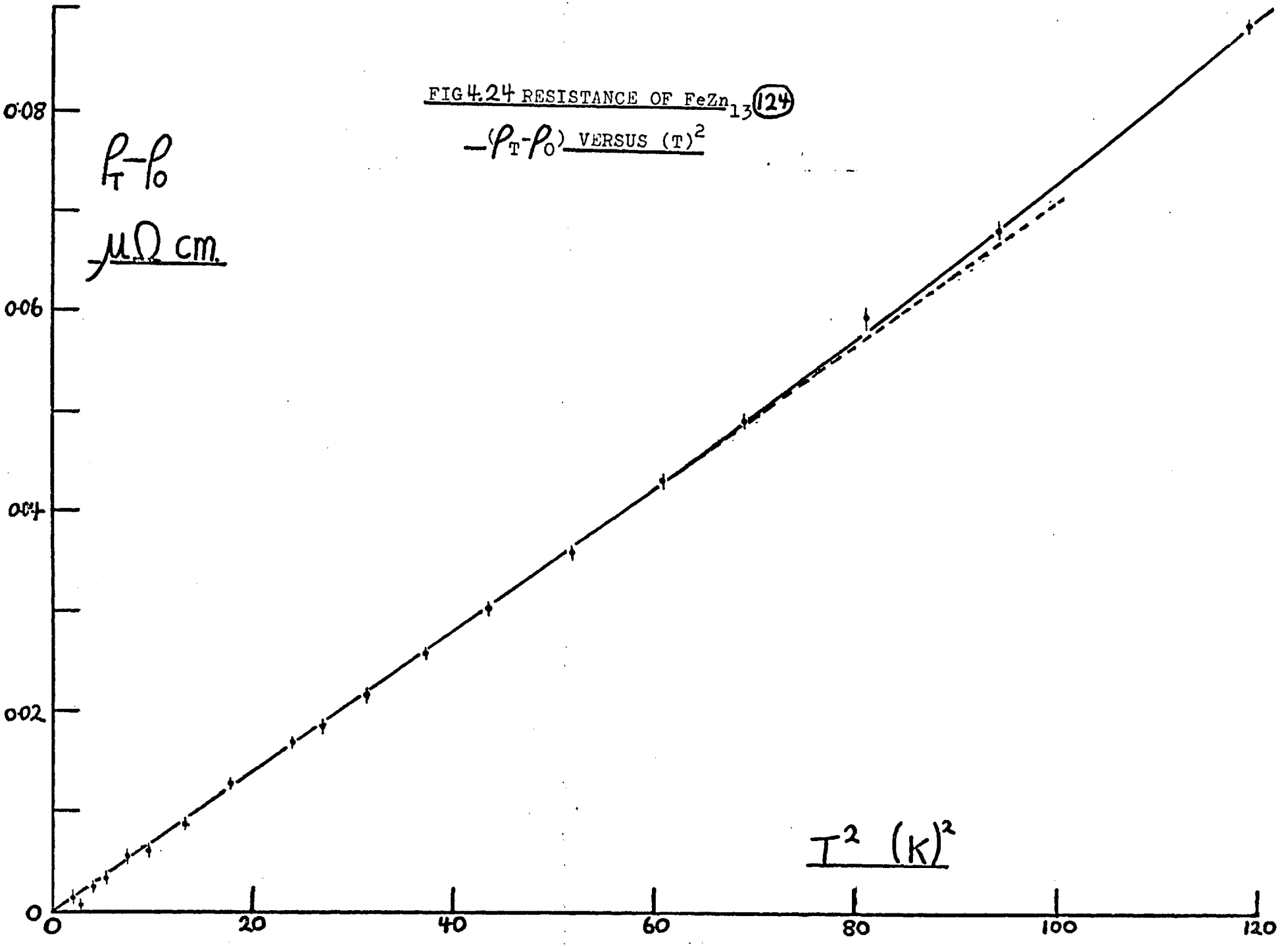


FIG 4.24 RESISTANCE OF $FeZn_{13}$ (124)

$-(\rho_T - \rho_0)$ VERSUS $(T)^2$

FIG 425 RESISTIVITY OF $FeZn_{13}$. SPECIMEN NUMBER (126)

$-\rho$ VERSUS TEMPERATURE

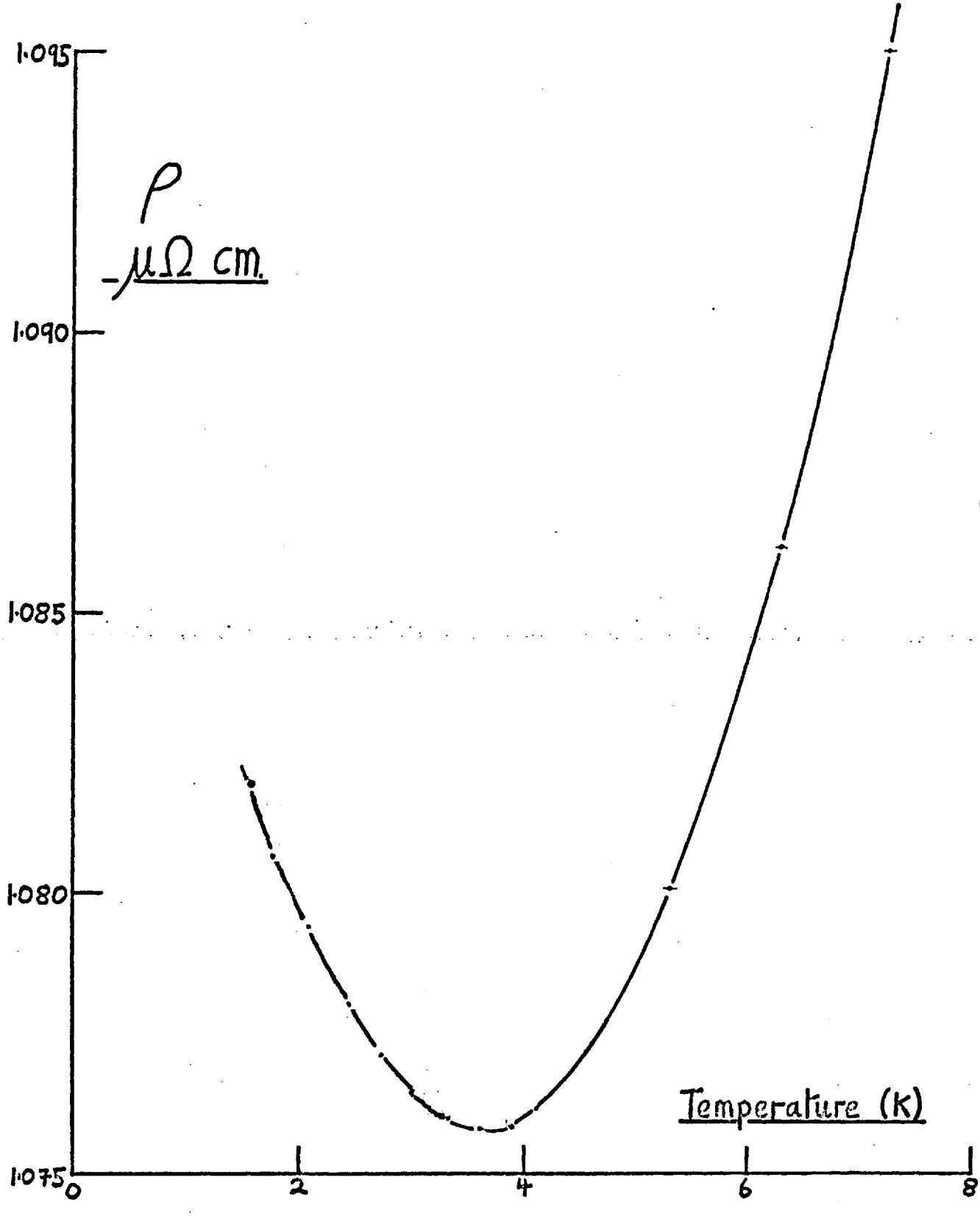


FIG 4.26 RESISTIVITY OF $FeSn_{13}$ - (126)

$-(\rho_T - \rho_0)$ VERSUS TEMPERATURE . Corrected for lnT term

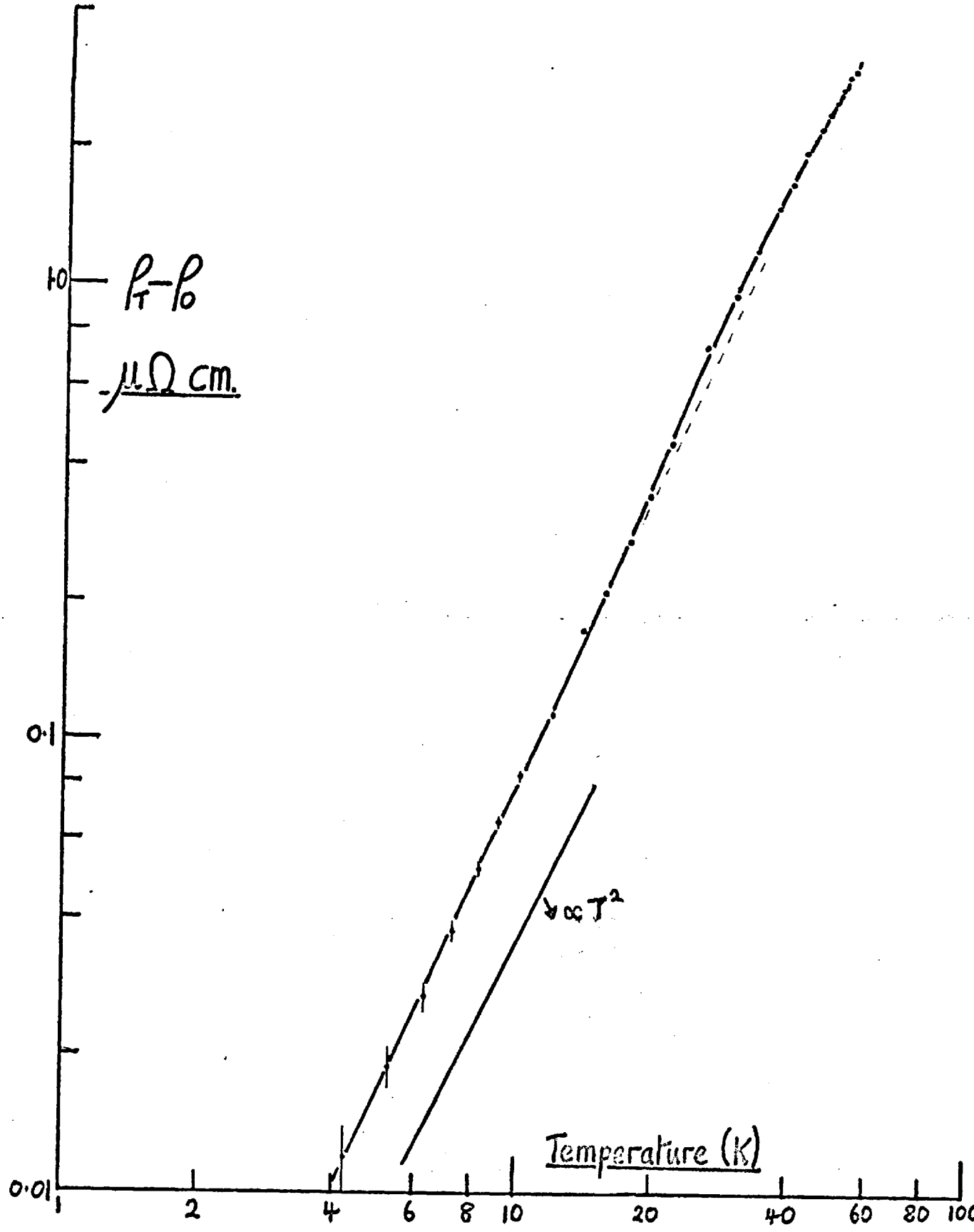


FIG 4.27 TEMPERATURE DEPENDANT PART OF THE RESISTIVITY OF $MnZn_{13}$.(136) (LOG-LOG PLOT)

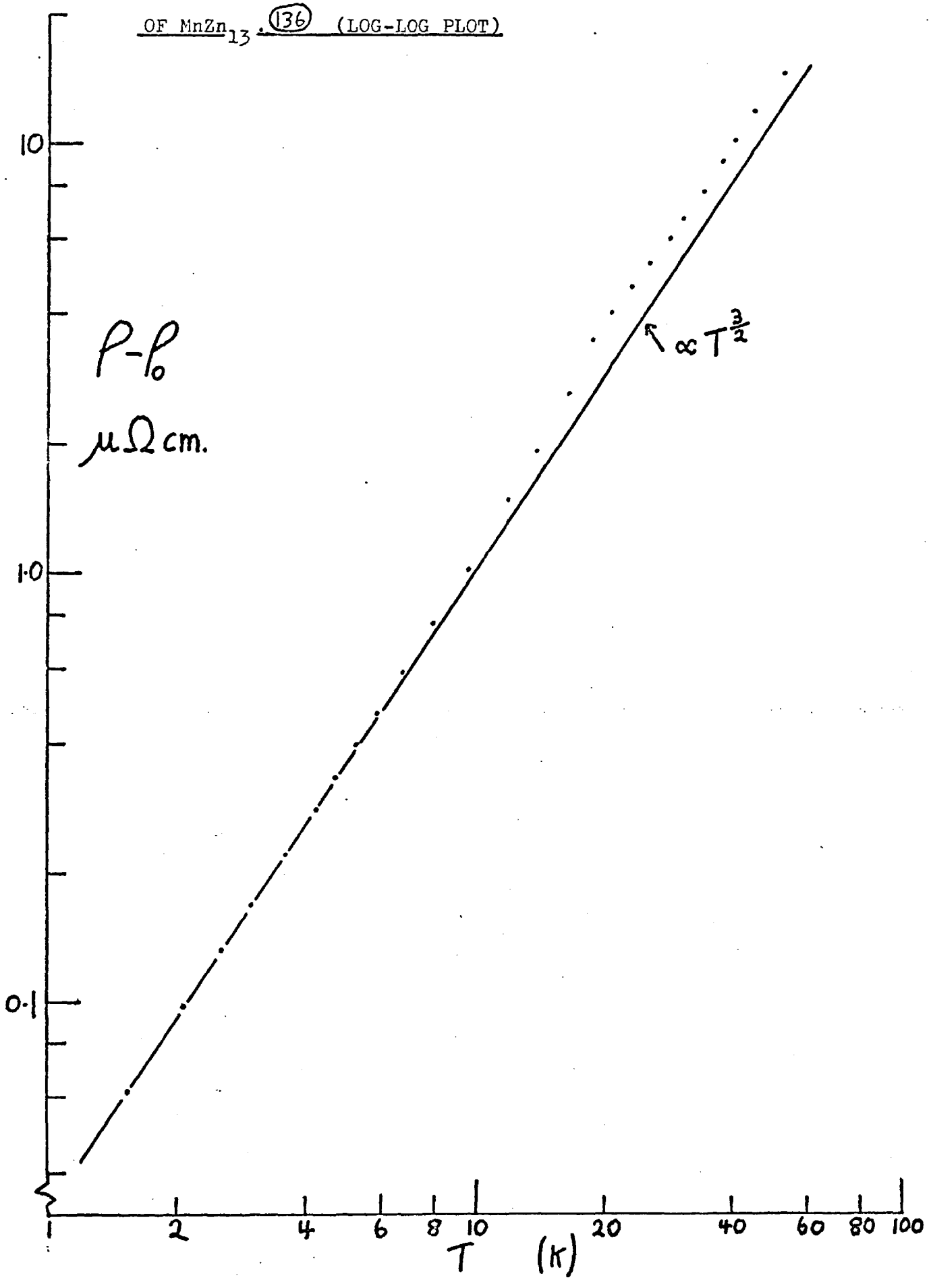


FIG 4.28 RESISTIVITY OF $MnZn_{13}$ PLOTTED VERSUS $T^{\frac{3}{2}}$

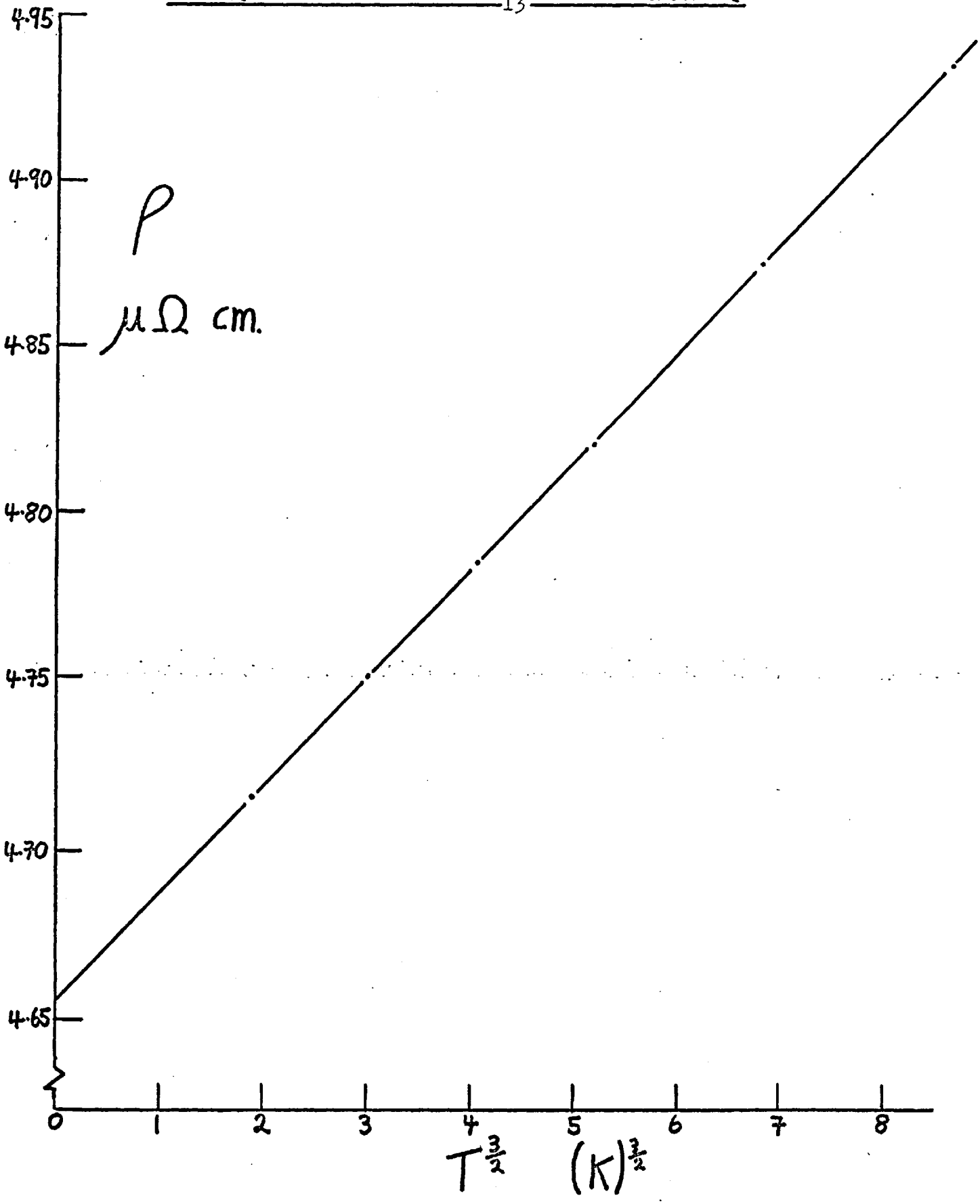
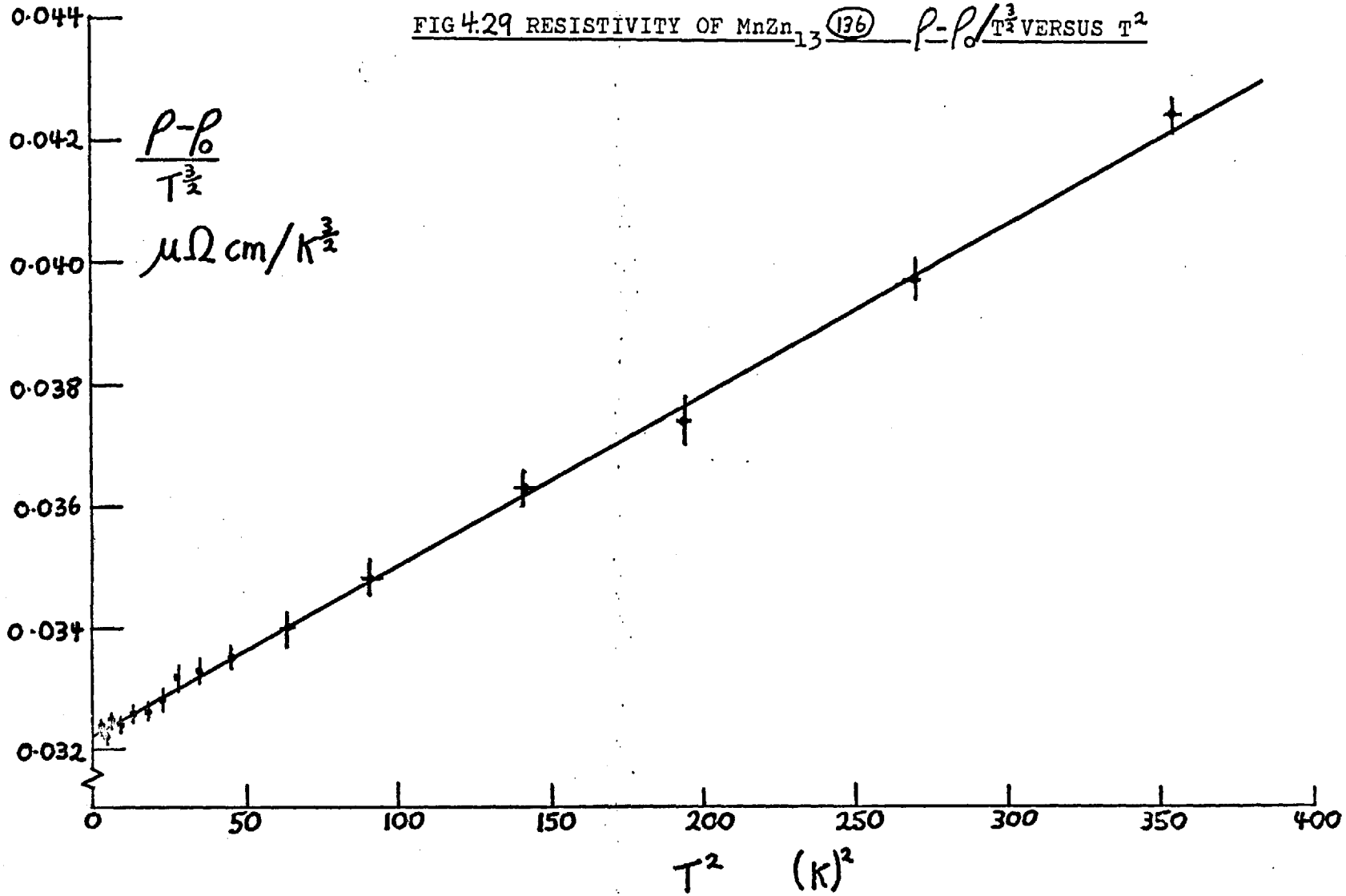


FIG 4.29 RESISTIVITY OF $MnZn_{13}$ (136) $\rho-\rho_0/T^{\frac{3}{2}}$ VERSUS T^2



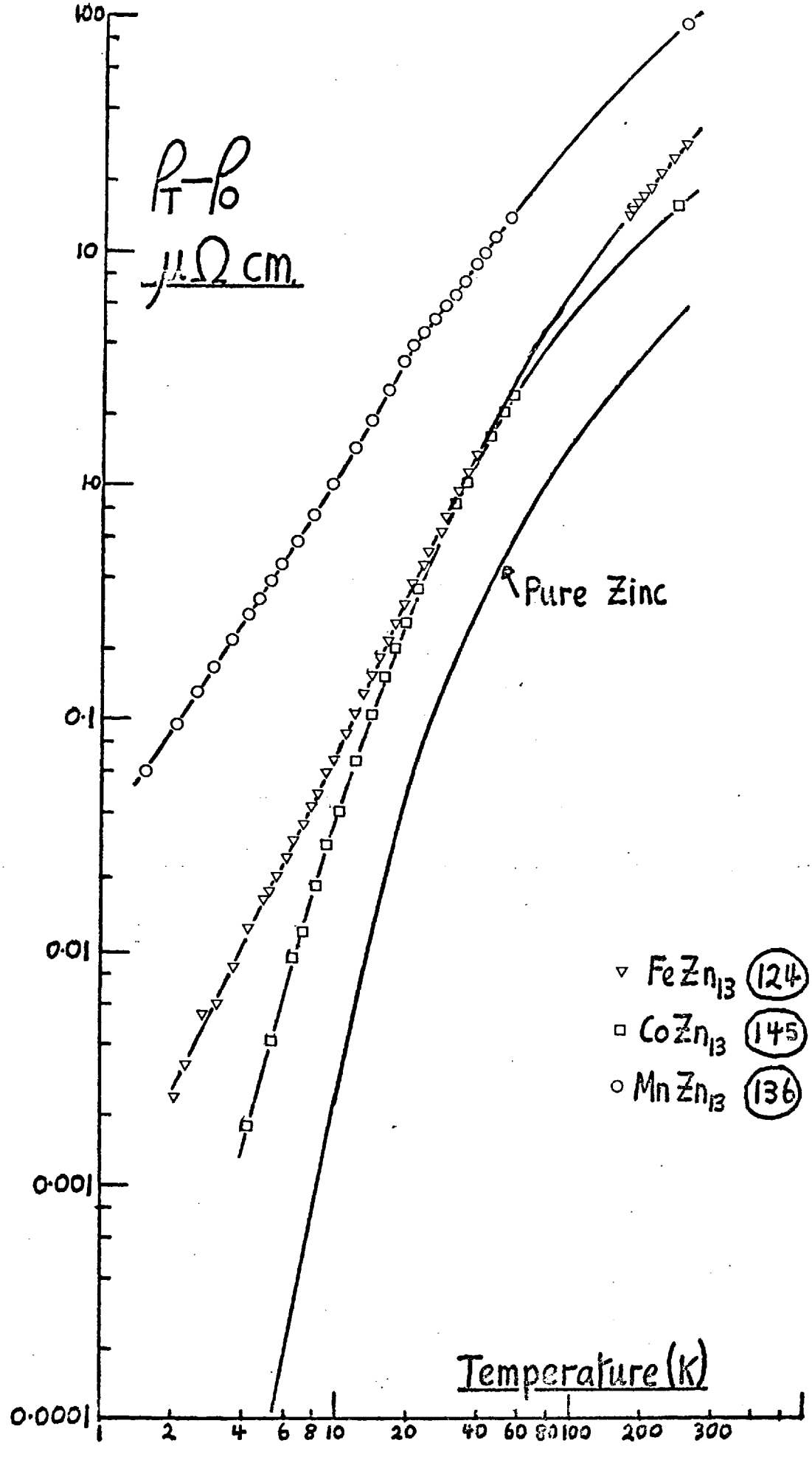


FIG 4.30 RESISTIVITIES OF THE THREE ζ-PHASES.

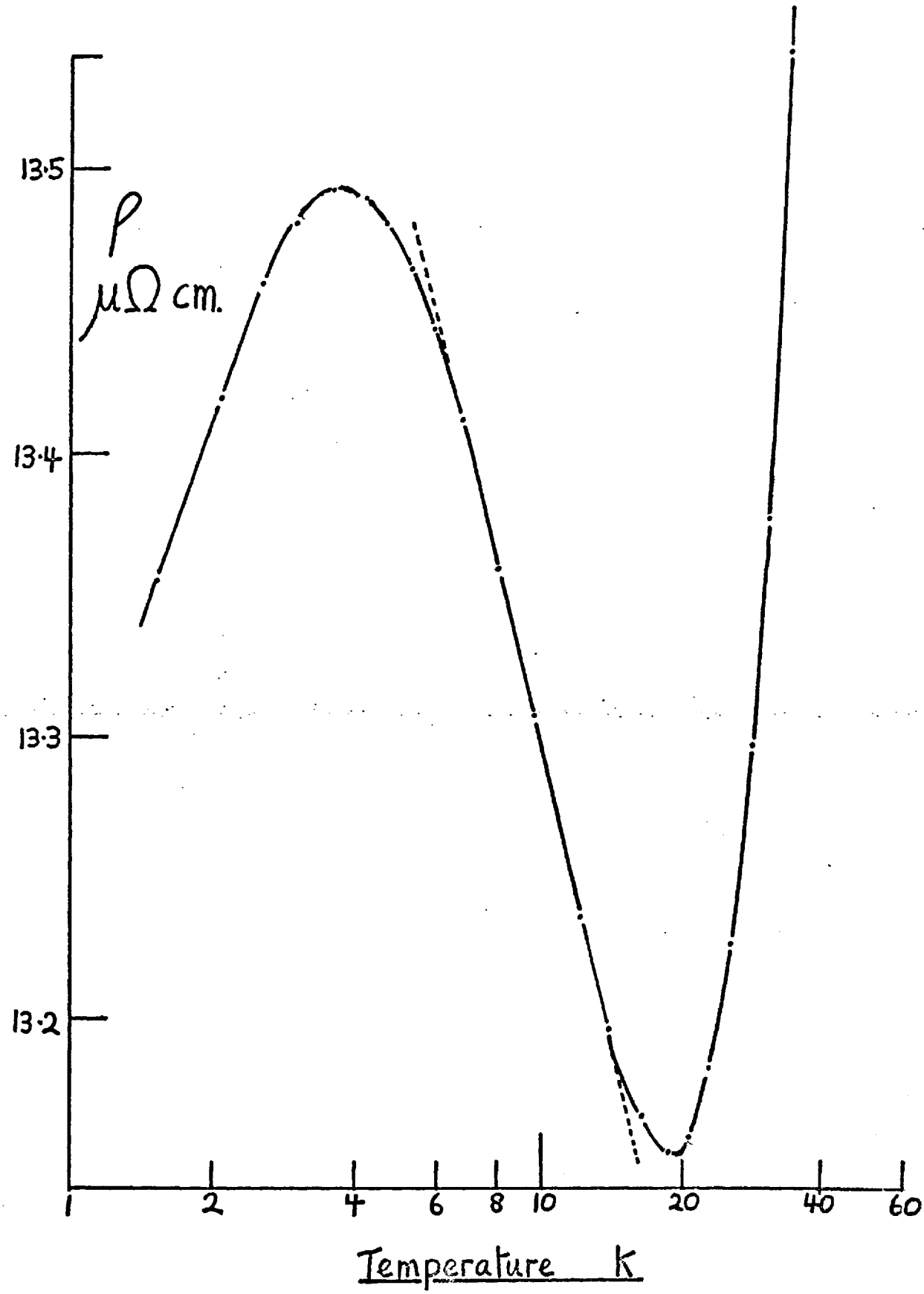


FIG 4.31 RESISTIVITY OF $Mn_{0.05}Fe_{0.95}Zn_{13}$ PLOTTED VERSUS LOG(T)

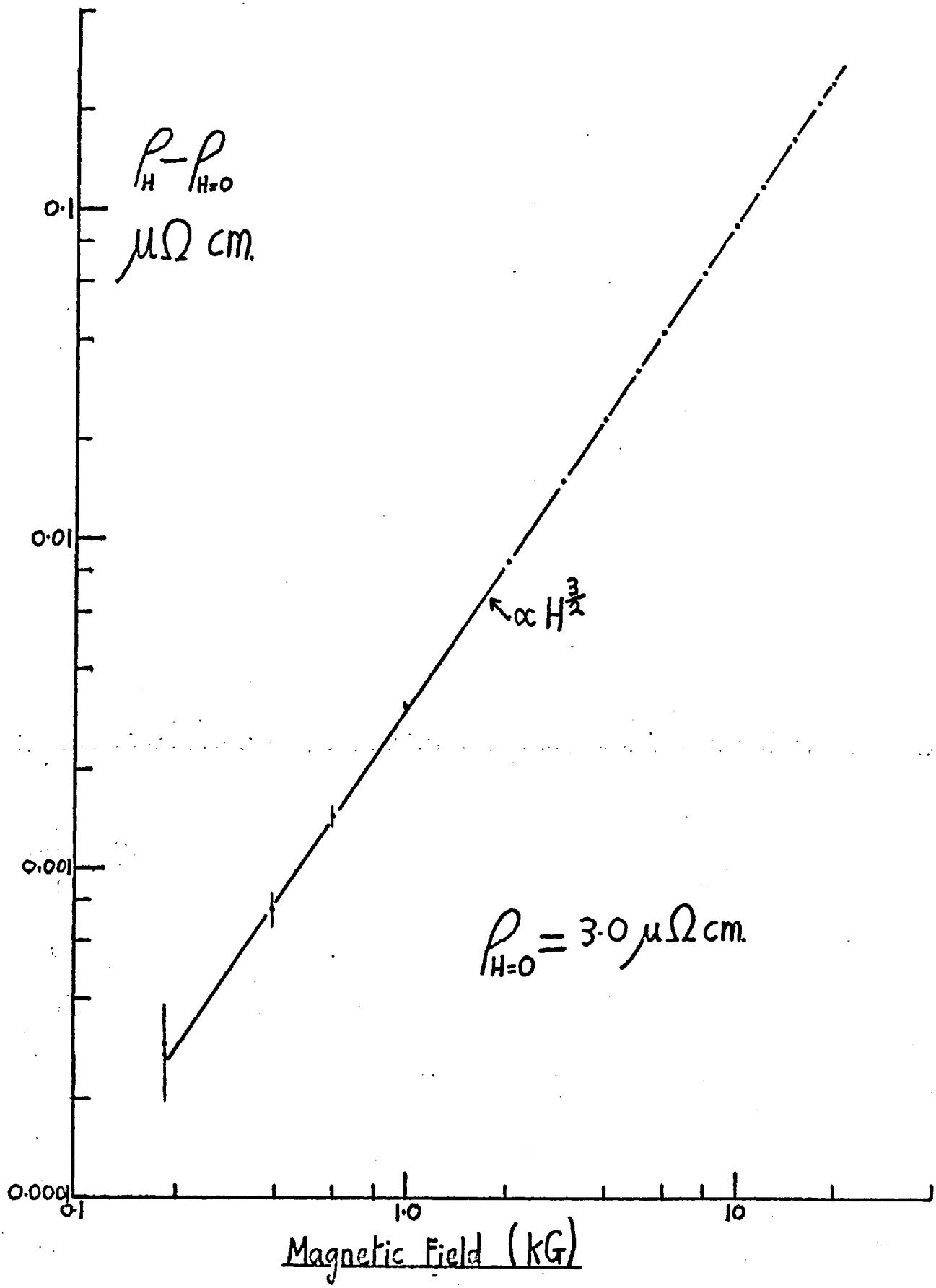


FIG 4.32 MAGNETO-RESISTANCE AT 4.2K OF $CoZn_{13}$

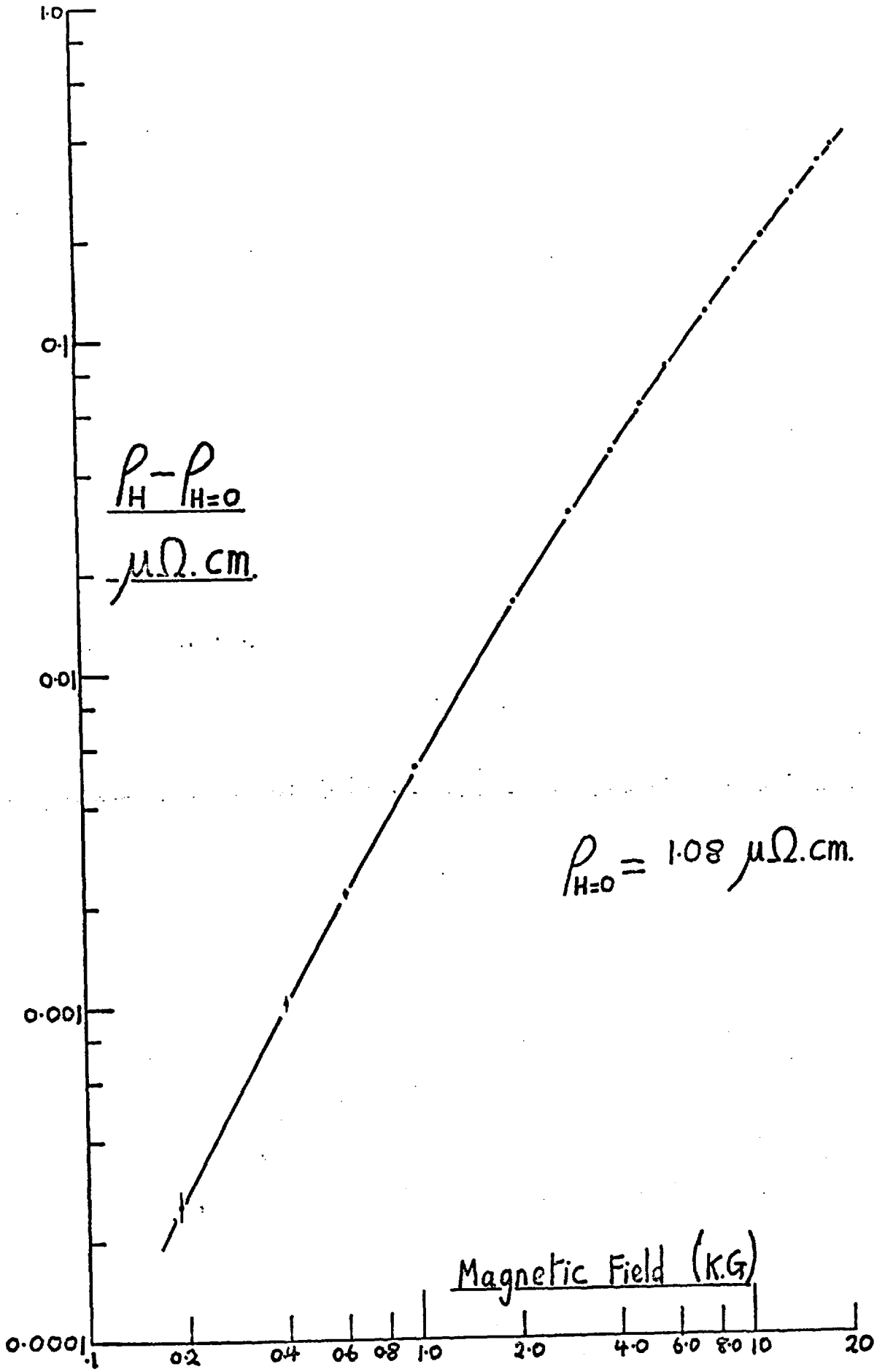


FIG 4·33 MAGNETO-RESISTANCE OF $FeZn_{13}$ (126) AT 4.2 K

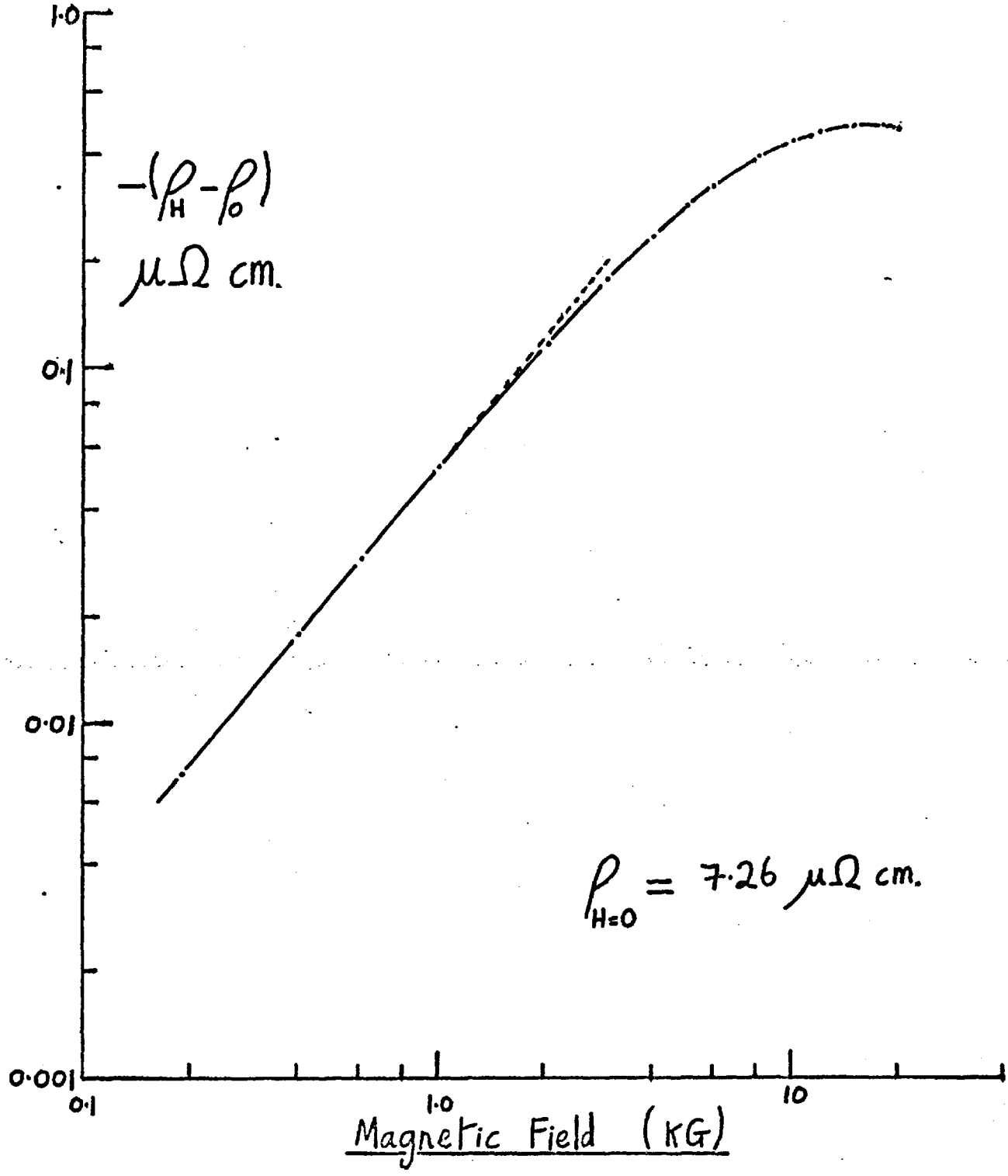
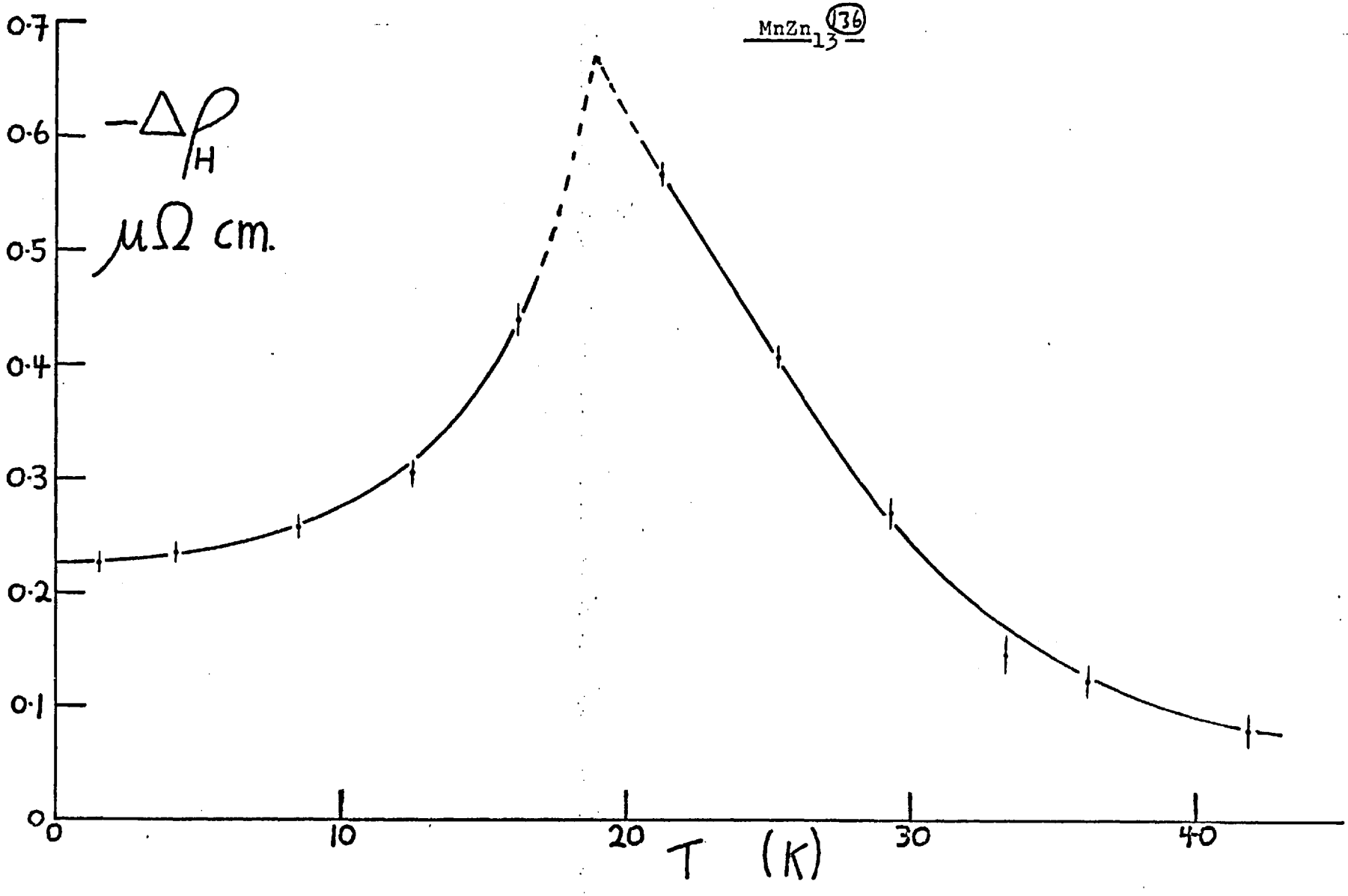


FIG 4.34 MAGNETO-RESISTANCE AT 4.2K OF $MnZn_{13}$

FIG 4.35 MAGNETO-RESISTANCE IN A FIELD OF 18 kG VERSUS TEMPERATURE



E.S.R.

Taylor has carried out E.S.R. experiments on two powdered samples of $MnZn_{13}$ (numbers (135) and (136)) using an X-band spectrometer. His results for both the resonant field (and hence the g-value) and the linewidth are shown in figures 4.36 to 4.39. No signal is observable from room temperature down to ~200 K where an increasingly strong signal appears. The g-value is close to 2 at first but an increasing positive g-shift occurs at lower temperatures until g = 3 at 4.2 K. No correction has been made for demagnetizing fields as at the most they would only account for 20% of the observed shift.

A search was made for a resonance signal in the $Mn_{0.05}Fe_{0.95}Zn_{13}$ specimen with a negative result.

Neutron Diffraction

A neutron diffraction experiment on a polycrystaline specimen of $MnZn_{13}$ was undertaken at Harwell by Dr. J.B. Forsyth. The neutron diffraction pattern at room temperature is shown in figure 4.40. The observed neutron lines have been indexed on the ζ-phase structure out to $2\theta = 23^{\circ}$ and the large peak at $2\theta = 24.4^{\circ}$ corresponds to the group of strong lines observed in the X-ray powder pattern. On cooling down to 4.2 K no new lines were observed such as would be expected if the compound had undergone a transition into an anti-ferromagnetic structure or even one of the complex long wavelength spiral or screw structures.

FIG 4.36 E.S.R. RESONANT FIELD OF ζ-PHASE $MnZn_{13}$ -(135)

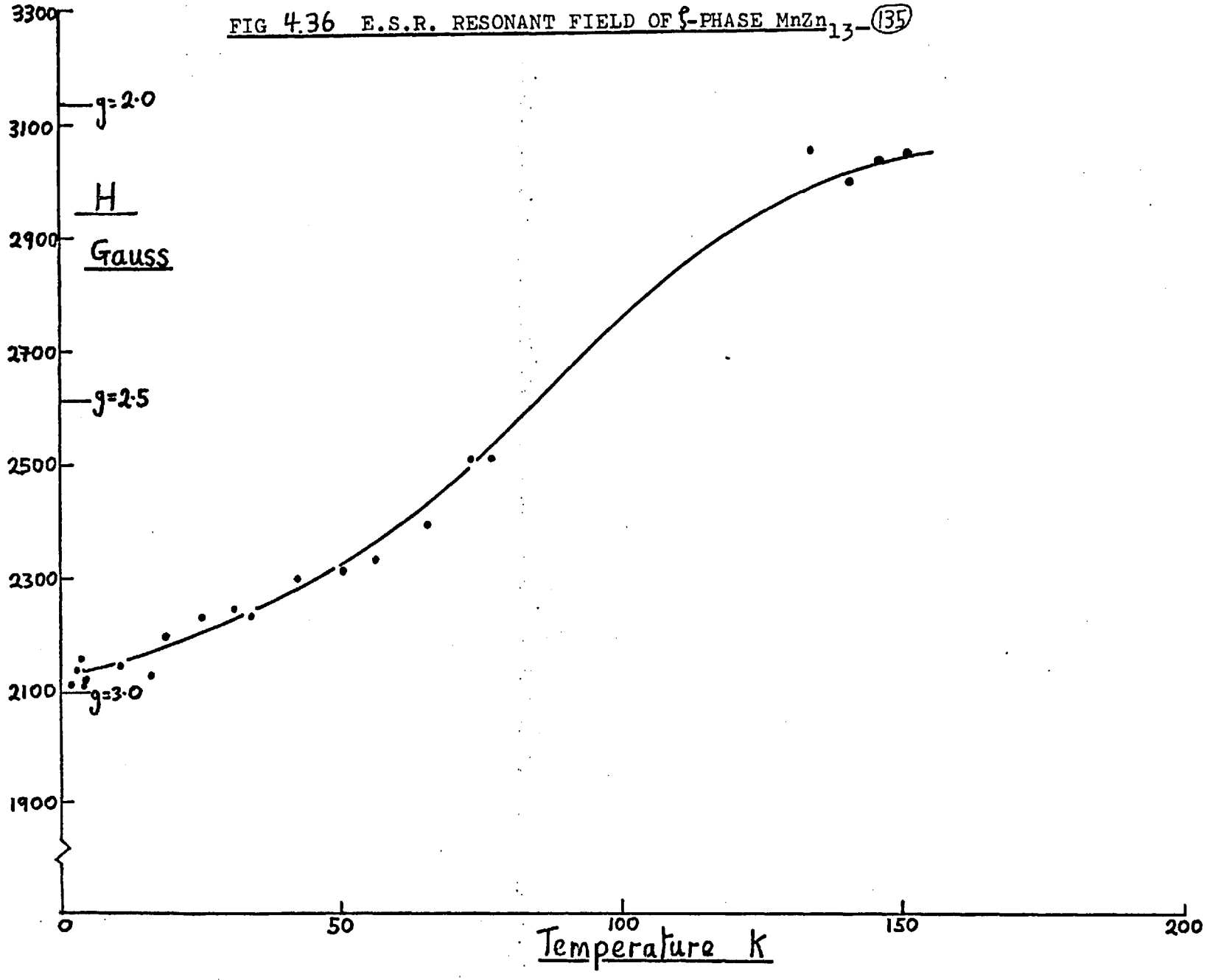
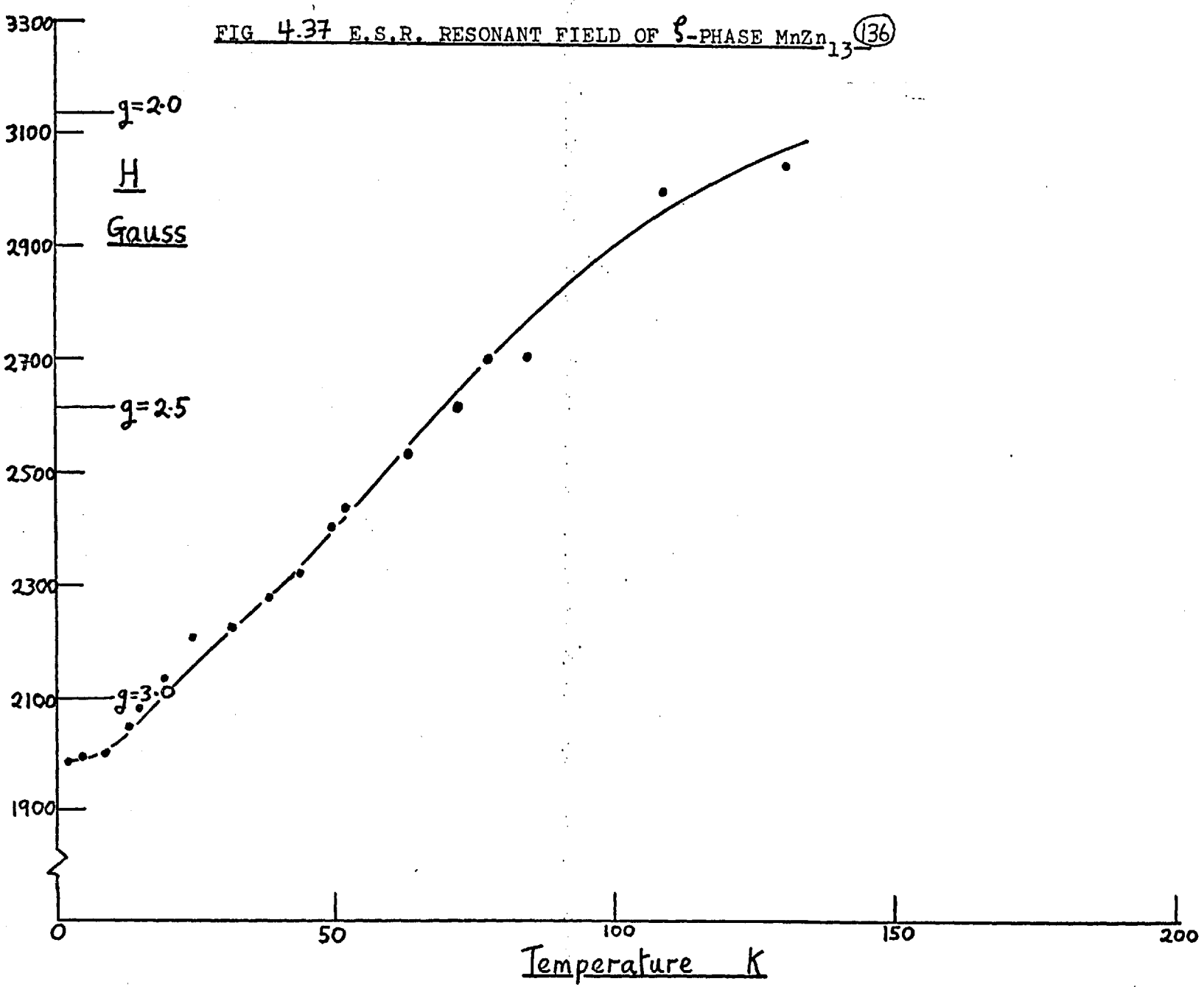


FIG 4.37 E.S.R. RESONANT FIELD OF ζ-PHASE $MnZn_{13}$ (136)



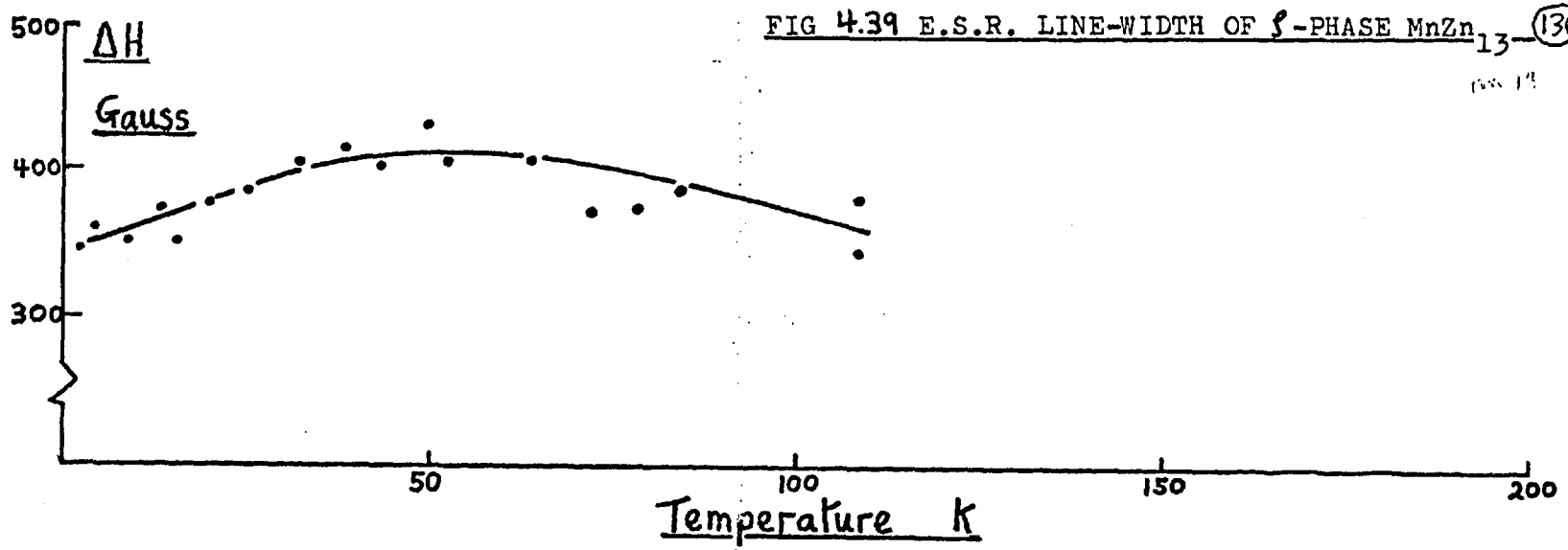


FIG 4.39 E.S.R. LINE-WIDTH OF ℓ-PHASE $MnZn_{13}$ (136)

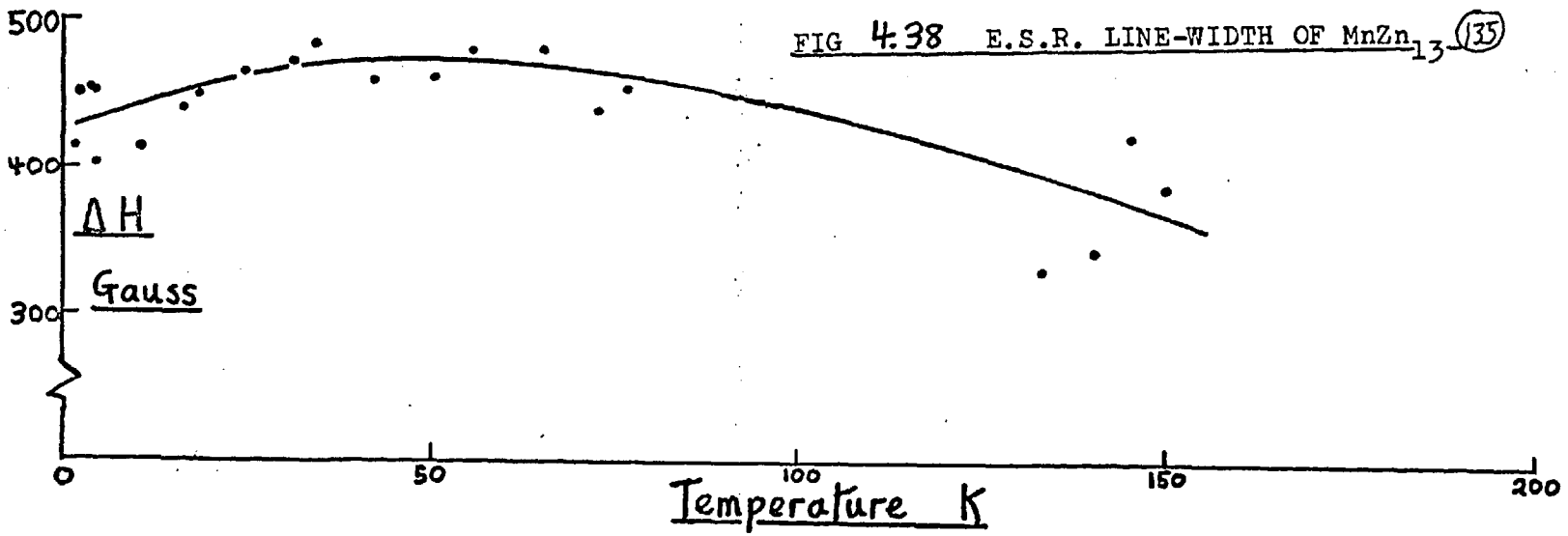


FIG 4.38 E.S.R. LINE-WIDTH OF $MnZn_{13}$ (135)

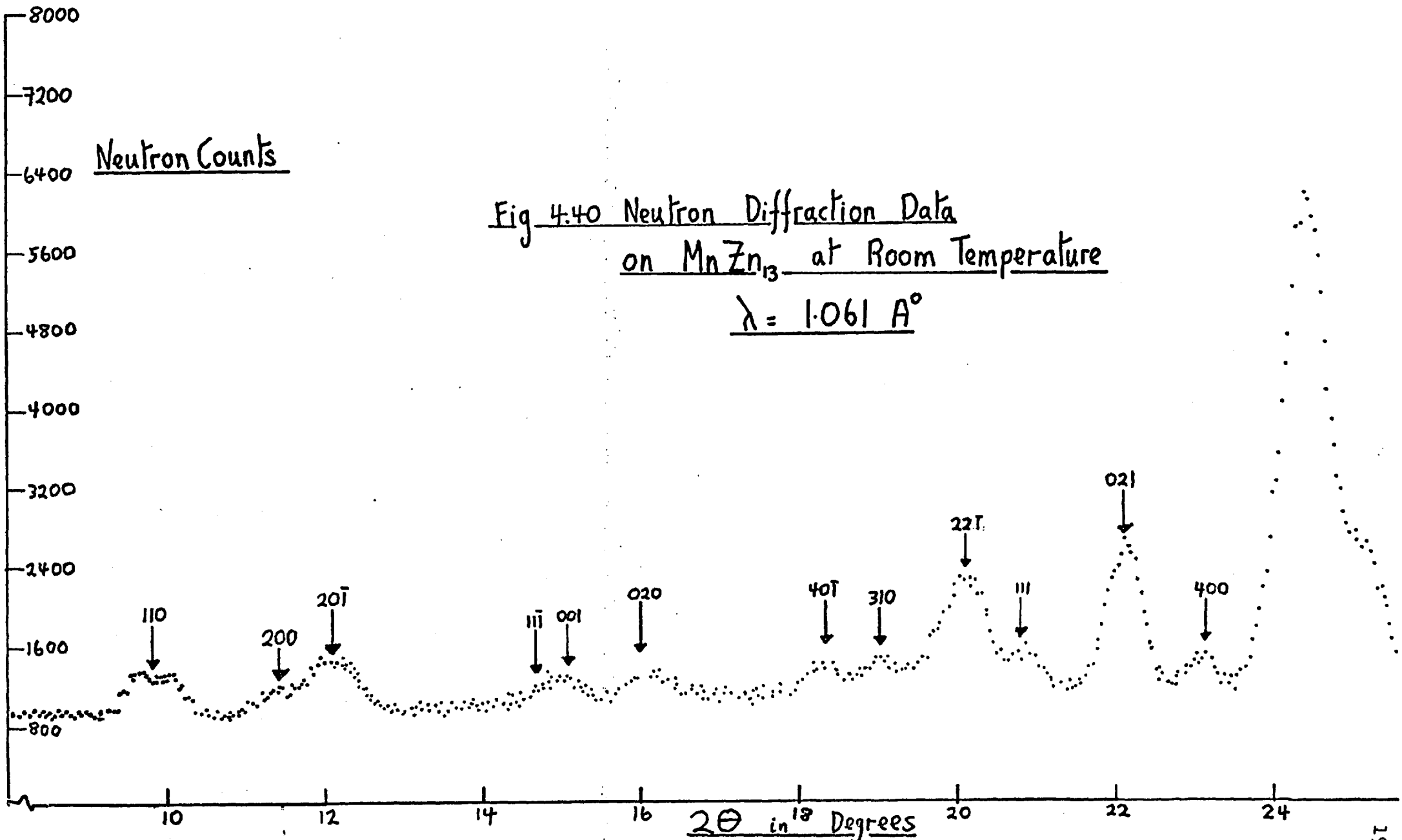


Fig 4.40 Neutron Diffraction Data on $MnZn_{13}$ at Room Temperature

$\lambda = 1.061\ A^{\circ}$

CHAPTER 5

DISCUSSION

Introduction

In the ζ-phase compounds $CoZn_{13}$, $FeZn_{13}$ and $MnZn_{13}$ the transition metal atoms are well separated ($\sim 5A^{o}$) and each is surrounded by a slightly distorted sphere of zinc atoms. It therefore seems reasonable to think of each individual transition metal atom as forming a virtual bound state and that the s - d hybridization at each atomic site is the most important interaction and not d - d overlap. In these circumstances, one can imagine a d "band" which is simply a super-position of the individual virtual bound states on the transition metal atoms. This "band" may be described in terms of the same parameters as are used in Anderson's model of the isolated solute atom virtual bound state, i.e. E_d, U, Δ etc., although the actual numerical values of the parameters may be modified from their dilute limit values because of interactions between the virtual bound states via the conduction electrons (see section 1.3). In principle it is possible to determine the values of these parameters from the results of specific heat and magnetic susceptibility measurements.

Doubts as to the Validity of a Free-electron Model for the Conduction Electrons in the ζ-phases

In the interpretation of experimental results for the specific heat and magnetic susceptibility, the conduction electron contribution has also to be taken into account. Unfortunately, in the absence of a band structure calculation for the ζ-phase crystal structure, the conduction electron density of states at the

Fermi level, $\rho_c(E_F)$, and the Fermi-surface area, S, are unknown. However by examining the relationship between a free-electron Fermi sphere and the Jones zone of the ζ-phase structure it is possible to obtain some indication of the expected modification of $\rho_c(E_F)$ from that derived from the free-electron approximation. The Jones zone of a given crystal structure is constructed from the sets of crystal planes (h,k,ℓ) with large structure factors and these are the same sets of planes which give rise to strong reflections in an X-ray pattern.

The Fermi wave vector, k_F, is given in the free-electron approximation by

$$k_F = \left(\frac{3\pi^2}{\Omega}\right)^{\frac{1}{3}} . N^{\frac{1}{3}}$$

where Ω is the volume of the crystal unit cell and N the total number of conduction electrons per unit cell. If each transition metal atom in the ζ-phase compounds contributes n_c electrons to the conduction band and each zinc atom contributes 2, then k_F has the following values.

n_c	k_F $(A^o)^{-1}$
-2	1.50
-1	1.52
0	1.54
1	1.56
2	1.58

TABLE 5.1

In table 5.2 we tabulate the strongest observed lines in the X-ray powder spectrum of the ζ-phase structure together with their $\frac{1}{d}$ values. By comparing the $\frac{1}{d}$ values with $\frac{k_F}{\pi}$ we are directly comparing the Fermi-wave vector k_F with the distance from the origin of k-space to the Jones zone planes.

Strong Line (h,k,ℓ)	$\left(\frac{1}{d}\right)_{h,k,\ell}$ $(A^\circ)^{-1}$
$42\bar{1}$	0.396
$60\bar{1}$	0.456
$11\bar{2}$	0.461
$60\bar{2}$	0.469
$42\bar{2}$	0.475
330	0.482
510	0.487

$\frac{k_F}{\pi} = 0.494\ (A^\circ)^{-1}$ with n_c = 1 conduction electron/transition metal atom

TABLE 5.2 $\left(\frac{1}{d}\right)_{h,k,\ell}$ for Strong X-ray Lines

From this table it is clear that a free-electron Fermi-sphere will have made contact with the Jones zone and, depending upon the size of the energy gaps at each face, the amount of free-electron-like Fermi-surface may be greatly reduced.

In figures 5.1 to 5.3 the (h,k,0), ($\bar{h}$,k,1) and (h,k,2) planes in reciprocal space have been drawn. The size of the spot on each (h,k,ℓ) co-ordinate is approximately proportional

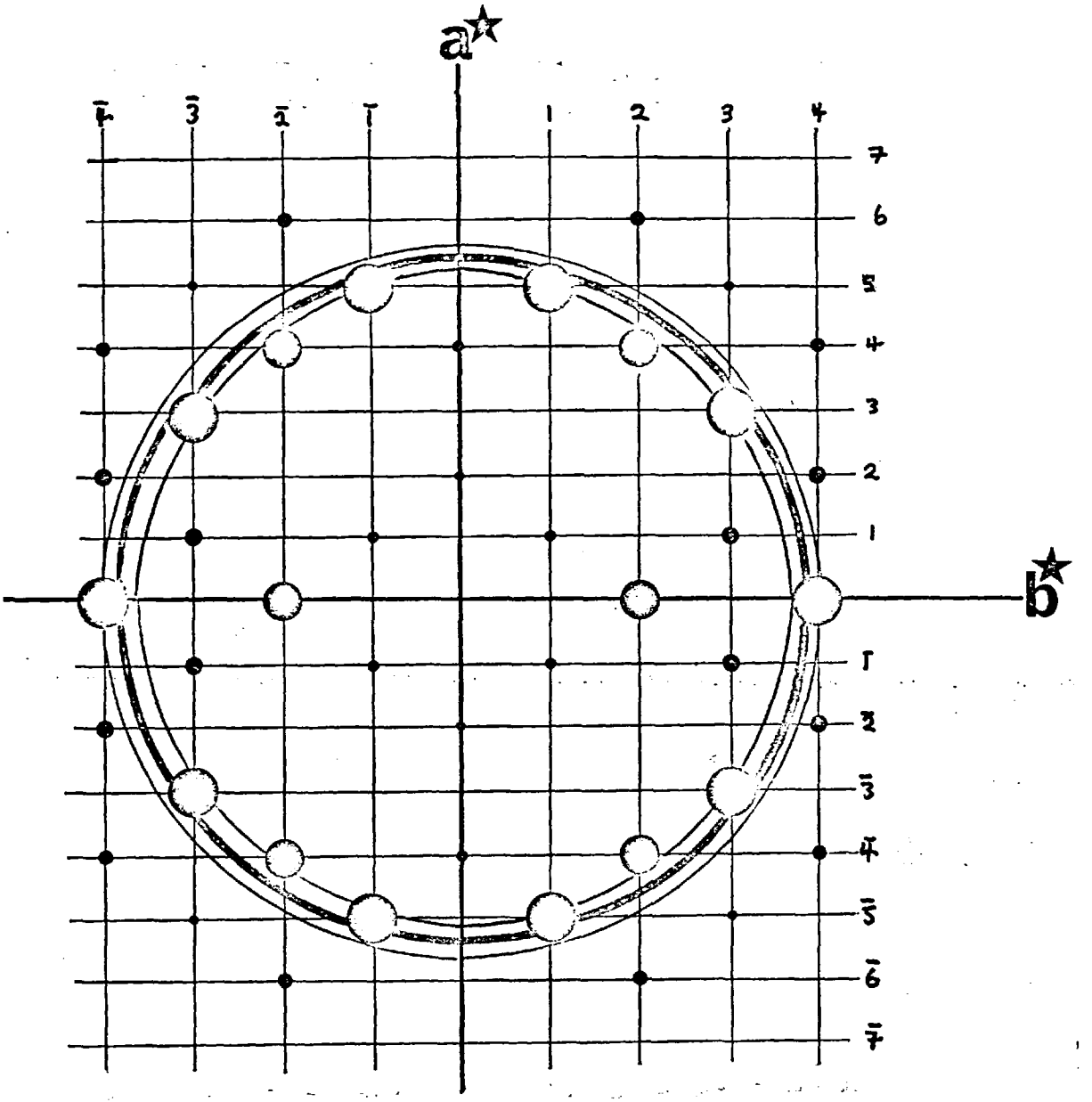


FIG 5.1 CIRCLE OF INTERSECTION OF A FREE-ELECTRON FERMI SPHERE WITH THE (h,k,0) RECIPROCAL LATTICE PLANE

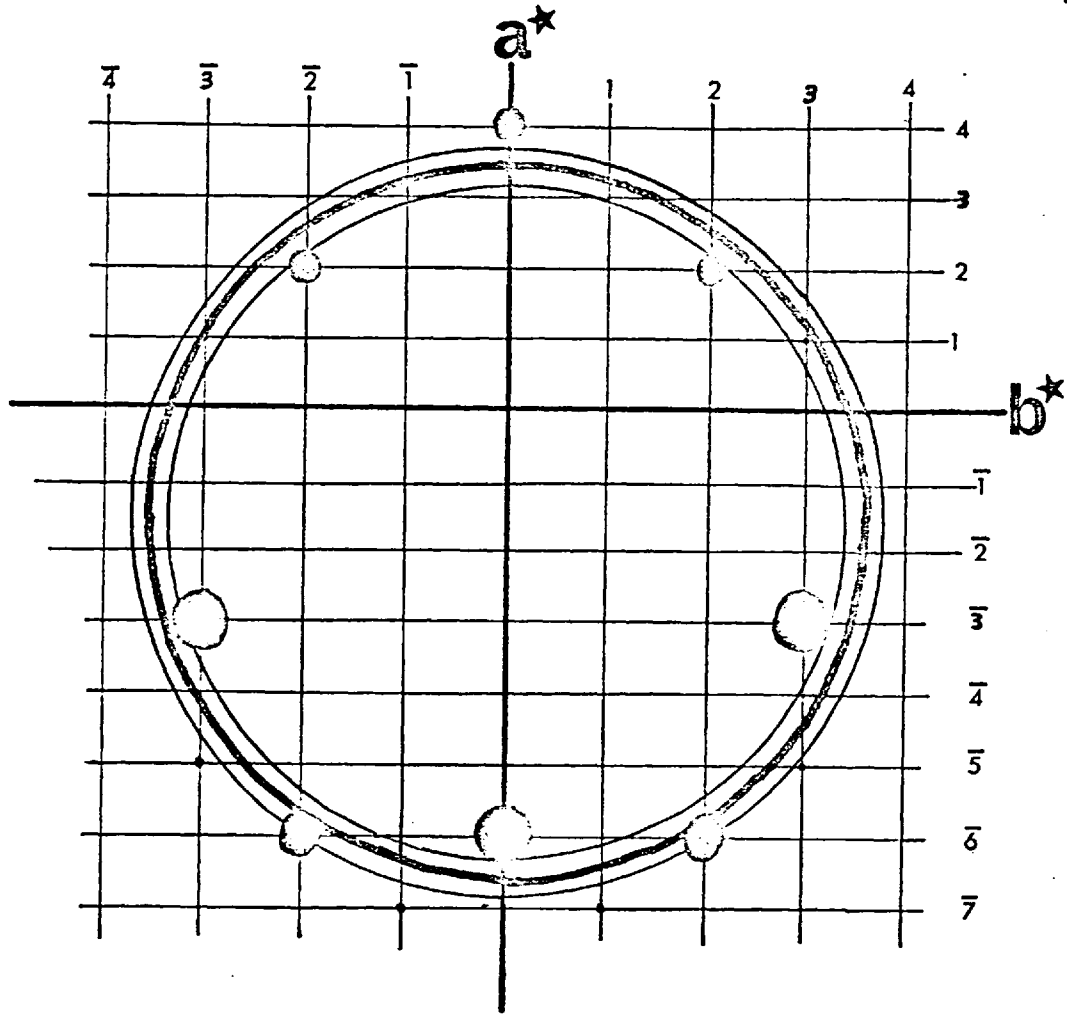


FIG 5.2 (ABOVE) INTERSECTION OF A FREE-ELECTRON FERMI SPHERE WITH THE (h,k,1) RECIPROCAL LATTICE PLANE

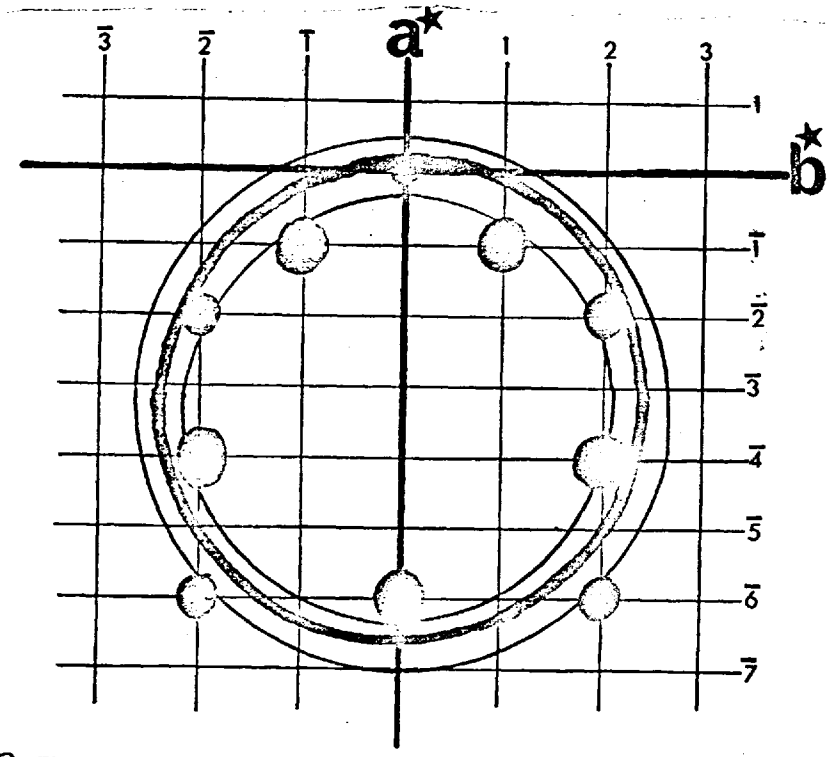


FIG 5.3 INTERSECTION OF A FREE-ELECTRON FERMI-SPHERE WITH THE (h,k,2) RECIPROCAL LATTICE PLANE

to the size of the calculated X-ray structure factor. A free-electron Fermi-sphere (drawn to the correct scale) will intersect these planes to form the "heavy" circles superimposed on the reciprocal lattice. The two fainter circles on either side of the main ones represent a 5% variation of $\frac{k_F}{\pi}$ from the free-electron value. It may also be noted in figures 5.2 and 5.3 that the origin of each Fermi "circle" is displaced along the a^* axis, this is due to the fact that the reciprocal lattice for the ζ-phase structure is of mono-clinic type, as is the real space lattice, and the c^* axis is not perpendicular to the a^* axis.

Again it is clear that the free-electron Fermi-sphere will have made contact with the Jones zone with the result that parameters such as $\rho_c(E_F)$ and the Fermi-surface area, S, may show marked deviations from their free-electron values.

Specific Heat Results

The measured electronic specific heat coefficients for the three ζ-phase compounds, and the corresponding densities of states are shown below.

	$CoZn_{13}$	$FeZn_{13}$	$MnZn_{13}$
γ mJ./mole(formula unit) K^2	8.1	17.6	62.3
Total $\rho(E_F) = \rho_c(E_F) + \rho_d(E_F)$ states/eV. atom(formula unit)	3.34	7.48	26.5

Considering firstly the "non-magnetic" compounds, there is clear evidence for an increased density of states at the Fermi level in $FeZn_{13}$ relative to $CoZn_{13}$. If we make the assumption that the virtual bound state on each Fe atom contains 7 d electrons, which

is the number deduced by Ford et.al.(71) to fit the measured residual resistivity of Fe impurities in zinc, and the further (and obviously false) assumption that the conduction electron density of states is vanishingly small i.e. $\rho_c(E_F) = 0$, then the virtual bound state width may be deduced from the expression

$$\rho_d(E_F) = \frac{10}{\pi\Delta} \sin^2\left(\frac{\pi n_d}{10}\right) = 7.48 \text{ states/e.V. atom}$$

giving $\underline{\Delta = 0.28 \text{ eV}}$.

If the virtual bound state has the same width Δ for Co in $CoZn_{13}$, then the number of d electrons per Co atom virtual bound state required to account for the observed γ value is

$$\underline{n_d = 8.2 \text{ electrons}}$$

Martin's (74) specific heat measurements on pure zinc give $\gamma = 0.64$ mJ/mole.K^2, which corresponds to a density of states of 0.27 states/eV. atom. If the average density of states per atom in the ζ-phases is the same, then the conduction electron density of states per formula unit would be

$$\rho_c(E_F) = 3.50 \text{ states/eV.atom(formula unit)}$$

comparable to that of $CoZn_{13}$, and would imply that the Co virtual bound state is full.

The true physical situation will lie between the two extremes considered above, although without an independent estimate of the conduction electron density of states it is impossible to say exactly where.

However it is possible to select a value of $\rho_c(E_F)$ such that, with 7 d electrons on Fe atoms and 9 on Co atoms, the virtual bound state width is the same in each case. This value is $\rho_c(E_F) = 2.64$ states/eV. atom (formula unit)

(approximately 70% of that for pure zinc) and the virtual bound state width in each compound is:

$$\Delta = 0.43 \text{ eV}.$$

The choice of 9 d electrons per Co atom is not physically unreasonable, and charge transfer effects of this size have been observed in cobalt - aluminium intermetallic compounds(87).

$MnZn_{13}$ is magnetically ordered in the temperature region in which the specific heat measurements were taken and, although the data gave a satisfactory fit to the relationship $\frac{C}{T} = \gamma T + \beta T^3$, the possibility still remains that there is a spin-wave contribution to the measured γ.

Magnetic Susceptibility

The magnetic susceptibilities of the three ζ-phases demonstrate in the clearest possible way the contrasting magnetic character of the transition metal atoms in each compound. $CoZn_{13}$ has a temperature independent diamagnetic susceptibility, $FeZn_{13}$ shows an enhanced Pauli paramagnetism and $MnZn_{13}$ a definite Curie-Weiss behaviour, albeit with a rather low value of p_{eff}.

The susceptibility of $CoZn_{13}$ at 4.2 K is -0.12×10^{-6} e.m.u./gm. and is slightly more paramagnetic than pure zinc $\left(\chi_{Zn} = -0.16 \times 10^{-6} \text{ e.m.u./gm. (111)}\right)$. It is impossible to separate out the expected small Pauli paramagnetism of the almost full cobalt virtual bound state from the other contributing terms, such as the conduction electron diamagnetism and ion-core diamagnetism.

The contribution to the Pauli paramagnetism per virtual bound state is given by (equation 1.94)

$$\chi_d = \eta \mu_B^2 \rho_d(E_F)$$

where the enhancement factor $\eta = \left[1-(U + 4J) \frac{\rho_d(E_F)}{10}\right]^{-1}$

The total molar susceptibility of the $CoZn_{13}$ compound will be

$$\chi^{Co}_{Tot.} = \chi_{ion\text{-}core} + \chi_{\substack{c.e. \\ diamag.}} + \chi_{\substack{c.e. \\ paramag.}} + N\eta^{Co} \mu_B^2 \rho_d^{Co}(E_F)$$

while the total molar susceptibility of $FeZn_{13}$ will be

$$\chi^{Fe}_{Tot.} = \chi_{ion\text{-}core} + \chi_{\substack{c.e. \\ diamag.}} + \chi_{\substack{c.e. \\ paramag.}} + N\eta^{Fe} \mu_B^2 \rho_d^{Co}(E_F)$$

and the ion-core diamagnetism, conduction electron diamagnetism and conduction electron paramagnetism will be the same for each compound (except for the small difference between the ion-core diamagnetism of Fe and Co, which is ignored).

Therefore

$$\chi^{Fe}_{Tot.} - \chi^{Co}_{Tot.} = N\eta^{Fe} \mu_B^2 \rho_d^{Fe}(E_F) - N\eta^{Co} \mu_B^2 \rho_d^{Co}(E_F) \qquad 5.1$$

By subtracting the susceptibilities of $FeZn_{13}$ and $CoZn_{13}$ we have eliminated the troublesome terms.

The measured susceptibilities at room temperature for $FeZn_{13}$ and $CoZn_{13}$ are 0.30×10^{-6} e.m.u./gm. and -0.16 e.m.u./gm. respectively and their difference is 0.46×10^{-6} e.m.u./gm.

Using equation 5.1 $\eta^{Fe} \rho_d^{Fe}(E_F) - \eta^{Co} \rho_d^{Co}(E_F) =$ <u>13 states/e.V. atom</u>

From the electronic specific heat coefficients $\rho_d^{Fe}(E_F) = 4.84$ and $\rho_d^{Co}(E_F) = 0.7$, where again we have <u>assumed</u> that the conduction electron density of states = 2.65 states/eV.atom(formula unit) and $n_d = 7$ for Fe and 9 for Co. As the virtual bound state

on the Co atoms is well into the non-magnetic region, $\eta^{Co} \approx 1$. Using these values

$$\eta^{Fe} = 2.8, \text{ hence } \underline{U + 4J = 1.3 \text{ eV}}.$$

The critical condition for the occurrence of magnetism is

$$(U + 4J) \frac{\rho_d(E_F)}{10} = 1$$

And for $FeZn_{13}$ this ratio is

$$(U + 4J) \frac{\rho_d(E_F)}{10} \approx 0.6$$

The calculated values for the parameters (U + 4J) and η^{Fe} are dependent on the choice of the conduction electron density of states $\rho_c(E_F)$ of the ζ-phases, as this is needed to deduce $\rho_d(E_F)$ from the measured γ values. Selecting a lower value of $\rho_c(E_F)$ has the effect of reducing the apparent (U + 4J).

An upturn was observed in the susceptibilities of all three ζ-phase $FeZn_{13}$ compounds at low temperatures, in two cases the magnitudes were similar and the resistance ratios of these specimens was > 30. In the third specimen the magnitude of the low temperature increase was a factor of two larger, but this sample only had a resistance ratio of 7, which is poor compared with other $FeZn_{13}$ specimens measured. One possible explanation is that a fraction of the Fe atoms are occupying the wrong lattice positions resulting in nearest neighbour pairs. As the Fe atoms on their correct lattice sites are already close to the critical condition for magnetism, these nearest neighbour pairs could become magnetised via a direct transfer interaction (section 1.2) and give rise to a Curie-Weiss susceptibility. No firm conclusion can be reached on the basis of the existing measurements, however if a localised moment <u>does exist</u> on each Fe atom its magnitude is

only of the order of $p_{eff} \simeq 0.14\ \mu_B$.

The susceptibility of $MnZn_{13}$ obeys a Curie-Weiss law above 120 K, with an effective moment $p_{eff} = 1.82\ \mu_B$ and a θ of 36 K. The predominant magnetic interaction between the Mn atoms will be of the Caroli form, which arises from the consecutive resonant scattering of conduction electrons by the spin-split virtual bound states (see section 1.2). In the molecular field theory and assuming a free-electron-like conduction band Caroli and Blandin (46) have shown that the Curie-Weiss θ is given by (see equation 1.72):

$$k_B\theta = \frac{25\ E_F}{6\pi} \sum_{R \neq 0} \sum_{\sigma,\sigma'} \sigma\sigma' \sin\phi^{\sigma} \sin\phi^{\sigma'} \frac{\cos(2k_F R + \phi^{\sigma} + \phi^{\sigma'})}{(k_F R)^3}$$

where the summation is over all the Mn atoms in the crystal (excluding the one at the origin) and ϕ^{σ} is the phase shift for spin σ.

The measured moment on each Mn atom corresponds to a spin of 0.55 and may be pictured in terms of a partially spin-split virtual bound state. The difference in spin $\uparrow$ and spin $\downarrow$ occupation numbers is

$$n_d^{\uparrow} - n_d^{\downarrow} = 1.1$$

The actual values $n_d^{\uparrow}$ and $n_d^{\downarrow}$ depend upon the number of conduction electrons which Mn contributes to the conduction band.

With 5 localised d electrons on each Mn atom (i.e. 2 have been contributed to the conduction band):

$$n_d^{\uparrow} + n_d^{\downarrow} = 5$$

and $$n_d^{\uparrow} - n_d^{\downarrow} = 1.1$$

$$\therefore \quad n_d^{\uparrow} = 3.05 \quad \text{and} \quad \phi^{+} = \frac{\pi}{5} n_d^{\uparrow} = 0.61\pi$$

and $$n_d^{\downarrow} = \cancel{2.45}\ 1.95 \quad \text{and} \quad \phi^{-} = \frac{\pi}{5} n_d^{\downarrow} = 0.39\pi$$

The d occupation numbers and phase shifts assuming 6 localised electrons are

$$n_d^{\uparrow} = 3.55 \quad \text{and} \quad \phi^{+} = 0.71\pi$$
$$n_d^{\downarrow} = 2.45 \quad \text{and} \quad \phi^{-} = 0.49\pi$$

and with 7 localised electrons

$$n_d^{\uparrow} = 4.05 \quad \text{and} \quad \phi^{+} = 0.81\pi$$
$$n_d^{\downarrow} = 2.95 \quad \text{and} \quad \phi^{-} = 0.59\pi$$

In the free-electron approximation the Fermi energy E_F is given by

$$E_F = 36.1 \left(\frac{n_c}{\Omega}\right)^{\frac{2}{3}}$$

where n_c is the number of "free" electrons per unit cell and Ω is the unit cell volume in $(A^{\circ})^3$. Assuming that each Mn atom contributes 2 electrons and each zinc 2, then

$$E_F = 9.4 \text{ eV.}$$

and $k_B\theta = 12.2 \sum_R \cdots$ eV.

$$\text{Hence } \theta = 14.2 \times 10^4 \sum_R \cdots \text{ K}$$

The lattice sum of an expression $\dfrac{\cos(2k_F R + \phi)}{(k_F R)^3}$ has been computed as a function of ϕ for various values of k_F using the lattice parameters of Brown (93), and the results are shown in figure 5.4.

To check on the convergence of the summation the computer was asked to print out values of the sum over successively larger spherical volumes of the crystal out to $50A^{\circ}$ and typical results are shown below for $k_F = 1.58\ (A^{\circ})^{-1}$ and $\phi = 0.0\pi$

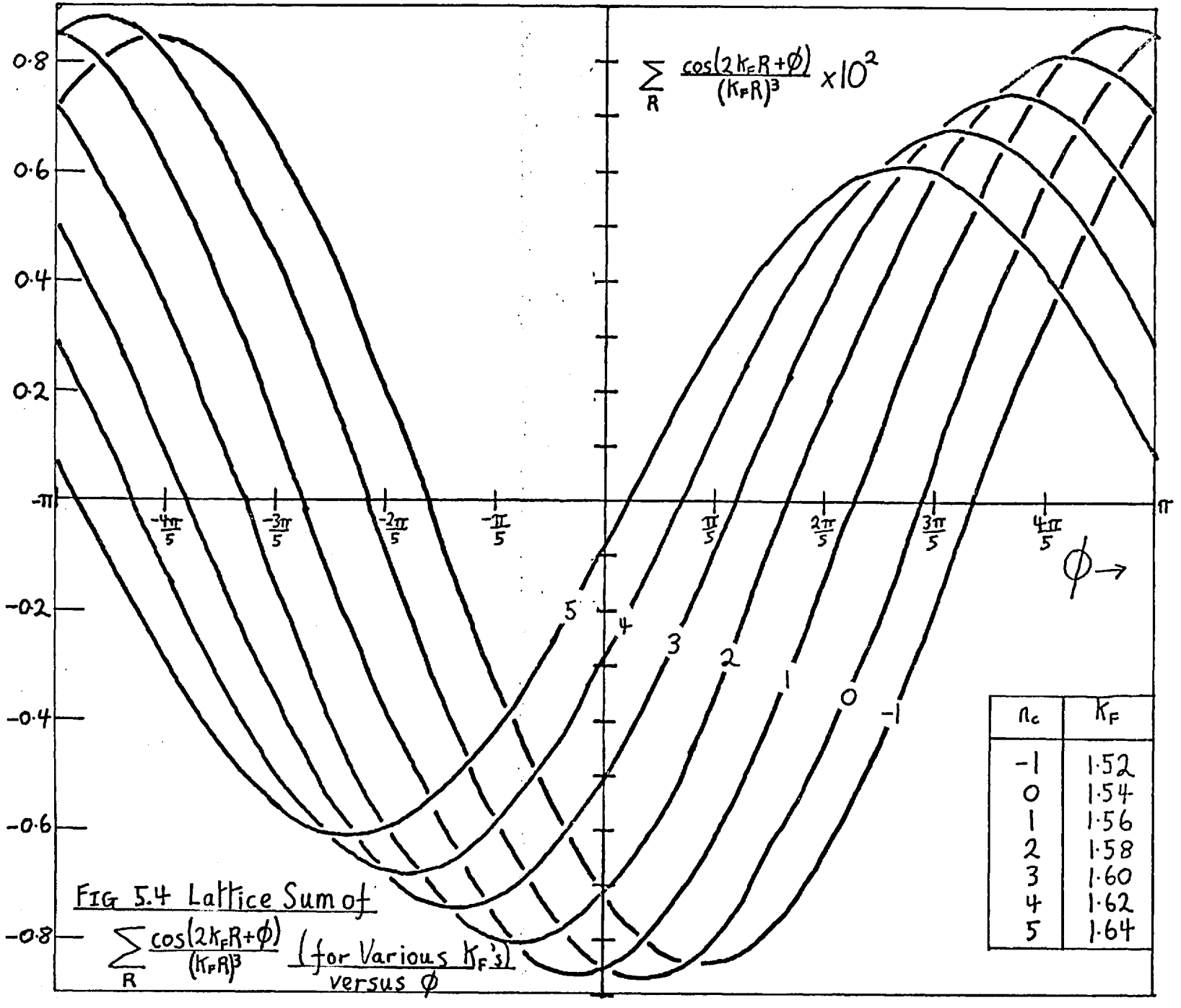


FIG 5.4 Lattice Sum of $\sum_R \frac{\cos(2k_F R+\phi)}{(k_F R)^3}$ (for Various k_F's) versus ϕ

Radius of Spherical Volume	6A°	10A°	20A°	30A°	40A°	50A°
$\sum_R \frac{\cos(2k_F R + \phi)}{(k_F R)^3} \times 10^2$	0.3719	0.5255	0.7497	0.7863	0.8040	0.8032

Using the computed values of the lattice sum the Curie-Weiss θ has been calculated for n_d = 5, 6 and 7 electrons as a function of k_F and the results are shown in figure 5.5. The range of possible values is large ($\pm$ 500 K) compared with the measured θ of 36 K. Choosing n_d = 6 electrons a 1% variation from the free-electron value of k_F is required to fit the experimental θ. This variation is plausible in view of the previous discussion about conduction electrons in the ζ-phases, in fact it is surprising that a calculation based on the free-electron model gives even this degree of agreement with experiment.

The high temperature effective moment on each Mn atom in $MnZn_{13}$ is small compared to the value found in dilute ZnMn alloys, where a moment of $4.1\mu_B$ is observed (72). There are two possible explanations for this behaviour. The low moment could be due to some feature of the immediate local environment at each transition metal site i.e. due to the distribution of the 12 zinc nearest neighbours, or alternatively it could be due to the fact that the Mn atoms lie on a regular crystal lattice.

To check these possibilities a specimen of $Mn_{0.05}Fe_{0.95}Zn_{13}$ was prepared. This composition represents a 5% solution of $MnZn_{13}$ in $FeZn_{13}$ and the Mn atoms substitute for Fe atoms at random sites, but they retain the same local

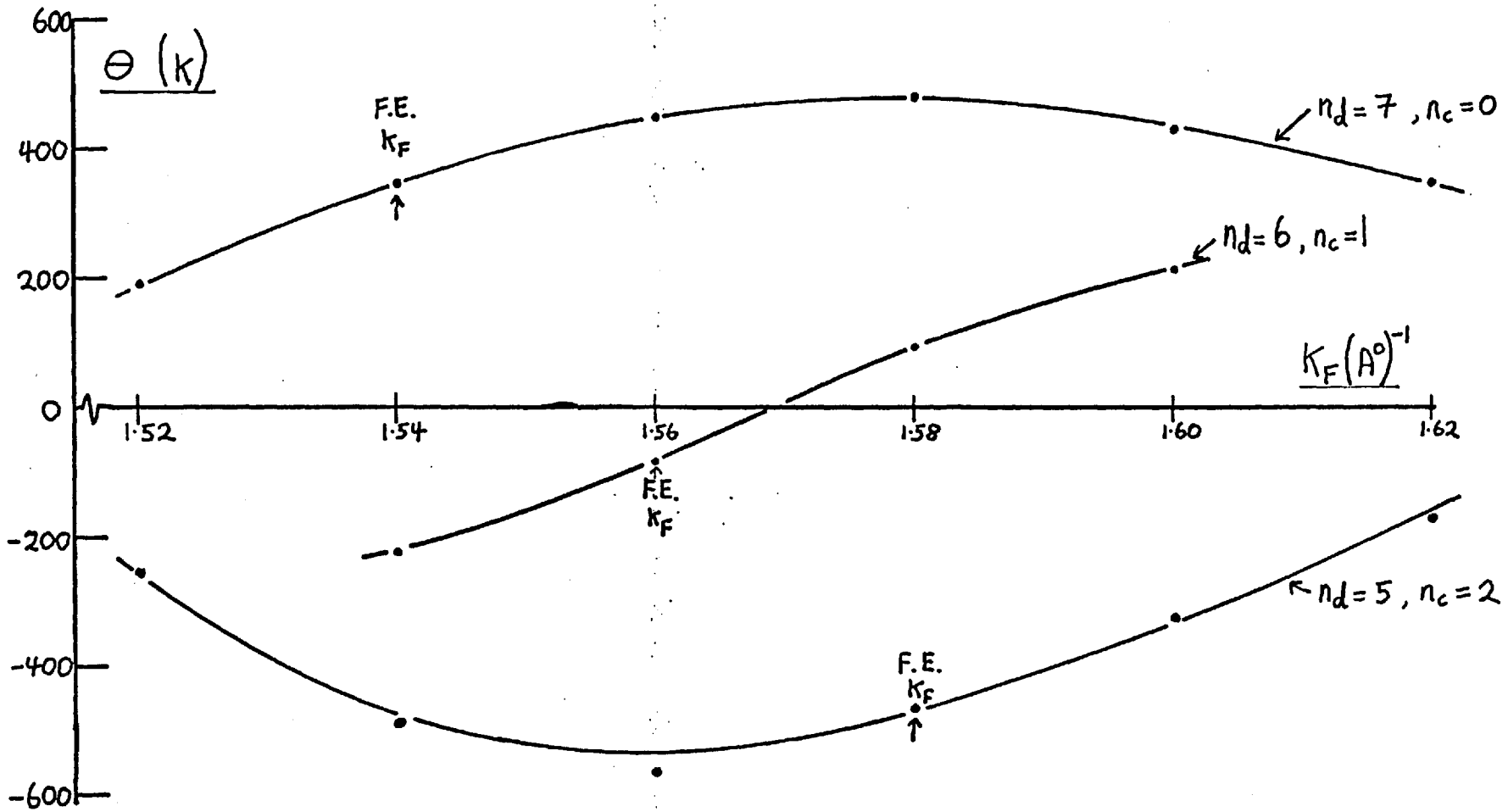


Fig 5.5 Calculated Curie-Weiss Θ as a Function of K_F for Different Numbers of Localized d-electrons in $MnZn_{13}$

(i.e. nearest neighbour) environment as in the pure $MnZn_{13}$. The magnetic susceptibility of this sample showed a Curie law susceptibility above 20 K and an effective moment per Mn atom of $4.0\,\mu_B$, the same value as found in dilute Zn-Mn alloys. This indicates that the translational symmetry of $MnZn_{13}$ is an important factor in modifying the virtual bound state parameters which characterise the transition metal atom d states - in this particular case it may be interpreted as an increase in the amount of overlap between the spin ↑ and spin ↓ halves of the virtual bound state. In Daniel's model (47) for dilute transition metal intermetallic compounds (discussed in section 1.3), coherent hybridization between the conduction electrons and the d electrons on each transition atom which does yield such a broadening is assumed to be important only in the magnetically ordered regime, when the conduction electron scattering at each site is coherent. ζ-phase $MnZn_{13}$ provides an example of a situation where some component of the hybridization has remained coherent into the paramagnetic regime, although the spin dependent electron scattering is now incoherent from site to site.

The apparent low aligned moment of $0.3\,\mu_B$ on each Mn atom in the magnetically ordered regime is difficult to explain, particularly if the form of the order is simple ferromagnetism. The neutron diffraction measurements on a polycrystaline sample of $MnZn_{13}$ produced no evidence for the existence of antiferromagnetism or of complex long wavelength screw or spiral types of order, but until a suitably sized single crystal is available it is impossible to be certain. However a low effective moment is at least consistent with Daniel's suggestion that the d states

in a dilute transition metal intermetallic compound will be broadened by coherent hybridization with the conduction electrons in the magnetically ordered regime. This would result in an increase in the amount of overlap between the two halves of the virtual bound state and reduce the effective moment.

Electrical Resistivities

The electrical resistivities of the three ζ-phases again demonstrate the contrasting behaviour of the transition metal atoms in each compound. The room temperature resistivities are high - 100, 30 and 20 $\mu\Omega$cm. for $MnZn_{13}$, $FeZn_{13}$ and $CoZn_{13}$ respectively, but they have quite good resistance ratios, - generally between 10 and 40. The resistivities of all three compounds are strongly temperature-dependent at low temperatures, although showing a different power law in each case.

The resistivity of $MnZn_{13}$ below 4.2 K is exactly proportional to $T^{\frac{3}{2}}$. This form of temperature dependence has also been observed by Stewart (112) in certain dilute intermetallic compounds of Rare-Earth metals with zinc below their magnetic ordering temperatures. Liu (64) has predicted (see section 1.4) that in ferromagnetic materials in which the coupling between the local magnetic moments is mediated entirely via the conduction electrons there should be a $T^{\frac{3}{2}}$ term in the resistivity in addition to the T^2 term previously predicted ((63) and section 1.4). Both $MnZn_{13}$ and the dilute Rare-Earth-zinc compounds investigated by Stewart, are obvious choices for systems which satisfy Liu's conditions for the coupling mechanism, although in neither case has the form of the magnetic ordering been determined with certainty. At temperatures closer to the

ordering temperature the resistivity is described by an equation of the form $\rho(T) = \rho_0 + AT^{\frac{3}{2}} + BT^{\frac{5}{2}}$, a T^2 term is not observed. No explanation for this particular dependence is offered, but it is surprising that a two polynomial fit should be applicable to within 3 K of the transition temperature.

The resistivity of $FeZn_{13}$ below 8 K is well described by a T^2 law, $\rho = \rho_0 + AT^2$ with $A=0.7 \times 10^{-3}\ \mu\Omega cm./K^2$.

A similar dependence has been observed by Schindler and Coles (113) in pure Pd and Pd-Ni dilute alloys, where the exchange enhancement of the pure Pd susceptibility may be increased by the addition of Ni. Their value of A for pure Pd is $0.026 \times 10^{-3}\ \mu\Omega cm./K^2$ and increases to $0.513 \times 10^{-3}\ \mu\Omega cm./K^2$ for a Pd - 1.66 at.% Ni alloy and the behaviour is interpreted in terms of electron scattering by localised spin fluctuations in the Pd d band.

The resistivity behaviour of $FeZn_{13}$ may be explained in terms of a virtual bound state picture. At T = 0 the strong electron scattering at each transition atom site is repeated in each unit cell and, as the transition atoms lie on a regular crystal lattice, the total scattering will be coherent and non-dissipative leading to a vanishing resistivity. At finite temperatures the spin $\uparrow$ and spin $\downarrow$, virtual bound states fluctuate $\sim kT$ about the Fermi energy with resulting changes in their occupancy. The scattering phase shifts are no longer the same in each unit cell and this leads to a finite resistivity. The effect of the enhancement factor η is to introduce correlations into the spin $\uparrow$ and spin $\downarrow$ occupation numbers and increase the magnitude of these fluctuations to $\pm \eta kT$. This

description is essentially equivalent to that of s - d electron-electron scattering in materials such as Pd and Pd-Ni, except that it is inappropriate to speak of a d band in the ζ-phases, and also any enhancement effects are occurring locally on the transition atom sites. A parallel may also be drawn with the localised spin fluctuation theory for the resistivities of dilute alloys of the Al-Mn type (discussed in section 1.1). In these alloys the electron scattering phase shift is the same at each Mn atom at T = 0, but as the atoms are randomly distributed the resistivity is still finite. In ζ-phase $FeZn_{13}$ however we have seen that the resistivity is zero at T = 0 because of the translational symmetry. The effect of a fluctuating virtual bound state occupancy at finite temperatures leads to a decrease in the resistivity of Al-Mn while just the opposite effect is expected in an ordered compound. The observed temperature dependence of T^2 is characteristic of electron-electron scattering.

The failure to observe a T^2 term in the resistivity of $Co\text{-}Zn_{13}$ may be due to a combination of reasons. The phonon resistivity of all three ζ-phases is large (which itself could be due to a reduction in the Fermi-surface area due to Jones zone contact) and this, combined with a rather large residual resistivity, would tend to mask a small T^2 term until very low temperatures - even the large T^2 term in the resistivity of $FeZn_{13}$ is overtaken at 10 K by the phonon resistivity. If the virtual bound state on each Co atoms contains $\sim$9 electrons the d-like density of states will be correspondingly reduced compared to that for $FeZn_{13}$ and the change in electron scattering

phase shift as the virtual level fluctuates by $\pm$ kT will also be reduced. In addition to this the enhancement factor for the Co virtual bound state is effectively 1. An alternative explanation, and one which neither the specific heat nor magnetic susceptibility measurements have been able to conclusively rule out, is that the virtual bound state is <u>full</u> in $CoZn_{13}$, in which case the T^2 term would not exist. On the basis of the accuracy of the resistivity measurements the T^2 term in $CoZn_{13}$, if one exists at all, must be at least a factor of ten smaller than for $FeZn_{13}$.

It is difficult to offer an explanation for the low temperature magneto-resistance of $CoZn_{13}$ where an $H^{\frac{3}{2}}$ dependence is observed up to the maximum available field of 20 K.Gauss to within the accurracy of measurement. This may be compared with the commonly found dependencies of H or H^2 depending upon the topography of the Fermi surface, although in certain circumstances the magneto-resistance may show an initial dependence of H^2 which slowly goes over to a linear dependence in very high fields (for a discussion see (114)).

The electrical resistivity of the $Mn_{0.05}Fe_{0.95}Zn_{13}$ specimen shows a typical Kondo anomaly and the position of the minimum coincides with that observed in a dilute <u>Zn</u>-0.4 at.% Mn alloy by Collings et.al. (115). This provides further evidence that a Mn atom in the immediate local environment provided by the ζ-phase structure, but without the translational symmetry of the <u>pure</u> $MnZn_{13}$ compound, shows the same behaviour as when in dilute solution in zinc.

The extraordinarily large g-shift of $MnZn_{13}$ at low temperatures is difficult to understand. A resonance has previously been reported in a Zn-0.4 at.% Mn alloy (115), however Taylor (116) has recently been unable to confirm this finding in his measurements on Zn-0.1 at.% Mn and Zn-0.4 at.% Mn alloys in both annealed and un-annealed states. This again might suggest that some feature of the immediately local environment (i.e. the nearest neighbour Zn atoms) is responsible for the fact that a resonance is observed at all in $MnZn_{13}$. However a search for a resonance in the $Mn_{0.05}Fe_{0.95}Zn_{13}$ specimen down to 2 K failed to show any signal and in this mixed compound the Mn atoms are surrounded by an identical local arrangement of zinc atoms to that in pure $MnZn_{13}$.

One feature of the observed resonance which may be of significance is that the g-shift begins, and in fact the signal itself appears, at a temperature close to where the first deviations from a pure Curie-Weiss susceptibility behaviour are observed (120 K). In this case the E.S.R. signal and its behaviour may be a manifestation of the onset of short-range magnetic order at temperatures a factor 4 or 5 times higher than the critical temperature for the onset of long-range order.

Conclusion

A close correlation has been found between the magnetic properties of the transition metal atoms in the ζ-phase compounds and the corresponding dilute solid solution in zinc, where Mn, Fe and Co are magnetic, on the borderline and non-magnetic respectively. This offers support to the suggestion

that the magnetic state of the transition metal atom is determined by its local environment and that s - d hybridization is the dominant interaction. The magnetic and electronic properties of the compounds have been described in terms of a virtual bound state picture and the findings are consistent with d occupation numbers of 6, 7 and 9 for Mn, Fe and Co respectively, although the possibility of a completely full virtual bound state in the case of $CoZn_{13}$ cannot be excluded.

There is evidence from the unusual magnetic properties of $MnZn_{13}$ that the periodicity of the structure has its role to play in modifying the character of the virtual bound state, however a theoretical account of how this might occur still awaits development.

REFERENCES

1. J. H. WASZINK, Thesis, University of London, 1965
2. J. FRIEDEL, Can. J. Phys. 34, 1190, 1956

   " Nuovo Cimento. Suppl. 7, 287, 1958
3. W. KOHN and S. H. VOSKO, Phys. Rev. 119, 912, 1960
4. M. H. MARCH and A. M. MURRAY, Proc. Roy. Soc. A261, 119, 1961
5. A. BLANDIN and J. FRIEDEL, J. Phys. Rad. 20, 160, 1959
6. P. W. ANDERSON, Phys. Rev. 124, 41, 1961
7. K. YOSIDA; A. KIJI, and S. CHIKAZUMI, Prog. Theor. Phys. (Kyoto), 33, 559, 1965
8. A. P. KLEIN and A. J. HEEGER, Phys. Rev. 144, 458, 1966
9. P. A. WOLFF, Phys. Rev. 125, 439, 1962
10. B. T. MATTHIAS, M. PETER, H. J. WILLIAMS, A. M. CLOGSTON, E. CORENZWIT, and R. C. SHERWOOD, Phys. Rev. Letters, 5, 542, 1960

    A. M. CLOGSTON, Phys. Rev. 125, 439, 1962
11. G. F. KOSTER and J. C. SLATER, Phys. Rev. 96, 1208, 1954
12. J. R. SCHRIEFFER and D. C. MATTIS, Phys. Rev. 140, A1412, 1965
13. B. KJÖLTERSTRÖM, D. J. SCALAPINO and J. R. SCHRIEFFER, Phys. Rev. 148, 665, 1966
14. J. R. SCHRIEFFER and P. A. WOLFF, Phys. Rev. 149, 491, 1966
15. J. KONDO, Prog. Theor. Phys. 32, 37, 1964
16. T. KASUYA, Prog. Theor. Phys. 16, 45, 1956
17. K. YOSIDA, Phys. Rev. 106, 893, 1957
18. M. P. SARACHIK, J. Appl. Phys. 35, 1094, 1964

    M. P. SARACHIK, E. CORENZWIT and L. D. LONGINOTTI, Phys. Rev. 135, A1041, 1964
19. A. A. ABRIKOSOV, J. Exptl. Theor. Phys. (U.S.S.R.), 48, 990, 1965

19. A. A. ABRIKOSOV, Physics, 2, 5, 1965

20. H. SUHL, Phys. Rev. 138, A515, 1965

" Phys. Rev. 141, 483, 1966

21. Y. NAGAOKA, Phys. Rev. 138, A1112, 1965

22. D. R. HAMANN, Phys. Rev. 158, 570, 1967

23. P. E. BLOOMFIELD and D. R. HAMANN, Phys. Rev. 164, 856, 1967

24. J. ZITTARTZ and E. MULLER-HARTMANN, Z. Physik, 212, 380, 1968

25. P. LEDERER and D. L. MILLS, Phys. Rev. 165, 837, 1968

26. A. D. CAPLIN and C. RIZZUTO, Phys. Rev. Letters, 21, 746, 1968

27. N. RIVIER and M. J. ZUCKERMANN, Phys. Rev. Letters, 21, 904, 1968

28. H. SUHL, Phys. Rev. Letters, 19, 442, 1967

M. J. LEVINE and H. SUHL, Phys. Rev. 171, 567, 1968

29. H. ALLOUL, P. BERNIER, H. LAUNOIS and J. POIJET, Tech. Report of I.S.P. University of Tokyo, Series A, No. 442 1970

30. N. RIVIER, Thesis, University of Cambridge, 1968

31. C. ZENER, Phys. Rev. 81, 440, 1951

32. H. FROHLICH and F. R. N. NABARRO, Proc. Roy. Soc. A175, 382, 1940

33. A. H. MITCHELL, Phys. Rev. 105, 1439, 1957

34. R. E. WATSON and A. J. FREEMAN, Phys. Rev. 152, 566, 1966

" " Phys. Rev. 178, 725, 1969

35. M. A. RUDERMAN and C. KITTEL, Phys. Rev. 96, 99, 1954

36. P. G. DE GENNES, J. Phys. Rad. 23, 510, 1962

37. B. CAROLI, Thesis, University of Paris, 1966

" J. Phys. Chem. Sol. 28, 1427, 1967

38. S. ALEXANDER and P. W. ANDERSON, Phys. Rev. 133, A1594, 1964

39. T. MORIYA, Prog. Theor. Phys. 33, 157, 1965

40. D. J. KIM, Phys. Rev. B, 1, 3725, 1970

41. M. W. KLEIN and R. BROUT, Phys. Rev. 124, 2412, 1958

42. M. W. KLEIN, Phys. Rev. 136, A1156, 1964

" Phys. Rev. 141, 489, 1966

43. S. H. LIU, Phys. Rev. 157, 411, 1967

44. B. R. COLES, W. HUME-ROTHERY and H. P. MYERS, Proc. Roy. Soc. 196A, 125, 1949

45. D. P. OXLEY, R. S. TEEBLE and K. C. WILLIAMS, J. Appl. Phys. 34, 1362, 1963

46. B. CAROLI and A. BLANDIN, J. Phys. Chem. Solids, 27, 503, 1966

47. E. DANIEL, Sol. Stat, Comm. 9, 1359, 1971

48. D. BIJL, Prog. Low Temp. Phys. 2, 395, 1957

49. J. VAN KRONENDANK and J. H. VAN VLECK, Rev. Mod. Phys. 30, 1, 1958

50. A. R. MACKINTOSH, Phys. Letters, 4, 140, 1963

51. J. H. VAN VLECK, "The Theory of Electric and Magnetic Susceptibilities", Oxford University Press, 1932

52. N. F. MOTT and H. JONES, "The Theory of the Properties of Metals and Alloys", Clarendon Press, Oxford, 1936.

53. C. P. FLYNN, D. A. RIGNEY and J. A. GARDNER, Phil. Mag. 15, 1255, 1967

54. VAN LEEUWEN, Thesis, Leiden, 1919

55. R. E. PEIERLS, Zeits. for Physik, 80, 786, 1933

56. MOTT and JONES, p. 208 see ref(52)

57. E. GRUNEISEN, Ann. PHYSIK, 16 (5), 530, 1933

58. ZIMAN, "Electrons and Phonons", Oxford University Press, p. 360 and 373, 1960

59. N. F. MOTT, Proc. Phys. Soc. 47, 571, 1935

60. W. G. BABER, Proc. Roy. Soc. 158A, 383, 1937

61. ZIMAN, "Electrons and Phonons" p. 416

62. G. K. WHITE and S. B. WOODS, Phil. Trans. Roy. Soc. (London), Series A251, 273, 1959

63. I MANNARI, Prog. Theor. Phys. 22, 335, 1959

64. S. H. LIU, J. Appl. Phys. 35, 1087, 1964

65. J. FRIEDEL and P. DE GENNES, J. Phys. Chem. Solids, 4, 71, 1958

66. A. A. ABRIKOSOV, Physics, 2, 5, 1965

67. G. BOATO, M. BUGO and C. RIZZUTO, Nuovo Cimento, 45, 226, 1966

68. F. T. HEDGCOCK and W. B. MUIR, Phys. Rev. 129, 2045, 1963

69. F. T. HEDGCOCK and C. RIZZUTO, Phys. Rev. 163, 517, 1967

70. D. L. MARTIN, Phys. Rev. 167, 640, 1968

71. P. J. FORD, C. RIZZUTO and E. SALAMONI, to be published

72. E. W. COLLINGS, F. T. HEDGCOCK and Y. MUTO, Phys. Rev. 134, 1521, 1964

73. D. L. MARTIN, Phys. Rev. 167, 640, 1968

74. D. L. MARTIN, Phys. Rev. 186, 642, 1969

75. G. BOATO, C. RIZZUTO and J. VIG, Proc. L.T.10, Moscow, 4, 292, 1966

76. G. BOATO, G. GALLINARO and C. RIZZUTO, Phys. Rev. 148, 353, 1966

77. A. D. CAPLIN, Phys. Letters, 26A, 46, 1967

78. J. H. WASZINK and B. R. COLES, Proc. Phys. Soc. 92, 731, 1967

79. J. SCHRAMM, Z. Metallk, 30, 327, 1938

80. Y. NAKAGAWA, S. SAKAI and T. HARI, J. Phys. Soc., Japan 17, Suppl. B1, 168, 1962

81. A. HERR, Thesis, Strasbourg, 1970

82. N. M. WOLCOTT and R. L. FALGE, Phys. Rev. 171, 591, 1968

83. G. FOËX and J. WUCHER, J. Phys. Radium, 17, 454, 1956

84. M. A. TAYLOR, Proc. Phys. Soc. 78, 1244, 1961

85. G. V. RAYNOR, Prog. Metal Phys. 1, 1, 1949

86. W. HUME-ROTHERY and B. R. COLES, Adv. Phys. 3, 149, 1954

87. A. WENGER, G. BURRI and S. STEINEMANN, Sol. State, Comm. 9, 1125, 1971

88. HANSEN, "Constitution of Binary Alloys", 2nd Edition, McGraw-Hill Book Company, 1958

89. J. SCHRAMM, Z. Metallk. 29, 222, 1937

90. J. SCHRAMM, Z. Metallk. 30, 10, 1938

" " 30, 122, 1938

91. J. SCHRAMM, Z. Metallk. 32, 399, 1940

" " 30, 131, 1938

92. F. GOTZL, F. HALLA and J. SCHRAMM, Z. Metallk. 33, 373, 1941

93. P. J. BROWN, Acta Cryst. 15, 608, 1962

94. J. SCHRAMM, Z. Metallk, 30, 10, 1938

95. Int. Tab. X-ray Cryst. Vol. III page 218, Kynoch Press, 1962

96. G. W. BRINDLEY, Phil. Mag. 36, 347, 1945

97. G. V. RAYNOR and D. W. WAKEMAN, Proc. Roy. Soc. A190, 82, 1947

G. V. RAYNOR and B. J. WARD, J. Inst. Metals, 86, 182, 1957/58

98. J. W. H. CLARE, J. Inst. Metals, 89, 232, 1961

99. H. HARTMANN, W. HOFFMANN, D. MÜLLER, Abhandl. Baunschweig. Wiss. Ges. 7, 100, 1955

100. H. E. N. STONE, Private Communication

101. J. SCHRAMM, Z. Metallk, 32, 399, 1940

102. D. GRIFFITH, Thesis, University of London, 1961

103. G. WILLIAMS, Thesis, University of London, 1967

104. LANDAU and LIFSHITZ, "Electro-dynamics of Continuous Media" London, Pergamon

105. A. P. MURANI, Thesis, University of London, 1969

106. F. E. HOARE and F. WALLING, Proc. Roy. Soc. 212, 139, 1952

107. A. ARROTT, Phys. Rev. 108, 1394, 1957

108. G. K. WHITE, "Experimental Techniques in Low Temperature Physics", Oxford, Clarendon Press, 1959

109. R. L. ROSENBAUM, Rev. Sci. Instrum. 39, 890, 1968

110 POWELL, BURCH, CORRUCINI, Cryogenics, 1, 139, 1960

111. A. E. BELL, Private communication

112. A. M. STEWART, Thesis, University of London, 1971

113. A. I. SCHINDLER and B. R. COLES, J. Appl. Phys. 39, 956, 1968

114. For a discussion of magneto-risistance see ZIMAN "Electrons and Phonons"

115. E. W. COLLINGS, F. T. HEDGCOCK and W. B. MUIR L.T.8 .Proc , 25. LONDON. 1962

116. R. H. TAYLOR, Private communication